Space-, Time-, and Frequency-Domain Permutation Modulation Designed for Microwave and Optical Wireless Communications

Naoki Ishikawa

Supervisors: **Dr. Shinya Sugiura.**

Dr. Keiichi Kaneko.

Department of Electronic and Information Engineering

Graduate School of Engineering

Tokyo University of Agriculture and Technology

This dissertation is submitted for the degree of

Doctor of Philosophy in Engineering

February 2017

Dedicated to my family

Acknowledgements

I would like to acknowledge my sincere appreciation to Associate Prof. Shinya Sugiura, who has continuously supervised me for four years. He has made extensive contributions to this endeavor. Four years ago, in my third year of undergraduate studies, I was given a laboratory assignment at the beginning of March. From that time on, he has taught me the following skills on an almost daily basis: how to survey literature, establish a research topic, plan my research, simulate a system, write a strong academic paper, create a presentation, and apply for public funding, among other skills. Since I was the first student in his research group, I was fortunate to receive a wealth of educational resources from my supervisor. His constant and generous supervision helped me to complete this doctoral thesis; thanks to him, I was able to proceed with my research in a privileged environment, which led to success with my PhD degree.

This thesis contains the contributions of our collaborative research with the University of Southampton. During my stay at the university as a short-term academic visitor, I became indebted to Prof. Lajos Hanzo, Associate Prof. Mohammed El-Hajjar, Dr. Rakshith Rajashekar, and Dr. Chao Xu. Thanks to their warm and welcoming attitude, I was able to focus on my research topic and explore a new research field. Although I have returned to Japan, with invaluable memories, I am glad that our collaborative research has continued.

It was a pleasure to have taken the thesis examination with Prof. Keiichi Kaneko, Prof. Nariyoshi Yamai, Associate Prof. Hironori Nakajo, and Associate Prof. Shun Watanabe. I greatly appreciate the precious time they devoted to my research. Their valuable insights and comments have clearly refined this thesis.

I would also like to express my gratitude to the faculty and staff at our university. Associate Prof. Yuichi Tanaka and Associate Prof. Kentaro Iwami helped me to apply for the JSPS research fellowship, which is known as a gateway to academic research in Japan. Associate Prof. Takako Ochi at the International Center supervised my application for the short-term study-abroad fund. The secretaries for our research group have helped me to complete paperwork daily. The university staff has supported my fund applications with unceasing dedication. Their voluntary contributions indirectly helped me to develop this thesis.

In addition, I am grateful to the students and researchers who provided insightful comments at the international and domestic conferences. In particular, Prof. Hideki Ochiai pointed out a critical aspect related to the origin of subcarrier index modulation. The outstanding PhD candidates I met at the summer school held by the IEEE Communications

Society motivated me to accomplish my thesis. Although the academic review is a voluntary task, anonymous reviewers made a number of fairly important comments. They definitely contributed to improving my papers, which are the basis of this thesis.

I owe my thanks to every student in my group. I feel quite nostalgic when I remember our travels to Yatsugatake, Chichibu, Akihabara, and Seoul. I am proud to have finished my PhD journey with you.

The research topics for this thesis consist of the permutation-based modulation techniques for single- and multi-carrier microwave communications, as well as visible light communications. It was a huge burden for me to survey and establish each research topic, because I began my studies in the department of information engineering. Throughout my graduate school days, my dear friends, some of whom are aspiring PhD candidates, have supported and encouraged my PhD journey. Indeed, every time I talked with my friends, I felt peace of mind. I appreciate their unofficial support of my thesis.

My parents, Satoru and Atsuko, have raised me and my brothers, Takumi and Shinya, with unconditional love and extreme patience. Because they gave me various opportunities to challenge anything, I am about to obtain my PhD and begin my life as a doctoral researcher.

Many thanks to everyone who has contributed to this thesis.

With gratitude,
Naoki Ishikawa

List of Publications

Journal papers (4)

1. **N. Ishikawa**, R. Rajashekar, S. Sugiura, and L. Hanzo, "Generalized spatial modulation based reduced-RF-chain millimeter-wave communications," *IEEE Transactions on Vehicular Technology (Correspondence)*, vol. 66, no. 1, pp. 879–883, 2017.

2. **N. Ishikawa**, S. Sugiura, and L. Hanzo, "Subcarrier-index modulation aided OFDM – will it work ?" *IEEE Access*, vol. 4, pp. 2580–2593, 2016.

3. **N. Ishikawa** and S. Sugiura, "Maximizing constrained capacity of power-imbalanced optical wireless MIMO communications using spatial modulation," *Journal of Lightwave Technology*, vol. 33, no. 2, pp. 519–527, 2015.

4. **N. Ishikawa** and S. Sugiura, "Unified differential spatial modulation," *IEEE Wireless Communications Letters*, vol. 3, no. 4, pp. 337–340, 2014.

Conference papers (2)

5. **N. Ishikawa** and S. Sugiura, "EXIT-chart-based design of irregular-precoded power-imbalanced optical spatial modulation," in IEEE 82nd Vehicular Technology Conference (VTC Fall), Boston, USA, September 2015, 5 pages.

6. **N. Ishikawa** and S. Sugiura, "Single- and multiple-RF aided non-coherent generalized spatial modulation," in IEEE 79th Vehicular Technology Conference (VTC Spring), Seoul, Korea, May 2014, 5 pages.

Related journal paper (1)

7. R. Rajashekar, **N. Ishikawa**, S. Sugiura, K. V. S. Hari, and L. Hanzo, "Full-diversity dispersion matrices from algebraic field extensions for differential spatial modulation," *IEEE Transactions on Vehicular Technology*, vol. 66, no. 1, pp. 385–394, 2017.

Abstract

In this thesis, we propose the permutation modulation (PM) based encoding schemes for the multiple-input multiple-output (MIMO) microwave and visible light communications (VLCs) systems.

In Chapter 1, we reconstitute the Slepian's PM concept, which was originally proposed in 1965. The extended PM concept subsumes the conventional low-complexity schemes, such as the spatial modulation and the subcarrier index modulation, both of which were proposed in 2008 and 2009, respectively.

In Chapter 2, we review the PM schemes having been proposed for the single and multicarrier microwave as well as VLCs. We introduce the three performance metrics: throughput, reliability, and complexity, which are useful tools for evaluating the positive and negative effects of the PM concept.

In Chapter 3, we propose the PM-based differential MIMO scheme, which depends on the permutation matrix. Different from the conventional binary-based scheme, the proposed scheme has a flexible dispersion matrix architecture. The proposed scheme enables both the single radio frequency (RF) operation at the transmitter and the channel-estimation free detection at the receiver. In addition, the flexible architecture achieves a higher diversity order than the conventional scheme.

In Chapter 4, we propose the PM-based millimeter-wave scheme. We reveal that the proposed PM-based millimeter-wave transmitter is capable of reducing the number of RF chains. More specifically, the proposed scheme maintains the near-capacity performance of the conventional spatial multiplexing scheme, while the beamforming gain of the proposed scheme is lower than that of the conventional scheme.

In Chapter 5, we apply the PM concept to MIMO-VLC, where we introduce a flexible power allocation method for combating the highly-correlated VLC channels. We propose a unified architecture that subsumes the conventional PM-based schemes. Then, we design our proposed scheme so as to maximize the mutual information. From the information-theoretic perspective, we conclude that the proposed scheme has performance advantages over the conventional schemes.

In Chapter 6, we analyze the PM-based orthogonal frequency-division multiplexing (OFDM) scheme. We provide the information-theoretic analysis in terms of minimum Euclidean distance, unconstrained and constrained mutual information, and peak-to-average power ratio. Then, the upper-bound of the minimum Euclidean distance is derived for constituting the design guidelines of the PM-based scheme. According to our analysis, the PM-based OFDM scheme is beneficial over the conventional OFDM scheme for low-rate scenarios.

Contents

List of Figures

List of Tables

Nomenclature

Roman Symbols

a_m	The mth power-imbalance factor.
$a_{q,m}$	The mth dispersion coefficient of the qth DM.
$\mathbf{a}_q$	The qth DM activation vector.
$\mathbf{a}_{\text{Rx}}$	The phase-weights vector associated with receive antennas.
$\mathbf{a}_{\text{Tx}}$	The phase-weights vector associated with transmit antennas.
$\arg\max_x f(x)$	The argument x that maximizes $f(x)$.
$\arg\min_x f(x)$	The argument x that minimizes $f(x)$.
A_{PD}	The physical area of the PD at the receiver.
$\mathbf{A}_q$	The qth element of the DMs set $\{\mathbf{A}_1 \cdots \mathbf{A}_Q\}$.
b_k	The kth input bit of $\mathbf{b} = [b_1, \cdots, b_B]^{\text{T}}$.
$\mathbf{b}$	A bit sequence.
B	The length of input bits $\mathbf{b}$ associated with a codeword $\mathbf{S}$.
B_w	System bandwidth.
$\text{concat}(\cdots)$	The horizontal matrix concatenation.
C	Ergodic capacity.

$\mathbf{C}_{M,P}$	The combination matrix where P out of M elements are activated.
d	The spacing between antenna elements.
$d[n,m]$	The distance between the mth source light and the nth PD.
d_{Rx}	The spacing between receive antennas or receive PDs.
d_{Tx}	The spacing between transmit antennas or source lights.
$\mathrm{d_H}(\mathbf{b},\mathbf{b}')$	The Hamming distance between the bit sequences $\mathbf{b}$ and $\mathbf{b}'$.
$\mathrm{diag}(\cdot)$	Diagonal operation.
D	Diversity order.
D_{H}	The distance between the transmitter and the receiver.
D_{R}	The spacing between receiver subarrays.
D_{T}	The spacing between transmitter subarrays.
e	The base of the natural logarithm.
$\exp(\cdot)$	Exponential function.
$\mathrm{E}[x]$	The average of random variable x.
$\mathbf{f}_k$	The analog BF weights associated with the kth transmitter subarray.
F_d	The maximum Doppler frequency.
$\mathbf{F}$	The analog BF weights at the transmitter.
h_m	The mth element of $\mathbf{h}$.
$h[n,m]$	The nth row and mth column of $\mathbf{H}$.
$\mathbf{h}$	A channel vector.
$\mathbf{H}$	A channel matrix.
$\mathbf{H}_0$	The channel matrix that follows Rayleigh distribution.
$\mathbf{H}_b$	The subarray-to-subarray channel matrix.
$\mathbf{H}_{\mathrm{LoS}}$	The channel matrix that represents LoS elements.

$\mathbf{H}_{\text{NLoS}}$	The channel matrix that represents non-LoS elements.
$\mathbf{H}_{\text{VLC}}$	The LoS channel coefficients of VLC.
$H(\cdot)$	The binary entropy function.
i	Transmission index.
I_A	An *a priori* information.
I_C	Unconstrained AMI.
I_D	Constrained AMI.
$I_E^{(p)}$	The EXIT function of the pth inner sub-code.
I_E^{RSC}	The EXIT function of the outer RSC code.
$I(\cdot)$	Mutual information.
$\mathbf{I}_n$	The identity matrix having the size of n.
j	Imaginary number.
$J_n(\cdot)$	Bessel function.
K	The Rician factor.
l	The index of the $\mathcal{L}$–APSK constellation.
$\ln(\cdot)$	The natural logarithm.
$\log_2(\cdot)$	The logarithm to base 2.
$\mathbf{L}$	The vector indicating multiple constellation sizes.
$L(\cdot)$	Log-likelihood ratio.
m	Transmit antenna index.
$\max(\cdot)$	The maximum of a sequence or a function.
$\min(\cdot)$	The minimum of a sequence or a function.
$\bar{M}$	Number of embedded symbols in a space-time codeword.
M	Number of transmit antennas or number of subcarriers in a subgroup.

M_R	Number of subarrays at the receiver.
M_T	Number of subarrays at the transmitter.
n	Receive antenna index.
N	Number of receive antennas or number of whole subcarriers.
N_a	Number of activation patterns.
N_c	Number of codewords.
N_{in}	Number of inner iterations.
N_{out}	Number of outer iterations.
N_R	Number of antenna elements at the receiver.
N_{RF}	Number of RF chains.
N_s	Number of isotropic scatterers.
N_T	Number of antenna elements at the transmitter.
$p(\cdot)$	Probability density function.
P	Number of activated elements.
Q	Number of DMs.
$Q(\cdot)$	The Q-function, which represents the tail probability of Gaussian distribution.
$r[n,m]$	The distance between the nth receive antenna element and the mth transmit antenna element.
$\text{rank}(\cdot)$	Matrix rank.
R	Transmission rate.
R_c	The mean rank of the channel matrix $\mathbf{H}$.
R_{PD}	The response of a PD.
R_{RSC}	The RSC code rate.

R	The spatial correlation at the receiver.
s	A complex-valued symbol.
s_m	The mth element of **s**.
$s[m,t]$	The mth row and tth column of **S**.
s	A vector codeword.
$\mathbf{s}^{(k)}$	The kth vector element of the codewords set $\left\{ \mathbf{s}^{(1)} \cdots \mathbf{s}^{(2^B)} \right\}$.
S	A space-time codeword.
$\mathbf{S}^{(k)}$	The kth element of the codewords set $\left\{ \mathbf{S}^{(1)} \cdots \mathbf{S}^{(2^B)} \right\}$.
t	Time slot index.
T	Number of time slots in a codeword.
T_s	Symbol duration.
T_t	Delay spread.
T	The spatial correlation at the transmitter.
$\mathbf{T}_a$	The permutation-table.
U_{R}	Number of receive antenna elements embedded in a subarray.
U_{T}	Number of transmit antenna elements embedded in a subarray.
v_m	The mth element of **v**.
$v[n,t]$	The nth row and tth column of **V**.
v	A noise vector.
V	A noise matrix.
$\mathbf{w}_k$	The analog BF weights associated with the kth receiver subarray.
$W(\cdot)$	The Lambert function.
W	The analog BF weights at the receiver.
x_n	The nth frequency-domain symbol.

$x(t)$	Time-domain signals.
x	GSM symbol vector.
X	The data matrix, which is generated in advance of the differential encoding.
$\tilde{\mathbf{X}}$	The data-carrying Hermitian matrix.
y_m	The mth element of **y**.
$y[n,t]$	The nth row and tth column of **Y**.
y	A vector of received symbols.
Y	A matrix of received symbols.

Greek Symbols

β	The single power-imbalance factor.
γ	Signal-to-noise ratio.
$\zeta(\cdot)$	Cayley transform.
θ	Receiver tilt.
θ_{AoA}	Angle-of-arrival.
θ_{AoD}	Angle-of-departure.
θ_{I}	The random phase fluctuation in the in-phase component.
θ_{Q}	The random phase fluctuation in the quadrature component.
κ	The correlation coefficient of **H**.
λ	Wavelength.
λ_i	Eigenvalue of an arbitrary matrix.
λ	The irregular partition ratio.
ξ	The subcarrier-activation ratio P/M.
π	The circular constant.
$\prod$	Product of a sequence.

$\boldsymbol{\Pi}$	Interleaver.
ρ_{target}	The target SNR.
$\sigma_r^{(n)}$	The received optical power at the nth PD.
σ_s^2	The variance of APSK symbols s.
σ_v^2	The variance of v_m or $v[n,t]$.
σ_x^2	The variance of x_n.
$\sum$	Summation.
$\boldsymbol{\Sigma}$	The variance–covariance matrix of $\mathbf{H}$.
$\phi[n,m]$	The angle of incidence from the mth source light to the nth PD.
$\Phi_{\frac{1}{2}}$	The transmitter semi angle.
$\Psi_{\frac{1}{2}}$	The field of view semi angle of the receiver.

Superscripts

$(\cdot)^{\mathrm{H}}$	Hermitian transpose.
$(\cdot)^{\mathrm{T}}$	Matrix transpose.
$(\cdot)^{-1}$	Matrix inverse.
$(\hat{\cdot})$	The estimate of a symbol, a vector, or a matrix.

Other Symbols

$\mathbf{0}$	The zero vector.
$\mathbf{1}$	The one vector.
$\mathbb{B}$	The ring of binary numbers $[0,1]$.
$\mathbb{C}$	The field of complex numbers.
$\mathbb{R}$	The field of real numbers.
$\mathbb{S}$	The set of codewords.
$\mathbb{Z}$	The ring of integers.

$\mathcal{CN}(\mu,\sigma^2)$ The complex-valued Gaussian distribution having the mean μ and the variance σ^2.

$\mathcal{L}$ Constellation size.

$\mathcal{N}(\mu,\sigma^2)$ The real-valued Gaussian distribution having the mean μ and the variance σ^2.

$O(\cdot)$ The big O notation, which is also known as Bachmann-Landau notation.

$\lceil \cdot \rceil$ Ceiling function.

$\binom{M}{P}$ The binomial coefficient indexed by M and K.

$(\cdot)!$ Factorial.

$\lfloor \cdot \rfloor$ Floor function.

$\otimes$ Kronecker product.

Acronyms / Abbreviations

ABF   Analog BeamForming

AMI   Average Mutual Information

AoA   Angle-of-Arrival

AoD   Angle-of-Departure

APSK   Amplitude and Phase-Shift Keying

ASTSK   Asynchronous Space-Time Shift Keying

AWGN   Additive White Gaussian Noise

BER   Bit Error Rate

BF   BeamForming

BLAST   Bell Laboratories Layered Space-Time

BPF   BandPass Filter

BPSK   Binary Phase-Shift Keying

CCDF	Complementary Cumulative Distribution Function
CCMC	Continuous-input Continuous-output Memoryless Channel
CMOS	Complementary Metal–Oxide–Semiconductor
CP	Cyclic Prefix
D/A	Digital-to-Analog
DBF	Digital BeamForming
DCMC	Discrete-input Continuous-output Memoryless Channel
DLDC	Differential Linear Dispersion Code
DM	Dispersion Matrix
DMT	Diversity and Multiplexing Tradeoff
DOSTBC	Differential Orthogonal Space-Time Block Code
DSM	Differential Spatial Modulation
DSTBC	Differential Space-Time Block Code
DSTSK	Differential Space-Time Shift Keying
EXIT	EXtrinsic Information Transfer
FSK	Frequency Shift Keying
GSM	Generalized Spatial Modulation
GSSK	Generalized Space Shift Keying
GSTSK	Generalized Space-Time Shift Keying
i.i.d.	independent and identically distributed
ICI	Inter-Channel Interference
IFT	Inverse Fourier Transform
IM/DD	Intensity Modulation and Direct Detection
Irr-PI-OSM	Irregular-precoded PI-OSM

ITU   International Telecommunication Union

LDC   Linear Dispersion Code

LDPC   Low-Density Parity-Check

LED   Light Emitting Diode

LLR   Log-Likelihood Ratio

LoS   Line-of-Sight

LPF   Low-Pass Filter

LUT   Look-Up Table

MAP   Maximum *A Posteriori*

MAR   Maximum Achievable Rate

MED   Minimum Euclidean Distance

MIMO   Multiple-Input Multiple-Output

MLD   Maximum Likelihood Detection

mmWave   millimeter Wave

MWCs   Millimeter Wave Communications

NBC   Natural Bit Coding

NCGSM   Non-Coherent Generalized Spatial Modulation

OFDM   Orthogonal Frequency-Division Multiplexing

OSM   Optical Spatial Modulation

OSTBC   Orthogonal Space-Time Block Code

PAM-RC   PAM Repetition-Code

PA   Power Allocation

PAPR   Peak-to-Average Power Ratio

PC   Parallel Combinatory

pdf	probability density function
PD	PhotoDetector
PEP	Pairwise-Error Probability
PI-OSM	Power-Imbalanced OSM
PI	Power-Imbalanced
PM	Permutation Modulation
PPM	Pulse Position Modulation
PSD	Power Spectral Density
QAM	Quadrature Amplitude Modulation
QPSK	Quaternary Phase-Shift Keying
RDC	Rank- and Determinant-Criterion
RF	Radio Frequency
RSC	Recursive Systematic Convolutional
S/P	Serial-to-Parallel
SCIP	Solving Constraint Integer Programs
SIM	Subcarrier Index Modulation
SISO	single-input single-output
SM	Spatial Modulation
SNR	Signal-to-Noise Ratio
SSK	Space Shift Keying
STBC	Space-Time Block Code
UDSM	Unified Differential Spatial Modulation
ULA	Uniform Linear Array
UNESCO	United Nations educational, scientific and cultural organization

UN   United Nations

URC   Unity Rate Code

VLCs   Visible Light Communications

Wi-Fi   Wireless Fidelity

Chapter 1

Introduction

F ueled by the massive population growth in the Middle East and Africa, the demands for mobile telecommunications have rapidly increased all over the world. As compared to 2015, the number of mobile phone subscriptions is almost set to double by 2021 [8]. UNESCO[1] reported that the wide-spreading mobile phone subscriptions have improved the literacy rate in developing countries [9]. Mobile telecommunication is a powerful lifeline to cooperation, especially when we encounter the catastrophic situations, such as international terrorism and natural disaster. For example, in the immediate aftermath of the Great East Japan earthquake on 11th March, 2011, which was a 9.0 magnitude megathrust earthquake, the satellite telecommunication systems had supported the instantaneous restoration of communication infrastructures in isolated areas [10][2]. It is beyond controversy that mobile telecommunication network is one of the critical infrastructures in our daily lives, while in most countries, the telecommunications infrastructure has been served by private companies.

Mobile wireless communications rely on radio waves. Private mobile operators have to support the rapidly increasing demands of consumers within the finite radio spectrum. Since the radio spectrum is a physically limited public resource, the international telecommunication union (ITU), which is an agency of the United Nations (UN), has tried to coordinate the fair use of spectrum. In most countries, the government allocates the coordinated spectrum to private companies through public auctions or public competitions. Hence, inevitably, the spectrum bandwidths are costly for the private companies. For example, the auctions in Europe for third generation cellular networks cost approximately 100 billion dollars [11]. In order to improve the efficient use of the finite spectrum, one of the promising solutions is

---

[1]United Nations educational, scientific and cultural organization (UNESCO).
[2]The 90% of cellular facilities were restored by the end of March [10].

the multiple-input multiple-output (MIMO) technology [12, 13], where multiple antennas are employed at the transmitter and/or the receiver. The MIMO wireless communications systems have played a key role in numerous communication standards, such as cellular networks [14] and Wi-Fi[3] networks [15].

In 1948, Shannon formulated the Ergodic capacity of single-input single-output (SISO) channels as follows [16]:

$$C = B_w \log_2 (1 + \gamma) \ \text{[bits/sec]}, \tag{1.1}$$

where the transmitted signals are fluctuated by the noise signals that follow Gaussian distribution. Here, the noise is termed as additive white Gaussian noise (AWGN). The adjective "white" means that the power spectrum of AWGN is ideally flat over the entire frequency bandwidth. Hence, AWGN follows Gaussian distribution in the time domain, while it exhibits the "white" spectrum in the frequency domain. In Eq. (1.1), B_w represents the system bandwidth and γ represents the received signal-to-noise ratio (SNR). Thus, the capacity linearly increases with the bandwidth B_w and logarithmically increases with the SNR γ.

Since Eq. (1.1) represents the performance upper-limit of communication systems, Eq. (1.1) is known as the "Shannon limit". The state-of-the-art channel coding schemes, such as the turbo codes [17] and the low-density parity-check (LDPC) codes [18, 19], are capable of nearly achieving the Shannon limit, with the aid of the redundant bits and the iterative decoding algorithm [20]. After applying the channel coding schemes, there is no approach to increase the capacity C of SISO channels except for increasing B_W or γ.

1.1   General MIMO System Model

Radio waves are propagated at the speed of light[4], attenuated by distance, and reflected by cluster of scatterers. The scatterers create the independent paths and delay the radio waves because the distance of each path differs from each other. Here, the "delay spread" T_t [sec] is an important metric, which is defined by the duration between the first and the last arrivals of the radio propagation. If the delay spread is larger than the inverse of the bandwidth B_w^{-1}, the received signals will be significantly distorted. The independent multi-paths also cause the amplitude and phase fluctuation in a short time, which is called fading. In addition, when the mobile terminal moves faster, the received radio waves are distorted by the Doppler shift,

---

[3]Wireless fidelity (Wi-Fi).
[4]The speed of light is approximately 3.0×10^8 [km/h].
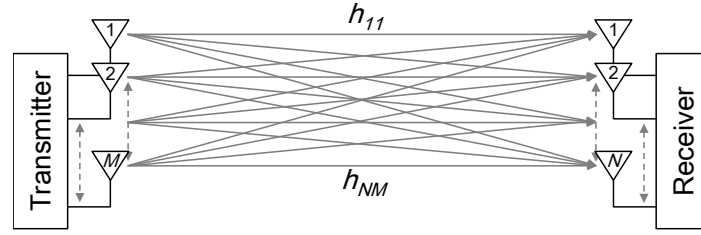
Figure 1.1 The MIMO channel model, where the transmitter and the receiver are equipped with M and N antennas, respectively.

which is typically severe in high-speed trains and airplanes. The random and time-varying behavior of radio waves makes the wireless channel unreliable.

In this thesis, we assume the narrowband statistical channel models, such as the Rayleigh, the Rician, and the Jakes channels, where the delay spread T_t is much smaller than the inverse of the bandwidth B_w^{-1}. Fig. 1.1 shows the system model of the MIMO wireless channel. Later, the numbers of the transmit and the receive antennas are denoted by M and N, respectively. At the transmission index i ($i \geq 0$), based on the input bits having the length of B, a space-time codeword $\mathbf{S}(i) \in \mathbb{C}^{M \times T}$ is generated out of the $N_c = 2^B$ number of codewords. Basically, the codeword $\mathbf{S}(i)$ contains the complex-valued amplitude and phase-shift keying (APSK) symbols, such as binary phase-shift keying (BPSK), quaternary phase-shift keying (QPSK), and quadrature amplitude modulation (QAM). Then, the codeword $\mathbf{S}(i)$ is transmitted through the M antennas over $T \cdot T_s$ [sec] symbol duration. The discrete-time and baseband representation of the received block is given by

$$\mathbf{Y}(i) = \mathbf{H}(i)\mathbf{S}(i) + \mathbf{V}(i), \tag{1.2}$$

where we have the variables defined in Table 1.1. We omit the transmission index i if there is no need to denote.

In Eq. (1.2), $y[n,t]$ denotes the symbol received at the nth antenna at the time index t. The channel coefficient $h[n,m]$ denotes the amplitude and phase fluctuation between the mth transmit and the nth receive antennas. The symbol $s[m,t]$ is transmitted through the

Table 1.1 The general MIMO parameters.

Variable	Definition	Elements	Domain
$\mathbf{Y}(i) \in \mathbb{C}^{N \times T}$	The ith received block	$y[n,t] \in \mathbb{C}$	($1 \leq n \leq N$, $1 \leq t \leq T$)
$\mathbf{H}(i) \in \mathbb{C}^{N \times M}$	The ith channel matrix	$h[n,m] \in \mathbb{C}$	($1 \leq n \leq N$, $1 \leq m \leq M$)
$\mathbf{S}(i) \in \mathbb{C}^{M \times T}$	The ith space-time codeword	$s[m,t] \in \mathbb{C}$	($1 \leq m \leq M$, $1 \leq t \leq T$)
$\mathbf{V}(i) \in \mathbb{C}^{N \times T}$	The ith AWGN	$v[n,t] \in \mathbb{C}$	($1 \leq n \leq N$, $1 \leq t \leq T$)

mth antenna at the time index t, which is between the duration $(i \cdot T \cdot T_s + (t-1)T_s)$ and $(i \cdot T \cdot T_s + tT_s)$ [sec]. We assume that the noise $v[n,t]$ follows the independent and identically distributed (i.i.d.)[5] AWGN with the variance of σ_v^2, namely, $\mathcal{CN}(0, \sigma_v^2)$. Note that the variance-covariance matrix of $\mathbf{V}$ is calculated by $\mathrm{E}\left[\mathrm{vec}(\mathbf{V}) \cdot \mathrm{vec}(\mathbf{V})^{\mathrm{H}}\right]$, which converges into $\sigma_v^2 \cdot \mathbf{I}_{NT}$ since $v[n,t]$ follows the i.i.d. AWGN. The received SNR γ is defined by

$$\gamma = \frac{\sum_{k=1}^{2^B} \left\|\mathbf{S}^{(k)}\right\|_{\mathrm{F}}^2}{M \cdot T \cdot \sigma_v^2}, \tag{1.3}$$

where $\mathbf{S}^{(k)}$ denotes the space-time codeword associated with the B input bits. Throughout our simulations, we adjust the mean power $\sum_{k=1}^{2^B} \left\|\mathbf{S}^{(k)}\right\|_{\mathrm{F}}^2$ to $M \cdot T$ for all the schemes for fair comparisons. The random channel matrix $\mathbf{H}(i)$ is generated by following the considered channel environment. Let us review the diverse channel models, such as the uncorrelated/correlated Rayleigh, the Rician, and the Jakes fading channels.

Rayleigh fading without spatial correlations The Rayleigh fading channel model is a basic statistical model that assumes the large number of scatterers. If the scatterers are uniformly distributed, the channel coefficients are approximated by Gaussian random process [11], based on the central limit theorem. Furthermore, if the transmit and the receive antennas are sufficiently separated, for example there is a spacing over ten times as large as the wave length, the correlation between the adjacent channel coefficients can be ignored. Then, each channel coefficient $h[n,m]$ in the channel matrix $\mathbf{H}$ is approximated by the i.i.d. complex-valued Gaussian symbol $h[n,m] = x + jy$, where x and y follow independent Gaussian distribution having the mean of zero and the variance of $1/2$, i.e. $\mathcal{N}(0, 1/2)$. The complex-valued Gaussian distribution of $h[n,m] = x + jy$ is later denoted by $h[n,m] \sim \mathcal{CN}(0, 1)$. The distribution of the norm of $|x + jy|$ follows Rayleigh distribution defined as follows:

$$\frac{|x+jy|}{\sigma^2} \exp\left(-\frac{|x+jy|^2}{2\sigma^2}\right), \tag{1.4}$$

where σ^2 denotes the variance of x and y. Alternatively, the channel coefficient $h[n,m]$ can be represented by $h[n,m] = x + jy = a\exp(j\phi)$, where a follows Rayleigh fading of Eq. (1.4) and ϕ follows a uniform distribution ranging in $[0, 2\pi)$. Here, a represents the turbulence in amplitude and ϕ represents the turbulence in phase.

---

[5]The i.i.d. assumption implies that each random variable is mutually independent and follows the identical distribution.

Rayleigh fading with spatial correlations   Different from the previous uncorrelated case, if the transmit and the receive antennas are not sufficiently separated, the correlation between the channel coefficients cannot be ignored. For example, let us consider the radio waves having the frequency of 2.5 [GHz]. The associated wavelength is calculated by $\lambda = 3.0 \times 10^8 / (2.5 \times 10^9) = 12$ [cm]. Then, if the transmit antennas are separated with $0.1\lambda = 1.2$ cm, there will be a strong correlation between the channel coefficients, because the separation is smaller than 0.4λ [11]. In such case, the MIMO wireless systems are unable to achieve the expected performance gains due to the severe correlations. The channel matrix $\mathbf{H}$ that considers correlations is given by $\mathbf{H} = \mathbf{R}\mathbf{H}_0\mathbf{T}$ [21, 11], where $\mathbf{H}_0$ is the channel matrix without correlations. Here, $\mathbf{R} \in \mathbb{C}^{N \times N}$ and $\mathbf{T} \in \mathbb{C}^{M \times M}$ are defined as follows.

$$\mathbf{R}[k_1, k_2] = J_0 \left(2\pi d_{\mathrm{Rx}} |k_1 - k_2| / \lambda\right) \ (1 \leq k_1, k_2 \leq N) \tag{1.5}$$

$$\mathbf{T}[k_1, k_2] = J_0 \left(2\pi d_{\mathrm{Tx}} |k_1 - k_2| / \lambda\right) \ (1 \leq k_1, k_2 \leq M) \tag{1.6}$$

In Eq. (1.5), d_{Rx} denotes the spacing between the receive antennas. Similarly, d_{Tx} denotes that of the transmit antennas. Bessel function is given by

$$J_n(x) = \frac{1}{2\pi} \int_{-\pi}^{\pi} \exp(j(n\theta - x\sin(\theta)))d\theta. \tag{1.7}$$

Note that each channel coefficient $h[n,m]$ in the channel matrix $\mathbf{H} = \mathbf{R}\mathbf{H}_0\mathbf{T}$ follows $\mathcal{CN}(0,1)$. The variance–covariance matrix of $\mathbf{H}$ is given by $\boldsymbol{\Sigma} = \mathrm{E}\left[\mathrm{vec}(\mathbf{H})\mathrm{vec}(\mathbf{H})^{\mathrm{H}}\right] \in C^{NM \times NM}$. Then, the correlation coefficient is denoted by $\kappa = \boldsymbol{\Sigma}[k_1, k_2] \ (1 \leq k_1, k_2 \leq NM \wedge |k_1 - k_2| = 1)$. For example, if we have a single receive antenna and two transmit antennas with the spacing of 0.1λ, $\mathbf{R}$ and $\mathbf{T}$ are given by $\mathbf{R} = [1]$ and

$$\mathbf{T} = \begin{bmatrix} J_0(2\pi \cdot 0.1 \cdot 0) & J_0(2\pi \cdot 0.1 \cdot 1) \\ J_0(2\pi \cdot 0.1 \cdot 1) & J_0(2\pi \cdot 0.1 \cdot 0) \end{bmatrix} \approx \begin{bmatrix} 1.00 & 0.90 \\ 0.90 & 1.00 \end{bmatrix}, \tag{1.8}$$

respectively. Here, the variance-covariance matrix of $\mathbf{H} = \mathbf{R}\mathbf{H}_0\mathbf{T}$ is calculated by $\boldsymbol{\Sigma} = \mathbf{T}$. Hence, we have the correlation coefficient of $\kappa = 0.90$ in Eq. (1.8).

Rician fading   If the line-of-sight (LoS) element has a dominant effect in the channel matrix, its radio propagations may be modeled by Rician fading [22]. The channel matrix $\mathbf{H}$

that follows Rician fading is given by [22, 23]

$$\mathbf{H} = \sqrt{\frac{1}{K+1}}\mathbf{H}_0 + \sqrt{\frac{K}{K+1}}\mathbf{H}_{\text{LoS}}, \qquad (1.9)$$

where $\mathbf{H}_0$ denotes the channel matrix without correlations and K denotes the Rician factor, which represents the power ratio of LoS elements. In Eq. (1.9), $\mathbf{H}_{\text{LOS}} = \mathbf{a}_{\text{Tx}}\mathbf{a}_{\text{Rx}}^{\text{T}}$ denotes the LoS elements, where the vectors $\mathbf{a}_{\text{Tx}} \in \mathbb{C}^{N \times 1}$ and $\mathbf{a}_{\text{Rx}} \in \mathbb{C}^{M \times 1}$ are given by

$$\mathbf{a}_{\text{Tx}} = [1 \quad \exp(j2\pi d_{\text{Tx}} \cdot 1 \cdot \cos(\theta_{\text{AoD}})) \quad \cdots \quad \exp(j2\pi d_{\text{Tx}} \cdot (M-1) \cdot \cos(\theta_{\text{AoD}}))] \qquad (1.10)$$

$$\mathbf{a}_{\text{Rx}} = [1 \quad \exp(j2\pi d_{\text{Tx}} \cdot 1 \cdot \cos(\theta_{\text{AoA}})) \quad \cdots \quad \exp(j2\pi d_{\text{Rx}} \cdot (N-1) \cdot \cos(\theta_{\text{AoA}}))] \qquad (1.11)$$

Here, θ_{AoD} and θ_{AoA} represent the angle-of-departure and angle-of-arrival of radio waves, respectively.

Jakes fading   For the time-variant scenario, we assume the Jakes channel model [24], where the receiver is surrounded by the N_s number of the isotropic scatterers. The nth row and mth column of the channel matrix $\mathbf{H}$ is defined by

$$h[n,m] = \frac{1}{\sqrt{N_s}} \sum_{k=1}^{N_s} \cos\left(2\pi \cos\left(\theta_{\text{AoA}}[n,m]\right) F_d T_s i + \theta_{\text{I}}[n,m]\right)$$

$$+ \frac{1}{\sqrt{N_s}} \sum_{k=1}^{N_s} \sin\left(2\pi \cos\left(\theta_{\text{AoA}}[n,m]\right) F_d T_s i + \theta_{\text{Q}}[n,m]\right) j,$$

where the angle-of-arrival $\theta_{\text{AoA}}[n,m]$, the phase differences $\theta_{\text{I}}[n,m]$ and $\theta_{\text{Q}}[n,m]$ are uniformly distributed random variables $[0, 2\pi)$. Here, F_d represents the maximum Doppler frequency, which is normalized by the symbol duration T_s. For example, if we have $T_s = 3.2$ [μsec] and 5.0 [GHz] carrier-frequency, the normalized maximum Doppler frequency is calculated by $F_d T_s \approx 1.48 \cdot 10^{-5}$ for 1.0 [km/h], $F_d T_s \approx 1.48 \cdot 10^{-4}$ for 10.0 [km/h], and $F_d T_s \approx 1.48 \cdot 10^{-3}$ for 100.0 [km/h]. Fig. 1.2 exemplifies such scenarios, where the normalized maximum Doppler frequency $F_d T_s = 10^{-4}$ and 10^{-3} were considered. As shown in Figs. 1.2(a) and (b), the Jakes channel coefficients fluctuated as the transmission index i increased.

Let us now review the Ergodic capacity of the MIMO channels. A MIMO channel is equivalent to multiple SISO channels [12]. If we assume the Rayleigh fading scenarios, the rank of the channel matrix is proportional to the number of transmit and receive antennas,

(a) $F_d T_s = 10^{-4}$.   **(b)** $F_d T_s = 10^{-3}$.
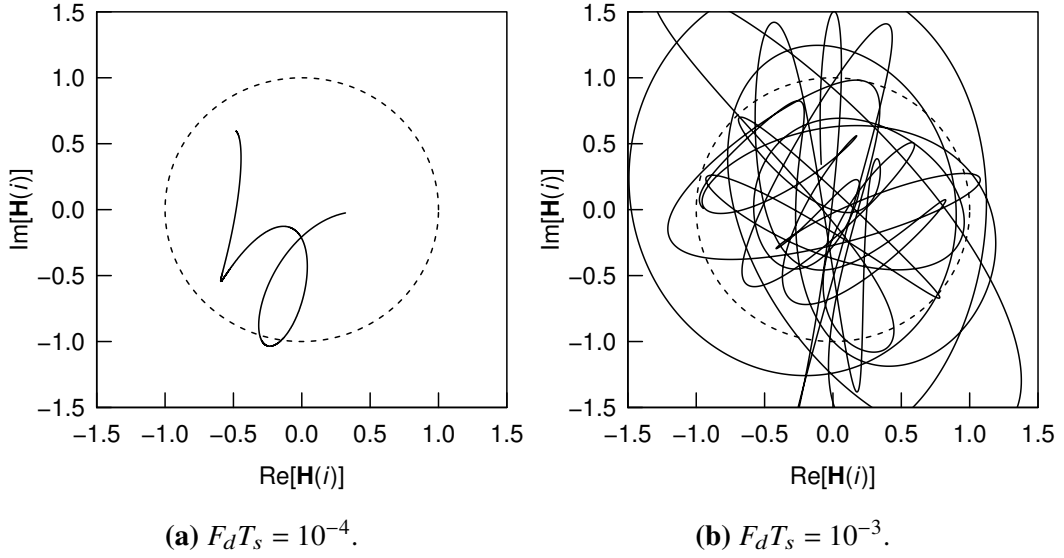
Figure 1.2 Examples of the channel coefficients that follow the Jakes channel model, where we have $(M,N) = (1,1)$ and $N_s = 10$. The transmission index was set to $i = 1, 2, \cdots, 2 \times 10^4$.

namely, $E_\mathbf{H} [\text{rank}(\mathbf{H})] = \min(N, M)$. Thus, the capacity of the MIMO channels linearly increases with the number of antennas [12, 25], which implies the substantial performance advantages of the MIMO communications systems. The Ergodic capacity of the MIMO channels is given by [12]

$$C = E_\mathbf{H} \left[\sum_{i=1}^{R_c} \log_2 \left(1 + \rho \lambda_i \right) \right] \text{ [bits/symbol]}, \tag{1.12}$$

where we have

$$\mathbf{Q} = \begin{cases} \mathbf{H}\mathbf{H}^\mathrm{H} \in \mathbb{R}^{N \times N} & (N < M) \\ \mathbf{H}^\mathrm{H}\mathbf{H} \in \mathbb{R}^{M \times M} & (N \geq M) \end{cases}.$$

In Eq. (1.12), R_c denotes the mean rank of channels $R_c = E_\mathbf{H} [\text{rank}(\mathbf{Q})]$ and λ_i denotes the ith eigenvalue of $\mathbf{Q}$. Eq. (1.12) implies that the capacity of the MIMO wireless system linearly increases with the rank of channels $R_c = \min(N, M)$. Hence, we can improve the system capacity upon increasing the number of antennas, instead of increasing either the bandwidth B or the received SNR ρ in Eq. (1.1). Also, as given in Eq. (1.12), the MIMO communication channel is decomposed into the R_c number of the independent SISO channels [26, 12, 25], where the SNR ρ is scaled by the associated eigenvalue of λ_i.

The basic functions of MIMO consist of the three components: the spatial multiplexing, the diversity, and the beamforming [27]. The MIMO channels offer the R_c number of the data streams. Hence, the same number of data symbols can be multiplexed, which is referred to as the spatial multiplexing gain [13]. Also, a data symbol transmitted through the different streams experiences different channel coefficients. The diversity of the received symbol improves the reliability of the system, which is referred to as the diversity gain [28]. In addition, if the channel matrix $\mathbf{H}$ is known at the transmitter, it is capable of radiating the radio waves into a desired direction. For example, if we multiply the transmitting codewords by the inverse of the channel matrix, i.e. $\mathbf{H}^{-1}\mathbf{S}$, the received symbol would be $\mathbf{Y} = \mathbf{H}\mathbf{H}^{-1}\mathbf{S} + \mathbf{V} = \mathbf{S} + \mathbf{V}$. The simplest scheme is the conjugate beamfroming, where the transmitting codewords are multiplied by the Hermitian transpose of the channel matrix, i.e. $\mathbf{H}^H\mathbf{S}$ [29]. The beamforming scheme improves the received SNR and the spectrum efficiency, as well as the inter-user interference, which is referred to as the beamforming gain [30, 31]. There is a trade-off between the spatial multiplexing and diversity gains [32], because the number of available data streams is limited to a finite number, which is given by R_c. Thus, if we maximize the spatial multiplexing gain, the diversity gain vanishes. Also, if we maximize the diversity gain, the multiplexing gain disappears. This trade-off is known as the diversity and multiplexing tradeoff (DMT) [32].

In 1973, Schmidt *et al.* patented the space-division multiple access concept, where receivers are spatially separated by directional antennas [30]. The basic concept of [30] is related to the current MIMO concept in terms of the spatial multiplexing gain. In 1987, Winters derived the Ergodic capacity of the MIMO channels [12]. This analysis was inspired by the dually polarized SISO channel [26], which is equivalent to the 2×2 MIMO channel. With the aid of the virtual independent paths, the spatial multiplexing scheme of [13, 33, 34] works efficiently in the rich-scattering scenarios. The spatial multiplexing scheme is also known as the bell laboratories layered space-time (BLAST) transmission. The M independent symbols are transmitted through the M antennas, and then received at the M antennas. The key contribution of [13] is the successive nulling concept, where the transmitted symbols are copied over M time slots. This redundancy mitigates the inter-channel interference at the receiver and improves the communications reliability. The spatial multiplexing scheme maximizes the multiplexing gain, while the orthogonal space-time block code (OSTBC) scheme [28] maximizes the diversity gain. The simple OSTBC scheme of [28] embeds the two APSK symbols in a 2×2 space-time codeword. The embedded symbols are copied over the two time slots. As proved in [35], it is impossible to break the DMT due to the limited number of independent data streams. The OSTBC scheme is also capable of avoiding the inter-channel interference at the receiver, with the aid of the unitary characteristic of the

OSTBC codewords. Note that the conventional BLAST and OSTBC schemes have been subsumed by the general MIMO schemes [36, 27], in order to analyze the substantial gains in a comprehensive manner. The contributions to STBC are summarized in Table 1.2.

The coherent MIMO scheme [13, 33, 34, 28, 36, 27] relies on the perfect estimates of the channel matrix $\mathbf{H}$ at the receiver. Here, the pilot symbols are transmitted in order to estimate the channel coefficients. For example, the simplest scheme transmits the pilot symbols of $\mathbf{I}_M$ through M antennas over M time slots. At the receiver, based on the receive symbols of $\mathbf{Y} = \mathbf{H}\mathbf{I}_M + \mathbf{V} = \mathbf{H} + \mathbf{V}$, the channel matrix is estimated by $\hat{\mathbf{H}} = \mathbf{H} + \mathbf{V}$. The estimated channel matrix $\hat{\mathbf{H}}$ contains AWGN of $\mathbf{V}$, which degrades the accuracy of the channel estimation. The inaccuracy of $\hat{\mathbf{H}}$ degrades the reliability of the coherent MIMO scheme, which exhibits an error-floor in error-rate comparisons [39]. In addition, the inserted pilot symbols also decrease the effective transmission rate. For example, the pilot symbols of $\mathbf{I}_M$ consume the M time slots, which linearly increases with the number of transmit antennas. If we consider the fast-fading scenarios, such as the Jakes channel having a large normalized Doppler frequency $F_d T_s$, it is a challenging task to accurately track the channel coefficients at the receiver because the channel coefficients change rapidly. Furthermore, the number of channel coefficients that have to be estimated is $N \cdot M$, which increases with the numbers of transmit and receive antennas. Hence, the channel estimation problem is especially severe for the large-scale MIMO systems in fast-moving environments.

Against the channel estimation problem, the differential space-time block code (DSTBC) was proposed in 2000 [40–42]. The DSTBC scheme circumvents the pilot insertion and the channel estimation process with the aid of the unitary matrices. The successive space-time codewords $\mathbf{S}(i-1)$ and $\mathbf{S}(i)$ have a certain relationship, which is called the differentially encoded symbols. At the receiver, the previously received symbol $\mathbf{Y}(i-1)$ is equivalent to the "pilot symbol" of the coherent MIMO scenario. Hence, the DSTBC scheme works without the estimated channel matrix $\hat{\mathbf{H}}(i)$. The major benefit of the DSTBC scheme is the increase in the effective transmission rate because there is no need to insert the pilot symbols. Basically, the DSTBC scheme relies on the unitary matrix [40, 41, 43, 42, 44, 45]. In contrast, some DSTBC schemes use the non-unitary matrix to increase the transmission rate [46–48]. The contributions to DSTBC are summarized in Table 1.3.

1.2   Millimeter-Wave and Visible Light Communications

As given in Eq. (1.1), the Ergodic capacity of the SISO channels linearly increases with the bandwidth B_w. In millimeter wave communications (MWCs) [50] and visible light

Table 1.2 Contributions to STBC and its background.

Year	Authors	Contribution
1942	Peterson [37]	Patented the diversity receiving system which exploits the diversity of the channel coefficients.
1973	Schmidt and Shimasaki [30]	Patented the space-division multiple access concept, where the multiple-antennas array is used to mitigate the inter-user interference. The concept of [30] was proposed for the satellite system based on the space-division scheme of [38], which uses the directional antenna.
1984	Amitay and Salz [26]	Proved that the 2×2 channel achieved with the dually polarized antenna is equivalent to the two independent channels in rich scattering scenarios.
1987	Winters [12]	Derived the Ergodic capacity of the MIMO channels based on the decomposition concept of [26].
1996	Foschini [13]	Proposed the layered space-time architecture, where the data stream is multiplexed to achieve a higher capacity. The key feature of [13] is the successive nulling detection, where the interference from the other data streams are canceled by the previously detected symbols.
1998	Foschini and Gans [33]	Investigated the Ergodic capacity of the multi-element array technology.
	Wolniansky *et al.* [34]	Proposed the vertical-BLAST architecture and demonstrated its performance gain in an indoor environment with the real-world prototype system.
	Alamouti [28]	Proposed the simple STBC scheme that achieves the transmit diversity order of two for the $M = 2$ antennas setup.
1999	Telatar [25]	Formulated the capacity of MIMO channels and justified its performance gain.
2002	Hassibi and Hochwald [36]	Proposed the LDC concept that subsumes the conventional coherent MIMO schemes, such as the BLAST [13] and the OSTBC [28] schemes.
2003	Zheng and Tse [32]	Proved that there is a fundamental trade-off between the diversity and multiplexing gains.
2012	Sugiura *et al.* [27]	Proposed the generalized system model that subsumes the previous coherent MIMO schemes and analyzed the proposed scheme in a comprehensive manner.

Table 1.3 Contributions to DSTBC.

Year	Authors	Contribution
2000	Hochwald and Marzetta [40]	Proposed the unitary space-time modulation, where the channel coefficients are unknown at the receiver. The derived capacity is asymptotic to the coherent setup as the number of time slot T increases.
	Tarokh and Jafarkhani [41]	Proposed the DSTBC scheme based on the OSTBC scheme of [28]. Different from [49], there is no need to insert the reference symbol $\mathbf{I}_m$ more than once.
	Hochwald *et al.* [43]	Proposed the systematic construction method for the unitary space-time codewords of [40].
	Hughes [42]	Proposed the DSTBC scheme based on the group-codes. The optimal design criterion was provided for the $M = 2$ transmit antennas setup.
	Hochwald and Sweldens [44]	Proposed the DSTBC scheme based on Abelian group. The proposed scheme of [44] activates only single antenna at any time because the space-time codewords are diagonal.
2002	Hassibi and Hochwald [45]	Proposed the DSTBC scheme based on the Cayley-transform. The low-complexity near-optimal detector of [45] is based on the successive nulling concept similar to the BLAST scheme [13].
	Xia [46]	Proposed the OSTBC-based differential scheme that is capable of transmitting APSK symbols, where the space-time codewords are normalized to maintain a constant transmit power.
2005	Zhu and Jafarkhani [47]	Proposed the quasi-orthogonal OSTBC scheme that supports the $M \geq 4$ transmit antennas.
2009	Bhatnagar *et al.* [48]	Derived the PEP of the orthogonal and non-orthogonal DSTBC schemes.

communications (VLCs) [51], relatively large bandwidths are available, as compared to the current mobile networks operated between 2 and 5 [GHz] spectrum. Visible light waves are the electromagnetic waves human can see, where the corresponding frequency is ranging from 430 to 770 [THz]. Millimeter waves have wavelengths ranging from 1 to 10 mm, where the associated frequency ranges from 30 to 300 [GHz]. Hence, in MWC and VLC, the resultant capacity is higher than the current networks with the aid of its wider bandwidth.

Typically, MWC suffers large propagation losses imposed by the nature of short wavelength. The channel models of the indoor and outdoor MWC have been extensively studied [52, 50, 53]. For example, if we consider the free-space path loss model, the loss increases with the square of the wavelength λ, i.e. $10\log_{10}\left(\lambda^2\right)$ [dB] [11]. In order to circumvent the large path-loss problem [50, 53], the millimeter wave (mmWave) transmitters and receivers have to obtain the beamforming (BF) gain with the larger number of antenna elements [54]. Here, it is unrealistic for commercial devices to use a large number of RF circuits connected with each antenna elements because the RF circuit for MWC is complicated, expensive and power-consuming [55]. In the microwave MIMO context, the hybrid BF scheme that jointly combines the analog beamforming (ABF) and the digital beamforming (DBF) has been proposed [56, 57]. Specifically, the hybrid scheme divides the large antenna elements into subarrays and each subarray is connected to a single RF circuit. This structure reduces the number of RF chains both at the transmitter and the receiver. It was demonstrated in [55, 58–61] that this hybrid BF approach is also effective for the MIMO-MWC. The contributions to the hybrid-array concept are summarized in Table 1.4.

Along with the development of light emitting diode (LED), its brightness, production cost, and response time have been improved, thanks to the invention of semiconductor materials such as the indium gallium nitride [64]. Based on the high-brightness and energy-efficient LEDs, the LED-aided VLC has been researched [65, 64, 51], where the LEDs are used as the illumination bulb as well as the wireless data transmitter. The transmitter modulates information bits onto the intensity of LEDs and the receiver directly detects the change in the intensity, which is referred to as the intensity modulation and direct detection (IM/DD). The available VLC bandwidth is ideally huge with the aid of the terahertz-order spectrum ranging from 430 to 770 [THz], while the practical VLC bandwidth is determined by modulator and LED, which is typically limited to several megahertz [66]. However, the license-free and security-aware bandwidth of several megahertz is still attractive for our daily lives, against the spectrum shortage in the current 2–5 [GHz] networks. In photodetector (PD)-aided VLC, the rank of channel matrix is typically low, while that of the complementary metal–oxide–semiconductor (CMOS) imaging sensor aided VLC is stable and high [35]. The contributions to VLC are summarized in Table 1.5.

Table 1.4 Contributions to MWC and its background.

Year	Authors	Contribution
1959	Van [54]	Patented the adaptive antenna array concept that efficiently combines incident waves.
2003	Zhang *et al.* [56]	Proposed the hybrid approach that integrates the switched beam process with the adaptive beamforming. The proposed scheme of [56] selects a reduced number of received signals and combines them, which reduces the complexity of the receiver.
2007	Bøhagen *et al.* [62]	Proposed the optimal antenna alignment technique for the uniform linear array, which combats the detriment effects of the LoS-dominant mmWave channels.
2008	Celik *et al.* [55]	Demonstrated that the conventional smart antenna approach of [56, 57] is also effective for MWC. The prototype system of [55] was built and experimented at 60 [GHz] band, which justified the cost-reduction effects of the smart antenna system.
2009	Shoji *et al.* [52]	Proposed the indoor mmWave channel model, where the LoS components have the dominant effect in the channel coefficients.
2011	Torkildson *et al.* [63]	Investigated the performance of the spatial-multiplexing scheme in indoor MWC, where the hybrid BF scheme was used.
2012	Guo *et al.* [58]	Proposed the hybrid-antenna-array concept that combines the analog subarrays and the low-complexity digital beamformer. The two schemes were introduced in [58]: the interleaved subarray and the side-by-side subarray. Both the schemes have a trade-off between the complexity and the performance.
2013	Alkhateeb *et al.* [59]	Reduced the complexity of the hybrid analog and digital BF approach [58] under practical hardware constraints. The proposed algorithm of [59] iteratively constructs the ABF and DBF matrices with periodical pilot signals so as to maximize the mutual information.
	Rappaport *et al.* [50]	Investigated the potential of cellular MWC in the 5G context. The basic propagation characteristics were measured in heavy and light urban areas.
2014	Ayach *et al.* [60]	Proposed the sparse-reconstruction-based precoder and combiner designs for the hybrid analog and digital MWC, where the mmWave channels can be considered as a sparse process. The proposed scheme of [60] is capable of achieving a near-optimal capacity.

Table 1.5 Contributions to VLC and its related area.

Year	Authors	Contribution
1880	Bell [67]	Invented the phone system that conveys sounds by means of sunlight. The distance between the transmitter and receiver was 213 [m].
2002	Kamiya [65]	Patented the indoor VLC system that uses energy-efficient white LEDs. Different from the conventional infrared communications, the proposed system of [65] uses the LED illumination as a data-conveying channel.
2003	Tanaka *et al.* [64]	Investigated the performance of the VLC system that uses white LEDs.
2004	Komine and Nakagawa [51]	Investigated the effects of multi-paths and inter-symbol interference in VLC.
2005	Simon and Vilnrotter [68]	Proposed the modification of the OSTBC scheme that can be applied to the optical wireless communications, such as visible light and free space optical wireless. The space-time codewords of [68] were mapped to real-valued matrices.
	Komine *et al.* [69]	Investigated the effects of shadowing in VLC. The simulation results of [69] revealed that the shadowing effects could be ignored if the transmitter uses more than three source lights.
2008	Minh *et al.* [66]	Improved the bandwidth of VLC. The modulation bandwidth of 25 [MHz] was achieved in [66], while the practical modulation bandwidth of VLC is typically limited to several megahertz.
	Safari and Uysal [70]	Revealed that the PAM-aided repetition codes outperformed the OSTBC scheme of [68] in FSO links, where IM/DD were considered. The performance gap increased upon increasing the number of transmit light sources.
2009	Zeng *et al.* [35]	Proposed the alignment-free VLC relying on the CMOS sensors and the associated optical lenses. The simulation results of [35] showed that the non-imaging optical MIMO systems had a penalty in the symmetrical scenarios.
2012	Khalid *et al.* [71]	Achieved the effective rate of 1 [Gbits/sec] at the standard illuminance level, where the white LED and the avalanche PD were used.
2013	Tian-Peng *et al.* [72]	Proposed the higher-order counterpart of the optical OSTBC scheme of [68], which revealed that the OSTBC scheme outperformed the repetition codes when the time-slot misalignment occurred.

1.3   Permutation Modulation Philosophy

In 1965, Slepian firstly proposed the "permutation modulation (PM)" concept [73], which was published on *Proceedings of the IEEE*. The PM codewords are generated by permuting the order of a set of numbers. In the original PM, the initial codeword is defined by [73]

$$\mathbf{s}^{(1)} = [\underbrace{\underbrace{\mu_1 \cdots \mu_1}_{M_1 \text{ rows}} \overbrace{\underbrace{\mu_2 \cdots \mu_2}_{M_2 \text{ rows}}}^{M \text{ rows}} \cdots \underbrace{\mu_k \cdots \mu_k}_{M_k \text{ rows}}]^{\mathrm{T}}, \tag{1.13}$$

where we have $M = M_1 + M_2 + \cdots + M_k$ and $\mu_1 < \mu_2 < \cdots < \mu_k$. In Eq. (1.13), μ_1 is repeated at M_1 times. Then, the other codewords are generated by permuting the order of Eq. (1.13). The total number of possible codewords is calculated by [73]

$$N_c = \frac{M!}{M_1! M_2! \cdots M_k!}. \tag{1.14}$$

The pulse position modulation (PPM) and pulse code modulation are included as special case of the PM scheme [73]. For example, we consider the following initial codeword:

$$\mathbf{s}^{(1)} = [\underbrace{\quad 0 \quad\quad 0 \quad\quad 0 \quad}_{M_1 = 3} \underbrace{\quad 1 \quad}_{M_2 = 1}]^{\mathrm{T}} \in \mathbb{R}^4,$$

where we have $M = M_1 + M_2 = 4$ and $(\mu_1, \mu_2) = (0, 1)$. The total $N_c = M!/(M_1! \cdot M_2!) = 4!/(3! \cdot 1!) = 4$ number of codewords are generated by the permutation of four from four as follows:

$$\mathbf{s}^{(1)} = [0\ 0\ 0\ 1]^{\mathrm{T}}, \mathbf{s}^{(2)} = [0\ 0\ 1\ 0]^{\mathrm{T}}, \mathbf{s}^{(3)} = [0\ 1\ 0\ 0]^{\mathrm{T}}, \mathbf{s}^{(4)} = [1\ 0\ 0\ 0]^{\mathrm{T}}, \tag{1.15}$$

which are the same with the codewords of the space shift keying (SSK). The SSK scheme uses only one antenna at any time and modulates the additional bits by selecting a single out of multiple transmit antenna. Similarly, the PPM scheme modulates the input bits by selecting a single time index. Thus, the SSK scheme is the spatial domain counterpart of the PPM scheme, which modulates the information bits onto the temporal domain. Let us check another example. If we have the initial codeword of $\mathbf{a}_1 = [1, 2] \in \mathbb{Z}^2$, all the $N_c = 2!/(1! \cdot 1!) = 2$ number of PM codewords are given by $\mathbf{a}_1 = [1, 2]$ and $\mathbf{a}_2 = [2, 1]$. Suppose that we map the

vectors $\mathbf{a}_1$ and $\mathbf{a}_2$ onto the space-time matrices, then one example is given by

$$\mathbf{A}_1 = \begin{bmatrix} 1 & 0 \\ 0 & 1 \end{bmatrix}, \mathbf{A}_2 = \begin{bmatrix} 0 & 1 \\ 1 & 0 \end{bmatrix}, \tag{1.16}$$

each of which is known as a "permutation matrix" in linear algebra. The permutation matrices of Eq. (1.16) are the basis of the STBC and DSTBC schemes of [27, 74].

In this thesis, we interpret the above PM concept in a broad sense. The diverse low-complexity schemes modulates the additional bits by selecting a spread sequence [75], a subcarrier-index [76], a transmit antenna [77], a dispersion matrix [27], a permutation matrix [74], and/or a transmit LED [78]. These schemes commonly rely on the permutation concept of [73]. Hence, we regard these schemes as a family of the PM concept. At the time of writing, no one has pointed out this perspective in the literature. More specifically, we regard a modulation scheme as a PM-aided scheme if it relies on the following combination matrix [76]

$$\mathbf{C}_{M,P} = \begin{bmatrix} \mathbf{1} & \mathbf{C}_{M-1,P-1} \\ \mathbf{0} & \mathbf{C}_{M-1,P} \end{bmatrix} \in \mathbb{B}^{\binom{M}{P} \times M}, \tag{1.17}$$

where P arbitrary elements are selected out of M candidates. In Eq. (1.17), $\mathbf{0}$ denotes a zero vector having the length of $\binom{M-1}{P}$. Similarly, $\mathbf{1}$ denotes a one vector having the length of $\binom{M-1}{P-1}$. Thus, the combination matrix of Eq. (1.17) represents the on-off of arbitrary elements, such as complex-valued symbols and dispersion matrices. For example, if we consider the $(M, P) = (4, 1)$ case, the combination matrix is given by

$$\mathbf{C}_{4,1} = \begin{bmatrix} 1 & 0 & 0 & 0 \\ 0 & 1 & 0 & 0 \\ 0 & 0 & 1 & 0 \\ 0 & 0 & 0 & 1 \end{bmatrix} \in \mathbb{B}^{4 \times 1}, \tag{1.18}$$

where each row is corresponding to the SSK codewords given in Eq. (1.15). Also, for the $(M,P) = (4,2)$ case, the combination matrix is given by

$$\mathbf{C}_{4,2} = \begin{bmatrix} 1 & 1 & 0 & 0 \\ 1 & 0 & 1 & 0 \\ 1 & 0 & 0 & 1 \\ 0 & 1 & 1 & 0 \\ 0 & 1 & 0 & 1 \\ 0 & 0 & 1 & 1 \end{bmatrix} \in \mathbb{B}^{6\times 4}, \tag{1.19}$$

where each row is the same with the PM codewords generated from $\mathbf{s}^{(1)} = [0\ 0\ 1\ 1]^{\mathrm{T}}$ having $(M_1, M_2) = (2,2)$. The contributions to the PM concept are summarized in Table 1.6.

Apart from the PM concept of [73], in 1991, another PM concept was proposed for the spread spectrum communications [75]. The PM-based spread spectrum scheme of [75] modulates the additional bits by selecting a spread sequence, which is referred to as the "parallel combinatory (PC)" concept. Based on the PC concept of [75], the PC-aided OFDM scheme was proposed [76], where a set of subcarriers were selected out of all the subcarrier-activation patterns. Since the subcarrier-activation process of [76] is based on the combination matrix of Eq. (1.17), in this thesis, the PC-aided schemes are considered as one of the PM family. Note that the modulation principle of the conventional PC-aided OFDM scheme [75] is the same with that of the newly proposed generalized spatial modulation (GSM) scheme [94]. From 2008, the PM-aided OFDM scheme has been gaining attention because it improves the frequency diversity and the coding gain of the conventional OFDM scheme [95–97].

The device complexity of MIMO systems is typically high due to the multiple radio frequency (RF) chains, which process high-frequency signals. Especially in massive MIMO systems, the large number of transmit antennas are used to achieve a competitive performance gain, which leads to high energy consumptions. To address this limitation, the SM scheme has been proposed for reducing the complexity both at the transmitter and the receiver, while keeping the same spectrum efficiency as the conventional systems. The SM scheme was firstly proposed in [77], which was independent from the conventional PM and PC contexts of [73, 75]. The SM-based research has attracted attention owing to its reduced number of RF chains. Fig. 1.3 shows the schematic of the multiple- and single-RF aided transmitters. As shown in Fig. 1.3, the RF chain is composed of the digital-to-analog (D/A) converter, low-pass filter (LPF), bandpass filter (BPF), synchronizer, and amplifier, which lead to high complexity and expensive production cost. It was shown in [98] that the BPSK-aided SM

Table 1.6 Contributions to PM as well as its background and applications.

Year	Authors	Contribution
1960	Lehmer [79]	Conceived the algorithm that generates a permutation of a sequence, which is later called "Lehmer code".
1965	Slepian [73, 80]	Proposed the PM concept, which generates codewords with permuting the initial sequence. Note that the PM concept was patented in [80].
1967	Schneider [81]	Combined the PM concept with the frequency shift keying (FSK), where multiple frequencies were simultaneously activated.
1972	Berger *et al.* [82]	Proposed the channel coding scheme based on the PM concept.
1989	Atkin and Corrales [83]	Proposed the PM-based FSK scheme that selects a group of elements, aiming at achieving a higher bandwidth efficiency.
1996	Li [84, 85]	Proposed the hybrid permutation scheme that combines the PSK-aided FSK with the PM concept. Later, the master thesis of [84] was presented at an IEEE conference [85].
1997	Savage [86]	Surveyed the combinatorial Gray codes, where the PM sequences were designed with the Gray mapping.
1999	Mittelholzer [87]	Applied the PM concept to steganography, which has robustness against attacks.
2001	King and Neifeld [88]	Applied the PM concept to the volume holographic memories in order to decrease the number of "on" state.
2005	Silva and Finamore [89]	Generalized the PM concept to support vectors.
2009	Anxiao *et al.* [90]	Applied the PM concept to the flash memory system in order to decrease the number of charged cells.
2010	Shi *et al.* [91]	Proposed the PM-based MIMO-CDMA system.
2013	Mittelholzer *et al.* [92]	Patented the PM concept applied to the solid-state storage device in order to mitigate the effects of drift noise.
2015	Ishimura and Kikuchi [93]	Applied the PM concept to the coherent optical communications.

(a) Practical multiple-RF aided transmitter.

(b) Ideal single-RF aided transmitter.
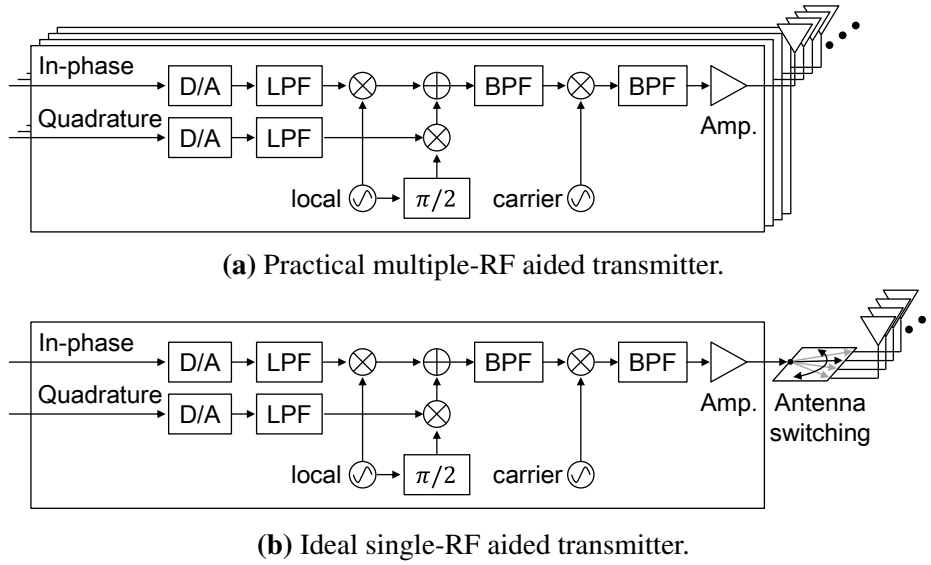
Figure 1.3 The schematic of multiple- and single-RF aided transmitter.

scheme is more beneficial than the conventional spatial multiplexing scheme when employing $M > 32$ transmit antennas. Also, the QPSK-aided SM scheme is beneficial when employing $M > 1024$ transmit antennas [98]. The results shown in [98] were hopeless. In this thesis, we adopt the opportunistic single-RF architecture of Fig. 1.3(b), while expecting the future technology innovations. However, the full-RF aided SM system still has advantages over the spatial multiplexing scheme in terms of the higher coding gain, the smaller computational complexity, and the possibility in massive MIMO scenarios. In addition, the SM scheme may be effective in MWC and VLC channels [99, 100], where the associated channel coefficients contain strong LoS elements due to its propagation nature, as introduced in Section 1.2. In such channels, the rank of channel matrices tends to be low and the performance gain of MIMO systems vanishes. Here, the SM scheme has solved this issue [99, 100], with the aid of the reduced number of data streams. Hence, the SM scheme is capable of supporting the low-rank channels. Note again that the SM scheme is a family of the PM concept. The detailed milestones of the above PM-related schemes are provided in Chapter 2.

1.4 Outline and Novel Contributions

1.4.1 Outline of the Thesis

The remainder of this thesis is organized as follows.

Chapter 2: Comprehensive Survey on Permutation Modulation Family

In Chapter 2, we review the PM schemes having been proposed for the single and multicarrier microwave as well as visible light communications. Section 2.2 introduces the performance metrics for the general MIMO system model of Eq. (1.2). Specifically, we review the metrics of throughput, reliability, and complexity, which are useful tools for evaluating the positive effects of the PM concept. Then, the PM-aided STBC and DSTBC schemes are introduced in Sections 2.3 and 2.4, respectively. The applications of the PM schemes are reviewed in Sections 2.5 and 2.6.

Chapter 3: Permutation Modulation Based Differential MIMO Communications

In Chapter 3, we propose a differentially-encoded counterpart of the SM scheme, which depends on the permutation matrix of Eq. (1.16). The proposed scheme is equivalent to the PM concept applied to DSTBC. The SM scheme has a difficulty in estimating the channel efficients efficiently due to the single-RF architecture. The proposed scheme enables both the single-RF operation at the transmitter and the channel-estimation free detection at the receiver. In Sections 3.2, we propose the PM-aided DSTBC scheme and provide its design criteria. In Section 3.3, we introduce the optimum detector as well as its theoretical error-rate analysis. In Section 3.4, we evaluate the computational complexity and the reliability of the proposed scheme. Here, the channel coding schemes such as the turbo and LDPC codes are not taken into account.

Chapter 4: Permutation Modulation Based MIMO Millimeter-Wave Communications

In Chapter 4, we investigate the achievable performance of the PM scheme applied to the mmWave domain. In the literature, the hybrid analog and digital BF scheme has been proposed for reducing the number of RF chains. However, the number of required RF chains increases upon increasing the spatial multiplexing gain, which is a substantial issue of the MIMO-MWC system. We reveal that the proposed PM-based mmWave transmitter is capable of reducing the number of RF chains, while maintaining the near-capacity performance of the spatial multiplexing scheme. The PM-aided mmWave scheme is basically the same with the conventional GSM scheme. In Section 4.2, we introduce the system model of the proposed transmitter, aiming at reducing the number of RF chains at the transmitter. In Sections 4.2.1 and 4.3.1, we provide the channel model assumed in Chapter 4. In Section 4.4, we simulate the directive BF gain and the AMI of the proposed and conventional schemes. In addition, we investigate the effects of misalignment and BF error.

Chapter 5: Permutation Modulation Based MIMO Visible Light Communications

In Chapter 5, we apply the PM concept to MIMO-VLC, where we introduce a flexible power allocation (PA) method for combating the highly-correlated VLC channels. The PD-equipped receiver is difficult to differentiate the light come from multiple LEDs. Thus, in spatially correlated VLC channels, the mean rank of the channel matrix is typically low. Against this limitation, we propose a unified architecture that subsumes the conventional scheme of [101]. Then, we design our proposed scheme so as to maximize the mutual information. In terms of the information-theoretic perspective, we conclude that the proposed PM-based scheme has performance advantages over the conventional schemes. In Section 5.2, we propose the unified PM-based MIMO-VLC scheme for uncoded/coded scenarios. In Section 5.3, we propose our design guidelines for the proposed scheme and its adaptive counterpart. In Section 5.4, we simulate the proposed and conventional schemes in uncoded/coded scenarios.

Chapter 6: Permutation Modulation Based Multicarrier Communications

In Chapter 6, we analyze the PM-aided scheme applied to the multicarrier communications. The PM-aided scheme activates a part of subcarriers, similar to the GSM's antenna-activation principle. In Section 6.2, we introduce the basic model of the PM-aided scheme. In Section 6.3, we provide the information-theoretic analysis, in terms of minimum Euclidean distance (MED), unconstrained/constrained AMI, and peak-to-average power ratio (PAPR). Then, the upper-bound of the MED is derived for constituting the design guidelines for the PM-aided scheme. In Section 6.4, we simulate the above metrics along with the theoretical results.

Chapter 7: Conclusions and Future Research

In Chapter 7, we summarize the positive and negative effects of the PM-aided schemes having been introduced in this thesis. Then, we outline the future research topics.

1.4.2   Novel Contributions of the Thesis

Against the above backcloth, the novel contributions of this thesis are as follows.

- The PM concept is reconstituted based on [73]. The current PC and SM concepts [75, 77] are regarded as an extension of the 1965's PM concept. Since the PC- or SM-based schemes having been proposed in the space, time, and frequency domains rely on the on-off combination matrix of Eq. (1.17), the conventional schemes are considered as a member of PM family.

- The PM-based scheme that dispenses with channel estimation is proposed [4], where the sparse and unitary space-time matrices are used. This scheme is highlighted with its single-RF structure, which reduces the number of RF chains at the transmitter. Especially, the proposed scheme performs better in correlated channels owing to the reduced number of data streams, as compared to the dense-matrix-based schemes.

- The PM-based MIMO-MWC system is proposed [1]. We provide the design criteria for the proposed system operated in the LoS-dominant and correlated channels. Then, we compare the proposed scheme with the conventional spatial multiplexing scheme in terms of its unconstrained and constrained AMI. We show that the proposed scheme is capable of reducing the number of RF chains, while maintaining the near-optimum capacity of the spatial multiplexing scheme.

- The PM-based MIMO-VLC system is proposed [3], where the flexible PA matrix is invoked for improving the performance in the LoS dominant channels. We design the PA matrix in terms of maximizing the constrained mutual information or minimizing the turbo-cliff SNR of the irregular-coded system. We compare the proposed scheme with the conventional counterpart in terms of the information-theoretic perspective.

- The PM-aided multicarrier scheme is analyzed in a comprehensive manner [2]. We derive the upper bound of the MED of the PM-aided system, which correlates with the error-probability at high SNRs. Then, we formulate the unconstrained and the constrained capacity for the PM-aided system. In addition, we demonstrate that the sparsity of the PM-aided system does not affect the PAPR of the time-domain signals. The numerical simulations are conducted to verify our theoretical results.

Chapter 2

Comprehensive Survey on Permutation Modulation Family

2.1 Introduction

B ased on the general MIMO system model introduced in Chapter 1, this chapter reviews the diverse PM-based schemes having been proposed for the single and multicarrier microwave as well as visible light communications. As discussed in Chapter 1, the MIMO technology [13] is an established communication scheme that has been adopted by numerous communication standards [15, 14]. Against the spectrum shortage problem, at the time of writing, researchers have focused their attention on the higher bandwidths such as the mmWave [50] and visible light [51] domains, aiming at supporting the growing demands for wireless communications. In parallel, the PM research has attracted increasing attention [102–104, 27, 105–107], with the aid of its potential of enabling the low-complexity but near-optimum communication system. In order to verify its potential, in this chapter, we reproduce the results reported in previous studies with our numerical simulations.

The remainder of this chapter is organized as follows. Section 2.2 introduces the performance metrics of the MIMO communication systems, such as throughput, reliability, and complexity, which justify the performance advantages of the PM concept. Sections 2.3, 2.4, 2.5, and 2.6 review the PM concept designed for the coherent MIMO, the differential MIMO, the visible light, and the multicarrier communications, respectively. Finally, Section 2.7 summarizes this chapter.

2.2   Performance Metrics

In this section, we introduce the performance metrics proposed for the general MIMO communication model. We consider the following metrics: the average mutual information (AMI), the MED, and the decoding-complexity at the receiver, which will be described in Sections 2.2.1, 2.2.2, and 2.2.3, respectively.

2.2.1   Average Mutual Information

The mutual information between the transmitted and received signals represents the maximum achievable rate, which is the maximum number of information bits that are successfully conveyed from the transmitter to the receiver per channel use. In the literature, there are two AMI metrics: the unconstrained AMI and the constrained AMI. The unconstrained AMI is derived by assuming the continuous input symbols, namely, the input signals follow Gaussian distribution, while the constrained AMI is derived by assuming the finite number of the discrete symbols. The mutual information is averaged over each channel realization. If the channel environment is static, such as the AWGN and VLC channels, we use the terminology of "MI" instead of "AMI". In the study of [3], the unconstrained and constrained AMI of the PM system were referred to as the continuous-input continuous-output memoryless channel (CCMC) and discrete-input continuous-output memoryless channel (DCMC) capacities, respectively. It is still unknown that the Gaussian input maximizes the AMI of the PM system [108]. Hence, in this thesis, we use the terminology of "AMI" instead of "capacity".

2.2.1.1   Unconstrained Average Mutual Information

The unconstrained AMI I_C of the general MIMO system model of Eq. (1.2) is given by [12, 109]

$$I_C = \mathrm{E}_\mathbf{H} \left[\sum_{i=1}^{\mathrm{rank}(\mathbf{Q})} \log_2 \left(1 + \mu_i \rho \right) \right] \text{ [bits/symbol]}, \tag{2.1}$$

where we have the Hermitian matrix of

$$\mathbf{Q} = \begin{cases} \mathbf{H}^\mathrm{H}\mathbf{H} & (N \geq M) \\ \mathbf{H}\mathbf{H}^\mathrm{H} & (N < M) \end{cases} \tag{2.2}$$

and the channel matrix $\mathbf{H} \in \mathbb{C}^{N \times M}$ is randomly generated through a sufficient number of trials. Here, μ_i and ρ represent the ith eigenvalue of the Hermitian matrix $\mathbf{Q}$ and the received SNR. Hence, the unconstrained AMI I_C is only composed of the channel matrix $\mathbf{H}$ and the received SNR ρ. Eq. (2.1) is derived under the assumption that the input signals follow the complex-valued Gaussian distribution and the signals are sampled at a discrete interval. Moreover, the number of parallel streams is equal to rank($\mathbf{Q}$). By replacing the channel matrix $\mathbf{H}$ with the designated channel matrix, Eq. (2.1) is directly applicable to the various channel models such as the mmWave channels. The unconstrained AMI I_C represents the upper-bound of the constrained AMI, which is later denoted by I_D. The constrained AMI I_D is asymptotic to the unconstrained AMI I_C at low SNRs upon increasing the transmission rate R.

2.2.1.2 Constrained Average Mutual Information

The constrained AMI represents the practical upper-bound of the mutual information, where a finite number of the input codewords are considered. Here, we review its derivation process in detail [109, 110, 39], in order to understand its background in an appropriate manner. We assume that we have the 2^B number of the space-time codewords $\mathbf{S}^{(1)}, \cdots, \mathbf{S}^{(2^B)} \in \mathbb{C}^{M \times T}$, which are associated with the input bits having the length of B. Later, 2^B is denoted by the number of codewords N_c, namely, $\log_2(N_c) = B$. The constrained AMI of the general MIMO system model of Eq. (1.2) is given by [110]

$$I_D = \frac{1}{T} \max_{\mathrm{p}(\mathbf{S}^{(1)}), \cdots, \mathrm{p}(\mathbf{S}^{(N_c)})} \sum_{f=1}^{N_c} \int_{-\infty}^{\infty} \cdots \int_{-\infty}^{\infty} \mathrm{p}\left(\mathbf{Y}|\mathbf{S}^{(f)}\right)$$

$$\cdot \mathrm{p}\left(\mathbf{S}^{(f)}\right) \log_2 \left[\frac{\mathrm{p}\left(\mathbf{Y}|\mathbf{S}^{(f)}\right)}{\sum_{g=1}^{N_c} \mathrm{p}\left(\mathbf{Y}|\mathbf{S}^{(g)}\right) \mathrm{p}\left(\mathbf{S}^{(g)}\right)} \right] d\mathbf{Y}. \tag{2.3}$$

Since we have the relationship of $\int_{-\infty}^{\infty} \cdots \int_{-\infty}^{\infty} \mathrm{p}\left(\mathbf{Y}|\mathbf{S}^{(f)}\right) d\mathbf{Y} = 1$, by applying the Monte-Carlo integration, Eq. (2.3) is simplified to

$$I_D = \frac{1}{T} \max_{\mathrm{p}(\mathbf{S}^{(1)}), \cdots, \mathrm{p}(\mathbf{S}^{(N_c)})} \sum_{f=1}^{N_c} \mathrm{E}\left[\mathrm{p}\left(\mathbf{S}^{(f)}\right) \log_2 \left[\frac{\mathrm{p}\left(\mathbf{Y}|\mathbf{S}^{(f)}\right)}{\sum_{g=1}^{N_c} \mathrm{p}\left(\mathbf{Y}|\mathbf{S}^{(g)}\right) \mathrm{p}\left(\mathbf{S}^{(g)}\right)} \right] \right]. \tag{2.4}$$

Eq. (2.4) is maximized when the codewords $\mathbf{S}^{(1)}, \cdots, \mathbf{S}^{(N_c)}$ are selected with the equal-probability of $1/N_c$. The idealized assumption of $\mathrm{p}\left(\mathbf{S}^{(1)}\right) = \cdots = \mathrm{p}\left(\mathbf{S}^{(N_c)}\right) = 1/N_c$ simplifies

Eq. (2.4) as follows:

$$I_D = \frac{1}{T} \sum_{f=1}^{N_c} \frac{1}{N_c} \mathrm{E}\left[\log_2 N_c - \log_2 \sum_{g=1}^{N_c} \frac{\mathrm{p}\left(\mathbf{Y}|\mathbf{S}^{(g)}\right)}{\mathrm{p}\left(\mathbf{Y}|\mathbf{S}^{(f)}\right)} \right]. \tag{2.5}$$

Since we have $\frac{1}{N_c} \sum_{f=1}^{N_c} \log_2 N_c = B$, Eq. (2.5) is transformed into

$$I_D = \frac{1}{T}\left(B - \frac{1}{N_c} \sum_{f=1}^{N_c} \mathrm{E}\left[\log_2 \sum_{g=1}^{N_c} \frac{\mathrm{p}\left(\mathbf{Y}|\mathbf{S}^{(f)}\right)}{\mathrm{p}\left(\mathbf{Y}|\mathbf{S}^{(g)}\right)} \right] \right). \tag{2.6}$$

Let us derive $\frac{\mathrm{p}\left(\mathbf{Y}|\mathbf{S}^{(f)}\right)}{\mathrm{p}\left(\mathbf{Y}|\mathbf{S}^{(g)}\right)}$ in Eq. (2.6). The conditional probability density function (pdf) of $\mathbf{Y}$ given $\mathbf{S}$ is defined as follows:

$$\mathrm{p}(\mathbf{Y}|\mathbf{S}) = \frac{1}{\left(\pi\sigma_v^2\right)^{NT}} \exp\left(-\frac{\|\mathbf{Y} - \mathbf{HS}\|_\mathrm{F}^2}{\sigma_v^2} \right). \tag{2.7}$$

Now, we assume the relationship of $\mathbf{Y} = \mathbf{HS}^{(f)} + \mathbf{V}$. Based on the definition of $\mathrm{p}\left(\mathbf{Y}|\mathbf{S}\right)$, $\frac{\mathrm{p}\left(\mathbf{Y}|\mathbf{S}^{(f)}\right)}{\mathrm{p}\left(\mathbf{Y}|\mathbf{S}^{(g)}\right)}$ is given by

$$\frac{\mathrm{p}\left(\mathbf{Y}|\mathbf{S}^{(f)}\right)}{\mathrm{p}\left(\mathbf{Y}|\mathbf{S}^{(g)}\right)} = \exp\left(\frac{-\left\|\mathbf{Y} - \mathbf{HS}^{(g)}\right\|_\mathrm{F}^2 + \left\|\mathbf{Y} - \mathbf{HS}^{(f)}\right\|_\mathrm{F}^2}{\sigma_v^2} \right) = \exp\left(\frac{-\left\|\mathbf{H}\left(\mathbf{S}^{(f)} - \mathbf{S}^{(g)}\right) + \mathbf{V}\right\|_\mathrm{F}^2 + \|\mathbf{V}\|_\mathrm{F}^2}{\sigma_v^2} \right).$$

Finally, we arrive at

$$I_D = \frac{1}{T}\left(B - \frac{1}{N_c} \sum_{f=1}^{N_c} \mathrm{E}_{\mathbf{H},\mathbf{V}}\left[\log_2 \sum_{g=1}^{N_c} e^{\eta[f,g]} \right] \right) \le \frac{B}{T} = R \text{ [bits/symbol]}, \tag{2.8}$$

where we have

$$\eta[f,g] = \frac{-\left\|\mathbf{H}\left(\mathbf{S}^{(f)} - \mathbf{S}^{(g)}\right) + \mathbf{V}\right\|_\mathrm{F}^2 + \|\mathbf{V}\|_\mathrm{F}^2}{\sigma_v^2}. \tag{2.9}$$

Note that the general AMI of Eq. (2.8) is directly applicable to the various channel models and codewords. For example, Eq. (2.8) supports the SISO symbols of $\mathbf{S} \in \mathbb{C}^{1\times1}$ and the SM symbols of $\mathbf{S} \in \mathbb{C}^{M\times1}$. The constrained AMI of I_D estimates the turbo-cliff SNR of the system, where the BER drops to an infinitesimal value, with the aid of the powerful channel coding schemes such as the turbo codes and LDPC codes [20].

2.2.2 Reliability

The reliability evaluation, which calculates the number of errors between the original bits and the estimated bits at the receiver, has been the most typical performance metric in the literature. Owing to its simple formulation, the powerful analytical frameworks [11] enable us to estimate the tight bound of error probabilities in uncoded scenarios, where no channel coding scheme is considered. The pairwise-error probability (PEP), where the transmitted symbol $\mathbf{S}$ is misdecoded as the wrong symbol $\mathbf{S}'$ at the receiver, is defined by [111]

$$\mathrm{PEP}(\mathbf{S} \to \mathbf{S}'|\mathbf{H}) = \mathrm{p}\left(\|\mathbf{Y}-\mathbf{HS}'\|_{\mathrm{F}} - \|\mathbf{Y}-\mathbf{HS}\|_{\mathrm{F}} < 0\right)$$

$$= \mathrm{Q}\left(\sqrt{\frac{\|\mathbf{HD}\|_{\mathrm{F}}^2}{2\sigma_v^2}}\right), \tag{2.10}$$

where we have the channel matrix $\mathbf{H}$ and $\mathbf{D} = (\mathbf{S}-\mathbf{S}')(\mathbf{S}-\mathbf{S}')^{\mathrm{H}}$. Note that $\mathrm{Q}(\cdot)$ denotes the Q-function[1]. Then, averaging Eq. (2.10) over the possible channel matrices yields [111]

$$\mathrm{PEP}(\mathbf{S} \to \mathbf{S}') = \frac{1}{\pi}\int_0^{\pi/2}\prod_{m=1}^M\left(1+\frac{\mu_m}{4\sigma_v^2\sin^2\theta}\right)^{-N}\mathrm{d}\theta. \tag{2.11}$$

Here, μ_m represents the mth eigenvalue of $\mathbf{D}$. Based on Eq. (2.11), the bit error rate (BER) is upper-bounded by [111]

$$\mathrm{BER} \le \frac{1}{B2^B}\sum_{\mathbf{S}}\sum_{\mathbf{S}\neq\mathbf{S}'}d_{\mathrm{H}}(\mathbf{b},\mathbf{b}')\mathrm{PEP}(\mathbf{S} \to \mathbf{S}'), \tag{2.12}$$

where $d_{\mathrm{H}}(\mathbf{b},\mathbf{b}')$ represents the Hamming distance between the bit sequences $\mathbf{b}$ and $\mathbf{b}'$, which are associated with $\mathbf{S}$ and $\mathbf{S}'$. For example, $\mathrm{d}_{\mathrm{H}}([0\ 0],[0\ 1])$ is calculated by 1.

---

[1]More specifically, the Q-function is defined by $\mathrm{Q}(\cdot) = \frac{1}{2}\left(1-\mathrm{erf}\left(\frac{x}{\sqrt{2}}\right)\right)$, where we have $\mathrm{erf}(x) = \frac{2}{\sqrt{\pi}}\int_0^\pi e^{-t^2}\mathrm{d}t$.

The rank- and determinant-criterion (RDC) maximize the coding gain while maintaining the maximum diversity order D. The diversity order represents the slope of the BER curve at high SNRs in uncoded scenarios. The higher the coding gain is, the lower BER is achievable for the communication system. At high SNRs, Eq. (2.11) is upper-bounded by [112, 113]

$$\text{PEP}(\mathbf{S} \rightarrow \mathbf{S}') \leq \underbrace{\frac{1}{\prod_{m=1}^{m'} \mu_m^N}}_{\text{coding gain}} \overbrace{\left(\frac{1}{4\sigma_v^2}\right)^{-\,m'N}}^{\text{diversity gain}},\qquad(2.13)$$

where m' represents the minimum rank of $\mathbf{D}$, namely, $m' = \min_{\mathbf{S},\mathbf{S}'} |\text{rank}(\mathbf{D})|$. In Eq. (2.13), the diversity order is given by $D = m'N$ and the coding gain is given by $\prod_{m=1}^{m'} \mu_m$. The coding gain $\prod_{m=1}^{m'} \mu_m$ is also known as the MED between the codewords $\mathbf{S}$ and $\mathbf{S}'$. Typically, the MIMO codewords are designed by RDC in uncoded scenarios, where the diversity and coding gains are maximized.

2.2.3 Complexity

We evaluate the PM schemes in terms of the computational complexity at the receiver. The PM scheme has a lower complexity when compared to the conventional schemes in general, with the aid of the reduced number of data streams. In this thesis, the computational complexity is approximated by the number of real-valued multiplications at the detection process, which is nearly equal to the number of multipliers in the receiver circuits. It was shown in [114] that, as the number of the multipliers increases, the computational time, the power consumption, as well as the hardware cost, also increase. More specifically, if we have the two complex-valued numbers $(a + bj) \in \mathbb{C}$ and $(c + dj) \in \mathbb{C}$, the total real-valued calculations of $(a + bj)(c + dj)$ is four because we have the relationship of $(a + bj)(c + dj) = ac - bd + (ad + bc)j$.

For example, if we consider the SM scheme designed for the microwave communications, as will be described in Section 2.3.1 in detail, the computational complexity of the receiver is calculated by $O(2^B N)$. Here, the detection criterion for the SM scheme is given by

$$\hat{\mathbf{S}} = \arg\min_{\mathbf{S}} \|\mathbf{Y} - \mathbf{H} \cdot \mathbf{S}\|_{\text{F}}^2.\qquad(2.14)$$

The receiver estimates the transmitted symbol $\mathbf{S}$ through the 2^B number of trials in Eq. (2.14). In each trial, the matrix multiplication of $\mathbf{H} \cdot \mathbf{S}$ includes N number of complex-valued multi-

plications, which is equivalent to $4N$ number of real-valued multiplications. In addition, the Frobenius norm calculation of $\|\mathbf{Y} - \mathbf{H} \cdot \mathbf{S}\|_F^2$ includes $2N$ number of real-valued multiplications. Hence, the computational complexity for the SM scheme is given by $2^B \cdot 6N \approx O(2^B N)$.

2.3 Permutation Modulation Based Coherent MIMO Communications

In this section, we review the PM concept having been proposed within the coherent space-time block code (STBC) framework. The PM-based coherent MIMO scheme was firstly proposed by Chau *et al.* in 2001 [77], which was termed as SSK. The spatial modulation (SM) as well as the SSK schemes have attracted attentions owing to its simplified transmitter and receiver structure. The contributions to the PM-based coherent MIMO schemes are summarized in Table 2.1.

2.3.1 Spatial Modulation / Space-Shift Keying

The SM [115, 116] is the PM scheme designed for the coherent MIMO system. The SM scheme activates a single out of multiple transmit antennas at any time. Hence, it circumvents the inter-channel interference (ICI) when assuming frequency-flat channels. The key feature of the SM scheme lies on its single-RF architecture, where the transmitter is equipped with the single-RF chain. This structure contributes to increasing the number of transmit antennas in the large-scale MIMO context [108]. Note that the SSK scheme is equivalent to the SM scheme having no constellation.

The SM encoding principle is twofold. The input $B = B_1 + B_2$ bits are serial-to-parallel (S/P) converted to $B_1 = \log_2(M)$ and $B_2 = \log_2(\mathcal{L})$ bits. Based on the first B_1 bits, the single qth transmit antenna out of the M numbers antennas is selected. Based on the second B_2 bits, the single $\mathcal{L}$–APSK symbol s is modulated. The transmission rate of the SM scheme is $R = B$ [bits/symbol]. Here, the SM scheme only increases the transmission rate, instead of the transmit diversity gain. The SM codeword $\mathbf{s} \in \mathbb{C}^{M \times 1}$ is given by

$$\mathbf{s} = [\underbrace{0 \cdots 0}_{q-1 \text{ rows}} \underbrace{s}_{\substack{\uparrow \\ q\text{th row}}} \underbrace{0 \cdots 0}_{M-q \text{ rows}}]^\mathrm{T}. \tag{2.15}$$

Table 2.1 Contributions to the PM-based coherent MIMO schemes.

Year	Authors	Contribution
2001	Chau and Yu [77]	Proposed the SSK scheme for the coherent MIMO communications.
2008	Mesleh *et al.* [115]	Proposed the SM scheme that activates a single antenna out of the multiple transmit antennas.
	Jeganathan *et al.* [116]	Proposed the optimum detector for the SM scheme of [115].
	Jeganathan *et al.* [94]	Extended the SSK concept to that uses the multiple transmit antennas at the same time.
	Yang *et al.* [117]	Derived the Ergodic capacity for the SM system.
2010	Sugiura *et al.* [39]	Generalized the SM concept and proposed its differential counterpart.
2011	Ngo *et al.* [118]	Applied the PM concept to the space-time-frequency domain.
	Sugiura *et al.* [119]	Proposed the GSTSK concept that subsumes the conventional MIMO schemes, such as the SM, the STSK, the OSTBC, and the BLAST schemes.
2012	Yang and Aíssa [120]	Derived the Ergodic capacity for the GSM system.
2014	Ishibashi and Sugiura [98]	Proposed the SM-specific shaping filter. It was proved that the BPSK-aided SM scheme is advantageous over the spatial multiplexing scheme when employing over $M > 32$ transmit antennas. Also, the QPSK-aided SM scheme has to employ over $M > 1024$ antennas.
2015	Basnayaka *et al.* [108]	Proved that the SM scheme is effective in the large-scale MIMO scenario in terms of its Ergodic capacity.
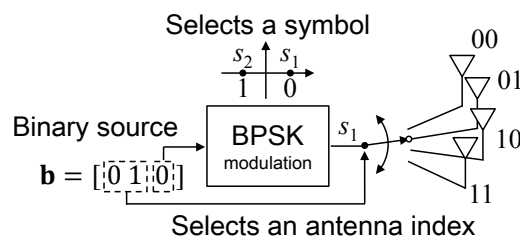
Figure 2.1 Schematic of the BPSK-aided SM transmitter, where the number of transmit antenna is $M = 4$.

Table 2.2 The bit mapping example of the BPSK-aided SM scheme.

Source (3 bits)	Activated antenna index q	Modulated symbol s	SM codeword $\mathbf{s}$
0 0 ¦ 0	1	+1	$[+1\ \ 0\ 0\ 0]^{\mathrm{T}}$
0 0 ¦ 1	1	−1	$[-1\ \ 0\ 0\ 0]^{\mathrm{T}}$
0 1 ¦ 0	2	+1	$[0 + 1\ 0\ 0]^{\mathrm{T}}$
0 1 ¦ 1	2	−1	$[0 - 1\ 0\ 0]^{\mathrm{T}}$
1 0 ¦ 0	3	+1	$[0\ 0 + 1\ 0]^{\mathrm{T}}$
1 0 ¦ 1	3	−1	$[0\ 0 - 1\ 0]^{\mathrm{T}}$
1 1 ¦ 0	4	+1	$[0\ 0\ 0 + 1]^{\mathrm{T}}$
1 1 ¦ 1	4	−1	$[0\ 0\ 0 - 1]^{\mathrm{T}}$

Fig. 2.1 shows the the schematic of the SM transmitter, where the constellation size is $\mathcal{L} = 2$ and the number of transmit antenna is $M = 4$. The length of the input bits is calculated by $B = B_1 + B_2 = \log_2(M) + \log_2(\mathcal{L}) = 2 + 1 = 3$ [bits]. In Fig. 2.1, the input $B = 3$ bits are divided into the two sequences. According to the first $B_1 = 2$ bits, the single transmit antenna out of the $M = 4$ number of antennas is selected. According to the second $B_2 = 1$ bit, the single BPSK symbol is modulated. Finally, the modulated BPSK symbol is transmitted from the selected single antenna. In addition, Table 2.2 exemplifies the bit mapping example of the BPSK-aided SM scheme, where the system parameters are the same with those used in Fig. 2.1.

2.3.2 Generalized Spatial Modulation

The GSM and generalized space shift keying (GSSK) schemes are the extensions of the SM and SSK schemes, where the arbitrary number of transmit antennas are activated simultaneously [94]. We use the notation of GSM(M,P), where M is the number of transmit antennas and P is the number of activated antennas. Note that the GSM(M,P) scheme having $\mathcal{L} = 1$ is equivalent to the GSSK scheme.

The GSM encoding principle is basically similar to that of the SM scheme. The input $B = B_1 + B_2$ bits are S/P converted to the two sequences: $B_1 = \log_2(N_a)$ and $B_2 = P\log_2(\mathcal{L})$ bits, with the relationship of $B = B_1 + B_2$. Based on the first B_1 bits, the qth antenna-activation indices set $\mathbf{a}_q$ is selected out of $N_a = 2^{\left\lfloor \log_2 \binom{M}{P} \right\rfloor}$ legitimate combinations for $1 \leq q \leq N_a$. Here, we represent the indices of non-zero elements in a GSM codeword as a vector $\mathbf{a}_i \in \mathbb{Z}^P$ $(1 \leq i \leq N_a)$. The vector $\mathbf{a}_i$ consists of the P number of sorted integers ranging from 1 to M, which represent the activated antenna indices. For example, $\mathbf{a}_1 = [1,2]$ implies
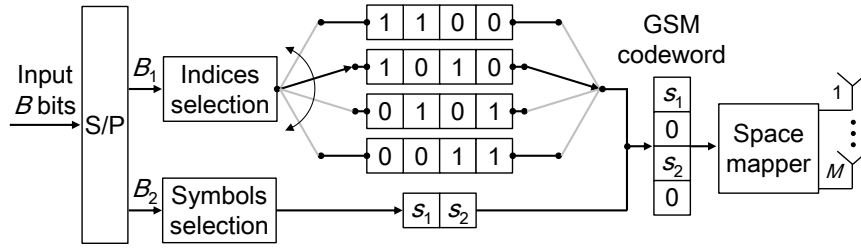
Figure 2.2 The schematic of the GSM(4,2) transmitter.

that the first and second transmit antennas are activated. Then, based on the second B_2 bits, P number of APSK symbols $s_1, \cdots, s_P$ are modulated with $\mathcal{L}$−point constellations. The indices of non-zero elements are determined by [76]

$$\mathbf{C}_{M,P} = \begin{bmatrix} \mathbf{1} & \mathbf{C}_{M-1,P-1} \\ \mathbf{0} & \mathbf{C}_{M-1,P} \end{bmatrix} \in [0,1]^{\binom{M}{P} \times M}, \tag{2.16}$$

where $\mathbf{0}$ denotes a zero vector having the length of $\binom{M-1}{P}$. Similarly, $\mathbf{1}$ denotes a vector having the length of $\binom{M-1}{P-1}$ containing only ones. The natural binary code (NBC) [76] maps $\mathbf{a}_i$ to the ith row of $\mathbf{C}_{M,P}$. In contrast, the look-up table (LUT) method [76, 96] maps $\mathbf{a}_i$ to the manually selected row of $\mathbf{C}_{M,P}$. Finally, based on the selected antenna-activation vector $\mathbf{a}_q$ and the modulated symbols $s_1, \cdots, s_P$, the GSM codeword $\mathbf{s} \in \mathbb{C}^{M \times 1}$ is given by

$$\mathbf{s} = [0 \ \cdots \ 0 \ \underbrace{s_1}_{\mathbf{a}_q(1)\text{th row}} \ 0 \ \cdots \ 0 \ \underbrace{s_2}_{\mathbf{a}_q(2)\text{th row}} \ 0 \ \cdots \ 0 \ \underbrace{s_P}_{\mathbf{a}_q(P)\text{th row}} \ 0 \ \cdots \ 0]^{\mathrm{T}}. \tag{2.17}$$

Note that the GSM(M,M) is equivalent to the conventional BLAST scheme, where the M number of the independent symbols are embedded in a codeword.

Let us check a detailed example. Fig. 2.2 shows the transmitter schematic of the GSM($M = 4$, $P = 2$) scheme. Here, we have the $N_{\mathrm{a}} = 2^{\lfloor \log_2 \binom{4}{2} \rfloor} = 2^2 = 4$ number of the antenna-activation patterns. If we assume that the constellation size is $\mathcal{L} = 2$, the input bits length is calculated by $B = B_1 + B_2 = \log_2(4) + 2 \log_2(2) = 4$. The antenna-activation matrix

Table 2.3 Bit mapping example of the BPSK-aided GSM(4,2).

Source (4 bits)	Indices $\mathbf{a}$	Symbols s_1, s_2	GSM codeword $\mathbf{S}$
0 0 ⁝ 0 0	$\mathbf{a}_1 = [1,2]$	+1,+1	$[+1,+1,\ 0,\ 0]^{\mathrm{T}}$
0 0 ⁝ 0 1	$\mathbf{a}_1 = [1,2]$	+1,−1	$[+1,−1,\ 0,\ 0]^{\mathrm{T}}$
0 0 ⁝ 1 0	$\mathbf{a}_1 = [1,2]$	−1,+1	$[−1,+1,\ 0,\ 0]^{\mathrm{T}}$
0 0 ⁝ 1 1	$\mathbf{a}_1 = [1,2]$	−1,−1	$[−1,−1,\ 0,\ 0]^{\mathrm{T}}$
0 1 ⁝ 0 0	$\mathbf{a}_2 = [1,3]$	+1,+1	$[+1,\ 0,+1,\ 0]^{\mathrm{T}}$
0 1 ⁝ 0 1	$\mathbf{a}_2 = [1,3]$	+1,−1	$[+1,\ 0,−1,\ 0]^{\mathrm{T}}$
0 1 ⁝ 1 0	$\mathbf{a}_2 = [1,3]$	−1,+1	$[−1,\ 0,+1,\ 0]^{\mathrm{T}}$
0 1 ⁝ 1 1	$\mathbf{a}_2 = [1,3]$	−1,−1	$[−1,\ 0,−1,\ 0]^{\mathrm{T}}$
1 0 ⁝ 0 0	$\mathbf{a}_3 = [2,4]$	+1,+1	$[\ 0,+1,\ 0,+1]^{\mathrm{T}}$
1 0 ⁝ 0 1	$\mathbf{a}_3 = [2,4]$	+1,−1	$[\ 0,+1,\ 0,−1]^{\mathrm{T}}$
1 0 ⁝ 1 0	$\mathbf{a}_3 = [2,4]$	−1,+1	$[\ 0,−1,\ 0,+1]^{\mathrm{T}}$
1 0 ⁝ 1 1	$\mathbf{a}_3 = [2,4]$	−1,−1	$[\ 0,−1,\ 0,−1]^{\mathrm{T}}$
1 1 ⁝ 0 0	$\mathbf{a}_4 = [3,4]$	+1,+1	$[\ 0,\ 0,+1,+1]^{\mathrm{T}}$
1 1 ⁝ 0 1	$\mathbf{a}_4 = [3,4]$	+1,−1	$[\ 0,\ 0,+1,−1]^{\mathrm{T}}$
1 1 ⁝ 1 0	$\mathbf{a}_4 = [3,4]$	−1,+1	$[\ 0,\ 0,−1,+1]^{\mathrm{T}}$
1 1 ⁝ 1 1	$\mathbf{a}_4 = [3,4]$	−1,−1	$[\ 0,\ 0,−1,−1]^{\mathrm{T}}$

$\mathbf{C}_{M,P}$ is given by

$$
\mathbf{C}_{4,2} = \begin{bmatrix} 1 & 1 & 0 & 0 \\ 1 & 0 & 1 & 0 \\ 1 & 0 & 0 & 1 \\ 0 & 1 & 1 & 0 \\ 0 & 1 & 0 & 1 \\ 0 & 0 & 1 & 1 \end{bmatrix} \in [0,1]^{6\times4}. \tag{2.18}
$$

If we use the NBC method, the antenna-activation vectors are given by $\mathbf{a}_1 = [1,2]$, $\mathbf{a}_2 = [1,3]$, $\mathbf{a}_3 = [1,4]$, and $\mathbf{a}_4 = [2,3]$ based on the first, second, third, and fourth rows of $\mathbf{C}_{4,2}$. In contrast, if we use the LUT method, the antenna-activation vectors are given by $\mathbf{a}_1 = [1,2]$, $\mathbf{a}_2 = [1,3]$, $\mathbf{a}_3 = [2,4]$, and $\mathbf{a}_4 = [3,4]$ based on the first, second, fifth, and sixth rows of $\mathbf{C}_{4,2}$. Table 2.3 shows the bit mapping example for the LUT method.
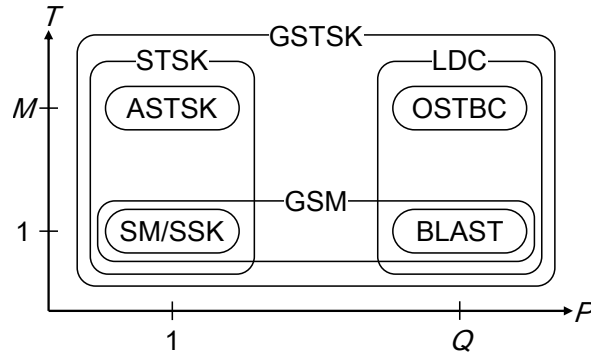
Figure 2.3 The relationship between the GSTSK and the other conventional schemes.
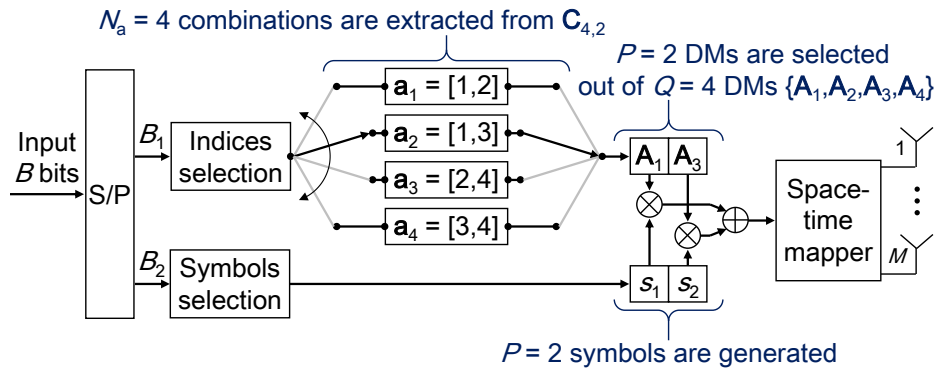
Figure 2.4 The schematic of the GSTSK transmitter.

2.3.3 Generalized Space-Time Shift Keying

The generalized space-time shift keying (GSTSK) scheme is capable of subsuming the conventional MIMO schemes, such as the SM, the SSK, and the BLAST schemes, with the aid of its flexible dispersion matrix (DM) architecture [119]. The GSTSK framework enables us to analyze all of the MIMO encoding schemes in a comprehensive manner. Fig. 2.3 shows the relationship between the GSTSK and the other MIMO encoding schemes. Later, each scheme in Fig. 2.3 is redefined by the GSTSK framework.

Fig. 2.4 shows the transmitter schematic of the GSTSK scheme. In advance of the symbol transmission, the Q number of the DMs $\mathbf{A}_q \in \mathbb{C}^{M \times T}$ $(1 \leq q \leq Q)$ are prepared. The DMs are designed to maximize the designated criterion, such as the constrained AMI of Section 2.2.1.2 and the RDC of Section 2.2.2. Here, each DM $\mathbf{A}_q$ has the following energy constraint:

$$\mathrm{tr}\left[\mathbf{A}_q \mathbf{A}_q^H\right] = \frac{T}{P} \ (1 \leq q \leq Q). \tag{2.19}$$

Table 2.4 Bit mapping example of the BPSK-aided GSTSK($M,N,T,3,2$), where we have $B = B_1 + B_2 = 1 + 2 = 3$ [bits]. There are the $N_a = 2$ activation patterns of $\mathbf{a}_1 = [1,2]$ and $\mathbf{a}_2 = [1,3]$.

Source (3 bits)	Selected pattern $\mathbf{a}_q$	Activated DMs $\mathbf{A}_{\mathbf{a}_q(1)}, \mathbf{A}_{\mathbf{a}_q(2)}$	BPSK symbols s_1, s_2	Codeword $\mathbf{S}$
0 ¦ 0 0	$\mathbf{a}_1 = [1, 2]$	$\mathbf{A}_1, \mathbf{A}_2$	$+1, +1$	$\mathbf{A}_1 + \mathbf{A}_2$
0 ¦ 0 1	$\mathbf{a}_1 = [1, 2]$	$\mathbf{A}_1, \mathbf{A}_2$	$+1, -1$	$\mathbf{A}_1 - \mathbf{A}_2$
0 ¦ 1 0	$\mathbf{a}_1 = [1, 2]$	$\mathbf{A}_1, \mathbf{A}_2$	$-1, +1$	$-\mathbf{A}_1 + \mathbf{A}_2$
0 ¦ 1 1	$\mathbf{a}_1 = [1, 2]$	$\mathbf{A}_1, \mathbf{A}_2$	$-1, -1$	$-\mathbf{A}_1 - \mathbf{A}_2$
1 ¦ 0 0	$\mathbf{a}_2 = [1, 3]$	$\mathbf{A}_1, \mathbf{A}_3$	$+1, +1$	$\mathbf{A}_1 + \mathbf{A}_3$
1 ¦ 0 1	$\mathbf{a}_2 = [1, 3]$	$\mathbf{A}_1, \mathbf{A}_3$	$+1, -1$	$\mathbf{A}_1 - \mathbf{A}_3$
1 ¦ 1 0	$\mathbf{a}_2 = [1, 3]$	$\mathbf{A}_1, \mathbf{A}_3$	$-1, +1$	$-\mathbf{A}_1 + \mathbf{A}_3$
1 ¦ 1 1	$\mathbf{a}_2 = [1, 3]$	$\mathbf{A}_1, \mathbf{A}_3$	$-1, -1$	$-\mathbf{A}_1 - \mathbf{A}_3$

Similar to the GSM encoding, we use the notations of $N_a = 2^{\left\lfloor \log_2 \binom{Q}{P} \right\rfloor}$ and the index vectors of $\mathbf{a}_i \in Z^P$ ($1 \leq i \leq N_a$). The input $B = B_1 + B_2$ bits are divided into the two sequences: $B_1 = \log_2(N_a)$ bits and $B_2 = P \log_2(\mathcal{L})$ bits. Based on the first B_1 bits, the qth index vector of $\mathbf{a}_q$ is selected out of the N_a combinations for $1 \leq q \leq N_a$. Then, based on the second B_2 bits, P number of the APSK symbols $s_1, \cdots, s_P \in \mathbb{C}$ are modulated. Finally, the space-time codeword of the GSTSK scheme is generated by

$$\mathbf{S} = \sum_{p=1}^{P} s_p \mathbf{A}_{\mathbf{a}_q(p)} \qquad (2.20)$$

The transmission rate of the GSTSK scheme is given by

$$R = \frac{B}{T} = \frac{B_1 + B_2}{T} = \frac{\left\lfloor \log_2 \binom{Q}{P} \right\rfloor + P \log_2 \mathcal{L}}{T}. \text{ [bits/symbol]} \qquad (2.21)$$

In this thesis, we use the notation of GSTSK(M,N,T,Q,P) for simplicity.

Table 2.4 shows the bit mapping example of the BPSK-aided GSTSK($M,N,T,3,2$) scheme. The input $B = 3$ bits are divided into the $B_1 = 1$ bit and the $B_2 = 2$ bits. Based on the B_1 bit, the $P = 2$ DMs are selected out of $Q = 3$ DMs. Then, based on the B_2 bits, the $P = 2$ BPSK symbols s_1 and s_2 are modulated. Finally, the space-time codeword $\mathbf{S}$ is generated by Eq. (2.42).

As shown in Fig. 2.3, the GSTSK scheme subsumes the conventional MIMO encodings. Here, we redefine the conventional schemes, including the OSTBC, the SM/SSK, the

asynchronous space-time shift keying (ASTSK), the BLAST, and the linear dispersion code (LDC) schemes, by invoking the GSTSK(M,N,T,Q,P) framework.

OSTBC: The space-time codewords of the OSTBC scheme having $M = 2$ are given by [28]

$$\mathbf{S}(i) = \frac{1}{\sqrt{2}} \begin{bmatrix} s_1 & -s_2^* \\ s_2 & s_1^* \end{bmatrix}, \tag{2.22}$$

where s_1 and s_2 denote the APSK symbols. The codeword of Eq. (2.22) is represented by the GSTSK($2,N,2,2,2$) having the following DMs:

$$\mathbf{A}_1 = \begin{bmatrix} \exp(0.25\pi j) & 0.0 \\ 0.0 & \exp(-0.25\pi j) \end{bmatrix}, \mathbf{A}_2 = \begin{bmatrix} 0.0 & \exp(-0.25\pi j) \\ \exp(0.25\pi j) & 0.0 \end{bmatrix}.$$

Then, the OSTBC codeword is redefined by

$$\mathbf{S}(i) = \frac{1}{\sqrt{2}} \begin{bmatrix} s_1 & -s_2^* \\ s_2 & s_1^* \end{bmatrix} = \frac{1}{\sqrt{2}} \sum_{q=1}^{2} \left(\text{Re}[s_q]\text{Re}[\mathbf{A}_q] + j\text{Im}[s_q]\text{Im}[\mathbf{A}_q] \right).$$

GSM/GSSK: The GSM scheme [94, 121] is represented by the GSTSK($M,N,1,M,P$) having the following DMs $\mathbf{A}_q \in \mathbb{C}^{M\times 1}$ ($1 \le q \le M$):

$$\mathbf{A}_1 = \begin{bmatrix} 1 \\ 0 \\ \vdots \\ 0 \end{bmatrix}, \mathbf{A}_2 = \begin{bmatrix} 0 \\ 1 \\ \vdots \\ 0 \end{bmatrix}, \cdots, \mathbf{A}_M = \begin{bmatrix} 0 \\ 0 \\ \vdots \\ 1 \end{bmatrix}. \tag{2.23}$$

For example, if we consider the SM scheme, which is equivalent to the GSM($M,1$), the antenna-activation matrix is calculated by $\mathbf{C}_{M,1} = \mathbf{I}_M$. Then, at any transmission index, a single out of the M transmit antennas is selected in accordance with the SM concept. For the qth index vector $\mathbf{a}_q$, the SM codeword is given by

$$\mathbf{S} = s_1 \mathbf{A}_{\mathbf{a}_q(1)} = s_1 \mathbf{A}_q = [0 \cdots 0 \underbrace{s}_{q\text{th row}} 0 \cdots 0]^{\text{T}}.$$

ASTSK: The ASTSK scheme is an extension of the SM scheme, where the codeword's time slot is increased to $T \geq 2$ [27], which is represented by the GSTSK($M,N,T,Q,1$). Each DM $\mathbf{A}_q \in \mathbb{C}^{M \times T}$ ($1 \leq q \leq Q$) has a single non-zero element in its column and row, and has the constraint of rank($\mathbf{A}_q$) = min(M,T). For example, if we consider the (M,Q) = (3,4) case, the DMs are given by

$$\mathbf{A}_1 = \begin{bmatrix} a_{11} & 0 & 0 \\ 0 & a_{12} & 0 \\ 0 & 0 & a_{13} \end{bmatrix}, \mathbf{A}_2 = \begin{bmatrix} a_{21} & 0 & 0 \\ 0 & 0 & a_{23} \\ 0 & a_{22} & 0 \end{bmatrix},$$

$$\mathbf{A}_3 = \begin{bmatrix} 0 & a_{32} & 0 \\ a_{31} & 0 & 0 \\ 0 & 0 & a_{33} \end{bmatrix}, \mathbf{A}_4 = \begin{bmatrix} 0 & 0 & a_{43} \\ 0 & a_{42} & 0 \\ a_{41} & 0 & 0 \end{bmatrix}.$$

Since the $P = 1$ modulated APSK symbol is copied over T time slots, the ASTSK scheme achieves the diversity order of T.

BLAST: The BLAST scheme [13] is represented by the GSTSK($M,N,1,M,M$), where the M number of the DMs are the same with those shown in the GSM case of Eq. (2.23). Note that the number of selected DMs $P = M$ denotes the number of required RF chains at the transmitter.

LDC: The LDC scheme [36] is represented by the GSTSK(M,N,T,Q,Q). The DMs of the LDC scheme have to be designed in advance of the transmission, similar to the DMs of the GSTSK scheme.

2.3.4 Optimum Hard and Soft Detectors

We review the hard and soft detectors for the GSTSK scheme. As introduced in Section 2.3.3, the GSTSK scheme is capable of subsuming the diverse MIMO encoding schemes. Hence the following detectors are applicable to the other MIMO schemes in general, such as the GSM and the BLAST schemes.

Firstly, let us review the hard detector of the GSTSK scheme. The maximum *a posteriori* (MAP) detector searches the best $\hat{\mathbf{S}}$ that maximizes the *a posteriori* probability of p($\mathbf{S}|\mathbf{Y}$), where the received symbol of $\mathbf{Y}$ is given. Based on Bayes' theorem[2], the relationship between

---

[2]Bayes' theorem [122] is given by p($X|Y$) = p($Y|X$) $\cdot$ p(X)/p(Y), where X and Y are random variables.

the *a priori* and *a posteriori* probabilities is given by

$$p(\mathbf{S}|\mathbf{Y}) = \frac{p(\mathbf{Y}|\mathbf{S})p(\mathbf{S})}{p(\mathbf{Y})}. \tag{2.24}$$

We assume that $p(\mathbf{S})$ is constant since the input bits are randomly generated and the associated codeword $\mathbf{S}$ is transmitted with the equal probability of $1/2^B$. In addition, the *a priori* probability $p(\mathbf{Y})$ is unknown at the hard decision process. Hence, maximizing *a posteriori* probability $p(\mathbf{S}|\mathbf{Y})$ is equivalent to maximizing the likelihood $p(\mathbf{Y}|\mathbf{S})$, which is given in Eq. (2.7). According to Eq. (2.7), the decision metric is given by

$$\hat{\mathbf{S}} = \arg\max_{\mathbf{S}} p(\mathbf{Y}|\mathbf{S}) = \arg\min_{\mathbf{S}} \|\mathbf{Y} - \mathbf{HS}\|_{\mathrm{F}}^2, \tag{2.25}$$

which is also known as the maximum likelihood detection (MLD). Note that the Frobenius norm calculation of Eq. (2.25) is carried out over the 2^B number of trials.

Next, let us review the log-likelihood ratio (LLR)-based soft detector designed for the channel coding schemes, such as the turbo codes and LDPC codes, where we use the *a priori* information. The space-time codeword $\left\{\mathbf{S}^{(1)}, \cdots, \mathbf{S}^{(2^B)}\right\}$ of the GSTSK scheme is associated with the input bits $\mathbf{b} = [b_1, \cdots, b_B]^{\mathrm{T}} \in \mathbb{B}^B$. The LLR of the bit b_k ($1 \le k \le B$) is given by [20]

$$L(b_k|\mathbf{Y}) = \ln\frac{p(b_k = 1|\mathbf{Y})}{p(b_k = 0|\mathbf{Y})}. \tag{2.26}$$

Later, we define $\ln(p(b_k = 1)/p(b_k = 0))$ as *a priori* information $L_a(b_k)$. Eq. (2.26) is rewritten as [20]

$$L(b_k|\mathbf{Y}) = L_a(b_k) + \ln\frac{\sum_{\mathbf{S}\in\mathbb{S}_1^k} p(\mathbf{Y}|\mathbf{S}) \cdot \exp\left(\sum_{j\neq k} b_j L_a\left(b_j\right)\right)}{\sum_{\mathbf{S}\in\mathbb{S}_0^k} p(\mathbf{Y}|\mathbf{S}) \cdot \exp\left(\sum_{j\neq k} b_j L_a\left(b_j\right)\right)}. \tag{2.27}$$

Here, $\mathbb{S}_0^k$ denotes the subset of $\mathbb{S} = \left\{\mathbf{S}^{(1)}, \cdots, \mathbf{S}^{(2^B)}\right\}$, which is defined by $\mathbb{S}_0^k = \{\mathbf{S} \in \mathbb{S} \wedge b_k = 0\}$. Similarly, $\mathbb{S}_1^k$ is defined by $\mathbb{S}_1^k = \{\mathbf{S} \in \mathbb{S} \wedge b_k = 1\}$. For example, if we have the $B = 2$ source bits and the $2^B = 4$ number of codewords, the mapping between the input bits and the associated codeword is given by Table 2.5. Hence, all the subsets $\mathbb{S}_0^0$, $\mathbb{S}_1^0$, $\mathbb{S}_0^1$, and $\mathbb{S}_1^1$ are defined by

$$\mathbb{S}_0^0 = \left\{\mathbf{S}^{(1)}, \mathbf{S}^{(3)}\right\}, \mathbb{S}_1^0 = \left\{\mathbf{S}^{(2)}, \mathbf{S}^{(4)}\right\}, \mathbb{S}_0^1 = \left\{\mathbf{S}^{(1)}, \mathbf{S}^{(2)}\right\}, \mathbb{S}_1^1 = \left\{\mathbf{S}^{(3)}, \mathbf{S}^{(4)}\right\}. \tag{2.28}$$

Table 2.5 Bit mapping example of the GSTSK scheme having $B = 2$.

Source bits		Codeword
$k = 1$	$k = 0$	$\mathbf{S}$
0	0	$\mathbf{S}^{(1)}$
0	1	$\mathbf{S}^{(2)}$
1	0	$\mathbf{S}^{(3)}$
1	1	$\mathbf{S}^{(4)}$

Substituting $p(\mathbf{S}|\mathbf{Y})$ for Eq. (2.7) yields

$$
L(b_k|\mathbf{Y}) = L_a(b_k) + \ln \frac{\sum_{\mathbf{S} \in \mathbb{S}_1^k} \exp\left(-\left(\frac{1}{\sigma_v^2}\right) \|\mathbf{Y} - \mathbf{HS}\|_{\mathrm{F}}^2 + \sum_{j \neq k} b_j L_a\left(b_j\right)\right)}{\sum_{\mathbf{S} \in \mathbb{S}_0^k} \exp\left(-\left(\frac{1}{\sigma_v^2}\right) \|\mathbf{Y} - \mathbf{HS}\|_{\mathrm{F}}^2 + \sum_{j \neq k} b_j L_a\left(b_j\right)\right)}, \tag{2.29}
$$

which is further simplified by [20]

$$
\begin{aligned}
L(b_k|\mathbf{Y}) = \underbrace{L_a(b_k)}_{L_{M,a}} \\
+ \underbrace{\max_{\mathbf{S} \in \mathbb{S}_1^k}\left[-\frac{\|\mathbf{Y} - \mathbf{HS}\|_{\mathrm{F}}^2}{\sigma_v^2} + \sum_{j \neq k} b_j L_a\left(b_j\right)\right] - \max_{\mathbf{S} \in \mathbb{S}_0^k}\left[-\frac{\|\mathbf{Y} - \mathbf{HS}\|_{\mathrm{F}}^2}{\sigma_v^2} + \sum_{j \neq k} b_j L_a\left(b_j\right)\right]}_{L_{M,e}}.
\end{aligned}
$$

$$
\tag{2.30}
$$

The powerful channel coding scheme iteratively exchanges the *a priori* $L_{M,a}$ and *a posteriori* $L_{M,e}$ information of Eq. (2.30). Through the iterative process, the LLR value of $L(b_k|\mathbf{Y})$ converges to a certain value. If the value is positive, $\hat{b}_k$ is set to one, otherwise $\hat{b}_k$ is set to zero. Refer to [20] for further details.

2.3.5 Performance Results

We evaluated the PM schemes introduced in Section 2.3, such as the SM and the GSTSK schemes. The benchmarks were the SISO and the OSTBC schemes. In order to conduct fair comparisons, the average transmit power was constrained to the same value for all the considered schemes. The DMs of the GSTSK scheme were listed in Appendix A.1, which were designed based on the RDC of Section 2.2.2. We assumed the frequency-flat Rayleigh

Table 2.6 Simulation parameters of the coherent MIMO schemes.

Number of transmit antennas	$M = 1, 2, 4, 8, 16$
Number of receive antennas	$N = 1, 2, 4, 8, 16$
Symbol duration in a space-time codeword	$T = M$
Number of DMs	$Q = 2, 3, 4, 16$
Number of activated DMs	$P = 1, 2, 3, 4$
Modulation	BPSK, QPSK, 8–PSK, 16–PSK, 16–QAM
Channel	Frequency-flat i.i.d. Rayleigh fading
Detector	Maximum-likelihood detection

fading and employed the hard-decision MLD of Eq. (2.25) at the receiver. The simulation parameters considered in this section are given in Table 2.6.

2.3.5.1 Constrained AMI

Fig. 2.5 shows the constrained AMI of the BPSK–aided SM scheme. The number of transmit antennas was set to $M = 2, 4, 8, 16$, where the associated transmission rate was $R = 2.0, 3.0, 4.0, 5.0$ [bits/symbol]. Observe in Fig. 2.5 that the constrained AMI of the SM scheme monotonically increased upon increasing the number of transmit antennas. This implies that the SM scheme has a scalability in terms of transmit antennas, where its benefit is explicit in the large-scale MIMO system.

Fig. 2.6 shows the constrained AMI of the BPSK–aided OSTBC scheme having $M = 2$ transmit antennas. The number of receive antennas was set to $N = 1, 2, 4, 8, 16$. The transmission rate was $R = 1.0$ [bits/symbol]. Observe in Fig. 2.6 that the SNRs achieving the half rate of 0.5 [bits/symbol] monotonically improved with the 3.0 [dB] gap upon increasing the number of receive antennas. The other schemes, such as the SM and GSTSK schemes, also exhibits this trend.

Fig. 2.7 shows the constrained AMI of the BPSK–aided GSTSK$(2,1,2,4,P)$ scheme. The number of selected DMs was set to $P = 1, 2, 3, 4$, where the associated transmission rate was $R = 1.5, 2.0, 2.5, 2.0$ [bits/symbol]. It was shown in Fig. 2.7 that the constrained AMI converged into the full transmission rate R. Also, at low SNRs, the constrained AMI for the $P = 1, 2, 3, 4$ cases were almost the same.

Fig. 2.8 shows the relationship between the constrained AMI and the BER at SNR = 15 [dB], where the BPSK–aided GSTSK$(2,1,2,2,1)$ scheme was considered. In order to investigate the relationship, the 7187 number of DMs were randomly generated. Observe in Fig. 2.8 that both the constrained AMI and BER had a certain relationship. Although the constrained AMI is an effective metric for the channel-coded system, at high SNRs, it is also
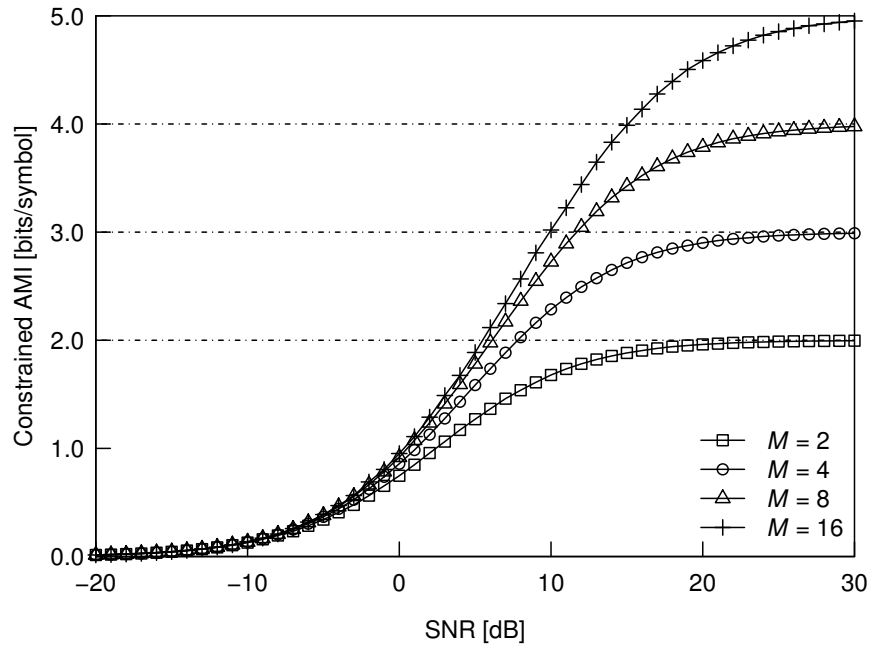
Figure 2.5 Constrained AMI comparisons of the BPSK–aided SM scheme having $M = 2$, 4, 8, 16. The number of receive antennas N was set to 1.
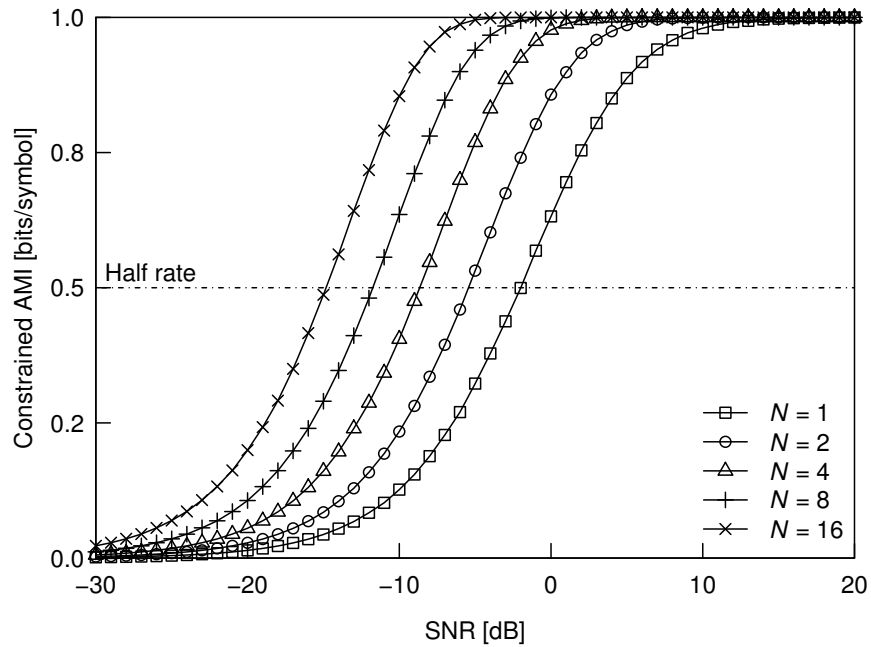
Figure 2.6 Constrained AMI comparisons of the BPSK–aided OSTBC scheme having $N = 1$, 2, 4, 8, 16. The number of transmit antennas M was set to 2.
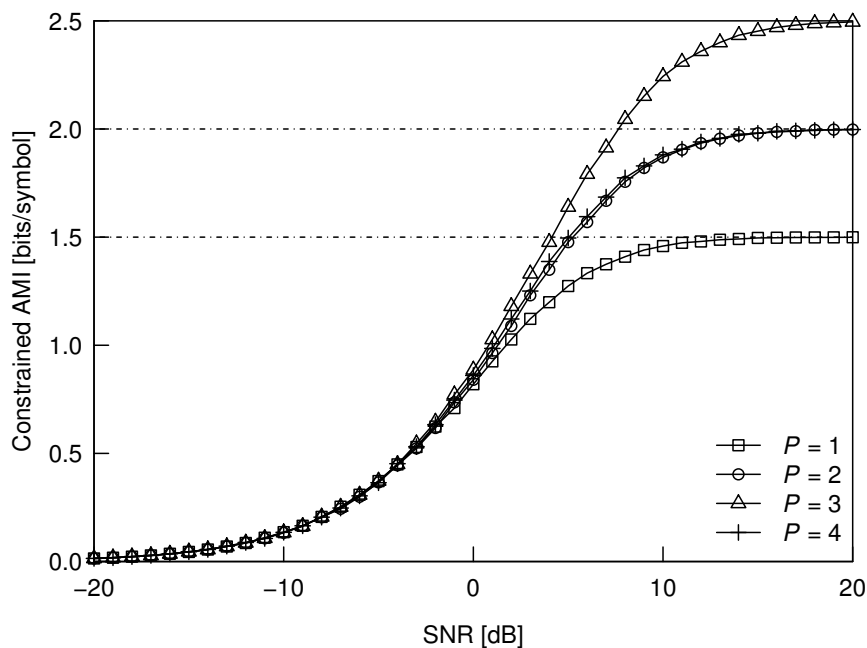
Figure 2.7 Constrained AMI comparisons of the BPSK–aided GSTSK$(2,1,2,4,P)$, where the number of selected DMs P was ranging from 1 to 4.
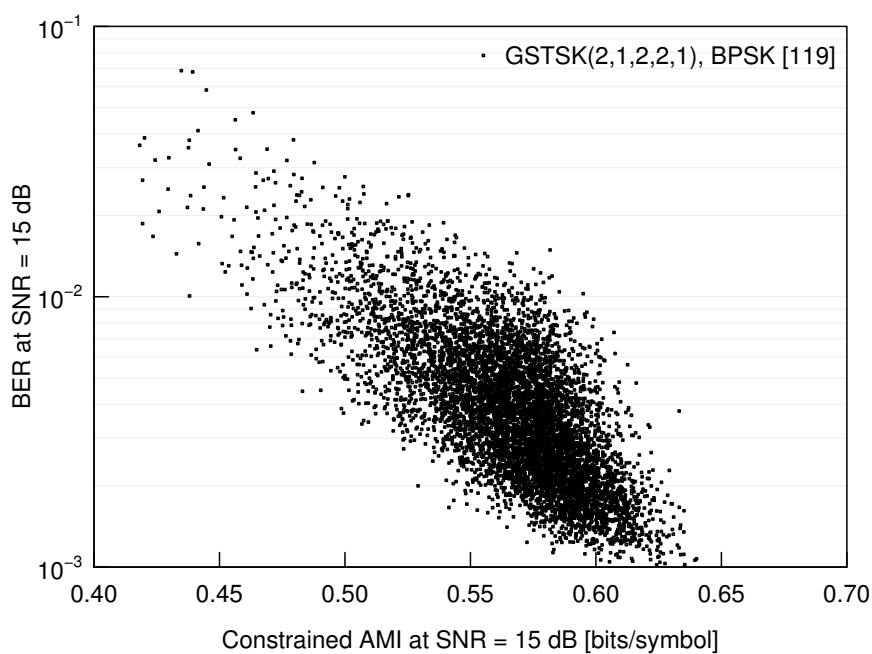
Figure 2.8 Relationship between the constrained AMI and BER, where SNR was set to 15 dB and 7187 DMs were randomly generated.
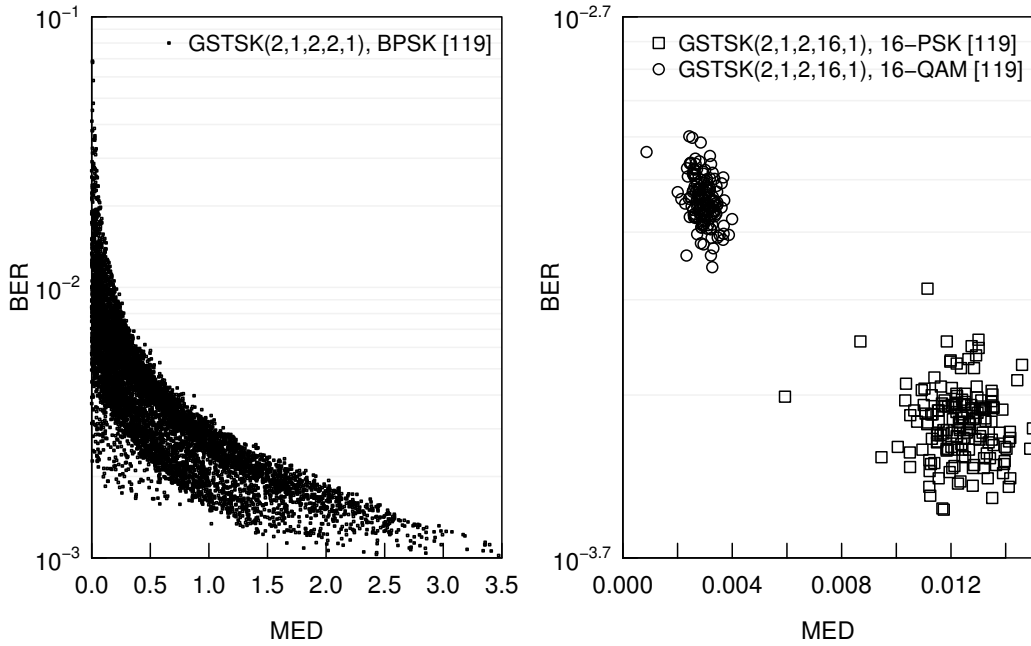
(a) $R = 2.0$ [bits/symbol] and SNR = 15 [dB]. **(b)** $R = 4.0$ [bits/symbol] and SNR = 20 [dB].

Figure 2.9 Correlation between the MED and BER.

effective for the uncoded system. More specifically, in the constrained AMI calculation of Eq. (2.9), approximating $\mathbf{V}$ to $\mathbf{0}$ yields

$$\eta[f,g] = -\frac{1}{\sigma_v^2} \left\| \mathbf{H}\left(\mathbf{S}^{(f)} - \mathbf{S}^{(g)}\right) \right\|_{\mathrm{F}}^2, \tag{2.31}$$

which contains the received MED of $\left\| \mathbf{H}\left(\mathbf{S}^{(f)} - \mathbf{S}^{(g)}\right) \right\|_{\mathrm{F}}^2$. Thus, the constrained AMI and the MED exhibit a correlation at high SNRs, which is caused by Eq. (2.31).

2.3.5.2 Reliability

Fig. 2.9 shows the relationship between the MED and the BER at high SNRs, where we considered the transmission rate of $R = 2.0$ and 4.0 [bits/symbol]. In Fig. 2.9(a), the BPSK–aided GSTSK(2,1,2,2,1) scheme was considered, while in Fig. 2.9(b), the 16-PSK– and 16-QAM–aided GSTSK(2,1,2,16,1) schemes were considered. Observe in Figs. 2.9(a) and (b) that the MED correlated with the BER at high SNRs, which were anticipated by the PEP upper-bound of Eq. (2.13). It was also shown in Fig. 2.9(b) that the 16-QAM–aided GSTSK achieved the lower BERs as compared to the 16-PSK–aided GSTSK case, where this trend was verified by the MED comparisons. Note that for the 16-PSK– and 16-QAM–aided

(a) $R = 2.0$ [bits/symbol].   **(b)** $R = 3.0$ [bits/symbol].
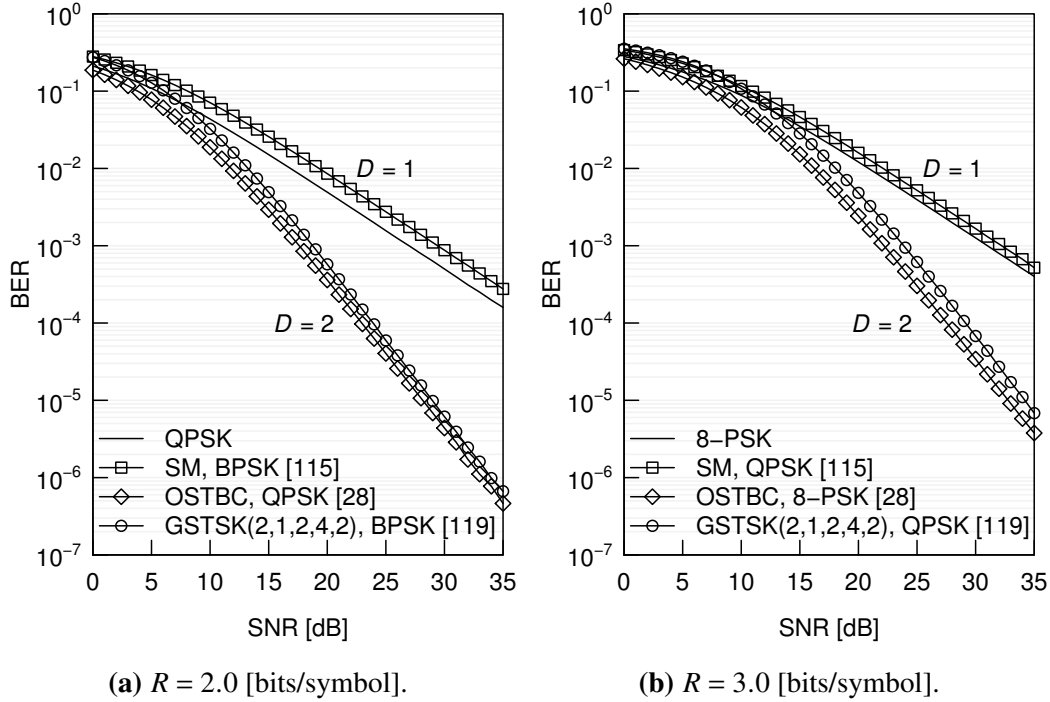
Figure 2.10 BER comparisons of the SISO, the SM, OSTBC, and GSTSK schemes, where the transmission rate was set to $R = 2.0, 3.0$ [bits/symbol]. The numbers of transmit and receive antennas were $(M, N) = (2, 1)$.

GSTSK(2,1,2,16,1) schemes, the DM optimization did not improve the BER. This was because the number of codewords was huge for the high-rate scenarios. Accordingly, the degree of freedom in terms of the DM design decreased.

Fig. 2.10 shows the BER comparisons of the GSTSK scheme and the other benchmark schemes, where we have $(M, N) = (2, 1)$. The transmission rate was set to $R = 2.0$ and 3.0 [bits/symbol]. It was shown in Figs. 2.10(a) and (b) that the GSTSK and the OSTBC achieved the full diversity of $D = MN = 2$. Note that the performance of the SM scheme was worse than that of the SISO scheme due to the low number of receive antenna $N = 1$.

Fig. 2.11 shows the BER comparisons of the SM scheme and the other benchmark schemes, where we have $(N, R) = (1, 4)$. The number of transmit antenna was changed from $M = 2$ to 8 for the SM scheme. It was shown in Fig. 2.11 that the performance of the SISO and the SM schemes were almost the same. The OSTBC scheme achieved the full diversity of $D = MN = 2$, similar to the results shown in Figs. 2.10(a) and (b). Note that for the $M > 2$ scenarios the transmission rate of the OSTBC scheme losses.

Fig. 2.12 shows the BER comparisons between the GSTSK and the benchmark SISO schemes, where we have $(N, R) = (1, 2)$. Observe in Figs. 2.12(a) and (b) that the achievable
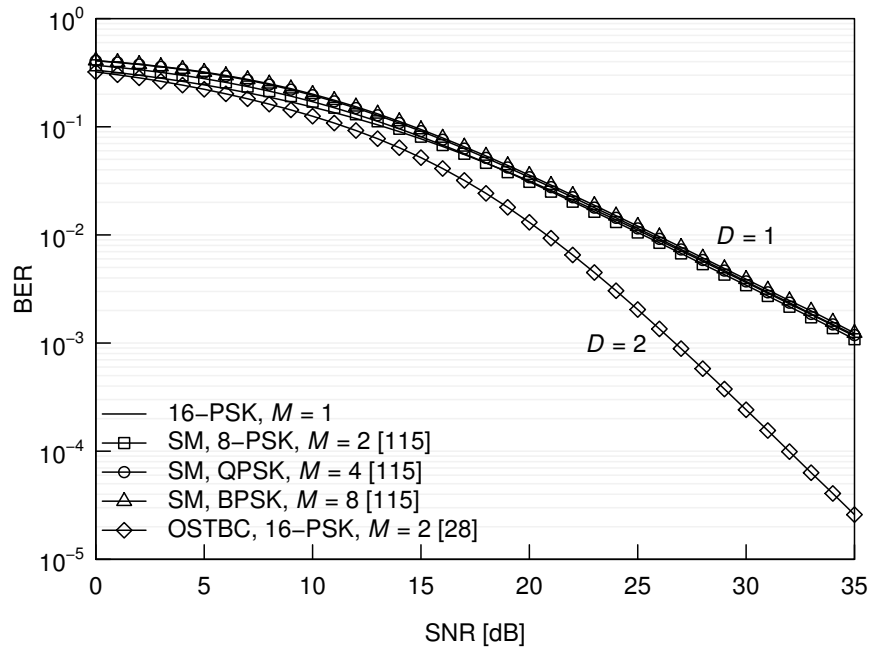
Figure 2.11 BER comparisons of the 16-PSK–aided SISO, the SM, and the 16-PSK–aided OSTBC schemes where the number of transmit antenna was set to $M = 1, 2, 4, 8$. The transmission rate was $R = 4.0$ [bits/symbol] and the number of receive antenna was $N = 1$.

(a) $M = 3$.   **(b)** $M = 4$.
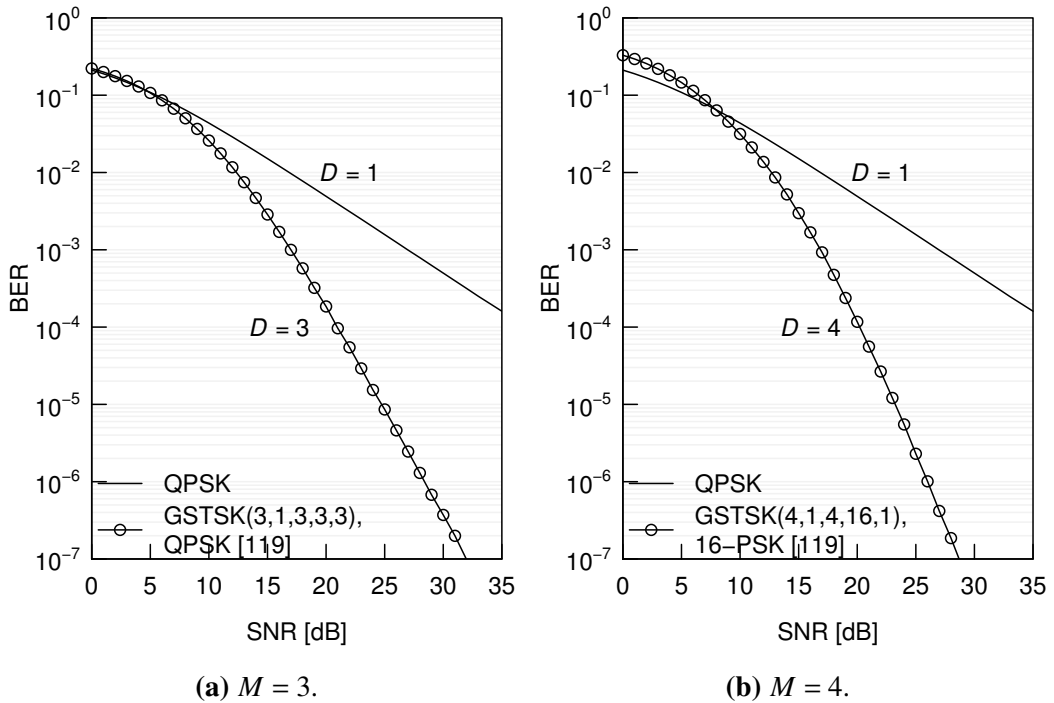
Figure 2.12 BER comparisons of the SISO and GSTSK schemes, where the number of transmit antenna was set to $M = 3, 4$. The number of receive antennas was $N = 1$ and the transmission rate was $R = 2.0$ [bits/symbol].
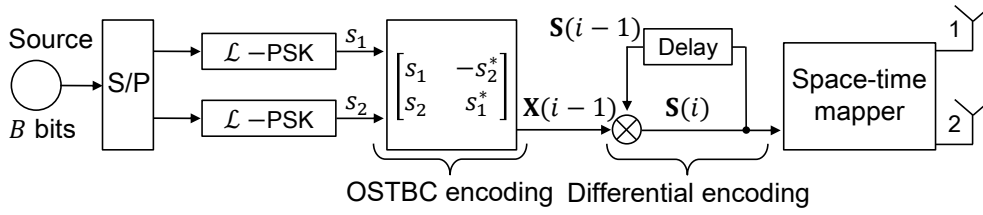
Figure 2.13 The schematic of the DOSTBC transmitter having $M = 2$.

diversity order of the GSTSK scheme was the optimum value of $D = MN$ upon increasing the number of transmit antennas M.

2.4 Permutation Modulation Based Differential MIMO Communications

In this section, we review the PM schemes having been proposed for the differential MIMO systems. In Section 2.3, we reviewed the PM schemes designed for the coherent MIMO systems, which need the precise estimates of the channel matrix $\mathbf{H}$ at the receiver. The channel estimation overhead reduces the effective transmission rate due to the insertion of the pilot symbols. In addition, the receiver has to estimate the channel matrix based on the received pilot symbols. Hence, in rapidly fading channels, it is a challenging task to obtain the perfect estimate of the channel matrix. Against this limitation, the DSTBC has been proposed for avoiding the channel estimation process. The DSTBC schemes rely on the differential encoding and decoding, where both the transmitter and the receiver exploit the unitary characteristic of the space-time codeword. The contributions to the PM-based differential MIMO schemes are summarized in Table 2.7.

Let us check the basic example of the DSTBC encoding. Here, we consider the differential orthogonal space-time block code (DOSTBC) scheme [41]. Fig. 2.13 shows the schematic of the DSTBC transmitter, where the number of transmit antennas is $M = 2$. Based on the input bits, the two number of $\mathcal{L}$–PSK symbols s_1 and s_2 are modulated. Then, a data matrix $\mathbf{X}(i)$ is given by

$$\mathbf{X}(i) = \frac{1}{\sqrt{2}} \begin{bmatrix} s_1 & -s_2^* \\ s_2 & s_1^* \end{bmatrix}, \tag{2.32}$$

Table 2.7 Contributions to the PM based differential MIMO schemes.

Year	Authors	Contribution
2000	Hughes [42]	Proposed the diagonal and anti-diagonal matrices based differential MIMO scheme relying on the group codes, which supports an arbitrary number of transmit antennas. If we limit the matrix "D" in [42] to the identity matrix, the space-time codewords result in sparse, which was not clearly mentioned.
	Hochwald and Sweldens [44]	Proposed the diagonal-matrix based differential MIMO scheme, which supports an arbitrary number of transmit antennas, achieves full diversity, and enables the single-RF transmission.
2007	Oggier [123]	Proposed the permutation-matrix based differential MIMO scheme relying on the cyclic division algebra, which has the similar advantages of [44].
2010	Sugiura *et al.* [39]	Proposed the differential counterpart of the coherent STSK scheme, which modulates the information bits by selecting a single out of the multiple DMs. The encoding principle is based on the differential LDC scheme of [45].
2011	Sugiura *et al.* [124]	Proposed the QAM-aided counterpart of [39]. In addition, its low-complexity detector was conceived.
2013	Bian *et al.* [74]	Proposed the differential counterpart of the SM scheme having $M = 2$ transmit antennas, which was termed as DSM. The space-time codewords of the DSM scheme are generated from the diagonal and anti-diagonal matrices. Note that the proposed DSM scheme of [74] is different from the scheme of [123] in terms of the spatial multiplexing gain.
2014	Wen *et al.* [125]	Derived the tight BER bound for the DSM scheme having $M = 2$.
	Ishikawa and Sugiura [6]	Generalized the encoding principle of [39], where an arbitrary number of DMs are activated.
2015	Bian *et al.* [126]	Proposed the generalized DSM scheme based on [74], which supports an arbitrary number of transmit antennas. The space-time codewords are generated from the permutation matrices. The DSM scheme of [126] maximizes the spatial multiplexing gain.

which is a unitary matrix when satisfying $|s_1|^2 = |s_2|^2 = 1$. More specifically, the unitary matrix $\mathbf{X}(i)$ satisfies the following relationship.

$$
\begin{aligned}
\mathbf{X}(i)\mathbf{X}(i)^{\mathrm{H}} &= \frac{1}{\sqrt{2}} \begin{bmatrix} s_1 & -s_2^* \\ s_2 & s_1^* \end{bmatrix} \frac{1}{\sqrt{2}} \begin{bmatrix} s_1^* & s_2^* \\ -s_2 & s_1 \end{bmatrix} \\
&= \frac{1}{2} \begin{bmatrix} |s_1|^2 + |s_2|^2 & 0 \\ 0 & |s_1|^2 + |s_2|^2 \end{bmatrix} = \mathbf{I}_2.
\end{aligned}
$$

The differential encoding process generates a space-time matrix $\mathbf{S}(i)$ based on the previous space-time matrix $\mathbf{S}(i-1)$ and the data matrix $\mathbf{X}(i)$ as follows:

$$
\mathbf{S}(i) = \mathbf{S}(i-1)\mathbf{X}(i). \tag{2.33}
$$

Here, the initial matrix is set to $\mathbf{S}(0) = \mathbf{I}_M$. Since the initial matrix $\mathbf{S}(0)$ and the data matrix $\mathbf{X}(i)$ are unitary, the norm of $\mathbf{S}(i)$ is kept to the constant value of $\|\mathbf{X}(i)\|_{\mathrm{F}}^2 = \|\mathbf{S}(i)\|_{\mathrm{F}}^2 = M$. The major drawback of the DSTBC scheme is the constraint of $M = T$, which makes it difficult to effectively increase the transmission rate owing to its high complexity both at the transmitter and the receiver. Later, in Section 2.4.1, we review the PM schemes designed for the differential MIMO systems with introducing the construction of the data matrix $\mathbf{X}(i)$. This section introduces two types of the unitary matrix constructions: the sparse-matrix-based method in Section 2.4.1 and the Cayley transform-based method in Section 2.4.2.

2.4.1 Differential Spatial Modulation

Motivated by the SM concept [77, 115], the differential counterpart of the SM scheme was proposed [74, 126], which was referred to as differential spatial modulation (DSM). The space-time codeword of the DSM scheme has a single non-zero element in its column and row. Hence, the DSM scheme is capable of enabling the single-RF operation, as well as dispensing with the channel estimation overhead. Note that the sparse space-time codewords were proposed in [123, 27] before the invention of the DSM concept.

Let us review the DSM encoding principle. Similar to the SM encoding, the DSM transmitter divides the input B bits into the two parts: $B_1 = \lfloor \log_2(M!) \rfloor$ bits and $B_2 = M \log_2(\mathcal{L})$ bits. Based on the first B_1 bits, the antenna-activation matrix $\mathbf{A}_q \in \mathbb{Z}^{M \times M}$ is selected out of the $Q = 2^{B_1}$ number of candidates. Based on the second B_2 bits, the M number of the $\mathcal{L}$–PSK symbols $s_1, \cdots, s_M$ are modulated. Finally, the corresponding data matrix is

given by

$$\mathbf{X}(i) = \text{diag}(s_1, \cdots, s_M) \cdot \mathbf{A}_q. \tag{2.34}$$

For example, if we consider the $M = 2$ case, the data matrix is given by

$$\mathbf{X}(i) = \left\{ \begin{bmatrix} s_1 & 0 \\ 0 & s_2 \end{bmatrix}, \begin{bmatrix} 0 & s_1 \\ s_2 & 0 \end{bmatrix} \right\}. \tag{2.35}$$

In addition, for the $M = 3$ case, the data matrix is given by

$$\mathbf{X}(i) = \left\{ \begin{bmatrix} s_1 & 0 & 0 \\ 0 & s_2 & 0 \\ 0 & 0 & s_3 \end{bmatrix}, \begin{bmatrix} s_1 & 0 & 0 \\ 0 & 0 & s_2 \\ 0 & s_3 & 0 \end{bmatrix}, \begin{bmatrix} 0 & s_1 & 0 \\ s_2 & 0 & 0 \\ 0 & 0 & s_3 \end{bmatrix}, \begin{bmatrix} 0 & 0 & s_1 \\ s_2 & 0 & 0 \\ 0 & s_3 & 0 \end{bmatrix} \right\}. \tag{2.36}$$

The transmission rate of the DSM scheme is defined by

$$R = \frac{B}{T} = \frac{B_1 + B_2}{M} = \frac{\lfloor \log_2(Q) \rfloor + M \log_2(\mathcal{L})}{M} \text{ [bits/symbol]} \tag{2.37}$$

The antenna-activation matrix $\mathbf{A}_q$ for $1 \le q \le Q$ is constructed based on the index-table $\mathbf{T}_a \in \mathbb{Z}^{M! \times M}$ which represents the non-zero positions in a sparse space-time codewords. More specifically, the index-table of $\mathbf{T}_a \in \mathbb{Z}^{M! \times M}$ is constructed by Algorithm 1, which is an alternative representation of the "permutation method" originally proposed in [126]. In Algorithm 1, $\mathbf{T}_b[m,x]$ and $\mathbf{T}_a[m,x]$ denote the mth row and xth column of the tables $\mathbf{T}_b$ and $\mathbf{T}_a$. Algorithm 1 is composed of two processes: the constructions of $\mathbf{T}_b$ and $\mathbf{T}_a$. For the integer $1 \le i \le M!$, the ith row of $\mathbf{T}_b$ contains i's factorial representation. For example, if we consider the $i = 4 < M! = 3!$ case, the $i = 4$th row of $\mathbf{T}_b$ is calculated by [1 1 0] because 4 is represented by $4 = 1 \cdot 2! + 1 \cdot 1! + 0 \cdot 0! = 2 + 1 + 1$. Based on $\mathbf{T}_b$, the index-table of $\mathbf{T}_a$ is constructed, which indicates the positions of non-zero elements in the DSM space-time codeword. For example, if we consider the $M = 2$ case, the index-tables $\mathbf{T}_b$ and $\mathbf{T}_a$ are given by

$$\mathbf{T}_b = \begin{bmatrix} 0 & 0 \\ 1 & 0 \end{bmatrix}, \mathbf{T}_a = \begin{bmatrix} 1 & 2 \\ 2 & 1 \end{bmatrix} \in \mathbb{Z}^{2! \times 2}. \tag{2.38}$$

Algorithm 1 Algorithm for constructing the index-table of the non-zero positions.

Input: The number of transmit antennas M
Output: The indices of the non-zero elements $\mathbf{T}_a$
    Initialization :
 1: Initialize the tables of $\mathbf{T}_a, \mathbf{T}_b \in \mathbb{Z}^{M! \times M}$
    Construction of the table $\mathbf{T}_b$:
 2: **for** $i = 1$ to $M!$ **do**
 3:    $\mathbf{T}_b[i,1] \leftarrow \lfloor (i-1)/(M-1)! \rfloor$
 4:    $i_a \leftarrow i - 1$
 5:    **for** $x = 1$ to $M - 1$ **do**
 6:       $i_a \leftarrow i_a - \mathbf{T}_b[i,x] \cdot (M-x)!$
 7:       $\mathbf{T}_b[i,x+1] \leftarrow \lfloor i_a/(M-x-1)! \rfloor$
 8:    **end for**
 9: **end for**
    Construction of the table $\mathbf{T}_a$:
10: **for** $i = 1$ to $M!$ **do**
11:    $\boldsymbol{\theta} \leftarrow [1, 2, \cdots, M] \in \mathbb{Z}^M$
12:    **for** $x = 1$ to M **do**
13:       $\mathbf{T}_a[i,x] \leftarrow \boldsymbol{\theta}[\mathbf{T}_b[i,x]]$
14:       Delete the $\mathbf{T}_b[i,x]$th element of $\boldsymbol{\theta}$
15:    **end for**
16: **end for**
17: **return** $\mathbf{T}_a$

Based on the $\mathbf{T}_a$ of Eq. (2.38), the following antenna-activation matrices are constructed.

$$\mathbf{A}_1 = \begin{bmatrix} 1 & 0 \\ 0 & 1 \end{bmatrix}, \mathbf{A}_2 = \begin{bmatrix} 0 & 1 \\ 1 & 0 \end{bmatrix}. \tag{2.39}$$

In addition, if we consider the $M = 3$ case, the index-tables $\mathbf{T}_b$ and $\mathbf{T}_a$ are given by

$$\mathbf{T}_b = \begin{bmatrix} 0 & 0 & 1 & 1 & 2 & 2 \\ 0 & 1 & 0 & 1 & 0 & 1 \\ 0 & 0 & 0 & 0 & 0 & 0 \end{bmatrix}^{\mathrm{T}}, \mathbf{T}_a = \begin{bmatrix} 1 & 1 & 2 & 2 & 3 & 3 \\ 2 & 3 & 1 & 3 & 1 & 2 \\ 3 & 2 & 3 & 1 & 2 & 1 \end{bmatrix}^{\mathrm{T}} \in \mathbb{Z}^{3! \times 3}. \tag{2.40}$$
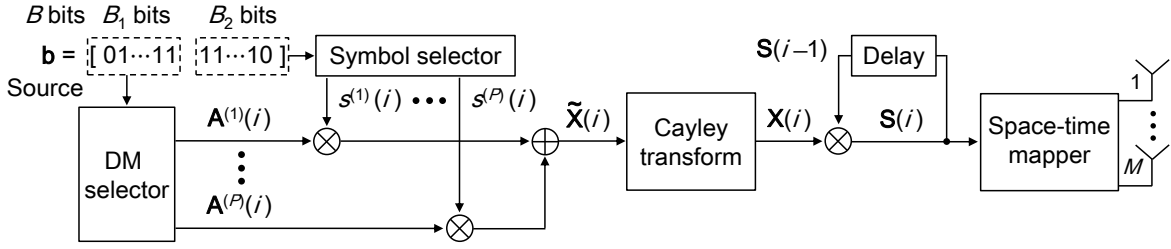
Figure 2.14 The transmitter schematic of the NCGSM.

Based on the $\mathbf{T}_a$ of Eq. (2.40), the following antenna-activation matrices are constructed:

$$\mathbf{A}_1 = \begin{bmatrix} 1 & 0 & 0 \\ 0 & 1 & 0 \\ 0 & 0 & 1 \end{bmatrix}, \mathbf{A}_2 = \begin{bmatrix} 1 & 0 & 0 \\ 0 & 0 & 1 \\ 0 & 1 & 0 \end{bmatrix}, \mathbf{A}_3 = \begin{bmatrix} 0 & 1 & 0 \\ 1 & 0 & 0 \\ 0 & 0 & 1 \end{bmatrix}, \mathbf{A}_4 = \begin{bmatrix} 0 & 0 & 1 \\ 1 & 0 & 0 \\ 0 & 1 & 0 \end{bmatrix}, \quad (2.41)$$

where the $Q = 2^{\lfloor \log_2(3!) \rfloor} = 4$ number of rows are selected from the table $\mathbf{T}_a$.

2.4.2   Non-Coherent Generalized Spatial Modulation

The non-coherent generalized spatial modulation (NCGSM) [6] is the differential counterpart of the GSTSK scheme, which is described in Section 2.3.3. Let us review the encoding principle of the NCGSM scheme. Fig. 2.14 shows the schematic of the NCGSM transmitter. Similar to the encoding principle of the GSTSK scheme, we use the notations of $N_a = 2^{\lfloor \log_2(\binom{Q}{P}) \rfloor}$ and the DM-activation vectors of $\mathbf{a}_i \in \mathbb{Z}^P$ ($1 \leq i \leq N_a$), since the P number of DMs are selected out of the Q number of DMs. The DMs are designed based on the RDC, which is also the same with the GSTSK scheme. Note that the constraint for the DMs is different from the GSTSK scheme. The DMs of the NCGSM scheme, which are denoted by $\mathbf{A}_1, \cdots, \mathbf{A}_Q \in \mathbb{C}^{M \times M}$, are the Hermitian matrix. Thus, each DM satisfies $\mathbf{A}_q = \mathbf{A}_q^H$.

The input B bits are divided into the two parts: $B_1 = \log_2(N_a)$ bits and $B_2 = P \log_2(\mathcal{L})$ bits. Based on the first B_1 bits, the single DM-activation vector $\mathbf{a}_q$ is selected out of the N_a number of combinations. Based on the second B_2 bits, the P number of the $\mathcal{L}$–PAM symbols $s_1, \cdots, s_P$ are modulated. Then, a Hermitian matrix $\tilde{\mathbf{X}}(i) \in \mathbb{C}^{M \times M}$ is generated as follows:

$$\tilde{\mathbf{X}}(i) = \sum_{p=1}^{P} s_p \mathbf{A}_{\mathbf{a}_q(p)}. \quad (2.42)$$

Since the DMs $\mathbf{A}_{\mathbf{a}_q(p)}$ are Hermitian as well as the PAM symbols s_p are real-valued, the summation of $\sum_{p=1}^{P} s_p \mathbf{A}_{\mathbf{a}_q(p)}$ is also a Hermitian matrix. Finally, a unitary matrix $\mathbf{X}(i) \in \mathbb{C}^{M \times M}$ is given by

$$\mathbf{X}(i) = \left(\mathbf{I}_M - j\tilde{\mathbf{X}}(i)\right)\left(\mathbf{I}_M + j\tilde{\mathbf{X}}(i)\right)^{-1} \equiv \zeta\left(\tilde{\mathbf{X}}(i)\right), \qquad (2.43)$$

which is referred to as the Cayley transform [45]. The Cayley transform is a mapping between a skew-Hermitian matrix and a unitary matrix. In Eq. (2.43), the skewed counterpart of $\tilde{\mathbf{X}}(i)$, which is calculated by $j\tilde{\mathbf{X}}(i)$, is mapped to the unitary matrix $\mathbf{X}(i)$. Later, the Cayley transform of Eq. (2.43) is denoted by $\zeta(\cdot)$. The matrix $\mathbf{X}(i)$ is unitary because we have the relationship of

$$\begin{aligned}
\mathbf{X}(i)\mathbf{X}(i)^{\mathrm{H}} &= \left(\mathbf{I}_M - j\tilde{\mathbf{X}}(i)\right)\left(\mathbf{I}_M + j\tilde{\mathbf{X}}(i)\right)^{-1}\left\{\left(\mathbf{I}_M - j\tilde{\mathbf{X}}(i)\right)\left(\mathbf{I}_M + j\tilde{\mathbf{X}}(i)\right)^{-1}\right\}^{\mathrm{H}} \\
&= \left(\mathbf{I}_M - j\tilde{\mathbf{X}}(i)\right)\left(\mathbf{I}_M + j\tilde{\mathbf{X}}(i)\right)^{-1}\left(\left(\mathbf{I}_M + j\tilde{\mathbf{X}}(i)\right)^{\mathrm{H}}\right)^{-1}\left(\mathbf{I}_M - j\tilde{\mathbf{X}}(i)\right)^{\mathrm{H}} \\
&= \left(\mathbf{I}_M - j\tilde{\mathbf{X}}(i)\right)\left(\mathbf{I}_M + j\tilde{\mathbf{X}}(i)\right)^{-1}\left(\mathbf{I}_M - j\tilde{\mathbf{X}}(i)\right)^{-1}\left(\mathbf{I}_M + j\tilde{\mathbf{X}}(i)\right) \\
&= \left(\mathbf{I}_M - j\tilde{\mathbf{X}}(i)\right)\left(\mathbf{I}_M + j\tilde{\mathbf{X}}(i)\right)^{-1}\left(\mathbf{I}_M + j\tilde{\mathbf{X}}(i)\right)\left(\mathbf{I}_M - j\tilde{\mathbf{X}}(i)\right)^{-1} \\
&= \left(\mathbf{I}_M - j\tilde{\mathbf{X}}(i)\right)\mathbf{I}_M\left(\mathbf{I}_M - j\tilde{\mathbf{X}}(i)\right)^{-1} \\
&= \mathbf{I}_M,
\end{aligned}$$

where the transition of $\left(\mathbf{I}_M - j\tilde{\mathbf{X}}(i)\right)^{-1}\left(\mathbf{I}_M + j\tilde{\mathbf{X}}(i)\right) = \left(\mathbf{I}_M + j\tilde{\mathbf{X}}(i)\right)\left(\mathbf{I}_M - j\tilde{\mathbf{X}}(i)\right)^{-1}$ is valid since we have $\left(\mathbf{I}_M + j\tilde{\mathbf{X}}(i)\right)\left(\mathbf{I}_M - j\tilde{\mathbf{X}}(i)\right) = \left(\mathbf{I}_M - j\tilde{\mathbf{X}}(i)\right)\left(\mathbf{I}_M + j\tilde{\mathbf{X}}(i)\right) = \mathbf{I}_M + \tilde{\mathbf{X}}^2(i)$. The transmission rate of the NCGSM scheme is given by

$$R = \frac{B}{M} = \frac{B_1 + B_2}{M} = \frac{\left\lfloor \log_2\binom{Q}{P} \right\rfloor + P\log_2(\mathcal{L})}{M} \quad \text{[bits/symbol]}. \qquad (2.44)$$

Table 2.8 shows the bit mapping example of the 2–PAM aided NCGSM($M,N,T,3,2$). The input $B = 3$ bits are divided into the $B_1 = 1$ bit and the $B_2 = 2$ bits. Based on the first B_1 bit, the DM-activation vector $\mathbf{a}_q$ is selected out of the $N_{\mathrm{a}} = 2$ combinations, which are given by $\mathbf{a}_1 = [1,2]$ and $\mathbf{a}_2 = [1,3]$. Then, based on the second B_2 bits, the $P = 2$ number of the 2–PAM symbols $s_1(i)$ and $s_2(i)$ are modulated. The Hermitian matrix is calculated by $\tilde{\mathbf{X}}(i) = s_1(i) \cdot \mathbf{A}_{\mathbf{a}_q(1)} + s_2(i) \cdot \mathbf{A}_{\mathbf{a}_q(2)}$. Finally, the unitary matrix $\mathbf{X}(i)$ is generated by the Cayley transform of the skew-Hermitian matrix $j\tilde{\mathbf{X}}(i)$.

Table 2.8 Bit mapping example of the 2–PAM aided NCGSM($M,N,T,3,2$), having the $B = B_1 + B_2 = 1 + 2 = 3$ bits. There are the $N_a = 2$ activation patterns of $\mathbf{a}_1 = [1,2]$ and $\mathbf{a}_2 = [1,3]$, which are the same with those shown in Table 2.4.

Source (3 bits)	Activated DMs $\mathbf{a}_q$	2–PAM symbols $s_1(i), s_2(i)$	Hermitian matrix $\tilde{\mathbf{X}}(i)$	Unitary matrix $\mathbf{X}(i)$
0 $\vert$ 0 0	$\mathbf{A}_1, \mathbf{A}_2$	$+1, +1$	$\mathbf{A}_1 + \mathbf{A}_2$	$\zeta(\mathbf{A}_1 + \mathbf{A}_2)$
0 $\vert$ 0 1	$\mathbf{A}_1, \mathbf{A}_2$	$+1, -1$	$\mathbf{A}_1 - \mathbf{A}_2$	$\zeta(\mathbf{A}_1 - \mathbf{A}_2)$
0 $\vert$ 1 0	$\mathbf{A}_1, \mathbf{A}_2$	$-1, +1$	$-\mathbf{A}_1 + \mathbf{A}_2$	$\zeta(-\mathbf{A}_1 + \mathbf{A}_2)$
0 $\vert$ 1 1	$\mathbf{A}_1, \mathbf{A}_2$	$-1, -1$	$-\mathbf{A}_1 - \mathbf{A}_2$	$\zeta(-\mathbf{A}_1 - \mathbf{A}_2)$
1 $\vert$ 0 0	$\mathbf{A}_1, \mathbf{A}_3$	$+1, +1$	$\mathbf{A}_1 + \mathbf{A}_3$	$\zeta(\mathbf{A}_1 + \mathbf{A}_3)$
1 $\vert$ 0 1	$\mathbf{A}_1, \mathbf{A}_3$	$+1, -1$	$\mathbf{A}_1 - \mathbf{A}_3$	$\zeta(\mathbf{A}_1 - \mathbf{A}_3)$
1 $\vert$ 1 0	$\mathbf{A}_1, \mathbf{A}_3$	$-1, +1$	$-\mathbf{A}_1 + \mathbf{A}_3$	$\zeta(-\mathbf{A}_1 + \mathbf{A}_3)$
1 $\vert$ 1 1	$\mathbf{A}_1, \mathbf{A}_3$	$-1, -1$	$-\mathbf{A}_1 - \mathbf{A}_3$	$\zeta(-\mathbf{A}_1 - \mathbf{A}_3)$

As we reviewed in Section 2.3.3, the GSTSK scheme subsumes the conventional STSK and LDC schemes. Similar to the GSTSK scheme, the NCGSM architecture subsumes the conventional DSTBC schemes which are relying on the Cayley transform. More specifically, the NCGSM scheme having $P = Q$ is equivalent to the differential linear dispersion code (DLDC) [45], which achieves a high transmission rate with the aid of the multiplexed PAM symbols. Also, the NCGSM scheme having $P = 1$ is equivalent to the differential space-time shift keying (DSTSK) [39], which is the differential counterpart of the STSK scheme introduced in Section 2.3.3.

Later, we use the notation of NCGSM(M,N,T,Q,P) for simplicity, similar to the GSTSK(M,N,T,Q,P) notation. Also, for the STSK, the DSTSK, the LDC, the DLDC schemes, the parameters are represented by the (M,N,T,Q,P) notation.

2.4.2.1 Single-RF Operation

The NCGSM scheme is capable of supporting the single-RF operation, with introducing the diagonal Hermitian DMs. Since the single-RF NCGSM codewords are diagonal, there is only a single non-zero element in each column and row. Hence, at any transmission index, a single transmit antenna is activated, which is similar to the SM and DSM schemes. More specifically, the DM $\mathbf{A}_q$ ($1 \leq q \leq Q$) designed for the single-RF NCGSM scheme is given by

$$\mathbf{A}_q = \text{diag}\left(a_{q,1}, \cdots, a_{q,M}\right) \in \mathbb{R}^{M \times M} \ (1 \leq q \leq Q), \quad (2.45)$$

where $a_{q,m}$ $(1 \leq m \leq M)$ represents a real-valued dispersion coefficient. Note that each DM $\mathbf{A}_q$ is Hermitian because it satisfies the relationship of $\mathbf{A}_q = \mathbf{A}_q^{\mathrm{H}}$. The Cayley transform $\zeta(\cdot)$ maps the real-valued diagonal matrix to the diagonal unitary matrix. For example, if we consider the 2–PAM aided Single-RF NCGSM$(2,N,2,2,1)$ scheme, the associated DMs $\mathbf{A}_1$ and $\mathbf{A}_2$ are given by

$$\mathbf{A}_1 = \begin{bmatrix} 0.41 & 0.00 \\ 0.00 & 2.41 \end{bmatrix}, \mathbf{A}_2 = \begin{bmatrix} 2.41 & 0.00 \\ 0.00 & 0.41 \end{bmatrix}. \tag{2.46}$$

Based on Eq. (2.46), the single-RF NCGSM codewords are generated as follows:

$$\{\mathbf{X}_1, \mathbf{X}_2, \mathbf{X}_3, \mathbf{X}_4\}$$
$$= \left\{ \begin{bmatrix} e^{0.25\pi j} & 0.00 \\ 0.00 & e^{0.75\pi j} \end{bmatrix}, \begin{bmatrix} e^{0.75\pi j} & 0.00 \\ 0.00 & e^{0.25\pi j} \end{bmatrix}, \begin{bmatrix} e^{-0.25\pi j} & 0.00 \\ 0.00 & e^{-0.75\pi j} \end{bmatrix}, \begin{bmatrix} e^{-0.75\pi j} & 0.00 \\ 0.00 & e^{-0.25\pi j} \end{bmatrix} \right\}.$$

2.4.3   Optimum Hard Detector

We introduce the general MLD designed for the DSTBC schemes. The following detector works for the DSM and the NCGSM schemes if and only if the data matrix $\mathbf{X}(i)$ is unitary. Here, we assume that the successive channel matrices $\mathbf{H}(i)$ and $\mathbf{H}(i-1)$ are the same, namely, $\mathbf{H}(i) = \mathbf{H}(i-1)$. We define this assumption as the quasi-static frequency-flat Rayleigh fading. Since we have the relationships of $\mathbf{S}(i) = \mathbf{S}(i-1)\mathbf{X}(i)$ and $\mathbf{Y}(i-1) = \mathbf{H}(i-1)\mathbf{S}(i-1) + \mathbf{V}(i-1)$, the received symbol $\mathbf{Y}(i)$ in the basic system model of Eq. (1.2) is rewritten as

$$\begin{aligned} \mathbf{Y}(i) &= \mathbf{H}(i)\mathbf{S}(i) + \mathbf{V}(i) \\ &= \mathbf{H}(i-1)\mathbf{S}(i-1)\mathbf{X}(i) + \mathbf{V}(i) \\ &= (\mathbf{Y}(i-1) - \mathbf{V}(i-1))\mathbf{X}(i) + \mathbf{V}(i) \\ &= \mathbf{Y}(i-1)\mathbf{X}(i) + \underbrace{\mathbf{V}(i) - \mathbf{V}(i-1)\mathbf{X}(i)}_{\equiv \mathbf{V}'(i)}. \end{aligned} \tag{2.47}$$

In Eq. (2.47), we represent the noise component of $\mathbf{V}(i) - \mathbf{V}(i-1)\mathbf{X}(i)$ as $\mathbf{V}'(i)$, which follows the complex-valued Gaussian distribution of $\mathcal{CN}(0, 2\sigma_v^2)$. Based on Eq. (2.47), the

MLD for the general DSTBC schemes is given by

$$\hat{\mathbf{X}}(i) = \arg\min_{\mathbf{X}} \|\mathbf{Y}(i) - \mathbf{Y}(i-1)\mathbf{X}\|_{\mathrm{F}}^2. \tag{2.48}$$

Observe in Eq. (2.48) that it does not contain the channel matrix $\mathbf{H}(i)$, which implies that the receiver is free from the complex channel estimation process. However, the noise variance of $\mathbf{V}'(i)$ is doubled as compared to that of the coherent case given in Eq. (2.25). This limitation imposes the well known 3 [dB] loss[3] on the differential scheme, where the BER curve of the differential scheme is shifted by 3 [dB] as compared to that of the coherent scheme having the perfect estimates of the channel matrix.

The computational complexity of the general DSTBC scheme is given by $2^{RM}(4NM^2 + 2NM)$. More specifically, in Eq. (2.48), $\hat{\mathbf{X}}(i)$ is determined through 2^{RM} number of trials. In each trial, $\mathbf{Y}(i-1)\mathbf{X}(i)$ includes the $N \cdot M^2$ number of complex-valued multiplications, which is equivalent to the $4N \cdot M^2$ number of real-valued multiplications. In addition, the Frobenius norm calculation of $\mathbf{Y}(i) - \mathbf{Y}(i-1)\mathbf{X}(i)$ includes the $2NM$ number of real-valued multiplications. Hence, the computational complexity of the DSTBC scheme is calculated by $2^{RM}(4NM^2 + 2NM) \approx O(2^{RM}NM^2)$.

2.4.4 Performance Results

We evaluated the PM-based DSTBC schemes introduced in Sections 2.4.1 and 2.4.2, such as the DSM and the NCGSM schemes, in terms of the reliability in uncoded scenarios. The benchmarks were the differential PSK, the DOSTBC, the DSTSK, the DLDC schemes. In order to conduct fair comparisons, the average transmit power was constrained to the same value for all the considered schemes. The DMs of the NCGSM scheme were listed in Appendix A.2, which were designed based of the RDC of Section 2.2.2. We assumed the frequency-flat Rayleigh fading and employed the hard-decision MLD at the receiver of Eq. (2.48). The simulation parameters considered in this section are given in Table 2.9.

2.4.4.1 Effects of the DM Design

Fig. 2.15 shows the relationship between the MED and BER, where the received SNR was 10 [dB]. The 3000 number of DM sets were randomly generated and each DM set is evaluated in terms of MED and BER. Observe in Figs. 2.15(a) and (b) that the MED correlated with the

---

[3]$10\log_{10} 2 = 3.01029\cdots \approx 3.0$ [dB]

Table 2.9 Simulation parameters of the differential MIMO schemes.

Number of transmit antennas	$M = 1, 2, 4, 8, 16$
Number of receive antennas	$N = 1, 2, 4, 8, 16$
Symbol duration in a space-time codeword	$T = M$
Number of DMs	$Q = 2, 3, 4, 16$
Number of activated DMs	$P = 1, 2, 3, 4$
Modulation	BPSK, QPSK, 8–PSK, 16–PSK, 16–QAM
Channel	Frequency-flat i.i.d. Rayleigh fading
Detector	Maximum-likelihood detection

(a) $R = 2.0$ [bits/symbol].   **(b)** $R = 3.0$ [bits/symbol].

Figure 2.15 The relationship between the MED and the BER at SNR = 10 [dB], where the NCGSM(2,2,2,4,2) scheme was considered. The constellation size was set to (a) $\mathcal{L} = 2$ and (b) $\mathcal{L} = 4$. For both cases at least 3000 DM sets were randomly generated.
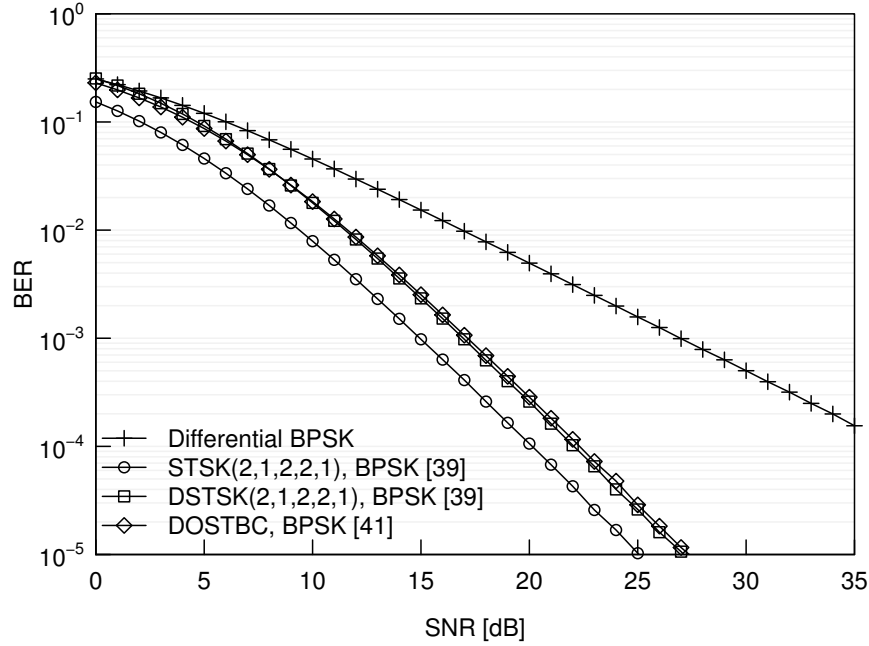
Figure 2.16 BER comparisons of the differential PSK, the STSK, the DSTSK, and the DOSTBC schemes where the constellation size was $\mathcal{L} = 2$ and the transmission rate was $R = 1.0$ [bits/symbol]. The numbers of transmit and receive antennas were $(M,N) = (2,1)$.

BER. Hence, we use the RDC to design the DMs of the NCGSM scheme, which maximizes the MED of its codewords.

2.4.4.2 Reliability

Fig. 2.16 shows the BER of the differential BPSK, the BPSK-aided STSK, the BPSK-aided DSTSK, and the BPSK-aided DOSTBC schemes, where the numbers of transmit and receive antennas were $(M,N) = (2,1)$, and the transmission rate was $R = 1.0$ [bits/symbol]. The BER curve of the differential BPSK was plotted for a reference. Observe in Fig. 2.16 that the STSK, the DSTSK, and the DOSTBC schemes achieved the full-diversity of $D = MN = 2$. The BER curves of both the DSTSK and DOSTBC schemes were almost the same, where there was the gap of 0.1 [dB]. The performance gap between the STSK and DSTSK schemes was about 2.0 [dB]. As reviewed in Section 2.4.3, the gap between the coherent and non-coherent schemes have to be 3.0 [dB]. This incoherence was caused by the difference in the system models. The STSK encoding principle relies on the single-stream model of Eq. (2.42), while the DSTSK relies on the Cayley transform of Eq. (2.43). Note that the constellation of the 2–PAM signaling is equivalent to the BPSK signaling.

(a) $R = 2.0$ [bits/symbol].   **(b)** $R = 3.0$ [bits/symbol].
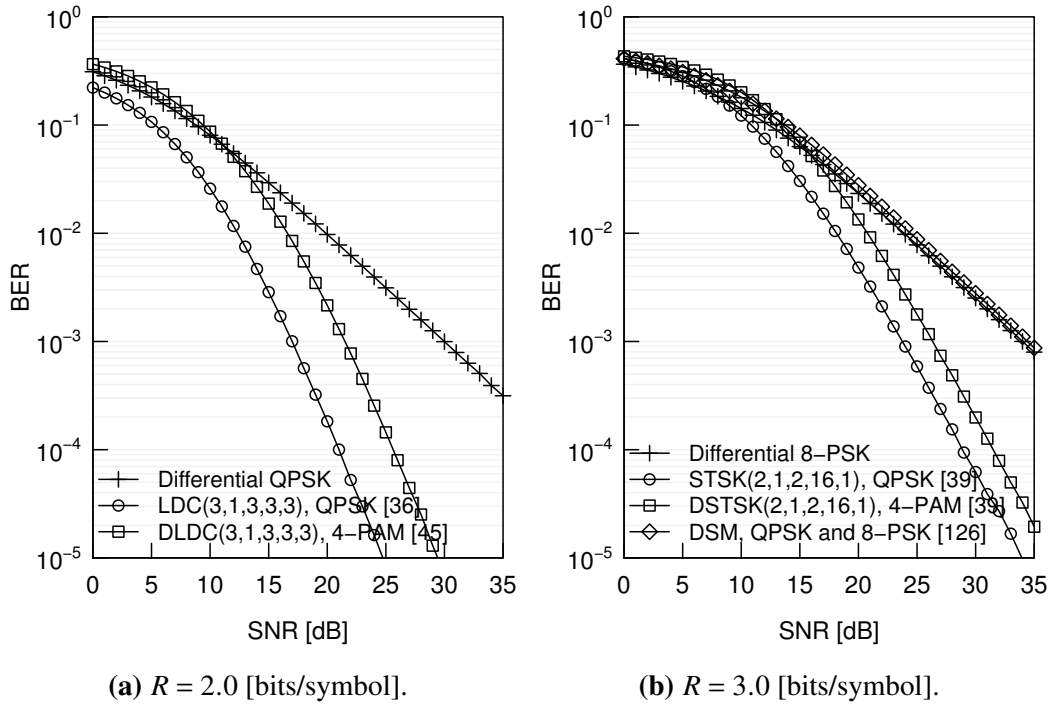
Figure 2.17 BER comparisons of the differential PSK, the LDC, the DLDC, the STSK, the DSTSK, the DSM schemes where the transmission rate was set to $R = 2.0$ and 3.0 [bits/symbol]. The numbers of the transmit and receive antennas were (a) $(M,N) = (3,1)$ and (b) $(M,N) = (2,1)$.

Fig. 2.17(a) shows the BER of the differential QPSK, the QPSK-aided LDC(3,1,3,3,3), and the 4–PAM aided DLDC(3,1,3,3,3), while Fig. 2.17(b) shows the BER comparisons of the differential 8–PSK, the QPSK-aided STSK(2,1,2,16,1), the 4–PAM aided DSTSK(2,1,2,16,1), and the (QPSK, 8–PSK) aided DSM. The number of receive antenna was $N = 1$ for simplicity. It was shown in Figs. 2.17(a) and (b) that the LDC, the DLDC, the STSK, and the DSTSK schemes achieved the full diversity of $D = MN$. Observe in Fig. 2.17(a) that the performance gap between the LDC and DLDC was 4.5 [dB], which was greater than 3.0 [dB]. However, as shown in Fig. 2.17(b), the performance gap between the STSK and DSTSK was 2.8 [dB], which was smaller than 3.0 [dB]. This implies that the BER performance of the STSK scheme may be improved. Also, the DSM scheme achieved almost the same performance with the differential 8–PSK scheme.

Fig. 2.18 shows the BER of the SM, the GSTSK(2,2,2,4,2), the NCGSM(2,2,2,4,2), and the DSM schemes, where the constellation size was $\mathcal{L} = 2$. The BER curve of the differential QPSK was plotted as a reference. In Fig. 2.18, we considered the effects of the channel estimation errors. More specifically, for the PCSI scenario, we assume that the receiver has the perfect estimate of the channel matrix $\mathbf{H}(i)$. In contrast, for the inaccurate CSI scenario, we assume that the receiver has the inaccurate estimate of $\mathbf{H}(i)$, where the channel matrix
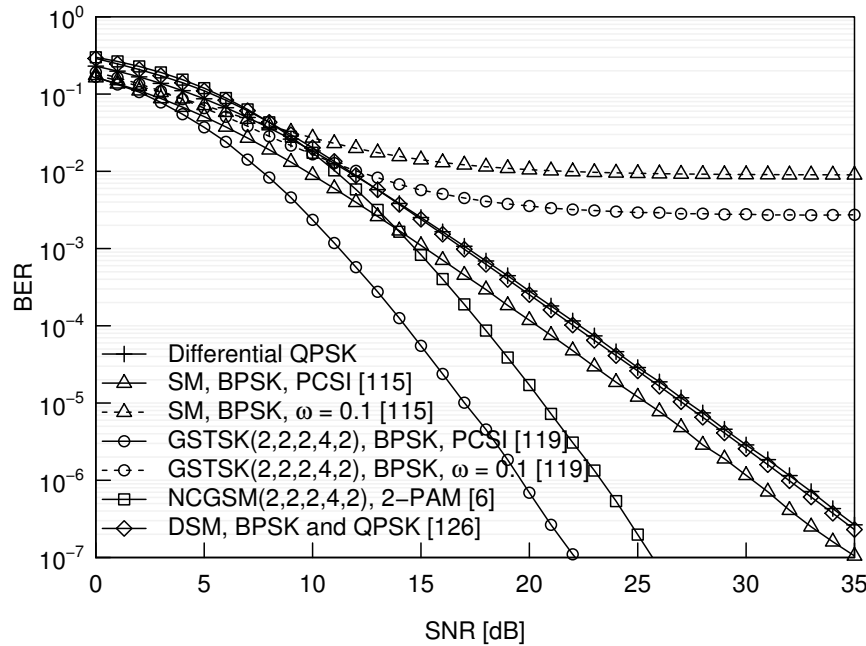
Figure 2.18 BER comparisons of the differential QPSK, the BPSK-aided SM, the BPSK-aided GSTSK(2,2,2,4,2), the 2–PAM aided NCGSM(2,2,2,4,2), and the (BPSK,QPSK) aided DSM where the channel estimation errors were considered. The numbers of the transmit and receive antennas were $(M, N) = (2, 2)$. The transmission rate was $R = 2.0$ [bits/symbol].

is contaminated by the complex-valued AWGN of $\mathcal{CN}(0, \omega)$. Observe in Fig. 2.18 that the coherent GSTSK achieved the best performance, while it exhibited an error-floor for the inaccurate CSI scenario. We observed the same trend for the SM scheme. Hence, the coherent MIMO schemes are difficult to attain a high performance for the inaccurate CSI scenario. The differential MIMO schemes are free from the channel estimation overheads. It was shown in Fig. 2.18 that the NCGSM scheme did not exhibit any error-floor. The performance gap between the GSTSK and NCGSM was 3.5 [dB], which is higher than 3.0 [dB]. Similar to Fig. 2.17(b), the DSM scheme achieved almost the same performance with the differential QPSK scheme.

Fig. 2.19 shows the high-rate counterpart of Fig. 2.18, where the transmission rate was increased to $R = 3.0$ [bits/symbol]. In Fig. 2.19, we compared the QPSK-aided SM and the 4–PAM aided NCGSM(2,2,2,4,2), and considered the channel estimation errors, similar to Fig. 2.18. The BER curve of the differential 8–PSK was plotted as a reference. Observe in Fig. 2.19 that the NCGSM scheme outperformed the coherent SM scheme having PCSI at the SNR of 27.0 [dB]. Similar to Fig. 2.18, the coherent SM scheme assuming the inaccurate CSI exhibited an error-floor. The DSM scheme performed better than the differential 8–PSK scheme, with the gap of 1.0 [dB].
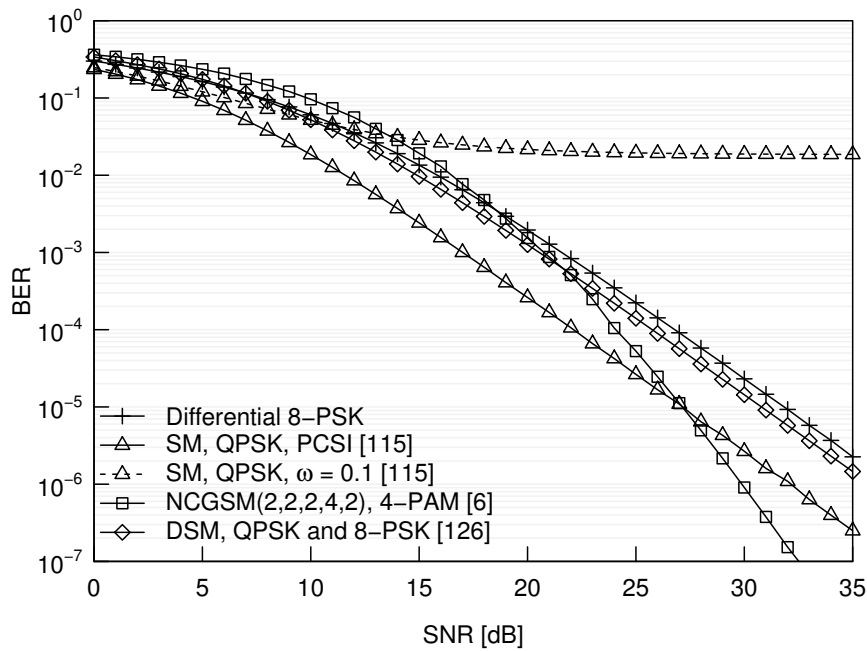
Figure 2.19 BER comparisons of the differential 8–PSK, the QPSK-aided SM, the 4–PAM aided NCGSM(2,2,2,4,2), and the (QPSK, 8–PSK) aided DSM where the channel estimation errors were considered. The numbers of the transmit and receive antennas were $(M,N) = (2,2)$. The transmission rate was $R = 3.0$ [bits/symbol].
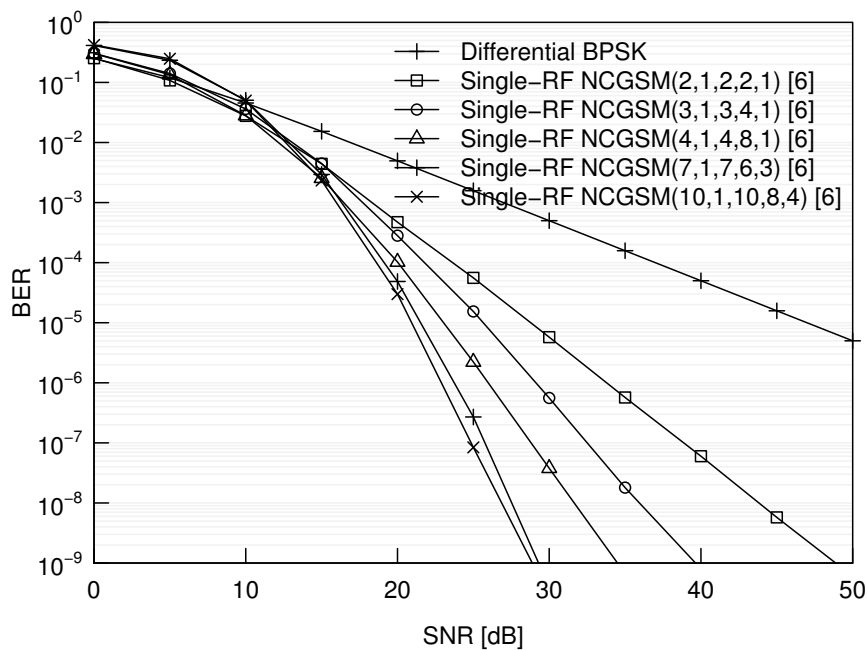
Figure 2.20 BER comparisons of the single-RF NCGSM scheme where the number of transmit antennas was set to $M = 2, 3, 4, 7, 10$. The number of receive antenna was $N = 1$. The transmission rate was constrained to $R = 1.0$ [bits/symbol].

Fig. 2.20 shows the BER of the single-RF NCGSM scheme, where the number of transmit antennas was monotonically increased from $M = 2$ to 10. For the NCGSM scheme, the best parameters (Q, P) were searched based on the RDC of Section 2.2.2. The BER curve of the differential BPSK was plotted as a reference. Observe in Fig. 2.20 that the achievable diversity order of the single-RF NCGSM scheme monotonically increased upon increasing the number of transmit antennas M. This implies the high scalability of the NCGSM scheme. Note that it is difficult to draw the DSM counterpart in Fig. 2.20 because the transmission rate of the DSM scheme is unable to be unified for the different M setups.

2.5 Permutation Modulation Based MIMO Visible Light Communications

The PM concept has been applied to the MIMO-VLC [78], where the channel coefficients are composed of the strong LoS elements. In such environment, the rank of the channel matrices is typically low. Accordingly, the MIMO diversity gain and the spatial multiplexing gain typically lost, which are originally the substantial performance advantages of the MIMO communications as described in Chapter 1. In order to combat this limitation, the precoding-like technique has been proposed, which compensates the low-rank channel observed in MIMO-VLC [101]. The contributions of the PM-based MIMO-VLCs are summarized in Table 2.10.

2.5.1 System Model

We assume the simplified path-loss channel model of [135, 101] in our simulations, where intensity modulation and direct detection (IM/DD) are employed. Based on the general MIMO system model of Eq. (1.2), only the channel matrix $\mathbf{H}$ is replaced with

$$\mathbf{H} = R_{\mathrm{PD}}\mathbf{H}_{\mathrm{VLC}} \in \mathbb{R}^{N \times M}, \tag{2.49}$$

Table 2.10 Contributions to OSM

Year	Authors	Contribution
2010	Mesleh *et al.* [99]	Applied the SM concept of [115] to the MIMO-VLCs, which was termed as OSM.
	Fath *et al.* [127]	Applied the SSK concept of [128] to MIMO-VLCs.
2011	Mesleh *et al.* [78]	Analyzed the OSM scheme of [99] in terms of the channel alignment and the theoretical BER in uncoded and coded scenarios.
	Fath *et al.* [129]	Combined the OSM scheme of [78] with the PAM, which improved the spectral efficiency of OSM.
2012	Popoola *et al.* [130]	Combined the OSM scheme of [78] with the pulse position modulation for improving the energy efficiency.
	Poves *et al.* [131]	Experimented on the OSM scheme of [78] in a real environment, where the numbers of source lights and PDs were $(M,N) = (4,1)$. The transmission rate of 18 [Mbits/s] was achieved.
2013	Popoola *et al.* [132]	Applied the GSSK concept of [121] to MIMO-VLCs, where the multiple source lights were simultaneously activated.
	Fath and Haas [133]	Combined the OSM scheme with the color-shift keying.
	Fath and Haas [101]	Compared the OSM scheme with the repetition coding and spatial multiplexing schemes. In addition, a power-imbalance scheme was proposed, which allocates independent power factors to each transmit LED, for combating the highly correlated LOS channel.
2014	Popoola and Haas [134]	Demonstrated the positive and negative effects of the GSSK scheme in a real environment. The transmission rate of 40 [Mbits/s] was achieved.

where $R_{PD} \in \mathbb{R}$ [A/W] denotes the response of PD. The nth row and mth column of $\mathbf{H}_{VLC}$ is given by [101]

$$h[n,m] = \begin{cases} \dfrac{(\xi+1)A_{PD}}{2\pi d[n,m]^2} \cos^{\xi+1} \phi[n,m] & \left(0 \le \phi[n,m] \le \Psi_{\frac{1}{2}}\right) \\ 0 & \left(\phi[n,m] > \Psi_{\frac{1}{2}}\right) \end{cases}, \qquad (2.50)$$

where we have $\xi = -\ln(2)/\ln\left(\cos\Phi_{\frac{1}{2}}\right)$. In Eq. (2.50), A_{PD} denotes the physical area of the PD at the receiver, $d[n,m]$ denotes the distance between the mth source light and the nth PD, and $\phi[n,m]$ denotes the angle of incidence from the mth source light to the nth PD. $\Phi_{\frac{1}{2}}$ represents the transmitter semi angle, while $\Psi_{\frac{1}{2}}$ represents the field of view semi angle of the receiver. The received SNR is defined as follows: [78]

$$\left(\frac{1}{N}\sum_{n=1}^{N}\sigma_r^{(n)}\right)^2 / \sigma_v^2, \qquad (2.51)$$

where $\sigma_r^{(n)}$ is the received optical power at the nth PD.

2.5.2   Repetition Coding

Before we review the PM scheme applied to MIMO-VLC, we revisit the simplest VLC scheme, which is referred to as PAM repetition-code (PAM-RC). The conventional PAM-RC based transmitter emits the same PAM symbol from all of the source lights. It was shown in [70] that the PAM-RC scheme is capable of outperforming the OSTBC scheme in the free-space optical wireless communications. The $\mathcal{L}$–PAM symbols are defined by [129]

$$s = \frac{2(l-1)}{\mathcal{L}-1} > 0, \qquad (2.52)$$

where l $(1 \le l \le \mathcal{L})$ is the modulation index. Then, the transmitting codeword of the PAM-RC scheme is given by

$$\mathbf{s}^{PAM-RC} = [s \quad s \quad \cdots \quad s]^T \in \mathbb{R}^M, \qquad (2.53)$$

which consists of the M number of the same PAM symbol s.

2.5.3   Equal-Power OSM Scheme

The first PM concept in MIMO-VLC was proposed in [99], which is referred to as "optical spatial modulation (OSM)". The OSM encoding principle is basically the same with the SM scheme proposed for the microwave communications, except for the symbol modulation. The $B = B_1 + B_2$ input bits are divided into the $B_1 = \log_2(M)$ and $B_2 = \log_2(\mathcal{L})$ bits. The first B_1 bits are used to select a single source light q out of the M number of lights. The second B_2 bits are modulated onto a $\mathcal{L}$–PAM symbol s as follows: [129]

$$s = \frac{2l}{\mathcal{L}+1} \cdot (1 \le l \le \mathcal{L}) \tag{2.54}$$

Then, the time-domain OSM symbols are defined by

$$\mathbf{s}^{\text{OSM}} = [\underbrace{0 \cdots 0}_{q-1 \text{ rows}} \underbrace{s}_{\substack{\uparrow \\ q\text{th row}}} \underbrace{0 \cdots 0}_{M-q \text{ rows}}]^{\text{T}} \in \mathbb{R}^M, \tag{2.55}$$

where there is a single non-zero element. The first OSM scheme proposed in [78] modulates the input bits by selecting the transmit source light, and the transmitting PAM symbol is constrained to be one, namely, $s = 1$. Note that since the VLC bandwidths are unlicensed, the OSM system is free from the pulse-shaping issue [98] imposed on the microwave SM systems.

2.5.4   Power-Imbalanced OSM Scheme

The power-imbalanced OSM (PI-OSM) concept was proposed in [101] for improving the performance of OSM system in highly correlated LoS channels. It was reported in [131] that the performance of the OSM scheme depends on the power differences between the channel paths. The time-domain PI-OSM symbols are defined by [101]

$$\mathbf{s}^{\text{PI-OSM}} = \text{diag}(a_1, \cdots, a_M)\, \mathbf{s}^{\text{OSM}} \in \mathbb{R}^M, \tag{2.56}$$

where the PA factors $a_1, \cdots, a_M$ are given by

$$a_m = \begin{cases} \dfrac{M}{\sum_{i=0}^{M-1} \alpha^i} & (m = 1) \\[2ex] \alpha a_{m-1} & (2 \le m \le M) \end{cases}. \tag{2.57}$$

Table 2.11 Simulation parameters of the MIMO-VLC schemes.

Number of transmit source lights	$M = 2, 4$
Number of receive PDs	$N = 1, 4$
Response of PD	$R_{\text{PD}} = 1$ [A/W]
Physical area of PD	$A_{\text{PD}} = 10^{-4}$ [m^2]
Field-of-view semi-angle of source light	$\Phi_{\frac{1}{2}} = 15°$
Field-of-view semi-angle of PD	$\Psi_{\frac{1}{2}} = 45°$
Height of the transmitter	2.5 [m]
Height of the receiver	0.75 [m]
Distance between the source lights	$d_{\text{Tx}} = 0.1, 0.6$ [m]
Distance between the PDs	$d_{\text{Rx}} = 0.1$ [m]
Channel	Indoor MIMO-VLC path-loss model [101]
Detector	Maximum-likelihood detection
Modulation	PAM ($\mathcal{L} = 2, 4, 16, 64, 256$.)

Here, the single parameter α in linear scale determines the M number of the PA factors, which is given by $\alpha = 10^{\frac{\beta}{10}}$. In [101], the single parameter β in dB was set to $\beta = 1, 3$, and 4 [dB].

2.5.5 Performance Results

We evaluated the PM-based MIMO-VLC schemes introduced in Sections 2.5.3 and 2.5.4, such as the equal-power OSM and PI-OSM schemes, in terms of the reliability in uncoded scenarios. The benchmarks were the PAM-RC and spatial multiplexing schemes. In order to conduct fair comparisons, the average transmit power was constrained to the same value for all the considered schemes. We assumed the indoor path-loss channel model provided in [101] and employed the hard-decision MLD at the receiver of Eq. (2.48). The PA factor was selected from $\beta = 1, 3, 4$ [dB] provided in [101], where only the best one was plotted. The simulation parameters considered in this section are given in Table 2.11.

Before our simulations, we review the theoretical BER upper-bound of the MIMO-VLC schemes, which is given by [101]

$$\text{BER} \leq \frac{1}{2^B B} \sum_{f=1}^{2^B} \sum_{g=1}^{2^B} d_{\text{H}}\left(\mathbf{b}^{(f)}, \mathbf{b}^{(g)}\right) \cdot Q\left(\frac{\left\|\mathbf{H}\left(\mathbf{s}^{(f)} - \mathbf{s}^{(g)}\right)\right\|}{2\sigma_v}\right), \quad (2.58)$$

where the symbol vectors $\mathbf{s}^{(f)}$ and $\mathbf{s}^{(g)}$ are associated with the sets of the input bits $\mathbf{b}^{(f)}$ and $\mathbf{b}^{(g)}$, respectively. Here, $d_{\text{H}}\left(\mathbf{b}^{(f)}, \mathbf{b}^{(g)}\right)$ denotes the Hamming distance between the bits $\mathbf{b}^{(f)}$
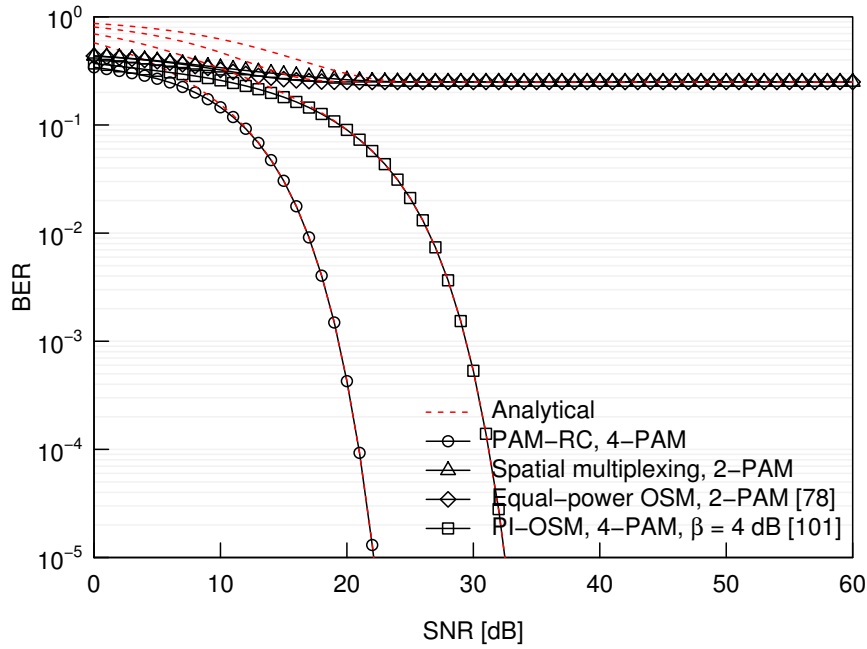
Figure 2.21 BER comparisons of the PAM-RC, the spatial multiplexing, and the equal-power OSM schemes, where the transmission rate was $R = 2.0$ [bits/symbol]. The numbers of source lights and receive PDs were $(M, N) = (2, 1)$. The distance between the source lights and the PDs was $d_{\text{Tx}} = d_{\text{Rx}} = 0.1$ [m].

and $\mathbf{b}^{(g)}$. The analytical BER of Eq. (2.58) was plotted for all the schemes simulated in coherent MIMO-VLC scenarios.

Fig. 2.21 shows the BER of the $\mathcal{L} = 4$–PAM aided RC, the $\mathcal{L} = 2$–PAM aided spatial multiplexing, and the $\mathcal{L} = 2$–PAM aided equal-power OSM, where we have $(M, N) = (2, 1)$ and $R = 2.0$ [bits/symbol]. Observe in Fig. 2.21 that the PAM-RC scheme achieved the BER of 10^{-5} at 22.1 [dB], while the spatial multiplexing and equal-power OSM schemes exhibited an error-floor. This was because of the low-rank channel matrix, which was calculated by rank($\mathbf{H}$) = 1. In contrast, upon incorporating the PA factor of Eq. (2.57), the PI-OSM scheme having $\beta = 4.0$ [dB] achieved the BER of 10^{-5} at 32.5 [dB].

Fig. 2.22 shows the BER of the $\mathcal{L} = 16$–PAM aided RC, the $\mathcal{L} = 2$–PAM aided spatial multiplexing, and the $\mathcal{L} = 4$–PAM aided equal-power OSM, where we have $(M, N) = (4, 4)$ and $R = 4.0$ [bits/symbol]. Observe in Fig. 2.22 that the PAM-RC scheme achieved the best performance. At the BER of 10^{-5}, the SNR gap between the PAM-RC and the PI-OSM schemes was 12.2 [dB]. Note that the PI-OSM scheme improved the performance of the equal-power OSM scheme with the gap of 5.9 [dB]. The spatial multiplexing scheme exhibited an error-floor, while the rank of channel matrix was rank($\mathbf{H}$) = 4.
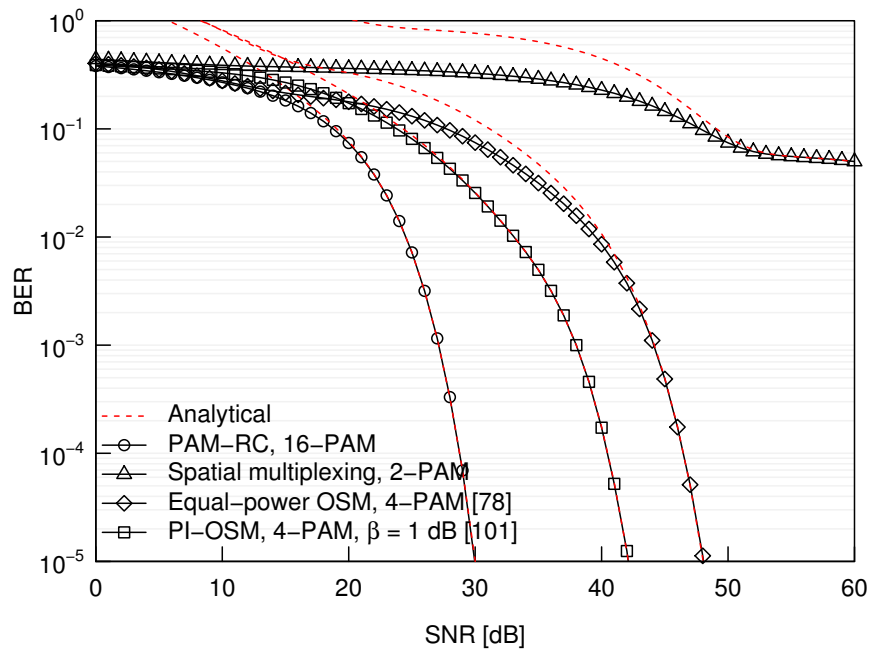
Figure 2.22 BER comparisons of the PAM-RC, the spatial multiplexing, the equal-power OSM, and the PI-OSM schemes, where the transmission rate was $R = 4.0$ [bits/symbol]. The numbers of source lights and receive PDs were $(M, N) = (4, 4)$. The other parameters were the same with those used in Fig. 2.21.
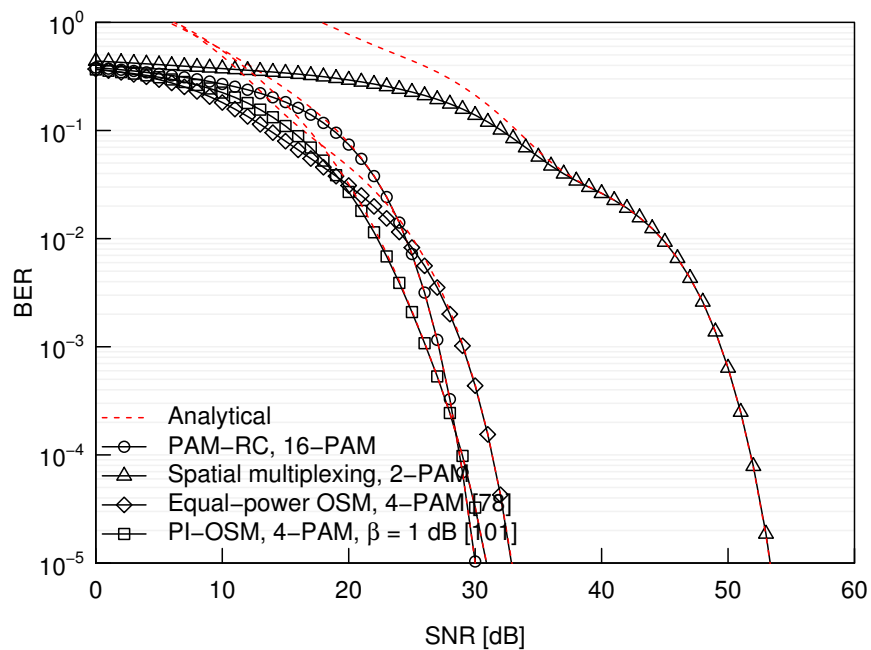
Figure 2.23 BER comparisons of the PAM-RC, the spatial multiplexing, the equal-power OSM, and the PI-OSM schemes. The other parameters were the same with those used in Fig. 2.22 except for the distance between the source lights $d_{\text{Tx}} = 0.6$ [m].
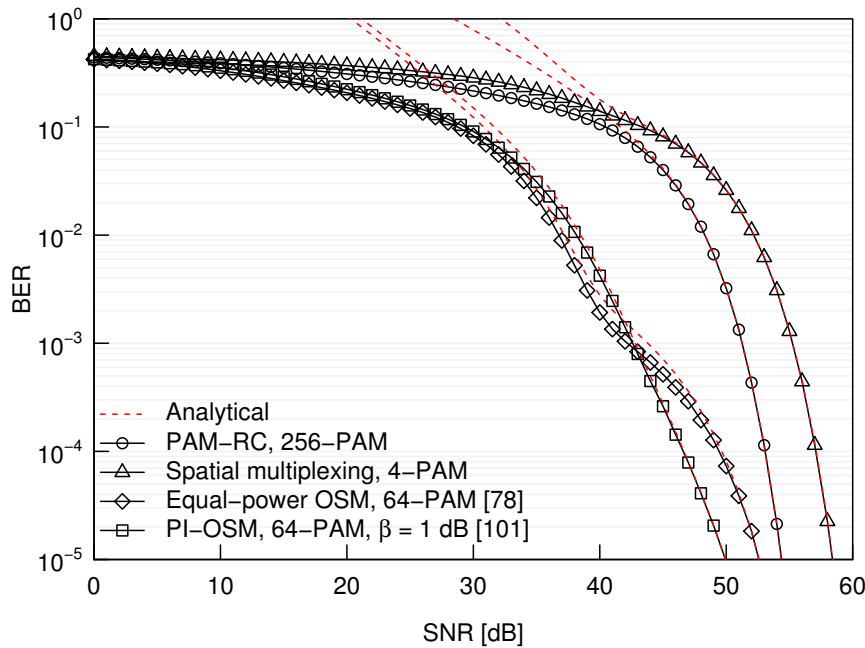
Figure 2.24 BER comparisons of the PAM-RC, the spatial multiplexing, the equal-power OSM, and the PI-OSM schemes. The other parameters were the same with those used in Fig. 2.23 except for the transmission rate $R = 8.0$ [bits/symbol].

Fig. 2.23 shows the BER comparisons based on Fig. 2.22, where the distance between the source lights was increased from $d_{Tx} = 0.1$ to $d_{Tx} = 0.6$ [m]. Observe in Fig. 2.23 that the performance of the MIMO schemes, including the spatial multiplexing, the equal-power OSM, the PI-OSM schemes, were significantly improved, as compared to Fig. 2.22. This was because the large distance between the source lights $d_{Tx} = 0.6$ [m] increased the difference between the adjacent channel coefficients in the channel matrix **H**. However, similar to Figs. 2.21 and 2.22, the PAM-RC scheme achieved the best performance.

Fig. 2.24 shows the high-rate counterpart of Fig. 2.23, where the transmission rate was increased to $R = 8.0$ from $R = 4.0$ [bits/symbol]. Observe in Fig. 2.24 that the PI-OSM scheme having $\beta = 1$ [dB] achieved the best performance. More specifically, the performance gap between the PI-OSM and PAM-RC schemes was 4.4 [dB]. For the higher rate cases, we observed that the performance advantage of the OSM schemes over the PAM-RC scheme improved with the aid of the reduced number of power levels $\mathcal{L}$.

2.6 Permutation Modulation Based Multicarrier Communications

The PM-aided multicarrier concept was originally constituted by Sasaki *et al.* in 1989 in the spread-spectrum context, which was firstly reported in the Japanese domestic society of wireless communications. Two years later, the original PM concept was termed as "parallel combinatory" and reported at an IEEE conference [75]. The parallel combinatory based scheme of [75] modulates additional bits onto a set of spread sequences, and hence it achieves a higher spectrum efficiency while maintaining a low-complexity transmitter. This original concept was also evaluated in a channel-coded system [136] and a multiple-access system [137]. It was shown in [75, 136, 137] that the PM concept applied to the spread-spectrum system achieved a higher performance than the conventional direct sequence spread-spectrum system.

Motivated by the parallel combinatory concept of [75, 136, 137], the PM concept was applied to orthogonal frequency-division multiplexing (OFDM) [76], where a part of all the subcarriers is activated. More specifically, the PM-aided OFDM scheme of [76] modulates the input bits by the same encoding principle of the GSM [121]. Note that the PM scheme of [76] was proposed in 1999, while the GSM scheme was proposed in 2010. Later, the PM-aided OFDM scheme of [76] was called the subcarrier index modulation (SIM) [95]. In [76], it was clarified that the SIM scheme is capable of striking the flexible trade-off between spectrum efficiency, PAPR, and reliability. The contributions to the SIM scheme are summarized in Table 2.12.

2.6.1 System Model

The key feature of the SIM symbols is the sparsity of the frequency domain symbols, where the P number of the subcarriers are activated out of the M number of subcarriers. For simplicity, we represent the SIM system having the parameters M and P as "SIM(M,P)". The encoding principle of the SIM(M,P) scheme is the same with the GSM(M,P) scheme, which is described in Section 2.3.2. Similar to the GSM(M,P) principle, we have the N_a number of the subcarrier-activation patterns, which are denoted by $\mathbf{a}_i$ for $1 \leq i \leq N_a$. The encoded symbols are represented as the column vectors $\mathbf{s} = [s_1, \cdots, s_m]^T \in \mathbb{C}^{M \times 1}$. We assume the idealized Rayleigh fading channel model, where the received symbols are given by [96]

$$y_m = h_m s_m + v_m \in \mathbb{C}, \ (1 \leq m \leq M) \tag{2.59}$$

Table 2.12 Contributions to SIM

Year	Authors	Contribution
1991	Sasaki *et al.* [75]	Proposed the spread-spectrum PM scheme.
1994	Sasaki *et al.* [136]	Evaluated the spread-spectrum PM scheme of [75], while combining it with the selection diversity method and the Reed-Solomon coding.
1995	Sasaki *et al.* [137]	Evaluated the spread-spectrum PM system of [75] in the multiple-access scenario.
1999	Frenger and Svensson [76]	Proposed the subcarrier-based PM in the OFDM context, where the basic modulation concept was based on [75]. This scheme is later called SIM in [95].
2005	Kitamoto and Ohtsuki [138]	Analyzed the SIM of [76] in VLC scenarios.
2007	Hou and Hamamura [139]	Developed the parallel multi-carrier modulation concept for improving the bandwidth efficiency of the SIM scheme.
2009	Abu-Alhiga and Haas [95]	Evaluated the BER performance of the SIM scheme in uncoded and coded scenarios, motivated by the development of the SM [104].
	Hou and Hase [140]	Proposed a phase-rotation scheme for reducing the PAPR of SIM systems.
2011	Tsonev *et al.* [141]	Improved the SIM structure proposed in [95] and analyzed the PAPR of SIM systems.
2013	Basar *et al.* [96]	Derived the attainable frequency diversity order of the SIM scheme in the closed form.
2014	Xiao *et al.* [142]	Proposed the subcarrier-level interleaving method for the SIM scheme.
	Fan *et al.* [143]	Proposed the SIM scheme that supports a flexible number of selected subcarriers, and performs independent PM on the in-phase and quadrature component per subcarrier.
2015	Basar [144]	Proposed an interleaving method for the SIM scheme combined with the space-time block codes.
	Zheng *et al.* [145]	Proposed a low-complexity detector for the SIM scheme, which performs independent PM on the in-phase and quadrature component.
	Basar [146]	Proposed the SIM scheme combined with the spatial multiplexing MIMO transmission, and develops its low-complexity detector.
	Datta *et al.* [147]	Incorporated the PM concept with the space- and frequency-dimensions and developed a Gibbs sampling based detection algorithm.
	Wen *et al.* [97]	Derived the maximum achievable rate of the SIM scheme and proposed an interleaved grouping method.
2016	Basar [148]	Investigated the performance of the SIM schemes operated in MIMO scenarios. In addition to the ML detector, low-complexity detectors were proposed.

where h_m and v_m follow the complex-valued Gaussian distribution of $\mathcal{CN}(0,1)$ and $\mathcal{CN}(0,\sigma_v^2)$, respectively. Here, the cyclic prefix (CP) insertion and the inter-subcarrier interference are ignored for simplicity. We define the received SNR as $1/\sigma_v^2$. Eq. (2.59) is alternatively represented as the vector form of

$$\mathbf{y} = \text{diag}(\mathbf{h})\mathbf{s} + \mathbf{v}, \tag{2.60}$$

where we have $\mathbf{h} = [h_1,\cdots,h_m]^{\mathrm{T}} \in \mathbb{C}^{M\times 1}$ and $\mathbf{v} = [v_1,\cdots,v_m]^{\mathrm{T}} \in \mathbb{C}^{M\times 1}$.

2.6.2   Optimum and Near-Optimum Low-Complexity Detectors

Based on Eq. (2.60), the optimum MLD for the SIM scheme is given by

$$\hat{\mathbf{s}} = \arg\min_{\mathbf{s}} \|\mathbf{y} - \text{diag}(\mathbf{h})\mathbf{s}\|^2. \tag{2.61}$$

The computational complexity of Eq. (2.61) is higher than the MLD of the OFDM scheme because in Eq. (2.61) the M number of subcarrier-symbols are considered at the same time, while the OFDM scheme demodulates symbols by subcarrier-by-subcarrier. Against this computational problem, the LLR-based low-complexity detector was proposed in [96]. Based on the received symbols $\mathbf{y}$ and the received SNR σ_v^2, the LLR-based detector of [96] firstly estimates the activated subcarriers $\mathbf{a}_{\hat{q}}$ out of the $(\mathbf{a}_1,\cdots,\mathbf{a}_{N_a})$ candidates. More specifically, the detector calculates the LLR values for each subcarrier as follows:

$$L^{(m)} = \ln(P) - \ln(M-P) + \frac{|y_m|^2}{\sigma_v^2} + \ln\left(\sum_{l=1}^{\mathcal{L}} \exp\left(-\frac{\left|y_m - h_m s^{(l)}\right|^2}{\sigma_v^2}\right)\right), \tag{2.62}$$

where $s^{(l)}$ ($1 \leq l \leq \mathcal{L}$) denotes the lth symbol of the $\mathcal{L}$–APSK modulation. Then, the detector estimates the activated subcarriers based on the following criterion.

$$\hat{q} = \arg\max_{1 \leq i \leq N_a} \sum_{p=1}^{P} L^{(\mathbf{a}_i(p))}. \tag{2.63}$$

Table 2.13 Simulation parameters of the multicarrier communications.

Number of transmit antenna	1
Number of receive antenna	1
Number of subcarriers	$M = 1, 2, 4, 8, 16$
Number of activated subcarriers	$P = 1, 2, 3, 8, 10, 15$
Modulation	BPSK, QPSK, 16–QAM, 32–PSK, 64–PSK, 64–QAM
Channel	i.i.d. Rayleigh fading
Detector	ML- and LLR-based detector

Next, based on the estimated activation indices $\mathbf{a}_{\hat{q}}$, the detector demodulates the received APSK symbols as follows:

$$(\hat{s}_1, \cdots, \hat{s}_P) = \arg \min_{(s_1, \cdots, s_P)} \sum_{p=1}^{P} \left| y_{\mathbf{a}_q(p)} - h_{\mathbf{a}_q(p)} s_p \right|^2. \tag{2.64}$$

The LLR-based low-complexity detector of [96] achieves the same performance with the ML-based detector if there is no inter-subcarrier interference, which is later shown in Section 2.6.3.

2.6.3   Performance Results

We evaluated the SIM and OFDM schemes in terms of the reliability in uncoded scenarios. In order to conduct fair comparisons, the average transmit power was constrained to the same value for both the schemes. We assumed the idealized Rayleigh fading channel model of Section 2.6.1. In our simulations the hard ML- and LLR-based detectors were employed. The simulation parameters considered in this section are given in Table 2.13.

Fig. 2.25 shows the BER of the SIM(4,2) scheme, where both the ML- and LLR-based detectors were considered. As shown in Fig. 2.25, the LLR-based detector of [96] achieved the optimum performance, which was the same with the ML-based detector.

Fig. 2.26 shows the BER of OFDM and SIM schemes, where the transmission rate was set to (a) $R = 1.0$ and (b) $R = 2.0$ [bit/s/Hz]. In Fig. 2.26(a), the BPSK-aided OFDM, the BPSK-aided SIM(2,1), and the BPSK-aided SIM(8,3) schemes were considered. The SIM(16,8) scheme having no APSK symbols, i.e. $\mathcal{L} = 1$, was plotted for a reference, where its transmission rate was $R = 0.81$ [bits/s/Hz]. In Fig. 2.26(b), the QPSK-aided OFDM, the QPSK-aided SIM(4,3), and the QPSK-aided SIM(16,10) schemes were considered. It was shown in Fig. 2.26(a) that the BPSK-aided SIM(2,1) and SIM(8,3) schemes achieved
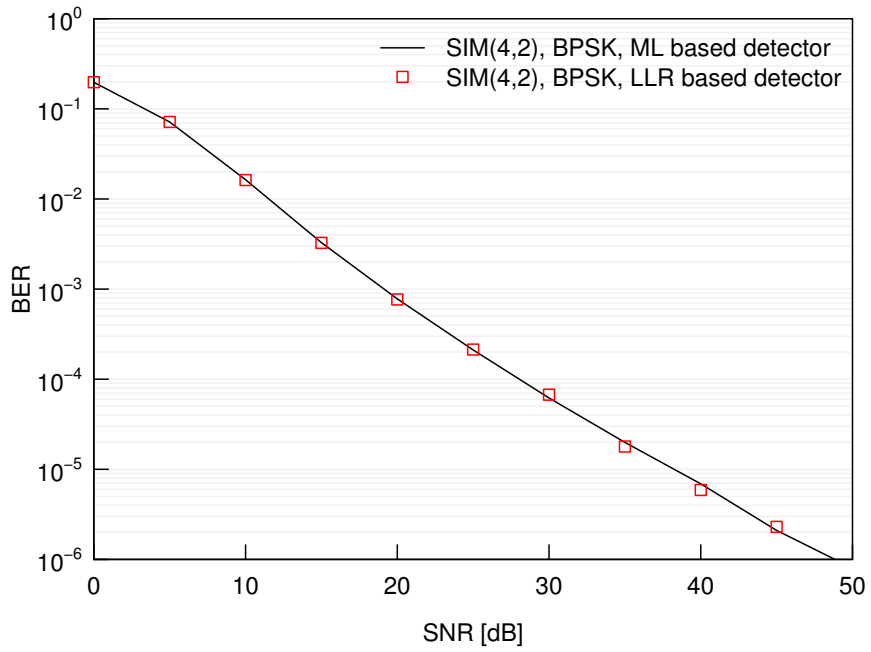
Figure 2.25 BER comparisons between the ML- and LLR-based detectors.

(a) $R = 1.0$ [bits/s/Hz].

(b) $R = 2.0$ [bits/s/Hz].
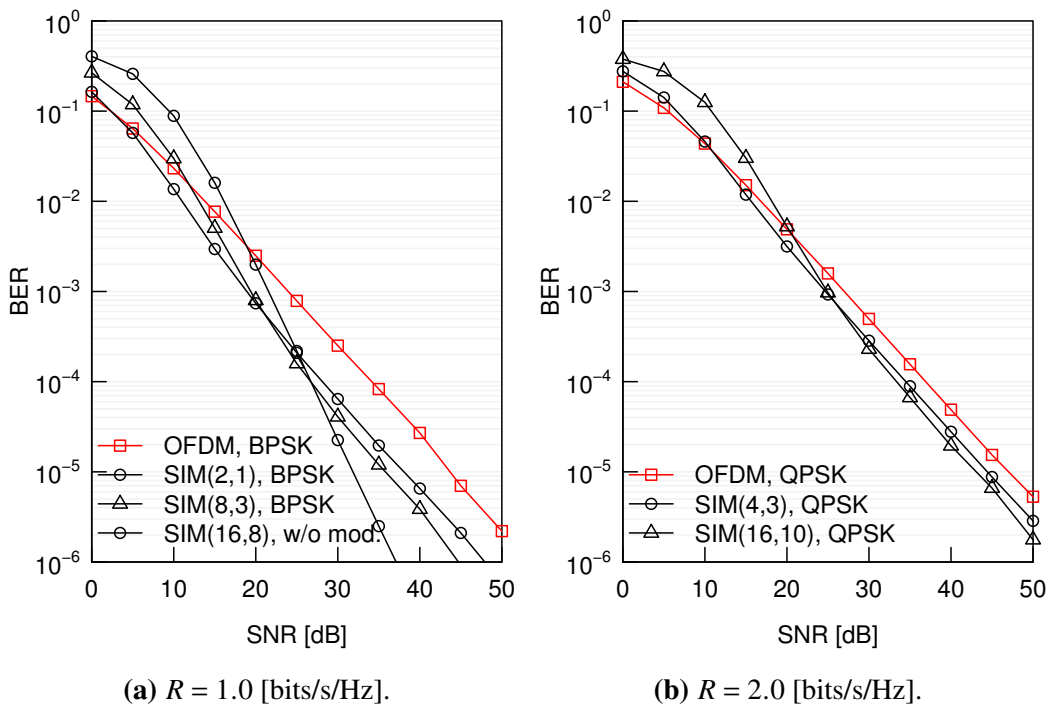
Figure 2.26 BER comparisons of the OFDM and SIM schemes, where the transmission rate was set to $R = 1.0$ and 2.0 [bits/symbol].

(a) $R = 4.0$ [bits/s/Hz].

(b) $R = 5.0$ [bits/s/Hz].
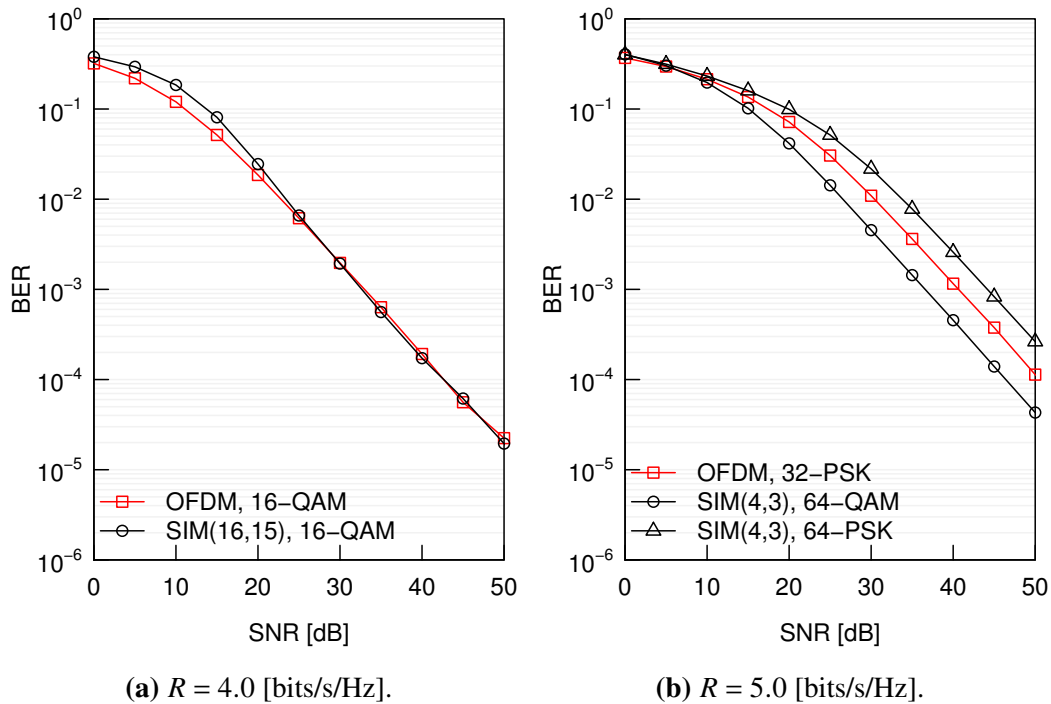
Figure 2.27 BER comparisons of the OFDM and SIM schemes, where the transmission rate was set to $R = 4.0$ and 5.0 [bits/symbol].

a significant gain over the OFDM counterpart. The SIM(16,8) scheme achieved a higher diversity order than the SIM schemes having BPSK symbols. This was caused by the frequency diversity of the Rayleigh fading channels, which was proved in [96]. It was shown in Fig. 2.26(b) that the SIM schemes achieved a higher performance than the conventional OFDM scheme, similar to Fig. 2.26(a).

Fig. 2.27 shows the BER of the OFDM and SIM schemes, where the transmission rate was set to (a) $R = 4.0$ and (b) $R = 5.0$ [bits/s/Hz]. Fig. 2.27(a) considers the 16–QAM aided OFDM and 16–QAM aided SIM(16,15) schemes, while Fig. 2.27(b) considers the 32–PSK aided OFDM, 64–PSK aided SIM(4,3), and the 64–QAM aided SIM(4,3) schemes. It was shown in Fig. 2.27(a) that the performance advantage of the SIM scheme over the conventional OFDM scheme was not observed. In contrast, in Fig. 2.27(b), the 64–QAM aided SIM(4,3) scheme achieved a higher performance than the 32–PSK aided OFDM scheme. This was because the OFDM scheme relied on the inefficient 32–PSK modulation, while the SIM scheme relied on the efficient 64–QAM modulation.

2.7 Chapter Summary

In this chapter, we reviewed the performance metrics, such as mutual information, reliability, and computational complexity, which are useful tools for evaluating the IM-aided schemes. The AMI of Section 2.2.1 analyzes the performance in channel-coded scenarios, while the reliability analysis of Section 2.2.2 estimates the performance upper-bound in uncoded scenarios. The computational complexity analysis of Section 2.2.3 is effective for the IM schemes, because the IM family typically exhibits a lower complexity than the conventional non-IM schemes. Next, we reviewed the IM family having proposed for the coherent MIMO, the differential MIMO, the MIMO-VLC, and the multicarrier communications. In Section 2.3, we reviewed the SM concept, which was the motivator of the current IM research in the field of communications from the early 2000s. Sections 2.4 and 2.5 introduced the IM schemes proposed for the differential MIMO and the MIMO-VLC scenarios, which were extended from the schemes of the coherent SM concept. In Section 2.6, we reviewed the original background of the IM concept having proposed for multicarrier communications.

In our simulations, we observed the performance advantages and disadvantages of the IM concept in the diverse channel models. In the following chapters, we propose the novel schemes that extend the conventional schemes introduced in this chapter, and provide our simulation results based on the performance metrics defined in this chapter.

Chapter 3

Permutation Modulation Based Differential MIMO Communications

3.1 Introduction

In Chapter 2, we reviewed the PM concept applied to diverse wireless systems such as coherent/non-coherent MIMO, visible light, and multi-carrier communications. As discussed in Chapter 1, the MIMO techniques have played a key role in numerous communications standards. Multiple symbol streams transmitted through the multiple antennas contribute to the increase of system capacity [25]. Since the signals transmitted from sufficiently separated antennas pass through uncorrelated channel paths, the diversity of received symbols also contributes to improving system reliability. In MIMO communication systems, transmitter and receiver typically have multiple RF chains, which consume static and dynamic power electricity. This energy consumption issue has been addressed by the SM concepts [103], with reducing the number of RF chains at the transmitter. However, in the SM scheme it is difficult to obtain the channel coefficients efficiently because the SIM transmitter is equipped with a single RF chain and is unable to transmit pilot symbols from multiple transmit antennas simultaneously.

In this chapter, we propose a differentially-encoded counterpart of the SM scheme, which enables both the single-RF operation at the transmitter and non-coherent detection at the receiver. The proposed scheme is equivalent to the PM concept applied to DSTBC. The proposed scheme is termed as unified differential spatial modulation (UDSM) [4]. The UDSM scheme has a flexibility that controls the spatial multiplexing gain and the diversity

Table 3.1 Overview of differential MIMO schemes

	Hermitian	Unitary	Non-unitary
$N_{\mathrm{RF}} = M$	NCGSM [6]	DOSTBC [149]	QAM-aided DOSTBC [46]
$1 < N_{\mathrm{RF}} < M$	—	—	DQOSTBC [47]
$N_{\mathrm{RF}} = 1$	Single-RF NCGSM [6]	**UDSM** / Group code [42]	—

gain. In order to maintain a practical MED of codewords, the UDSM employs the dispersion matrix (DM) architecture. We provide a design guideline for the DM set, which consists of sparse space-time matrices. Table 3.1 summarizes the DSTBC schemes having been proposed in the literature, which are classified in terms of the number of RF chains N_{RF} required at the transmitter and the type of space-time codewords.

The remainder of this chapter is organized as follows. In Section 3.2, we propose the UDSM scheme and provide its design criteria. In Section 3.3, we introduce the optimum detector as well as its theoretical analysis. In Section 3.4, we evaluate the computational complexity and the reliability of the UDSM scheme, where no channel coding scheme is considered. Section 3.5 concludes this chapter.

3.2   Modulation Concept

The UDSM transmitter modulates an input bit sequence having the length of B onto an output space-time matrix $\mathbf{S}(i)$, where i represents the transmission index. In advance of transmissions, Q number of DMs $\mathbf{A}_q \in \mathbb{C}^{M \times M}$ ($q = 1, \cdots, Q$) have to be prepared. Each DM $\mathbf{A}_q$ has a single non-zero unit-absolute-value element in its column and row. Here, we represent the non-zero element as $a_{q,m}$ ($1 \leq q \leq Q$, $1 \leq m \leq M$), where q denotes the DM index and m denotes the activated antenna index. The norm of the non-zero element is constrained to be $|a_{q,m}| = 1$ in order to maintain the unitary constraint. The followings are examples of $Q = 2$ DMs for the $M = 2$ transmit antennas case.

$$\mathbf{A}_1 = \begin{bmatrix} \exp(-j0.82\pi) & 0.00 \\ 0.00 & \exp(+j0.42\pi) \end{bmatrix}, \mathbf{A}_2 = \begin{bmatrix} 0.00 & \exp(-j0.01\pi) \\ \exp(+j0.10\pi) & 0.00 \end{bmatrix}. \quad (3.1)$$

As given in Eq. (3.1), the norm of any non-zero element is constrained to be 1. Hence, each DM $\mathbf{A}_1, \cdots, \mathbf{A}_Q$ is kept to be a unitary matrix. The DMs of Eq. (3.1) were found by the exhaustive search method, which will be detailed in Section 3.2.3. The comprehensive examples of DMs are available in Appendix. A.3.
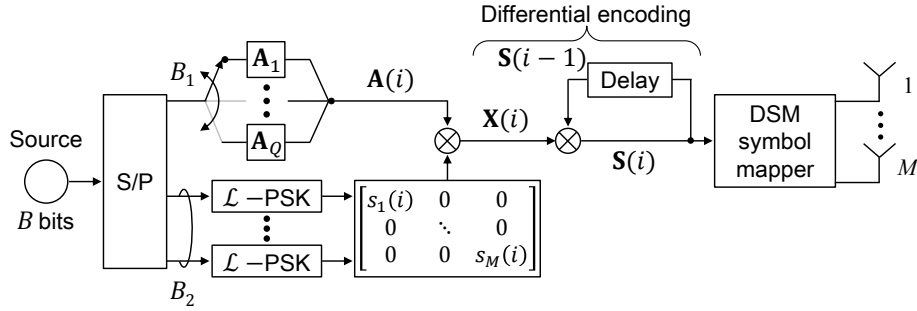
Figure 3.1 Schematic of the proposed UDSM transmitter.

Fig. 3.1 shows the transmitter structure of the proposed UDSM scheme. In Fig. 3.1, the input bits are S/P converted to $B_1 = \log_2(Q)$ bits and $B_2 = \log_2(\mathcal{L}_1 \cdots \mathcal{L}_M)$ bits. The first B_1 bits are mapped to selecting a DM $\mathbf{A}_q(i)$ out of Q number of DMs. The second B_2 bits are modulated to M number of PSK symbols $\mathbf{s}(i) = [s_1(i), \cdots, s_M(i)]$. A unitary matrix $\mathbf{X}(i) \in \mathbb{C}^{M \times M}$ is calculated as follows:

$$\mathbf{X}(i) = \mathrm{diag}(\mathbf{s}(i))\mathbf{A}_q(i), \tag{3.2}$$

which represents a conveyed data. In Eq. (3.2), $\mathrm{diag}(\cdot)$ denotes the diagonal operation that maps a vector to a diagonal matrix. The data matrix $\mathbf{X}(i)$ is a sparse matrix, where there is a single non-zero element in each column and row. The norm of each non-zero element in $\mathbf{X}(i)$ is also constrained to be 1, similar to the DM construction of $|a_{q,m}| = 1$. Finally, a space-time codeword $\mathbf{S}(i) \in \mathbb{C}^{M \times M}$ is differentially-encoded by the following multiplication:

$$\mathbf{S}(i) = \mathbf{S}(i-1)\mathbf{X}(i), \tag{3.3}$$

which is transmitted through M antennas over $T = M$ symbol duration. The initial codeword is set to the identity matrix $\mathbf{S}(0) = \mathbf{I}_M$. In Eq. (3.3), the Frobenius norm of codeword $\mathbf{S}(i)$ is maintained to the same value M because the data matrix $\mathbf{X}(i)$ is unitary. Since the number of non-zero element in each column and row is also constrained to one, the UDSM transmitter activates only one antenna at any transmission index.

The normalized transmission rate of UDSM is given by

$$R = \frac{B}{M} = \frac{\log_2(Q \cdot \mathcal{L}_1 \cdots \mathcal{L}_M)}{M} \text{ [bits/symbol].} \tag{3.4}$$

Suppose that the relationship of $\mathcal{L}_1 \cdots \mathcal{L}_M > \mathcal{L}$, the transmission rate of UDSM Eq. (3.4) is higher than that of the DSTSK, which is given by $\log_2(Q \cdot \mathcal{L})/M$. This is because the UDSM embeds multiple symbols in a space-time codeword.

3.2.1 Rate-Diversity Tradeoff

The proposed UDSM architecture enables a flexible trade-off between the transmission rate and the achievable diversity order, which is a substantial nature of MIMO communications systems [32]. As described in the UDSM modulation principle, the proposed encoding process embeds M number of PSK symbols. Here, the number of embedded symbols is generalized to the case of $1 \leq \bar{M} \leq M$, where $M/\bar{M}$ must be an integer. Later, the embedded symbols are denoted by $s_1, \cdots, s_{\bar{M}}$. In addition, the number of constellations associated with symbols $s_1, \cdots, s_{\bar{M}}$ are denoted by $\mathcal{L}_1, \cdots, \mathcal{L}_{\bar{M}}$. Hence, the integer $M/\bar{M}$ represents the maximum diversity order of the UDSM transmitter. For example, if we embed $\bar{M} = M$ symbols, then the maximum diversity order is $M/\bar{M} = 1$ and the transmission rate is maximized. If we embed a $\bar{M} = 1$ symbol, then $M/\bar{M}$ is equal to M and its diversity gain is maximized. Throughout this chapter, we employ the following notation of $\mathbf{L} \in \mathbb{Z}^M$.

$$\mathbf{L} = \begin{cases} [\underbrace{(\mathcal{L}_1, \cdots, \mathcal{L}_1)]}_{M \text{ elements}} & (\bar{M} = 1) \\ [\underbrace{(\mathcal{L}_1, \cdots, \mathcal{L}_1)}_{M/2 \text{ elements}}, \underbrace{(\mathcal{L}_2, \cdots, \mathcal{L}_2)]}_{M/2 \text{ elements}} & (\bar{M} = 2) \\ \quad \vdots \qquad\qquad\qquad \vdots \\ [\underbrace{\mathcal{L}_1, \mathcal{L}_2, \cdots, \mathcal{L}_M]}_{M \text{ elements}} & (\bar{M} = M) \end{cases} \tag{3.5}$$

The normalized transmission rate that takes into account the $\bar{M}$ notation is given by

$$R = \frac{B}{M} = \frac{\log_2(Q \cdot \mathcal{L}_1 \cdots \mathcal{L}_{\bar{M}})}{M}. \tag{3.6}$$

For example, if we consider the $M = 4$ and $\bar{M} = 2$ case, the embedded $\bar{M} = 2$ BPSK symbols are represented as follows

$$\mathrm{diag}\,(\mathbf{s}(i)) = \mathrm{diag}\,(s_1(i), s_1(i), s_2(i), s_2(i)) \tag{3.7}$$
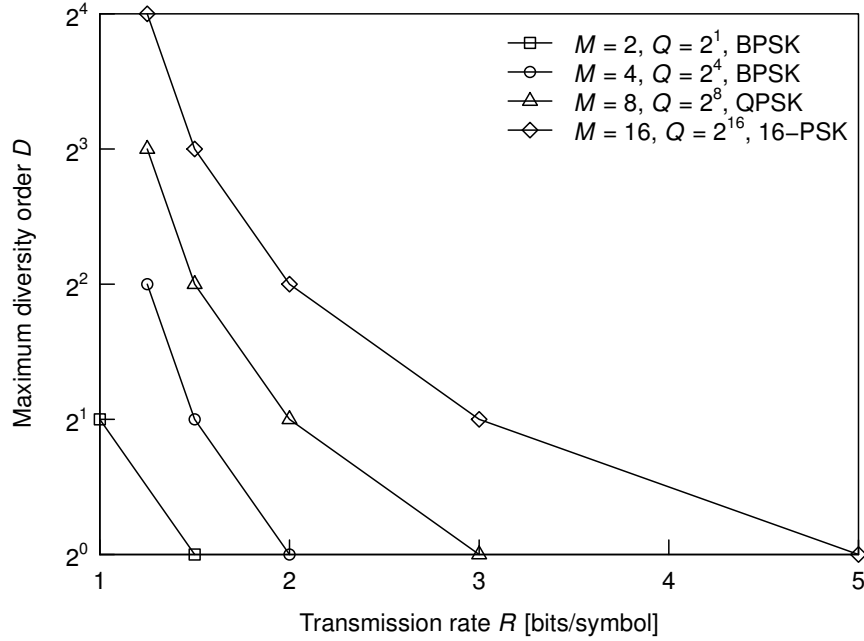
Figure 3.2 Trade-off between the transmission rate R and achievable diversity D, where the number of transmit antennas $M = 2,4,8,16$ were considered.

and the constellations are denoted by $\mathbf{L} = [(\mathcal{L}_1,\mathcal{L}_1),(\mathcal{L}_2,\mathcal{L}_2)] = [(2,2),(2,2)]$. In Eq. (3.7), the two BPSK symbols $s_1(i)$ and $s_2(i)$ are embedded in a space-time codeword. The configuration in Eq. (3.7) achieves a diversity order of $D = 2$ because each symbol is copied over two successive symbol transmissions.

Fig. 3.2 shows the flexible rate-diversity trade-off of the proposed UDSM. Here, the configurations $(M,Q) = \left(2,2^1\right),\left(4,2^4\right),\left(8,2^8\right),\left(16,2^{16}\right)$ were considered. The number of embedded symbols was ranging in $\bar{M} = 2^0,2^1,\cdots,2^{\log_2(M)}$. As shown in Fig. 3.2, the maximum diversity order D decreased with an increase in the transmission rate R. Similarly, R decreased with an increase in D.

Table 3.2 shows a mapping example of the UDSM scheme having $M = 4$ and $Q = 4$. Here, two BPSK symbols are embedded in each space-time codeword, namely, $\mathbf{L} = [(2,2),(2,2)]$. The first $B_1 = 2$ bits of the input $B = 4$ bits are mapped to select a single DM $\mathbf{A}_1$, $\mathbf{A}_2$, $\mathbf{A}_3$, or $\mathbf{A}_4$. The second $B_2 = 2$ bits of the input are modulated to BPSK symbols and are denoted by a vector $\mathbf{s}(i)$. Finally, the data matrix $\mathbf{X}(i)$ is generated based on Eq. (3.2).

3.2.2 Relationships with the Conventional Schemes

The UDSM architecture subsumes the conventional schemes, such as DSTSK of Section 2.3.3 and Binary DSM of Section 2.4.1.

Table 3.2 Mapping example of the UDSM scheme having $M = 4$, $Q = 4$, and $\mathbf{L} = \{(2,2),(2,2)\}$. The length of input bits is $B = 4$.

Source (4 bits)	Activated DM $\mathbf{A}_q(i)$	BPSK symbols $\mathbf{s}(i)$	Unitary matrix $\mathbf{X}(i)$
00 ┊ 00	$\mathbf{A}_1$	$\{+1,+1,+1,+1\}$	$\mathrm{diag}(+1,+1,+1,+1)\mathbf{A}_1$
00 ┊ 01	$\mathbf{A}_1$	$\{+1,+1,-1,-1\}$	$\mathrm{diag}(+1,+1,-1,-1)\mathbf{A}_1$
00 ┊ 10	$\mathbf{A}_1$	$\{-1,-1,+1,+1\}$	$\mathrm{diag}(-1,-1,+1,+1)\mathbf{A}_1$
00 ┊ 11	$\mathbf{A}_1$	$\{-1,-1,-1,-1\}$	$\mathrm{diag}(-1,-1,-1,-1)\mathbf{A}_1$
01 ┊ 00	$\mathbf{A}_2$	$\{+1,+1,+1,+1\}$	$\mathrm{diag}(+1,+1,+1,+1)\mathbf{A}_2$
01 ┊ 01	$\mathbf{A}_2$	$\{+1,+1,-1,-1\}$	$\mathrm{diag}(+1,+1,-1,-1)\mathbf{A}_2$
01 ┊ 10	$\mathbf{A}_2$	$\{-1,-1,+1,+1\}$	$\mathrm{diag}(-1,-1,+1,+1)\mathbf{A}_2$
01 ┊ 11	$\mathbf{A}_2$	$\{-1,-1,-1,-1\}$	$\mathrm{diag}(-1,-1,-1,-1)\mathbf{A}_2$
10 ┊ 00	$\mathbf{A}_3$	$\{+1,+1,+1,+1\}$	$\mathrm{diag}(+1,+1,+1,+1)\mathbf{A}_3$
10 ┊ 01	$\mathbf{A}_3$	$\{+1,+1,-1,-1\}$	$\mathrm{diag}(+1,+1,-1,-1)\mathbf{A}_3$
10 ┊ 10	$\mathbf{A}_3$	$\{-1,-1,+1,+1\}$	$\mathrm{diag}(-1,-1,+1,+1)\mathbf{A}_3$
10 ┊ 11	$\mathbf{A}_3$	$\{-1,-1,-1,-1\}$	$\mathrm{diag}(-1,-1,-1,-1)\mathbf{A}_3$
11 ┊ 00	$\mathbf{A}_4$	$\{+1,+1,+1,+1\}$	$\mathrm{diag}(+1,+1,+1,+1)\mathbf{A}_4$
11 ┊ 01	$\mathbf{A}_4$	$\{+1,+1,-1,-1\}$	$\mathrm{diag}(+1,+1,-1,-1)\mathbf{A}_4$
11 ┊ 10	$\mathbf{A}_4$	$\{-1,-1,+1,+1\}$	$\mathrm{diag}(-1,-1,+1,+1)\mathbf{A}_4$
11 ┊ 11	$\mathbf{A}_4$	$\{-1,-1,-1,-1\}$	$\mathrm{diag}(-1,-1,-1,-1)\mathbf{A}_4$

DSTSK   The special form of the UDSM scheme is equivalent to DSTSK. More specifically, the DSTSK modulation process embeds a single complex-valued symbol in a space-time codeword. This configurations is equivalent to the UDSM scheme having $\bar{M} = 1$. As mentioned in Section 3.2.1, the UDSM scheme has no limitation for $\bar{M}$ and hence achieves the flexible rate-diversity trade-off.

Binary DSM   The proposed UDSM scheme can be considered as a generalization of the conventional binary DSM scheme proposed in [126]. The DMs of the binary DSM have only non-zero elements of ones, namely, $a_{q,m} = 1$ ($1 \leq q \leq Q$, $1 \leq m \leq M$). The number of DMs Q is limited to $2^{\lfloor \log_2(M!) \rfloor}$, where $M! = M \cdot (M-1) \cdots 1$, due to the $a_{q,m} = 1$ limitation. For example, if we consider the $M = 3$ case, the number of DMs is defined by $Q = 2^{\lfloor \log_2(3!) \rfloor} = 2^{\lfloor 2.58... \rfloor} = 2^2 = 4$ and the DMs are given as follows.

$$\mathbf{A}_1 = \begin{bmatrix} 1 & 0 & 0 \\ 0 & 1 & 0 \\ 0 & 0 & 1 \end{bmatrix}, \mathbf{A}_2 = \begin{bmatrix} 1 & 0 & 0 \\ 0 & 0 & 1 \\ 0 & 1 & 0 \end{bmatrix}, \mathbf{A}_3 = \begin{bmatrix} 0 & 1 & 0 \\ 1 & 0 & 0 \\ 0 & 0 & 1 \end{bmatrix}, \mathbf{A}_4 = \begin{bmatrix} 0 & 0 & 1 \\ 0 & 1 & 0 \\ 1 & 0 & 0 \end{bmatrix}. \quad (3.8)$$

Furthermore, in the binary DSM codewords, the number of embedded symbols $\bar{M}$ is limited to M. This limitation imposes the diversity order of $D = 1$. In the UDSM codewords, no limitation is imposed for $a_{q,m}$, Q, and $\bar{M}$. The UDSM scheme supports the $Q > 2^{\lfloor \log_2(M!) \rfloor}$ case because $a_{q,m}$ is a complex value. For example, we consider the UDSM scheme having two DMs $\mathbf{A}_1$ and $\mathbf{A}_2$ where each DM has the same positions of non-zero elements. At the receiver, it can differentiate both DMs if the phases of non-zero elements are different.

$$\mathbf{A}_1 = \begin{bmatrix} \exp\left(\frac{\pi}{2}j\right) & 0 & 0 \\ 0 & 0 & \exp\left(\frac{\pi}{6}j\right) \\ 0 & \exp\left(\frac{\pi}{3}j\right) & 0 \end{bmatrix}, \mathbf{A}_2 = \begin{bmatrix} \exp\left(\frac{\pi}{4}j\right) & 0 & 0 \\ 0 & 0 & \exp\left(\frac{\pi}{2}j\right) \\ 0 & \exp(\pi j) & 0 \end{bmatrix}.$$

3.2.3   Dispersion Matrix Design Criteria

The performance of the UDSM scheme depends on the DM construction. The bad DM construction leads to a less coding gain or a less diversity order. In this subsection, design criteria for DMs and its construction method are described. Throughout this section, we employed the RDC [20] to maximize the coding gain. The other criteria are available for the UDSM scheme design, which are detailed in Section 2.2. Before the design process, the number of transmit antennas M and the transmittion rate R are assumed to be given. The DM search process consists of the following three steps.

1. According to the given parameters M and R, determine the number of DMs Q and the size of constellations $\mathbf{L} = [\mathcal{L}_1, \cdots, \mathcal{L}_{\bar{M}}]$. The performance of the UDSM improves with increasing Q, which also increases the computational complexity.

2. For the $Q \leq M!$ case, optimize the positions of non-zero elements in each DM $\mathbf{A}_q$ ($q = 1, \cdots, Q$) so as to maximize the minimum Hamming distance between $\mathbf{A}_q$ and $\mathbf{A}_{q'}$ ($q' = 1, \cdots, Q$). Here, $M \cdot Q$ number of non-zero elements is temporally assumed to be $a_{q,m} = 1$. For the $Q > M!$ case, the positions are jointly optimized with the next step.

3. Optimize the phases of non-zero elements $a_{q,m}$, where its norm is constrained to $|a_{q,m}| = 1$, so as to maximize the designate criterion such as the RDC and constrained AMI [20].

The number of possible activation patterns for Step. 2 is given by $\binom{M!}{Q}$. For example, if we have $(M,Q) = (4,16)$, there are $\binom{4!}{16} = 735471$ candidates for non-zero positions[1].

---

[1] If we limit the number of DMs $Q = M$, an algebraic construction method is available in [7].

3.3   Optimal ML Detector

The detection process at the receiver is the same with the conventional schemes described in Section 2.4. As described in Section 3.2, the UDSM scheme maps input bits $\mathbf{b}(i)$ having a length of B to the selected DM $\mathbf{A}_q$ and the modulated PSK symbols $s_1, s_2, \cdots, s_{\bar{M}}$. Based on the received symbol $\mathbf{Y}(i)$, the receiver estimates both the activated DM and the modulated symbols $(\hat{q}, \hat{s}_1, \cdots, \hat{s}_{\bar{M}})$. The ML detector for the UDSM scheme is given by

$$
\begin{aligned}
(\hat{q}, \hat{s}_1, \cdots, \hat{s}_{\bar{M}}) &= \arg \min_{(q, s_1, \cdots, s_{\bar{M}})} \left\| \mathbf{Y}(i) - \mathbf{Y}(i-1) \operatorname{diag}(s_1, \cdots, s_{\bar{M}}) \mathbf{A}_q \right\|_{\mathrm{F}}^2 \\
&= \arg \min_{(q, s_1, \cdots, s_{\bar{M}})} \| \mathbf{Y}(i) - \mathbf{Y}(i-1) \mathbf{X}(i) \|_{\mathrm{F}}^2 .
\end{aligned}
\tag{3.9}
$$

3.3.1   Theoretical BER Upper-Bound

The PEP of the differential MIMO scheme is given by [48]

$$
\mathrm{PEP}(\mathbf{X} \rightarrow \mathbf{X}') \leq \left(1 + \frac{1}{4\sigma_v^2} \left| \left(\Phi_k^0 \right)^* \Pi_{\Phi_k^{\mathrm{T}}}^{\perp} \left(\Phi_k^0 \right)^{\mathrm{T}} \otimes \mathbf{I}_N \right|^{\frac{1}{MN}} \right)^{-MN} ,
\tag{3.10}
$$

where we have

$$
\begin{cases}
\Phi_k^0 & = \operatorname{concat}(\mathbf{X}, \mathbf{I}_M) \\
\Phi_k & = \operatorname{concat}(\mathbf{X}', \mathbf{I}_M) \\
\Pi_{\Phi_k^{\mathrm{T}}}^{\perp} & = \mathbf{I}_{2M} - \Phi_k^{\mathrm{T}} \left(\Phi_k^* \Phi_k^{\mathrm{T}} \right)^{-1} \Phi_k^*
\end{cases}
.
\tag{3.11}
$$

In Eq. (3.11), concat($\cdot$) represents the matrix concatenation function. For example, concat($\mathbf{I}_2, \mathbf{I}_2$) is calculated as follows:

$$
\operatorname{concat}(\mathbf{I}_2, \mathbf{I}_2) = \begin{bmatrix} 1 & 0 & 1 & 0 \\ 0 & 1 & 0 & 1 \end{bmatrix} .
\tag{3.12}
$$

Finally, the upper-bound of the BER is calculated by Eq. (2.12), where the PEP function in Eq. (2.12) is replaced by Eq. (3.10). Generally, the theoretical analysis of the differential MIMO scheme is difficult due to the complex expression observed in Eq. (3.10). For the binary DSM scheme having $M = 2$, which is described in Section 2.4.1, its theoretical BER was derived in [125].

Table 3.3 Simulation parameters of the conventional and proposed DSM schemes.

Number of transmit antennas	$M = 2, 3, 4, 8, 16, 32, 64$
Number of receive antennas	$N = 1, 4$
Symbol duration in a space-time codeword	M
Number of DMs	$Q = 2, 4, 8, 16$
Number of activated DMs	1
Modulation	BPSK, QPSK, 16–PSK
Channel	Frequency-flat Rayleigh, Rician, Jakes fading
Number of scatterers	$N_s = 8$
Normalized Doppler frequency	$F_d T_s = 1.0 \times 10^{-4}, 7.5 \times 10^{-3}, 3.0 \times 10^{-2}$
Detector	Maximum-likelihood detection

3.3.2   Computational Complexity

We evaluate the computational complexity of the ML detection process of Eq. (3.9). The receiver estimates the DM index and the transmitted symbols $(\hat{q}, \hat{s}_1, \cdots, \hat{s}_{\bar{M}})$ through 2^{RM} number of trials, which is the same with the DSTBC case, as shown in Section 2.4.3. In each trial, the matrix multiplication of $\mathbf{Y}(i-1)\mathbf{X}(i)$ includes $N \cdot M$ number of complex-valued multiplications, which is equivalent to $4NM$ number of real-valued multiplications. In addition, the Frobenius norm calculation of $\|\mathbf{Y}(i) - \mathbf{Y}(i-1)\mathbf{X}(i)\|_{\mathrm{F}}^2$ includes $2NM$ number of real-valued multiplications. Hence, the computational complexity for the UDSM scheme is given by $2^{RM} \cdot 6NM \approx O(2^{RM}NM)$. The derived complexity $O(2^{RM}NM)$ is smaller than that of the general DSTBC $O(2^{RM}NM^2)$ because of the sparse structure of UDSM. With the aid of the sparse codewords, the number of real-valued calculations are reduced by the factor of M. Note that this improvement was obtained by ignoring the zero multiplications, namely, a complex value multiplied by $0 + j0$ has to be $0 + j0$.

3.4   Performance Results

In this section, the performance of the UDSM scheme was evaluated with numerical simulations. In order to perform fair comparisons, the transmission energy and rate of all schemes were unified. The simulation parameters considered in this section are given in Table 3.3. We assumed the frequency-flat Rayleigh fading as well as Rician fading. We employed the hard ML detector at the receiver of Eq. (3.9).
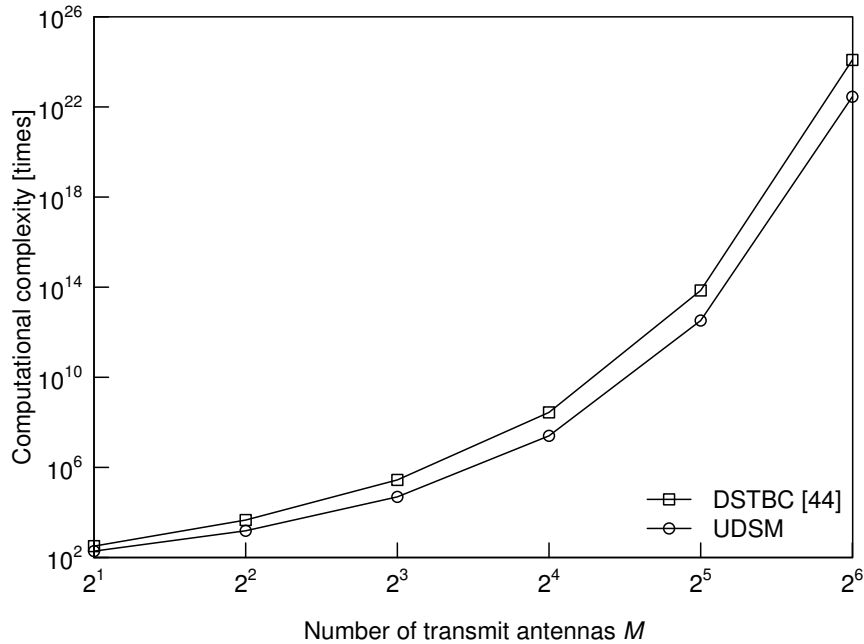
Figure 3.3 Computational complexity comparison between the general DSTBC and the proposed UDSM, where the number of transmit antennas M was set to $2^1, \cdots, 2^6$. The number of receive antennas was constrained to $N = 4$. The transmission rate was $R = 1.0$ [bits/symbol].

3.4.1 Complexity

Fig. 3.3 shows the computational complexity comparison. As described in Section 2.2.3, the computational complexity is assumed to be equal to the number of real-valued multiplications. In Fig. 3.3, the complexities of the general DSTBC and the proposed UDSM schemes were considered, where both complexities were provided in Sections 2.4.3 and 3.3.2, respectively. As shown in Fig. 3.3, the complexity of the UDSM scheme was continuously lower than that of the conventional DSTBC. This complexity improvement was obtained with the aid of the sparse space-time codewords of UDSM, where there is only one element in its column and row.

3.4.2 BER in Uncoded Scenarios

The BER performance of the UDSM scheme was evaluated with Monte-Carlo simulations. Here, no channel coding scheme was considered. The DMs of the UDSM scheme were obtained through the exhaustive search, as described in Section 3.2.3, so as to maximize the RDC. The obtained DMs are available in Appendix A.3. Throughout the simulations, the number of receive antenna was set to $N = 1$ for simplicity.

Figure 3.4 BER comparisons between the BPSK-aided UDSM and the conventional binary DSM, where $(M,Q) = (2,2)$. The BER curve of the coherent ASTSK was plotted for reference. The transmission rate was set to $R = 1.5$ [bits/symbol]. 10^7 bits were randomly generated at each SNR point.

Fig. 3.4 shows the BER comparisons between the proposed UDSM and conventional binary DSM. The BER curve of the ASTSK scheme [150] was simulated in coherent scenario, where the perfect channel coefficients were assumed to be available at the receiver. The number of transmit antennas and DMs were set to $(M,Q) = (2,2)$, respectively. Each scheme embeds two BPSK symbols in a space-time codeword, namely, $\mathbf{L} = [\mathcal{L}_1, \mathcal{L}_2] = [2,2]$. Here, the transmission rate can be calculated to $(\log_2 \mathcal{L}_1 + \log_2 \mathcal{L}_2 + \log_2 Q)/M = 3/2 = 1.5$ [bits/symbol]. It was shown in Fig. 3.4 that the performance gap between UDSM and ASTSK was exactly 3 [dB], which meant that the UDSM scheme had no performance loss without the noise-doubling effects. In contrast, the performance gap between Binary DSM and ASTSK was 8 [dB]. The performance gain of the UDSM scheme was achieved without any additional complexity, since the only difference lay on the construction of DMs.

Fig. 3.5 shows the effects of channel correlations on reliability. All simulation parameters were the same with those shown in Fig. 3.4 except for the channel environment. In Figs. 3.5(a) and (b), the channel matrix followed the correlated Rayleigh fading, which was described in Section 1.1, while in Fig. 3.4 the channel matrix followed the i.i.d. Rayleigh fading. The correlation coefficients κ were assumed to be (a) $\kappa = 0.7$ and (b) $\kappa = 0.9$, which were equivalent to the two transmit antennas separated with 0.181620λ and 0.100000λ. As shown
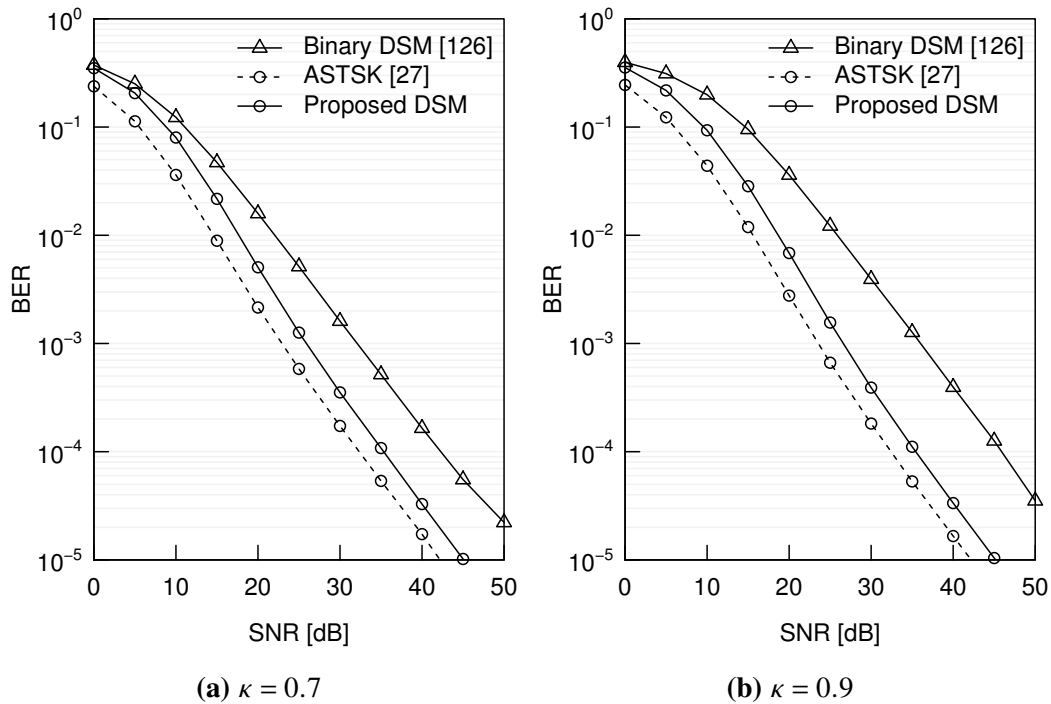
Figure 3.5 Effects of channel correlations. The channel correlation coefficients were set to (a) $\kappa = 0.7$ and (b) $\kappa = 0.9$. All simulation parameters except for the channel coefficients were the same with those shown in Fig. 3.4.

in Fig. 3.5, the performance gap between ASTSK and UDSM was exactly 3 [dB]. In contrast, the BER performance of the binary DSM decayed with increasing κ. The performance gaps between ASTSK and the binary DSM were (a) 8 [dB] and (b) 10 [dB], respectively.

Fig. 3.6 shows the effects of line-of-sight paths in channels. Similar to Fig. 3.5, only the channel environment is modified from Fig. 3.4. The definition of Rician fading is detailed in Section 1.1. The Rician factor was set to $K = 5$ [dB], namely, the power ratio of line-of-sight elements was 83%. As shown in Fig. 3.6, the gap between ASTSK and UDSM was 3 [dB], similar to Fig. 3.5. In contrast, the performance of the conventional binary DSM decayed with a gap of 16 [dB]. The coding gains were different from each other, while the diversity orders of all schemes were the same.

Fig. 3.7 shows the effects of Doppler frequency on the binary and proposed DSM schemes, where the Jakes channel having $N_s = 8$ was considered. In Fig. 3.7, the normalized Doppler frequency was changed from $F_d T_s = 1.0 \times 10^{-4}$ to 3.0×10^{-2} [151, 152]. The details of Jakes fading is found in Section 1.1. As shown in Fig. 3.7, both the binary and proposed DSM schemes exhibited error floors for the $F_d T_s \geq 7.5 \times 10^{-3}$ scenarios. Upon increasing the normalized Doppler frequency, the performance advantages of the proposed scheme were maintained.
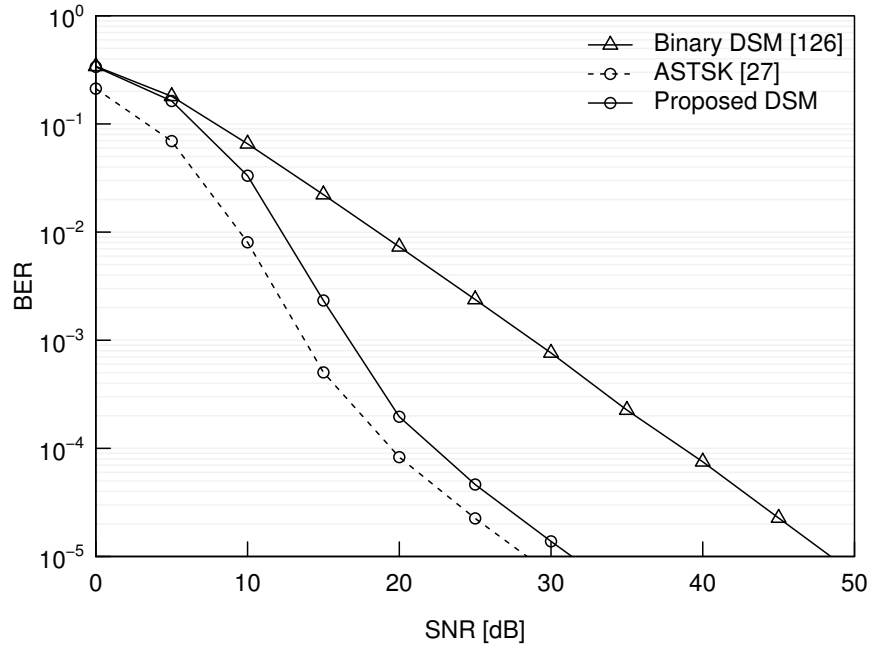
Figure 3.6 Effects of Rician channels. The Rician factor was set to $K = 5$ [dB]. All simulation parameters except for the channel coefficients were the same with those shown in Fig. 3.4.
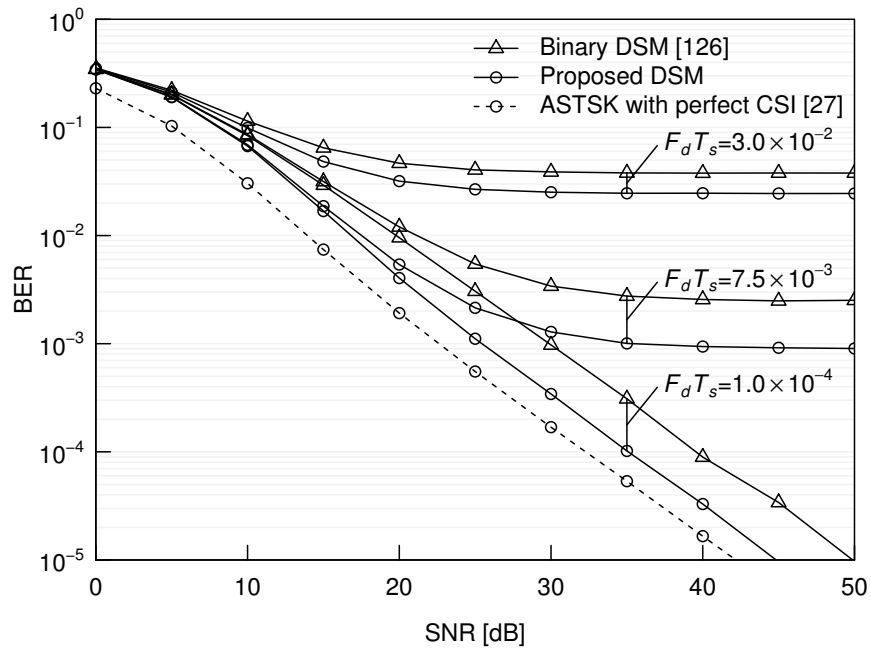
Figure 3.7 Effects of Jakes channels, where the number of scatterers $N_s = 8$. The normalized Doppler frequency was set to $F_d T_s = 1.0 \times 10^{-4}$, 7.5×10^{-3}, and 3.0×10^{-2}. All simulation parameters except for the channel coefficients were the same with those shown in Fig. 3.4.
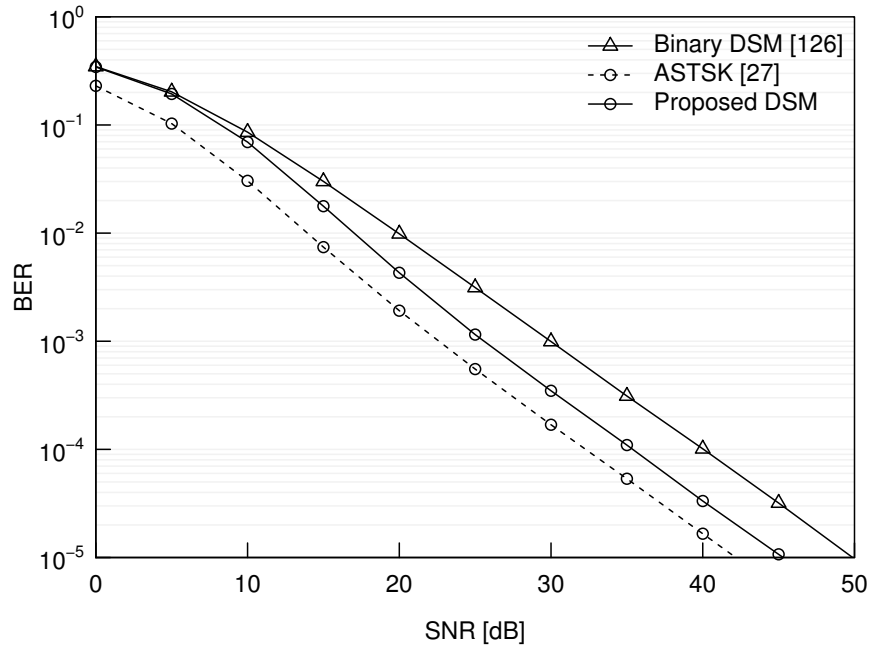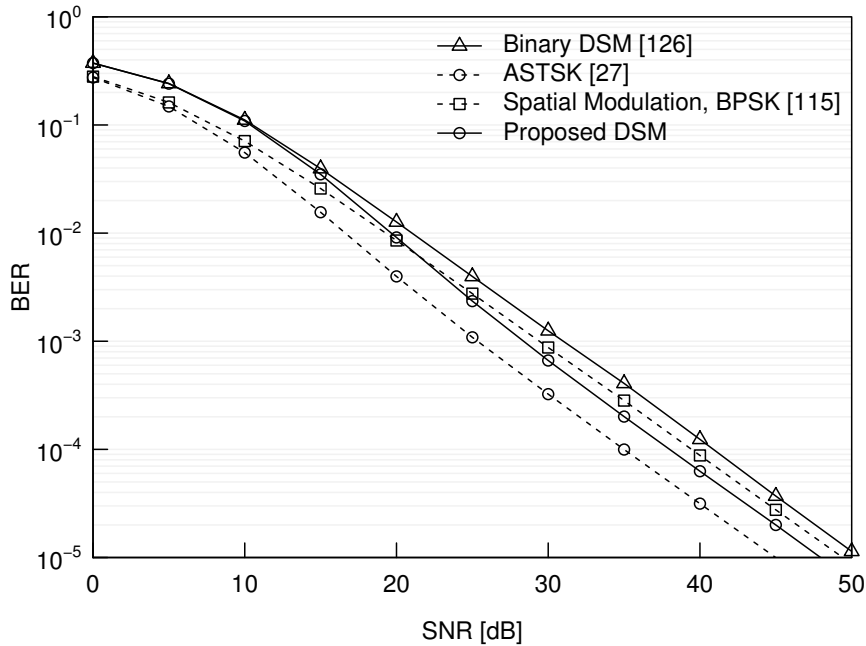
Figure 3.8 BER comparisons between the **L** = [2,4] aided UDSM and the conventional binary DSM, where $(M,Q) = (2,2)$. The BER curve of the BPSK-aided SM was plotted for reference. The transmission rate was set to $R = 2.0$ [bits/symbol]. 10^7 bits were randomly generated at each SNR point.

Fig. 3.8 shows the BER comparisons between the proposed UDSM and conventional binary DSM. The BER curve of the BPSK-aided SM scheme was simulated in a coherent scenario. The number of transmit antennas and DMs were set to $(M,Q) = (2,2)$, respectively. The UDSM scheme embeds a BPSK symbol and a QPSK symbol in s space-time codeword, namely, $\mathbf{L} = [\mathcal{L}_1,\mathcal{L}_2] = [2,4]$. Here, the transmission rate can be calculated to $(\log_2 \mathcal{L}_1 + \log_2 \mathcal{L}_2 + \log_2 Q)/M = 4/2 = 2.0$ [bits/symbol]. The transmission rate of the SM scheme was $\log_2 (M\mathcal{L}) = \log_2 4 = 2.0$ [bits/symbol], which is the same with the UDSM scheme. It was shown in Fig. 3.8 that the performance gap between UDSM and ASTSK was exactly 3 [dB]. In contrast, the performance gap between Binary DSM and ASTSK was 5 [dB]. In the high SNR region, which is greater than SNR = 22 [dB], the UDSM scheme simulated in a non-coherent scenario performed better than the SM scheme simulated in a coherent scenario. This incoherence was caused by the different structures of UDSM and SM. The codewords of UDSM are unitary matrices, while those of SM are vectors.

Fig. 3.9 shows the BER comparisons between the proposed UDSM and conventional binary DSM. The BER curve of the QPSK-aided SM scheme was simulated in a coherent scenario. As compared to Fig. 3.8, the transmission rate was increased from $R = 2.0$ to $R = 3.5$ [bits/symbol]. The UDSM scheme embeds two 8–PSK symbol in s space-time
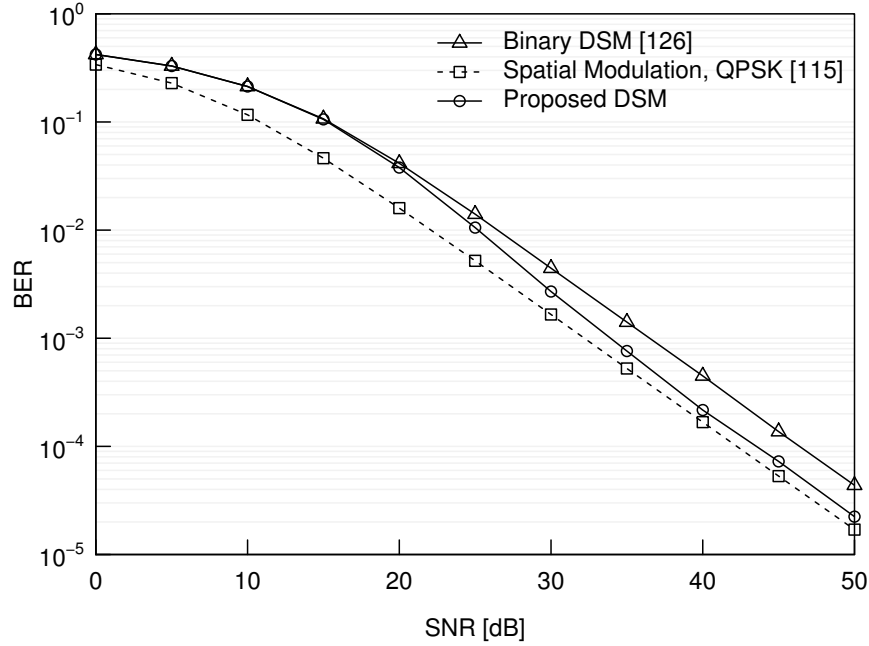
Figure 3.9 BER comparisons between the $\mathbf{L} = [8,8]$ aided UDSM and the conventional binary DSM, where $(M,Q) = (2,2)$. The BER curve of the QPSK-aided SM was plotted for reference. The transmission rate was set to $R = 3.5$ [bits/symbol]. 10^7 bits were randomly generated at each SNR point.

codeword, namely, $\mathbf{L} = [\mathcal{L}_1, \mathcal{L}_2] = [8,8]$. Here, the transmission rate can be calculated to $(\log_2 \mathcal{L}_1 + \log_2 \mathcal{L}_2 + \log_2 Q)/M = 7/2 = 3.5$ [bits/symbol]. The transmission rate of the SM scheme was $\log_2 (M\mathcal{L}) = \log_2 8 = 3.0$ [bits/symbol], which was plotted for a reference. The performance gap between UDSM and binary DSM was 3.0 [dB]. Throughout the simulations, it was observed that the performance gap between UDSM and SM increased with the increase in the transmission rate R.

Fig. 3.10 compares the achievable diversity order of the proposed UDSM scheme. The BER curves of the differential QPSK and the BPSK aided binary DSM were plotted for reference. The red and dotted lines in Fig. 3.10 represent the BER upper bounds [48] of the DSM schemes. The conventional binary DSM embeds four BPSK symbols, namely, $\mathbf{L} = [\mathcal{L}_1, \mathcal{L}_2, \mathcal{L}_3, \mathcal{L}_4] = [2,2,2,2]$. The proposed UDSM has a flexibility that controls the rate-diversity trade-off, which is detailed in Section 3.2.1. If we aim at the diversity order of four, the constellations of $\mathbf{L} = [(16,16,16,16)]$ are available, which embed $\bar{M} = 1$ 16–PSK symbol in a space-time codeword. If we also aim at the diversity order of two, the constellations of $\mathbf{L} = [(4,4),(4,4)]$ are available, which embed $\bar{M} = 2$ QPSK symbols in a space-time codeword. The transmission rate of each setting is the same, i.e. $\log_2 (Q \cdot \mathcal{L}_1 \cdots \mathcal{L}_{\bar{M}})/M = \log_2(256)/4 = 2.0$ [bits/symbol]. It was shown in Fig. 3.10 that the differential QPSk performed better than
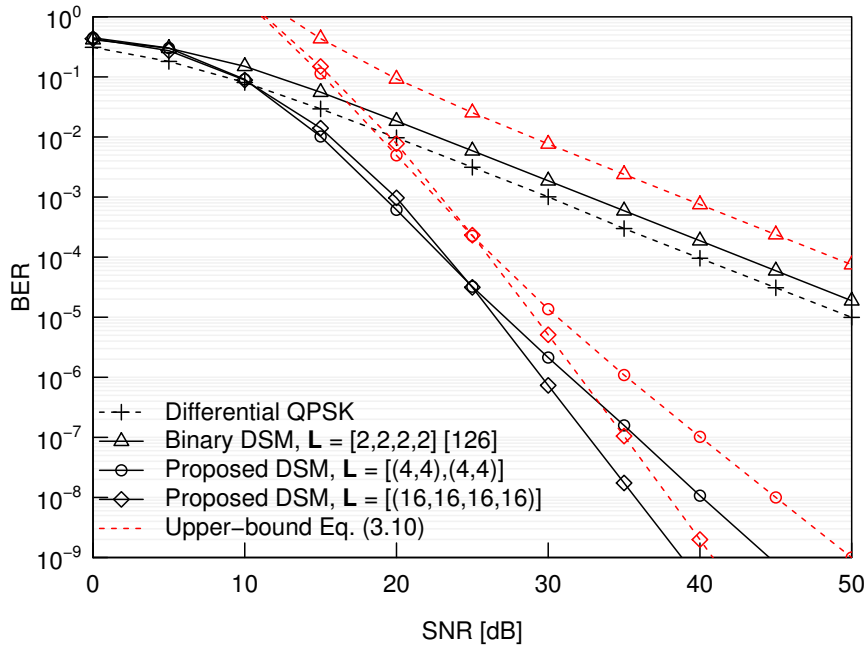
Figure 3.10 Flexible diversity of the $(M,Q) = (4,16)$ aided UDSM scheme. The number of embedded symbols was set to $\bar{M} = 1$ and 2. The BER curve of the differential QPSK was plotted for reference. The transmission rate was set to $R = 2.0$ [bits/symbol]. 10^{11} bits were randomly generated at each SNR point. The upper bounds were calculated based on Eq. (3.10).

the binary DSM. In the low SNR region, which was smaller than 10 [dB], all of the DSM schemes performed worse than the differential QPSK. The UDSM scheme having $\bar{M} = 1$ and 2 achieved higher diversity orders as expected. The simulated BER values of the DSM schemes matched with the analytical values of [48].

Fig. 3.11 shows the BER comparisons between UDSM and the single-RF NCGSM. The NCGSM schemes are detailed in Section 2.4.2. Both the UDSM and the single-RF NCGSM schemes were proposed for reduced-RF transmitters. The difference between both schemes can be highlighted by the structure of codewords: diagonal and sparse matrices. The number of transmit antennas was set to $M = 2,3,4$, while the number of receive antennas N was constrained to 1. In Fig. 3.11, the BER curves of the binary DSM were not listed because its transmission rate could not be adjusted to $R = 1.0$ [bits/symbol]. It was shown in Fig. 3.11 that the diversity orders of both UDSM and the single-RF NCGSM were improved as increasing the number of transmit antennas M. The performance gaps between UDSM and the single-RF NCGSM increased with an increase in M. More specifically, the gaps were 1, 2, and 3 [dB], which were associated with $M = 2, 3,$ and 4. The MED of the UDSM symbols was higher than that of the single-RF NCGSM.
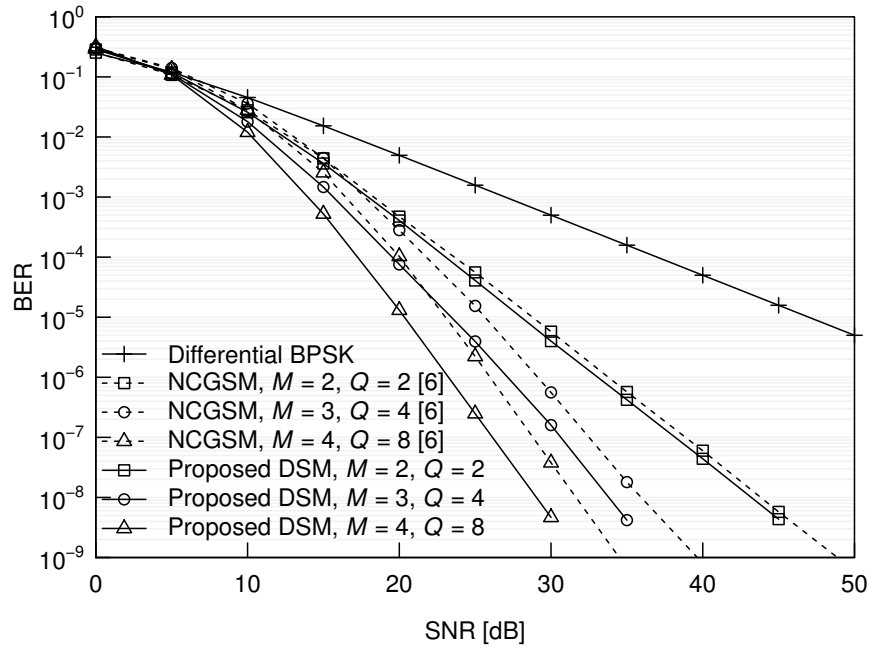
Figure 3.11 BER comparisons between the proposed UDSM and the conventional single-RF NCGSM, where $(M,Q) = (2,2),(3,4),(4,8)$. The BER curve of the differential BPSK was plotted for reference. The transmission rate was set to $R = 1.0$ [bits/symbol]. 10^{11} bits were randomly generated at each SNR point.

3.5 Chapter Conclusions

In this chapter, we proposed the flexible UDSM architecture.By changing the number of embedded symbols, the proposed UDSM scheme achieves the flexible trade-off between the transmission rate and the diversity order. The UDSM scheme is a differential counterpart of the SM scheme, where there is no need to estimate channel coefficients at the receiver. The reduced-RF operation contributes to increasing the number of transmit antennas, so as to maximize the performance of MIMO wireless systems. Our complexity comparisons showed that the computational complexity of the UDSM scheme is lower than that of the conventional DSTBCs with the aid of the sparse codewords. Our BER comparisons in uncoded scenarios demonstrated that the diversity order and the coding gain of the UDSM scheme were higher than those of the conventional schemes.

Chapter 4

Permutation Modulation Based MIMO Millimeter-Wave Communications

4.1 Introduction

In this chapter, the PM concept is applied to mmWave communications. As mentioned in Chapter 1, the available radio spectrum below 5 [GHz], which is mainly allocated for current wireless networks, such as cellular and Wi-Fi networks, is overloaded due to the popularization of mobile devices. One of the promising solutions for this problem is that we alternatively facilitate the mmWave frequencies over 30 up to 300 [GHz].

The sophisticated and cost-effective electronic technologies have enabled wireless communications operated at mmWave frequency bands spanning from 30 to 300 [GHz]. The corresponding wavelength ranges from 1 to 10 [mm][1]. The major benefit of mmWave communications is the wider bandwidth. The resultant channel capacity may increase as compared to the current mobile networks. However, mmWave suffers the large propagation losses due to its short wavelength [53]. In order to compensate this large path-loss problem, the mmWave transmitter and receiver in the literature have relied on the BF gain obtained with a larger number of antenna elements. Here, it is unrealistic for commercial devices to equip a large number of RF circuits, since the RF circuit designed for mmWave frequencies is complicated and power-consuming [58].

The hybrid BF scheme that joins the analog BF and the digital BF have been proposed [58, 60] for reducing the number of RF chains. Specifically, the hybrid scheme groups the

---

[1]The speed of light divided by 30 [GHz] is approximately 9.993 [mm].
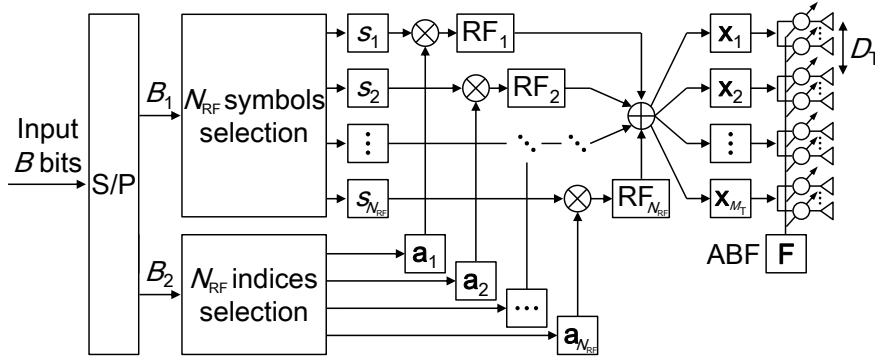
Figure 4.1 The schematic of our proposed GSM-based transmitter, which contains $N_{\mathrm{RF}} < M_{\mathrm{T}}$ number of RF chains. The symbol vector $\mathbf{x}$ is multiplied by an ABF array. Each subarray is separated by D_{T}.

large antenna array into subarrays and each subarray is connected to an RF circuit. The subarrays carry out the analog BF, while the RF circuits carry out the digital BF. This hybrid structure reduces the number of RF chains both at the transmitter and the receiver. Even when employing the hybrid structure, the conventional spatial-multiplexing scheme requires a number of RF chains, as we increase the spatial multiplexing gain. This substantial problem makes it difficult to increase the effective throughput of MIMO mmWave systems.

Against this backcloth, we investigate the achievable performance of the PM scheme applied to the mmWave domain, where the GSM scheme is invoked for reducing the complexity of the MIMO mmWave transmitter. We reveal that the proposed GSM transmitter is capable of reducing the number of RF chains, while maintaining the near-capacity performance.

The remainder of this chapter is organized as follows. Section 4.2 explains the system model of the GSM-based mmWave transmitter, which further reduces the number of RF circuits at the transmitter. Section 4.2.1 provides the channel model assumed in this chapter. Sections 4.3.1 and 4.3.2 provide the alignment of analog phase shifters and their optimal phase weights in terms of the rank of channel matrices. Finally, Section 4.5 concludes this chapter.

4.2   System Model

Let us consider a GSM transmitter that has N_{T} number of antenna elements and the same number of analog phase shifters. The transmit antennas are grouped into M_{T} groups of subarrays and each subarray has $U_{\mathrm{T}} = N_{\mathrm{T}}/M_{\mathrm{T}}$ antenna elements. The transmitter has $N_{\mathrm{RF}} < M_{\mathrm{T}}$ number of RF chains, while the conventional BLAST scheme requires full $N_{\mathrm{RF}} = M_{\mathrm{T}}$ RF

chains. Here, with the aid of the GSM concept, the number of RF chains is reduced from M_T to $N_{RF} < M_T$, which simplifies the complexity of the MIMO mmWave transmitter.

Fig. 4.1 shows the schematic of our GSM transmitter. The symbol vector $\mathbf{x} \in \mathbb{C}^{M_T \times 1}$ ($\|\mathbf{x}\|^2 = 1$) is constructed by the input B bits based on the GSM(M_T, N_{RF}) encoding, which is described in Section 2.3.2. The SM family suffers the antenna switching problem [98], which reduces the effective transmission rate. Note that in mmWave communications, this problem is relaxed because a wider bandwidth is available as compared to the communications operated below 5 [GHz]. In advance of transmissions, the symbol vector $\mathbf{x}$ is precoded by an ABF $\mathbf{F} = \text{diag}(\mathbf{f}_1, \cdots, \mathbf{f}_{M_T}) \in \mathbb{C}^{N_T \times M_T}$ [63, 153], where diag($\bullet$) represents the block diagonalization and $\mathbf{f}_i \in \mathbb{C}^{U_T \times 1}$ ($1 \le i \le M_T$) represents a weight vector of the ith ABF at the transmitter, which has the constraint of $\|\mathbf{f}_i\|^2 = 1$.

The receiver has N_R number of antenna elements, which are grouped into M_R groups of subarrays. Then, each subarray consists of $U_R = N_R/M_R$ antenna elements, similar to the transmitter's parameters (N_T, M_T, U_T). We assume that the receiver is equipped with the full-RF structure of $N_{RF} = M_R$. The received symbols are given by

$$\mathbf{y} = \underbrace{\mathbf{W}^H \mathbf{H} \mathbf{F}}_{\mathbf{H}_b} \mathbf{x} + \mathbf{v} \in \mathbb{C}^{M_R \times 1}, \tag{4.1}$$

where $\mathbf{H} \in \mathbb{C}^{N_R \times N_T}$ and $\mathbf{v} \in \mathbb{C}^{M_R \times 1}$ represent the channel matrix and the AWGN $\mathcal{CN}(0, \sigma_v^2)$. Here, the received SNR is defined by $1/\sigma_v^2$. The ABF weights $\mathbf{W} = \text{diag}(\mathbf{w}_1, \cdots, \mathbf{w}_{M_T}) \in \mathbb{C}^{N_R \times M_R}$ [63, 153] are associated with the analog phase shifters embedded in the receiver. Similar to the ABF weights $\mathbf{F}$ at the transmitter, $\mathbf{w}_k \in \mathbb{C}^{U_R \times 1}$ ($1 \le k \le M_R$) represents a weight vector of the kth ABF at the receiver and each weight $\mathbf{w}_k$ has the constraint of $\|\mathbf{w}_k\|^2 = 1$. In Eq. (4.1), $\mathbf{H}_b$ denotes the channel equivalent matrix, which consists of $\mathbf{W}$, $\mathbf{F}$, and $\mathbf{H}$. In this chapter, we assume that the accurate estimates of $\mathbf{H}_b$ can be obtained at the receiver, since the ABF weights $\mathbf{W}$ and $\mathbf{F}$ are calculated by the direction between the transmitter and the receiver. Note that it is a challenging task to obtain the accurate estimates of $\mathbf{H}$, as will be described in Section 4.3.2.

The MLD of the proposed GSM-based receiver is given by

$$\hat{\mathbf{x}} = \arg\min_{\mathbf{x}} \|\mathbf{y} - \mathbf{H}_b \mathbf{x}\|^2, \tag{4.2}$$

which is the same with the conventional MLD proposed in [104]. Hence, the low-complexity detectors [124, 154, 155] proposed for the GSM scheme are applicable to the proposed GSM-based mmWave receiver.
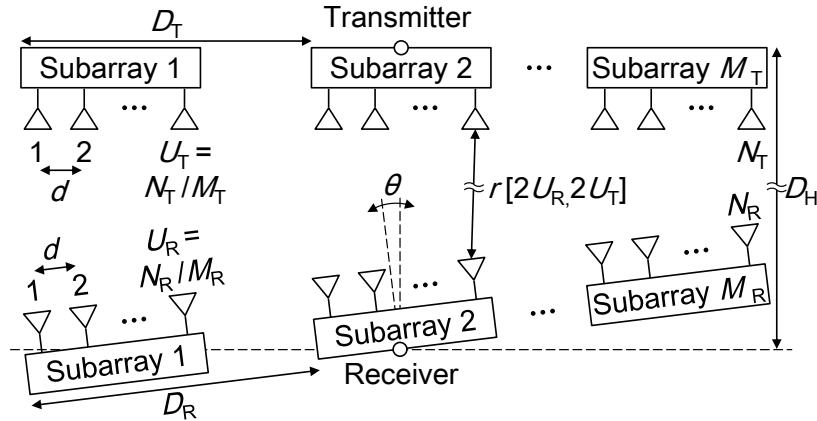
Figure 4.2 The physical arrangement of transmitter and receiver.

4.2.1   Channel Model

We consider the indoor and LoS-dominant mmWave communications [156, 52, 63, 153, 100], instead of outdoor or non-LoS channel environments. Throughout our simulations, we employ the frequency-flat Rician channel model. Fig. 4.2 shows the arrangement of transmitter and receiver, including the antenna elements and the ABF arrays. Each ABF array is separated by a spacing of D_T or D_R [m]. Also, each antenna element embedded in an ABF array is spaced with d [m]. The transmitter and the receiver are separated by a length of D_H [m]. The receiver is tilted at an angle of θ.

The channel matrices that follow the Rician fading channels are given by [62, 63, 100]:

$$\mathbf{H} = \sqrt{\frac{K}{K+1}}\mathbf{H}_{\text{LoS}} + \sqrt{\frac{1}{K+1}}\mathbf{H}_{\text{NLoS}} \in \mathbb{C}^{N_R \times N_T}, \qquad (4.3)$$

where K is the Rician factor, which represents the power ratio of LoS elements over non-LoS elements. It was reported in [156] that, in 60 [GHz] indoor communications scenarios, the Rician factor K was in the range between 8.34 and 12.04 [dB]. In Eq. (4.3), the nth row and mth column of $\mathbf{H}_{\text{LoS}}$ is defined by $\mathbf{H}_{\text{LoS}}[n,m] = \exp\left(-j \cdot (2\pi/\lambda) \cdot r[n,m]\right)$, where $r[n,m]$ is the distance between the mth transmit antenna element and the nth receive antenna element. Here, λ represents the wavelength of the transmitted signal. Also, the nth row and mth column of $\mathbf{H}_{\text{NLoS}}$ obeys the complex-valued Gaussian distribution of $\mathcal{CN}(0,1)$.

4.3   Optimal Design

4.3.1   Optimal Array Alignment

At the transmitter, a large number of antenna elements are packed in a small area in order to obtain the BF gain. Typically, the rank of the channel matrix of indoor mmWave communications is low because of the slight difference between the adjacent channel coefficients. In such a low-rank scenario, the performance gains offered by the MIMO technologies may decrease. In the literature, the optimum antenna alignment scheme has been proposed [62], which mitigates the above low-rank problem. The alignment criterion of [62] recovers the rank of the channel matrix in MIMO mmWave communications. In order to attain the optimum performance in terms of maximizing the channel rank, the separations of the ABFs D_T and D_R have to satisfy the following relationship: [62, 63, 153]

$$D_T D_R = \frac{\lambda R}{\max(M_T, M_R)\cos(\theta)}. \tag{4.4}$$

Note that the parameters λ, θ and D_H in Eq. (4.4) are given in Section 4.2.1. With the aid of Eq. (4.4), the channel rank is recovered to rank$(\mathbf{H}) = \min(M_T, M_R)$.

For example, if we have the transmitter height of $D_H = 5$ [m], the receiver tilt of $\theta = 0°$, and the carrier-frequency of 60 [GHz], its wavelength is calculated by 0.5 [cm]. Here, the spacing between antenna elements embedded in each subarray is calculated by $d = \lambda/2 = 0.25$ [cm]. Also, we consider having $N_T = N_R = 16$, $M_T = M_R = 4$, and $D_T = D_R$. Then, based on Eq. (4.4), the spacing between subarrays is derived by

$$D_T = D_R = \sqrt{\frac{\lambda D_H}{\max(M_T, M_R)\cos(\theta)}} = \sqrt{\frac{0.005 \times 5}{\max(4,4)\cos(0)}} \approx 7.91 \text{ [cm]}.$$

Fig. 4.3(a) illustrates the above $D_T = D_R = 7.91$ [cm] case, where we have $(N_T, M_T, N_R, M_R) = (16, 4, 16, 4)$. Furthermore, if we consider having $(N_T, M_T, N_R, M_R) = (32, 8, 16, 4)$, the spacing between subarrays is calculated by $D_T = D_R = 5.59$ [cm], which is illustrated in Fig. 4.3(b). In both cases, the mean rank of channel matrices is equal to E[rank$(\mathbf{H})] = \min(M_T, M_R) = 4$.

4.3.2   Beamforming Weights

In this section, we review the construction of ABF weights $\mathbf{F} = \text{diag}(\mathbf{f}_1, \cdots, \mathbf{f}_{M_T}) \in \mathbb{C}^{N_T \times M_T}$ and $\mathbf{W} = \text{diag}(\mathbf{w}_1, \cdots, \mathbf{w}_{M_T}) \in \mathbb{C}^{N_R \times M_R}$ proposed in [63, 153]. If we assume that the trans-
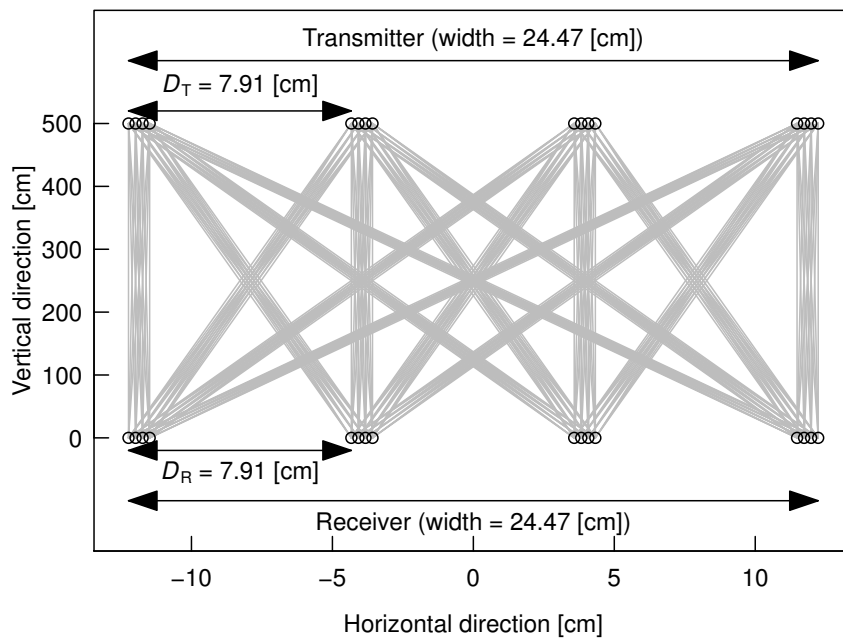
(a) $(N_T, M_T, N_R, M_R) = (16, 4, 16, 4)$.
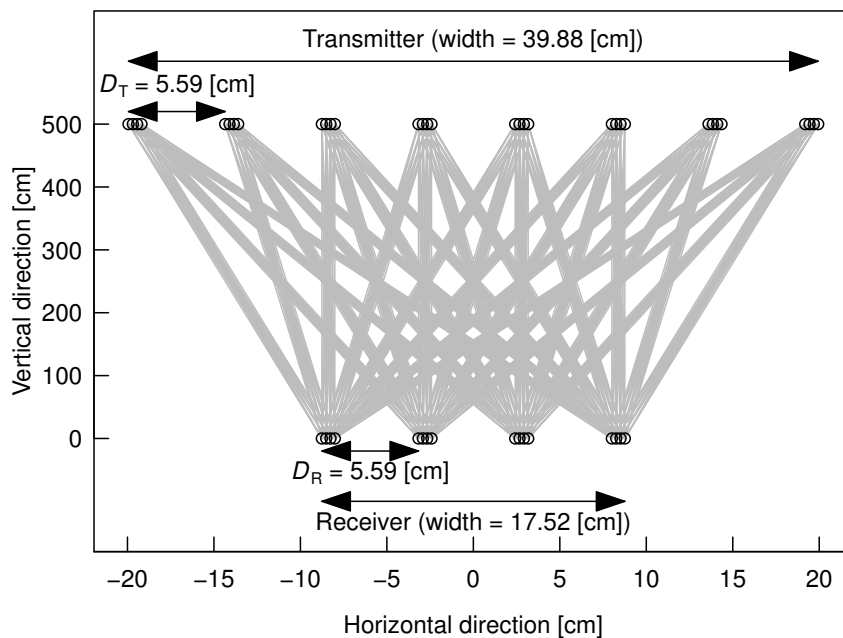
(b) $(N_T, M_T, N_R, M_R) = (32, 8, 16, 4)$.

Figure 4.3 Examples of ABF arrangement, where we have $(D_H, \lambda, d) = (500, 0.50, 0.25)$ [cm].

mitter obtains the perfect estimates of $\mathbf{H}$, it is possible to carry out the perfect precoding at the transmitter. However, in practical scenarios, this assumption is opportunistic because the numbers of the transmit and the receive antenna elements are large. It is a challenging task to obtain the accurate estimates of $\mathbf{H}$ that consists of $N_{\text{T}} \cdot N_{\text{R}}$ number of channel coefficients. In this chapter, we assume the angle-of-departure (AoD) θ_{AoD} and the angle-of-arrival (AoA) θ_{AoA} are perfectly known at the transmitter and the receiver, respectively. These two angles can be estimated from phase differences of received signals between adjacent antenna elements [58]. The optimum ABF weights $\mathbf{f}_i$ and $\mathbf{w}_i$ are given by [63, 58]

$$
\begin{cases}
\mathbf{f}_i = \dfrac{1}{\sqrt{U_{\text{T}}}} \left[1, \exp\left(j\delta_{\text{T}}^{(i)}\right), \cdots, \exp\left(j\left(U_{\text{T}}-1\right)\delta_{\text{T}}^{(i)}\right) \right]^{\text{T}} \\[2mm]
\mathbf{w}_k = \dfrac{1}{\sqrt{U_{\text{R}}}} \left[1, \exp\left(j\delta_{\text{R}}^{(k)}\right), \cdots, \exp\left(j\left(U_{\text{R}}-1\right)\delta_{\text{R}}^{(k)}\right) \right]^{\text{T}}
\end{cases}
, \tag{4.5}
$$

where we have

$$
\begin{cases}
\delta_{\text{T}}^{(i)} = d \cdot \left(\dfrac{2\pi}{\lambda}\right) \cdot \sin\left(\theta_{\text{AoD}}^{(i)}\right) \\[2mm]
\delta_{\text{R}}^{(k)} = d \cdot \left(\dfrac{2\pi}{\lambda}\right) \cdot \sin\left(\theta_{\text{AoA}}^{(k)}\right)
\end{cases}
. \tag{4.6}
$$

Here, $\theta_{\text{AoD}}^{(i)}$ and $\theta_{\text{AoA}}^{(k)}$ denote the AoD toward the ith ABF at the receiver and the AoA from the kth ABF at the transmitter, respectively. The above ABF weights reduce the number of channel coefficients that have to be estimated, namely from $(N_{\text{T}} \cdot N_{\text{R}})$ to $(M_{\text{T}} \cdot M_{\text{R}})$.

Potentially, it is difficult to obtain the BF gain with the GSM scheme because it only activates a subset of all transmit subarrays [104], while the conventional spatial-multiplexing schemes activate all of the transmit subarrays at the same time to obtain the BF gain. Since the GSM scheme requires a fewer number of RF chains, it may be possible to construct a large-scale mmWave system that achieves a higher throughput. If the channel state information is available at the transmitter, the phase-rotation-based precoding scheme of [157] may be invoked.

Let us check the example of the ABF weights for the $d = \lambda/2$ scenario. Under this assumption, $\delta_{\text{T}}^{(i)}$ of Eq. (4.6) is simplified to $\delta_{\text{T}}^{(i)} = \pi \cdot \sin\left(\theta_{\text{AoD}}^{(i)}\right)$. Then, the ABF weights vector $\mathbf{f}_i$ is given by

$$
\mathbf{f}_i = \frac{1}{\sqrt{U_{\text{T}}}} \left[1, \exp\left(j \cdot 1 \cdot \pi \sin\left(\theta_{\text{AoD}}^{(i)}\right)\right), \cdots, \exp\left(j \cdot \left(U_{\text{T}}-1\right) \cdot \pi \sin\left(\theta_{\text{AoD}}^{(i)}\right)\right) \right]^{\text{T}}.
$$

Here, if we have the relationships of $\theta_{\mathrm{AoD}}^{(i)} = \pi/3$ and $U_{\mathrm{T}} = 4$, the specific values are calculated by

$$\mathbf{f}_i = \frac{1}{2}\left[\exp\left(j \cdot \frac{0}{2} \cdot \pi\right), \exp\left(j \cdot \frac{1}{2} \cdot \pi\right), \exp\left(j \cdot \frac{2}{2} \cdot \pi\right), \exp\left(j \cdot \frac{3}{2} \cdot \pi\right)\right]^{\mathrm{T}}$$
$$= \frac{1}{2}\left[1, j, -1, -j\right]^{\mathrm{T}}.$$

Furthermore, if we consider the $M_{\mathrm{T}} = 4$ case, the ABF weights matrix $\mathbf{F}$ is derived by

$$\mathbf{F} = \mathrm{diag}(\mathbf{f}_1, \mathbf{f}_2, \mathbf{f}_3, \mathbf{f}_4)$$

$$= \frac{1}{2}\begin{bmatrix} 1 & j & -1 & -j & 0 & 0 & 0 & 0 & 0 & 0 & 0 & 0 & 0 & 0 & 0 & 0 \\ 0 & 0 & 0 & 0 & 1 & j & -1 & -j & 0 & 0 & 0 & 0 & 0 & 0 & 0 & 0 \\ 0 & 0 & 0 & 0 & 0 & 0 & 0 & 0 & 1 & j & -1 & -j & 0 & 0 & 0 & 0 \\ 0 & 0 & 0 & 0 & 0 & 0 & 0 & 0 & 0 & 0 & 0 & 0 & 1 & j & -1 & -j \end{bmatrix}^{\mathrm{T}} \in \mathbb{C}^{16 \times 4}.$$

4.4   Performance Results

We investigated the achievable performance of the proposed GSM-based scheme. The considered benchmark schemes were the single-stream BF and the spatial-multiplexing schemes, which requires a single RF chain and M_{T} number of RF chains, respectively. Later, the single-stream BF is referred to as the "BF" scheme in this chapter. We compared the directive BF gain and the constrained AMI for the proposed scheme and the benchmark schemes. Throughout the simulations, we assumed the indoor mmWave scenario of Fig. 4.2, where we have $D_{\mathrm{H}} = 5$ [m] and the channel matrices were randomly generated based on Eq. (4.3). The Rician factor K was set to 10.0 [dB] in accordance with [156, 153]. The carrier-frequency was assumed to 60 [GHz]. Since the speed of radio waves is approximated to 3.00×10^8 [m/s], the corresponding wavelength is given by $3.00 \times 10^8 / \left(60.0 \times 10^9\right) = \lambda = 5$ [mm]. The spacing between antenna elements in a subarray was fixed to half of the wavelength $d = \lambda/2$. Based on Eq. (4.4), each subarray was separated by $D_{\mathrm{T}} = D_{\mathrm{R}} = 7.91$ and 5.59 [cm] for the $(N_{\mathrm{T}}, M_{\mathrm{T}}, N_{\mathrm{R}}, M_{\mathrm{R}}) = (16, 4, 16, 4)$ and $(32, 8, 16, 4)$ scenarios, which are calculated by $D_{\mathrm{T}} = D_{\mathrm{R}} = \sqrt{\lambda D_{\mathrm{R}} / \min(M_{\mathrm{T}}, M_{\mathrm{R}}) / \cos(\theta)}$. We assumed the employment of omni-directional antenna elements both at the transmitter and the receiver. The simulation parameters considered in this section are given in Table 4.1.

Table 4.1 Simulation parameters of the MIMO mmWave schemes.

Number of transmit antenna elements	$N_\mathrm{T} = 16,\ 32$
Number of receive antenna elements	$N_\mathrm{R} = 16$
Number of transmit subarrays	$M_\mathrm{T} = 4,\ 8$
Number of receive subarrays	$M_\mathrm{R} = 4$
Number of RF chains	$N_\mathrm{RF} = 1,\ 2,\ 4,\ 8$
Carrier-frequency	60 [GHz]
Wavelength	$\lambda = 0.5$ [cm]
Spacing between antenna elements	$d = 0.25$ [cm]
Spacing between subarrays	$D_\mathrm{T} = D_\mathrm{R} = 5.59,\ 7.91$ [cm]
Spacing between the transmitter and the receiver	$D_\mathrm{H} = 5$ [m]
Receiver tilt	$0° \leq \theta \leq 90°$
Channel	Frequency-flat Rician fading
Rician factor	$K = 10$ [dB]
Detector	Maximum-likelihood detection
Modulation	PSK and QAM

4.4.1 Directive Beamforming Gain

Fig. 4.4 shows the achievable directive gains, where we have $N_\mathrm{T} = 16$ number of antenna elements and the receiver tilt of $\theta = 0°$. The number of subarrays was set to $M_\mathrm{T} = 1$ or 4. Fig. 4.4(a) illustrates the absolute values of array factor of a uniform linear array (ULA) with respect to the horizontal direction, where the BF scheme was considered. In Figs. 4.4(b) – (d), we considered the $M_\mathrm{T} = 4$ number of subarrays that were separated by the criterion of Eq. (4.4). It was shown in Figs. 4.4(a) and (b) that the optimum alignment of Eq. (4.4) changes the pattern of directive BF gains. The ULA without the alignment optimization was capable of steering a narrow beam into the designated direction $\theta = 0°$. Observe in Figs. 4.4(b) and (c) that the measured BF gain of BLAST was 6.0 [dB], while that of GSM was 4.3 [dB]. This means that the proposed GSM-based transmitter has a loss in the BF gain. Observe in Figs. 4.4(c) and (d) that the beam patterns are different for the positions of non-zero elements in the symbol vectors $\mathbf{x} = [s_1, s_2, 0, 0]^\mathrm{T}$ and $[s_1, 0, s_2, 0]^\mathrm{T}$. Hence, the proposed scheme modulates the additional information bits with the selection of beam patterns.

4.4.2 Average Mutual Information

We investigated the unconstrained and the constrained AMI for the proposed scheme and the benchmark schemes. Both AMI formulas were defined in Section 2.2.1, where we have $\mathbf{Q} = \mathbf{H}_b \mathbf{H}_b^\mathrm{H}$ in this chapter. The unconstrained AMI curves were plotted to clarify the

(a) BF having $\mathbf{x} = [s_1, s_1, s_1, s_1]^T$ without the alignment optimization.

(b) BLAST having $\mathbf{x} = [s_1, s_2, s_3, s_4]^T$ with the alignment optimization.

(c) GSM(4,2) having $\mathbf{x} = [s_1, s_2, 0, 0]^T$ with the alignment optimization.

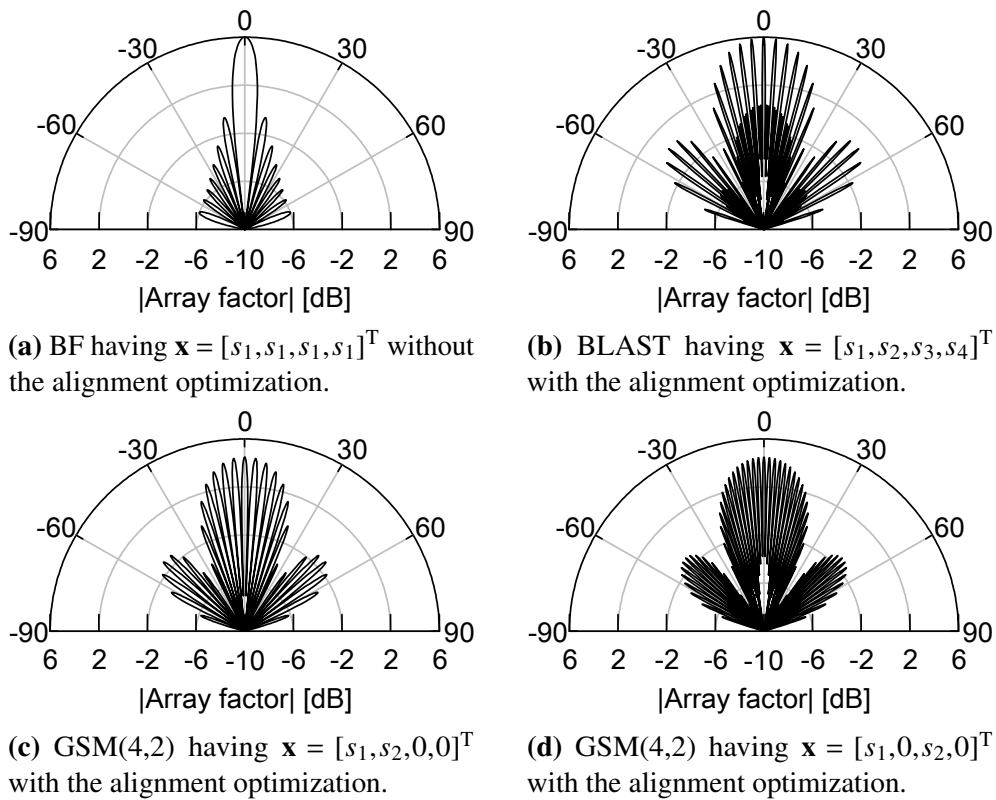**(d)** GSM(4,2) having $\mathbf{x} = [s_1, 0, s_2, 0]^T$ with the alignment optimization.

Figure 4.4 Directive BF gains with/without the ABF alignment optimization of Section 4.3.1, where we have $N_T = 16$ and $\theta = 0°$.

Table 4.2 System parameters considered in our comparisons.

	Rate [bits/symbol]	Scheme	N_{RF}	Constellation
	4.0	BF	1	16–QAM
	4.0	BLAST	2	QPSK
Fig. 4.5	4.0	BLAST	4	BPSK
	4.0	GSM	1	QPSK
	4.0	GSM	2	BPSK
	8.0	BF	1	256–QAM
	8.0	BLAST	2	16–QAM
Fig. 4.6	8.0	BLAST	4	QPSK
	8.0	GSM	1	64–QAM
	8.0	GSM	2	8–PSK
	8.0	BF	1	256-QAM
	8.0	BLAST	2	16–QAM
Fig. 4.7	8.0	BLAST	8	BPSK
	8.0	GSM	1	32–PSK
	8.0	GSM	2	QPSK
	16.0	BF	1	65536–QAM
	16.0	BLAST	2	256–QAM
Fig. 4.8	16.0	BLAST	8	QPSK
	17.0	GSM	1	16384–QAM
	16.0	GSM	2	64–QAM

associated upper bounds of the constrained AMI curves. Furthermore, the system parameters of the schemes considered in AMI comparisons were listed in Table 4.2.

Fig. 4.5 shows the constrained AMI comparisons of the proposed GSM, the single-stream BF, and the spatial-multiplexing schemes, where the number of antenna elements was $N_T = N_R = 16$ and the number of subarrays was $M_T = M_R = 4$. The specific system parameters are available in Table 4.2. The separation between ABFs was set to $D_T = D_R = 7.91$ [cm] based on Eq. (4.4). In this scenario, the mean rank of the channel matrix was rank($\mathbf{H}_b$) = min(4,4) = 4. In Fig. 4.5, we considered the 16–QAM aided BF, the spatial multiplexing having $N_{RF} = 2$ and 4, and the GSM having $N_{RF} = 1$ and 2. It was shown in Fig. 4.5 that the single-RF GSM outperformed the other schemes. Also, the constrained AMI of the GSM having $N_{RF} = 2$ was close to those of the spatial-multiplexing schemes having $N_{RF} = 2$ or 4.

In Fig. 4.6, we investigated the transmission rate $R = 8.0$ [bits/symbol] case of Fig. 4.5, where all simulation parameters except for the transmission rate were the same with those used in Fig. 4.5. In Fig. 4.6, we considered the 256–QAM aided BF, the spatial multiplexing having $N_{RF} = 2$ and 4, the GSM having $N_{RF} = 1$ and 2. It was shown in Fig. 4.6 that the constrained AMI of the single-RF GSM scheme was higher than that of the spatial-

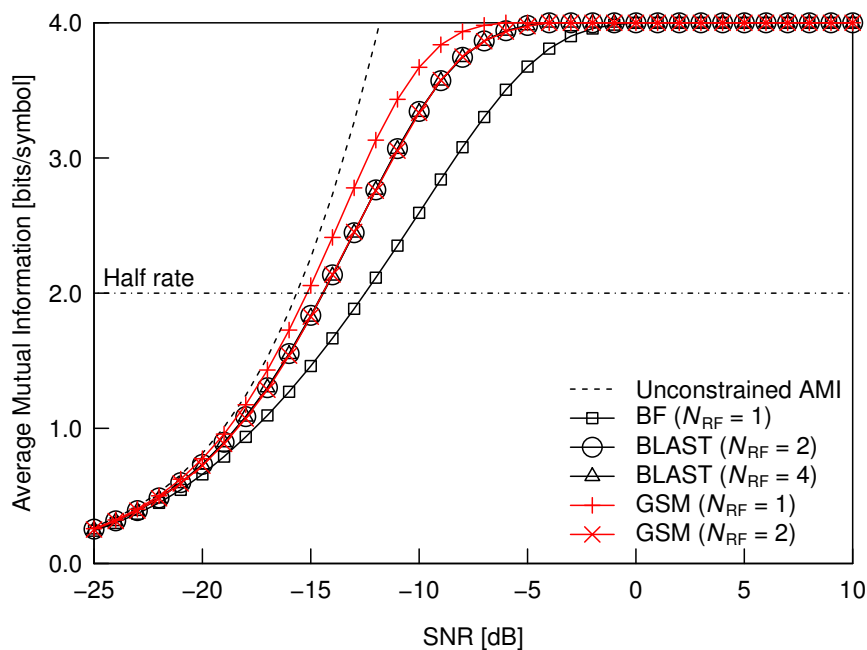**Figure 4.5** Constrained AMI comparisons between the GSM and the benchmark schemes. The transmitter and the receiver had $N_T = N_R = 16$ antenna elements and $M_T = M_R = 4$ separated ABFs. The transmission rate was $R = 4.0$ [bits/symbol].

Figure 4.6 Constrained AMI comparisons for the transmission rate $R = 8.0$ [bits/symbol] case. All other simulation settings were the same with those shown in Fig. 4.5.
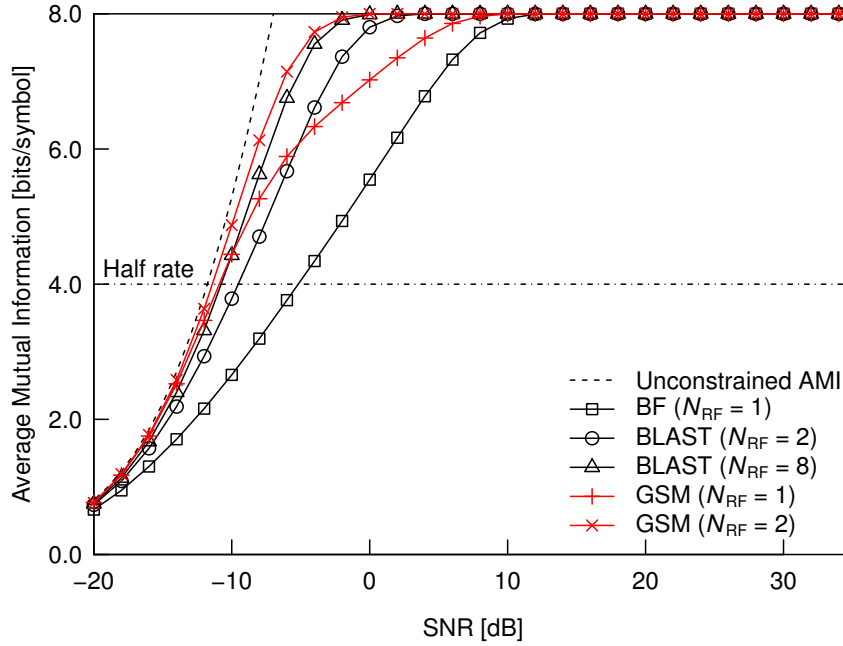
Figure 4.7 Constrained AMI comparisons between the GSM and the benchmark schemes. The transmitter had $N_T = 32$ antenna elements and $M_T = 8$ separated ABFs, while the receiver had $N_R = 16$ antenna elements and $M_R = 4$ separated ABFs. The transmission rate was $R = 8.0$ [bits/symbol].

multiplexing scheme having $N_{RF} = 2$ at the half-rate point of 4.0 [bits/symbol]. Also, the constrained AMI of the GSM scheme having $N_{RF} = 2$ was close to that of the spatial-multiplexing scheme having $N_{RF} = 4$.

Fig. 4.7 shows the constrained AMI comparisons of the proposed GSM, the single-stream BF, and the spatial-multiplexing schemes, where the number of transmit antenna elements was $N_T = 32$ and the number of subarrays was $M_T = 8$. The numbers of receive antenna elements and subarrays were the same with those used in Figs. 4.5, namely, $(N_R, M_R) = (16, 4)$. The specific system parameters are available in Table 4.2. The separation between ABFs was set to $D_T = D_R = 5.59$ [cm] based on Eq. (4.4). In this scenario, the mean rank of the channel matrix was $\text{rank}(\mathbf{H}_b) = \min(8, 4) = 4$. In Fig. 4.7, we considered the 256–QAM aided BF, the spatial multiplexing having $N_{RF} = 2$ and 8, and the GSM having $N_{RF} = 1$ and 2. It was shown in Fig. 4.7 that the GSM scheme having $N_{RF} = 2$ achieved the best constrained AMI between all schemes. Also, the constrained AMI of the GSM scheme having $N_{RF} = 1$ was close to that of the spatial-multiplexing scheme having $N_{RF} = 8$ at the half-rate point.

Fig. 4.8 considers the transmission rate $R = 16.0$ [bits/symbol] case of Fig. 4.7. In Fig. 4.6, all simulation parameters except for the transmission rate were the same with those used in Fig. 4.7. In Fig. 4.8, we considered the 65536–QAM aided BF, the spatial multiplexing having $N_{RF} = 2$ and 8, the GSM having $N_{RF} = 1$ and 2. For ease of comparison, the transmission rate
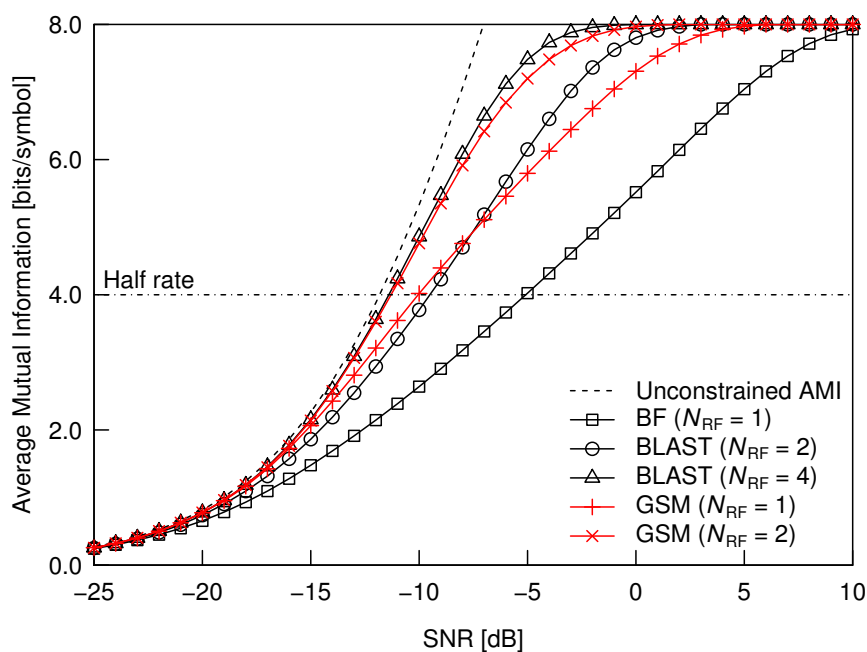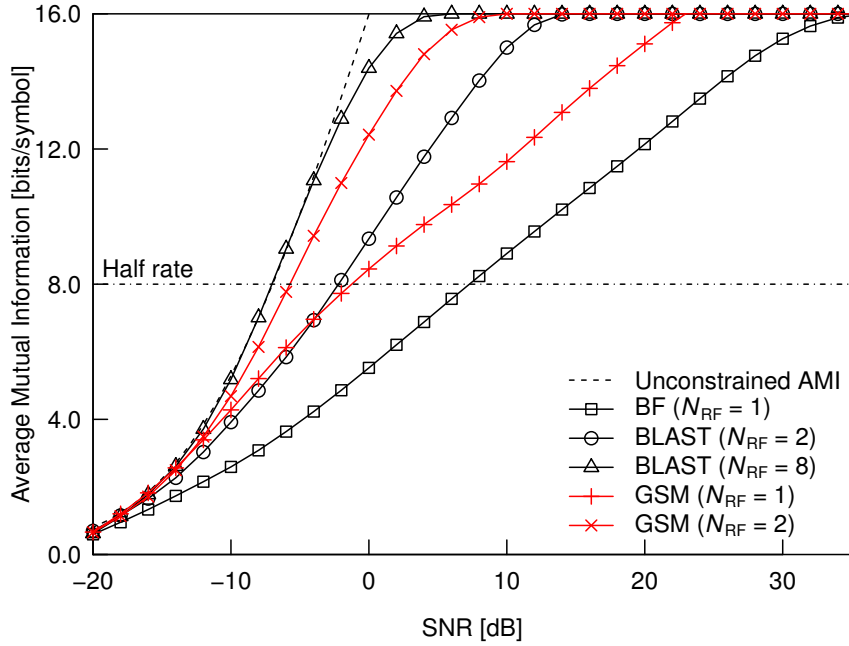
Figure 4.8 Constrained AMI comparisons for the transmission rate $R = 16.0$ [bits/symbol] case. All other simulation settings were the same with those shown in Fig. 4.7.

of the single-RF GSM was set to 17.0 [bits/symbol] in order to use the squared $\mathcal{L} = 16384$–QAM modulation. It was shown in Fig. 4.8 that the full-RF spatial-multiplexing scheme exhibited the highest constrained AMI over the entire SNR region. The constrained AMI of the GSM having $N_{\mathrm{RF}} = 2$ was close to that of the full-RF spatial-multiplexing scheme, where the performance gap was 1.2 [dB] at the half-rate point. Also, at the half-rate point, the GSM having $N_{\mathrm{RF}} = 1$ achieved a better AMI than the single-stream BF with a gap of 9 [dB], while the GSM scheme performed worse than the spatial-multiplexing scheme having $N_{\mathrm{RF}} = 2$ with a 1.0 [dB] gap.

4.4.3   Effects of the Distance between Transmitter and Receiver

Fig. 4.9 shows the effects of the change in the distance between the transmitter and the receiver, which is denoted by D_{H}. All the simulation parameters were the same with those shown in Fig. 4.5, except for the distance D_{H}. For the $D_{\mathrm{H}} = 1.0$ [m] case, the spacing between subarrays was $D_{\mathrm{T}} = D_{\mathrm{R}} = 3.54$ [cm], while for the $D_{\mathrm{H}} = 3.0$ [m] case, the spacing was $D_{\mathrm{T}} = D_{\mathrm{R}} = 6.12$. It was shown in Fig. 4.9(a) and (b) that the unconstrained and constrained AMI were almost the same with those shown in Fig. 4.5. This is because the received SNR for each scheme was relatively unchanged, and the mean of the rank of channel matrices was also unchanged with the aid of the optimum alignment of Eq. (4.4). We checked that the

(a) $D_H = 1.0$ [m].   **(b)** $D_H = 3.0$ [m].
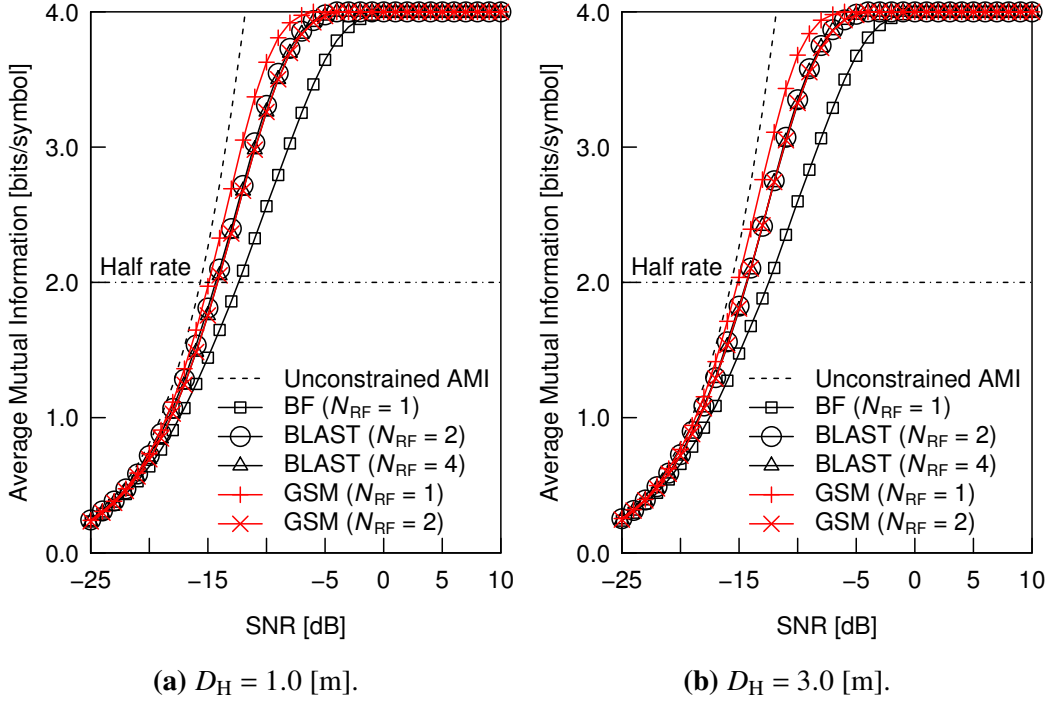
Figure 4.9 Effects of the distance D_H between the transmitter and the receiver. All simulation parameters except for the distance D_H were the same with those shown in Fig. 4.5, where D_H was originally set to 5.0 [m].

above results shown in Figs. 4.5, 4.6, 4.7, and 4.8 were unchanged for the $D_H = 1, 2, 3, 4$, and 5 [m] scenarios.

4.4.4   Effects of Beamforming Error

Fig. 4.10 shows the effects of the receiver tilt θ. In Fig. 4.10, the system parameters and the considered schemes were the same as those used in Fig. 4.6. The constrained AMI was calculated at SNR = -5 [dB]. For the missteered case, the estimated θ_{AoD} and θ_{AoA} were fixed to $0°$ although the receiver was tilted at an angle of $0° \leq \theta \leq 90°$. As shown in Fig. 4.10, the constrained AMI of the all schemes decreased from $\theta = 0°$ to $30°$, which corresponds to the main-lobe of the directive BF gain shown in Fig. 4.4. It was shown in Fig. 4.10 that the constrained AMI of the spatial-multiplexing and GSM schemes was higher than the half-rate 4.0 [bits/symbol] within the range of $0° \leq \theta \leq 18°$. For the steered case, θ_{AoD} and θ_{AoA} were accurately adjusted based on the perfect estimates of θ. As shown in Fig. 4.10, the constrained AMI of the spatial-multiplexing and the GSM schemes remained high within the range of $0 \leq \theta < 83°$.
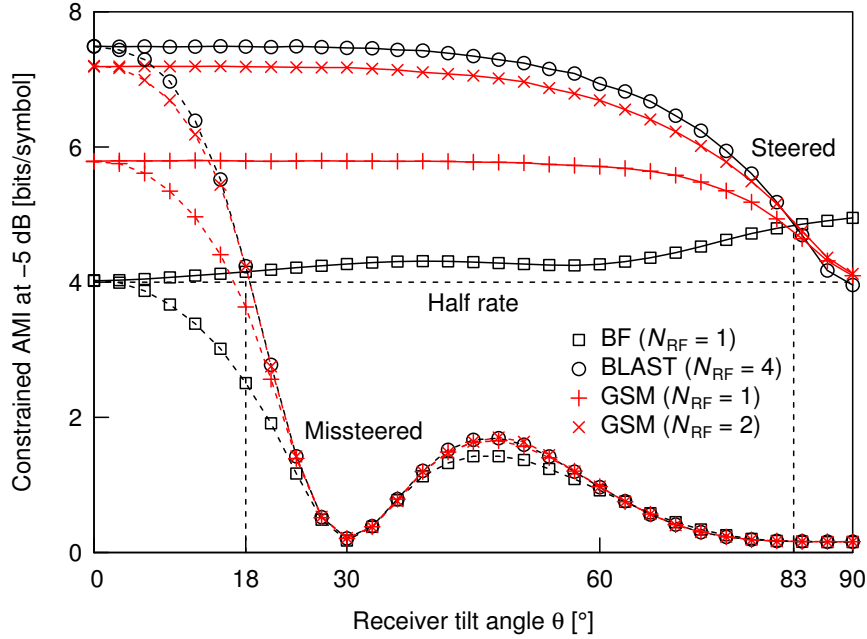
Figure 4.10 Effects of the receiver tilt on the constrained AMI at the SNR of −5 [dB]. The system parameters were inherited from Fig. 4.6. The constrained AMI at $\theta = 0°$ corresponded to that shown in Fig. 4.6, where SNR = −5 [dB].

4.5   Chapter Conclusions

In this chapter, we evaluated the PM scheme applied to the mmWave domain. More specifically, the GSM scheme was invoked for reducing the number of RF chains at the transmitter. Our simulation results demonstrated that the constrained AMI of the GSM-based transmitter was close to that of the full-RF spatial-multiplexing scheme, in terms of the SNR required for achieving the half transmission rate. Note that the achievable BF gain of the GSM family is lower than that of the spatial-multiplexing scheme since the GSM scheme activates a part of all subarrays. We conclude that the proposed GSM scheme has a possibility that is capable of reducing the number of RF chains by half or less.

Chapter 5

Permutation Modulation Based MIMO Visible Light Communications

5.1 Introduction

In this chapter, we apply the PM concept to VLCs, where we introduce a flexible PA method for attaining a higher mutual information. As mentioned in Chapter 1, the available radio spectrum is overloaded due to the popularization of mobile microwave devices. We reviewed the diverse PM-based schemes in Chapter 2 and applied the concept to the mmWave domain in Chapter 4. We considered facilitating the mmWave bands, aiming at unloading the large demands of wireless communications. In order to further circumvent the spectrum crisis, we try to exploit the visible light domain, in support of the current microwave communications. More specifically, the main difference from the microwave and mmWave domains is the channel model, where only LoS components having real-valued coefficients are considered.

Since the 2000s, indoor VLC have attracted attention due to its license-free and security-aware operations [51]. The energy-efficient and cost-effective LED has enabled the communication operated by visible lights, while its potential had been anticipated in the 1980s [51]. Theoretically, the larger bandwidths are available for VLC because the frequency of visible lights ranges from 430 to 770 [THz]. Although the bandwidths available by VLC modulators are limited in practice [66], the additional bandwidths for secured indoor wireless communications are attractive for our daily lives. As we reviewed in Section 2.5, the PM concept has been applied to the MIMO-VLC domain [78, 134, 131, 101, 133], which are referred to as

OSM. The SM scheme having been proposed in the microwave domain allocates additional bits by selecting a single antenna out of multiple transmit antennas. Similar to the microwave SM concept, the OSM scheme allocates additional bits by selecting a single source of light out of multiple transmit lights.

In [158, 134], the OSM scheme was evaluated in a realistic LoS highly-correlated channel. It was shown in [158, 134] that the OSM scheme is difficult to attain the performance gain in such channels. Here, in order to challenge the highly-correlated channels, the PA method was considered for the OSM scheme, which is referred to as power-imbalanced (PI) OSM [101]. The PA method of [101] mitigates the channel correlations with the aid of the power imbalanced parameters associated with the source lights. In [101], the PA parameters were considered for the four source lights case, which was generated from a single imbalanced parameter. However, the single parameter was determined in a heuristic manner and no design guideline was proposed in [101]. In addition, in the previous OSM studies [78, 134, 131, 101, 133], the performance advantages have been investigated in terms of BER in uncoded scenarios, instead of providing any information-theoretic analysis.

Against this backcloth, in this chapter, we propose a unified PI-OSM architecture that subsumes the conventional PI-OSM of [101]. We design our proposed PI-OSM so as to maximize the constrained MI. We analyze the conventional and proposed OSM schemes in terms of the constrained MI and reveal the performance upper-bounds. Moreover, we propose an irregular-precoded PI-OSM (Irr-PI-OSM) for channel-coded scenarios.

The remainder of this chapter is organized as follows. In Sections 5.2 and 5.2.1, we propose the unified PI-OSM scheme for uncoded/coded scenarios. Section 5.2.2 defines the channel model considered in our simulations. Section 5.3 proposes our design guidelines for the PI-OSM and Irr-PI-OSM schemes, while Section 5.3.3 proposes the adaptive counterparts of the PI-OSM and Irr-PI-OSM schemes. Section 5.4 provides our simulation results in uncoded/coded scenarios. Finally, Section 5.5 concludes this chapter.

5.2 System Model

In our system model, a MIMO-VLC transmitter equipped with M number of source lights transmits intensity-modulated pulses to a receiver equipped with N number of photodetectors (PDs) and the receiver directly detects the intensity-modulated signals.

In this section, we propose a PI-OSM architecture that subsumes the conventional schemes reviewed in Section 2.5. The key feature of the proposed PI-OSM constellation design lies on the flexible PA parameters at the transmitter, which mitigates the detrimental
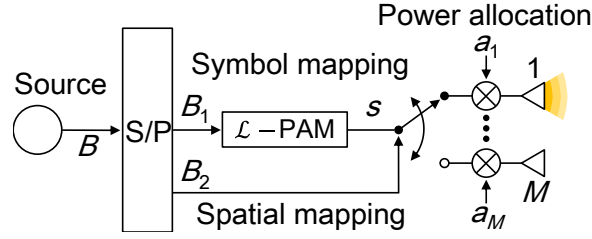
Figure 5.1 Schematic of our proposed PI-OSM transmitter.

effects imposed by a highly-correlated channel matrix. Fig. 5.1 shows the schematic of our PI-OSM transmitter, where we have M transmit light sources and the same number of associated PA multipliers $a_1, \cdots, a_M \in \mathbb{R}$. The SM encoding process that maps the input $B = B_1 + B_2$ bits to the associated codeword is detailed in Sections 2.3.1 and 2.5. Here, we provide the modulation process concatenated with the flexible PA design. The B input bits are S/P converted to $B_1 = \log_2 \mathcal{L}$ bits and $B_2 = \log_2 M$ bits. Then, at the symbol mapping block of Fig. 5.1, a PAM symbol $s \in \mathbb{R}$ is modulated according to the B_1 input bits. The lth $\mathcal{L}$–PAM symbol is defined by [101]

$$s = \frac{2l}{\mathcal{L}+1}. \quad (1 \leq l \leq \mathcal{L}) \tag{5.1}$$

According to the B_2 input bits, one out of M source lights is activated, which is represented by q, similar to the conventional OSM scheme of Section 2.5. Finally, the PI-OSM transmitter generates a non-negative symbol vector $\mathbf{s} \in \mathbb{R}^{M \times 1}$ as follows:

$$\mathbf{s} = \mathbf{A} \cdot s \cdot [0 \ \cdots \ 0 \ \underbrace{1}_{q\text{th row}} \ 0 \ \cdots \ 0]^{\mathrm{T}}, \tag{5.2}$$

where the PA matrix is given by

$$\mathbf{A} = \mathrm{diag}\left(a_1, \cdots, a_M\right). \tag{5.3}$$

Each PA parameter $a_m > 0$ $(1 \leq m \leq M)$ is associated with the mth source light. Here, we have the following constraint on the PA parameters:

$$\sum_{m=1}^{M} a_m = M. \tag{5.4}$$

Table 5.1 Bit mapping example of the $\mathcal{L} = 2$–PAM aided PI-OSM scheme, where we have $B = 3$ input bits and $M = 4$ source lights.

Input bits	s	q	PA parameter	$\mathbf{s}$
0 00	0.67	1	a_1	$[0.67a_1\ 0\ 0\ 0]^{\mathrm{T}}$
0 01	0.67	2	a_2	$[0\ 0.67a_2\ 0\ 0]^{\mathrm{T}}$
0 10	0.67	3	a_3	$[0\ 0\ 0.67a_3\ 0]^{\mathrm{T}}$
0 11	0.67	4	a_4	$[0\ 0\ 0\ 0.67a_4]^{\mathrm{T}}$
1 00	1.33	1	a_1	$[1.33a_1\ 0\ 0\ 0]^{\mathrm{T}}$
1 01	1.33	2	a_2	$[0\ 1.33a_2\ 0\ 0]^{\mathrm{T}}$
1 10	1.33	3	a_3	$[0\ 0\ 1.33a_3\ 0]^{\mathrm{T}}$
1 11	1.33	4	a_4	$[0\ 0\ 0\ 1.33a_4]^{\mathrm{T}}$

The design criteria for the PA parameters will be detailed in Section 5.3. The transmission rate is equal to the length of the input bits, namely, $R = B$ [bits/symbol].

Table 5.1 provides mapping examples of the $\mathcal{L} = 2$–PAM aided PI-OSM scheme having $M = 4$. In Table 5.1, the $B = 3$ input bits are S/P converted to $B_1 = 1$ bit and $B_2 = 2$ bits. According to the first B_1 bits, a binary PAM symbol is modulated by the power levels of $\{2/3, 4/3\} \approx \{0.67, 1.33\}$. According to the second B_2 bits, a single source light out of $M = 4$ lights is activated. The PA parameters a_m corresponds to the mth activated source light index. Finally, the symbol vector $\mathbf{s}$ is generated by multiplying the modulated binary PAM symbol and the activated PA parameter.

Our unified OSM architecture is capable of subsuming the previous PI-OSM scheme of [101], where the following PA parameters have been proposed:

$$a_m = \begin{cases} \dfrac{M}{\sum_{i=0}^{M-1} \alpha^i} & (m = 1) \\ \alpha a_{m-1} & (2 \le m \le M) \end{cases}. \tag{5.5}$$

Here, we have $\alpha = 10^{\frac{\beta}{10}}$ and $\beta \ge 0$. The PA parameters of Eq. (5.5) satisfy the constraint of Eq. (5.4). The single parameter β adjusts the M number of PA parameters $a_1, \cdots, a_M$. If we consider having $\beta = 0$ [dB], each PA parameter is equal to $a_m = 1$, which is equivalent to the equal-powered OSM scheme of Section 2.5.3. Note again that the optimization criterion designed for the single parameter β was not presented in [101].

The received signals expressed in the time domain may be modeled as follows [101]:

$$\mathbf{y} = R_{\mathrm{PD}}\mathbf{H}\mathbf{s} + \mathbf{v}, \tag{5.6}$$
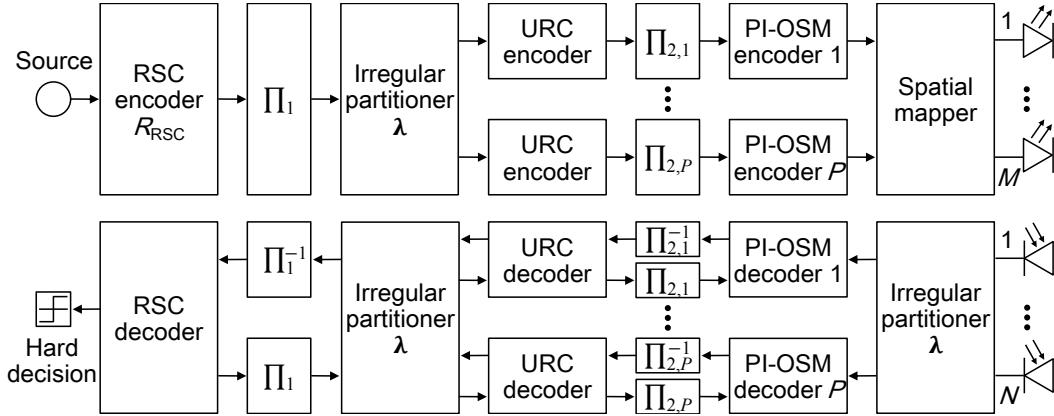
Figure 5.2 Block diagrams of the iterative encoding and decoding process of our proposed PI-OSM.

where $R_{\mathrm{PD}} \in \mathbb{R}$ [A/W] denotes the response of PD and $\mathbf{H} \in \mathbb{R}^{N \times M}$ denotes the channel matrix, having non-negative elements of $h[n,m] \in \mathbb{R}$ at nth row and mth column. The construction of the channel matrix $\mathbf{H}$ will be described in Section 5.2.2 The received signals are fluctuated by the AWGN $\mathbf{v} \in \mathbb{R}^{N \times 1}$ that follows the real-valued Gaussian distribution of $\mathcal{N}(0, \sigma_v^2)$.

The received electrical SNR ρ is defined as follows: [78]

$$\rho = \frac{\bar{\sigma}_r^2}{\sigma_v^2}, \tag{5.7}$$

where we have

$$\bar{\sigma}_r = \frac{1}{N} \sum_{n=1}^{N} \sigma_r^{(n)} \tag{5.8}$$

and $\sigma_r^{(n)}$ is the received optical power at the nth PD.

The MLD of the proposed PI-OSM receiver is given by

$$\hat{\mathbf{s}} = \arg\min_{\mathbf{s}} \|\mathbf{y} - \mathbf{H}\mathbf{s}\|^2, \tag{5.9}$$

which is the same with the conventional MLD.

5.2.1 Irregular Encoding and Decoding

In this section, we extend the proposed PI-OSM scheme into its irregular-precoded counterpart, motivated by the irregular precoding concept [20]. Fig. 5.2 shows the block diagrams

of the Irr-PI-OSM transmitter and receiver. The transmitter consists of a set of the PI-OSM encoders, while the receiver consists of the same number of the PI-OSM decoders.

At the transmitter of Fig. 5.2, the information bits, which are typically longer than 10^5 bits, are encoded by a half-rate recursive systematic convolutional (RSC) code. The RSC-encoded bits are interleaved by the interleaver $\mathbf{\Pi}_1$. The interleaved bits are divided into P number of sequences with weights-for-length of $\boldsymbol{\lambda} = [\lambda_1, \cdots, \lambda_P]^{\mathrm{T}}$. Note that $\boldsymbol{\lambda}$ is previously designed by the criteria, as will be proposed in Section 5.3.2. Then, the separated sequences are precoded by the recursive unity rate code (URC) encoders and are interleaved again by the interleavers $\mathbf{\Pi}_{2,p}$ ($1 \leq p \leq P$). Finally, the interleaved bits are modulated by the pth PI-OSM encoder.

The aggregate transmission rate is given by [20]

$$R = \frac{R_{\mathrm{RSC}}}{\sum_{p=1}^{P} \lambda_p / R_p}, \tag{5.10}$$

where R_{RSC} and R_p denote the transmission rates of the RSC code and the pth inner PI-OSM, respectively.

At the receiver of Fig. 5.2, the received symbols are divided into P number of sequences, with the irregular-partition ratios of $\boldsymbol{\lambda}$. For each sequence, the PI-OSM decoder calculates its LLR and outputs it as *a posteriori* probability. Based on Bayes' theorem, an extrinsic LLR is calculated by the *a posteriori* LLR subtracted by its *a priori* LLR. The *a priori* LLRs in the first iteration are set to zero and are updated based on the exchanged extrinsic information. Refer to [20] for further details. Later, we denote the number of iterations between the inner codes and the outer code as N_{in} and N_{out}, respectively.

5.2.2   Channel Model

In our simulations, we consider an indoor LoS-dominant MIMO channel, which is basically the same with [101]. Fig. 5.3 illustrates the indoor LoS environment, where the resultant channel matrix typically exhibits high correlations. Here, we assume that the source lights as well as the PDs are centered in the room and are symmetrically aligned. The distance between the transmitter and the receiver is set to 1.75 [m] [101].
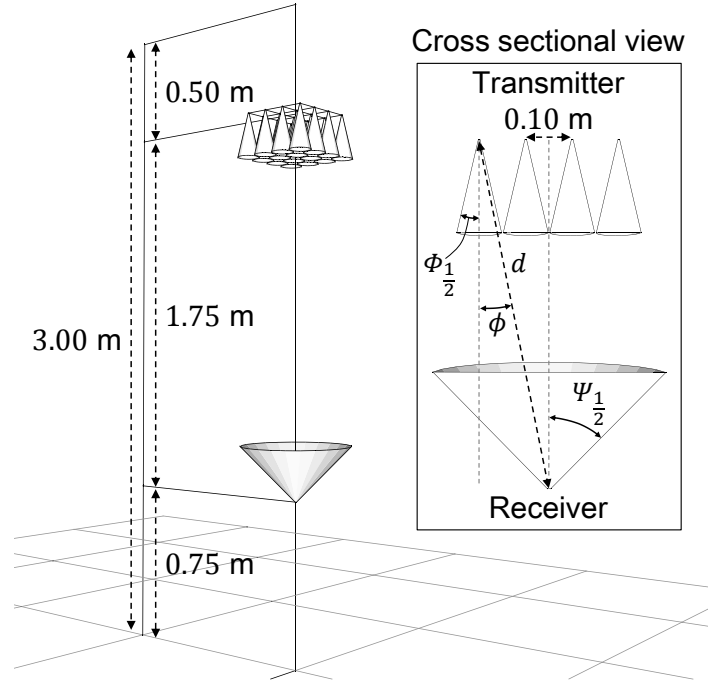
Figure 5.3 The VLC channel setup considered in this chapter. The distance between the transmitter and the receiver is set to 1.75 [m]. The alignments of source lights and detectors are described in Fig. 5.4.

We assume the path-loss channel model. The channel coefficient at the nth row and mth column of $\mathbf{H}$ is given by [101]

$$h[n,m] = \begin{cases} \dfrac{(\xi+1)A_{\mathrm{PD}}}{2\pi d[n,m]^2} \cos^{\xi+1} \phi[n,m] & \left(0 \leq \phi[n,m] \leq \Psi_{\frac{1}{2}}\right) \\ 0 & \left(\phi[n,m] > \Psi_{\frac{1}{2}}\right) \end{cases}, \qquad (5.11)$$

where we have

$$\xi = -\frac{\ln(2)}{\ln\left(\cos\Phi_{\frac{1}{2}}\right)}. \qquad (5.12)$$

In Eq. (5.11), $d[n,m]$ denotes the distance between the mth source light and the nth PD, and $\phi[n,m]$ denotes an angle of incidence from the mth source light to the nth PD. Also, A_{PD} is the physical area of the PD at the receiver. Moreover, $\Phi_{\frac{1}{2}}$ denotes the transmitter semi-angle, while $\Psi_{\frac{1}{2}}$ denotes a field-of-view semi-angle of the receiver.

Figure 5.4 The alignment of source lights at the transmitter and PDs at the receiver. Each value $2, \cdots, 256$ represents the number of source lights M and the number of PDs N.
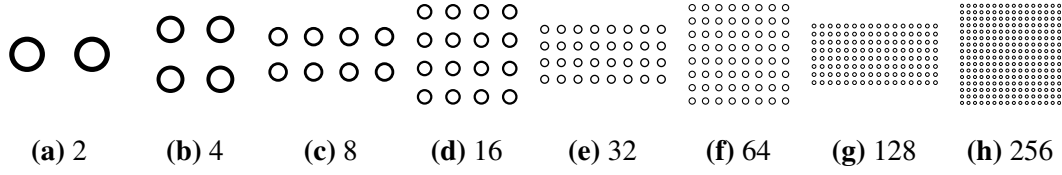
The alignments of source lights and PDs are illustrated in Fig. 5.4, which determine the physical distance $d[n,m]$ and angle $\phi[n,m]$ in Eq. (5.11). The spacing between each element is denoted by d_{Tx} at the transmitter and d_{Rx} at the receiver. The source lights are arranged in a matrix that has $2^{\lfloor \log_2 \lfloor \sqrt{M} \rfloor \rfloor}$ number of rows and $\lceil M/(\text{number of rows}) \rceil$ number of columns, where $\lfloor \cdot \rfloor$ and $\lceil \cdot \rceil$ denote the floor and ceiling functions, respectively. For example, if we consider the $M = 128$ case, the number of rows is calculated by $2^{\lfloor \log_2 \lfloor \sqrt{128} \rfloor \rfloor} = 2^{\lfloor \log_2 (11) \rfloor} = 2^3 = 8$ and the number of columns is calculated by $\lceil 128/8 \rceil = 16$.

For example, if we have $d_{\text{Tx}} = d_{\text{Rx}} = 0.1$ [m] and $\left(\Phi_{\frac{1}{2}}, \Psi_{\frac{1}{2}} \right) = (15°, 45°)$, the channel matrix $\mathbf{H}$ for the $(M, N) = (8, 1)$ case is given by

$$A_{\text{PD}} \cdot \begin{bmatrix} 0.96266 & 1.03734 & 1.03734 & 0.96266 & 0.96266 & 1.03734 & 1.03734 & 0.96266 \end{bmatrix}.$$

Also, the channel matrix $\mathbf{H}$ for the $(M, N) = (8, 2)$ case is given by

$$A_{\text{PD}} \cdot \begin{bmatrix} 1.01715 & 1.05597 & 1.01715 & 0.90973 & 1.01715 & 1.05597 & 1.01715 & 0.90973 \\ 0.90973 & 1.01715 & 1.05597 & 1.01715 & 0.90973 & 1.01715 & 1.05597 & 1.01715 \end{bmatrix}.$$

Moreover, the channel matrix $\mathbf{H}$ for the $(M, N) = (8, 4)$ case is given by

$$A_{\text{PD}} \cdot \begin{bmatrix} 1.03614 & 1.07571 & 1.03614 & 0.92662 & 0.99814 & 1.03614 & 0.99814 & 0.89296 \\ 0.92662 & 1.03614 & 1.07571 & 1.03614 & 0.89296 & 0.99814 & 1.03614 & 0.99814 \\ 0.99814 & 1.03614 & 0.99814 & 0.89296 & 1.03614 & 1.07571 & 1.03614 & 0.92662 \\ 0.89296 & 0.99814 & 1.03614 & 0.99814 & 0.92662 & 1.03614 & 1.07571 & 1.03614 \end{bmatrix}.$$

5.3   Design Criteria

In this section, we introduce the design guidelines for the proposed PI-OSM scheme. The PA parameters are designed so as to maximize the constrained MI. Furthermore, the proposed

Irr-PI-OSM concatenates the multiple PI-OSM schemes and its irregular-partition ratios λ are designed so as to fit the aggregated EXIT curve to that of the outer code.

5.3.1   Constrained MI Aided Design

Before designing the PA parameters, we assume that the system parameters $(M, N, \mathcal{L})$ are given in advance. Since the transmission rate of the PI-OSM scheme is upper-bounded by $R = \log_2(M \cdot \mathcal{L})$ [bits/symbol], the constrained MI at high SNRs is also bounded by the associated rate R. For the given SNR and the given geometry of the transmitter and the receiver, the PA parameters $\mathbf{A} = \mathrm{diag}(a_1, \cdots, a_M)$ are designed in order to maximize the constrained MI with the following steps.

1. Generate M number of random values that follow i.i.d Gaussian distribution. Specifically, each PA parameter a_m $(1 \leq m \leq M)$ is set to the absolute value of $\mathcal{N}(1,1)$.

2. At the target SNR, calculate the constrained MI for the PI-OSM scheme having the randomly generated PA parameters.

3. If the calculated constrained MI is higher than the previously calculated ones, update the best MI value.

4. If the best MI value has not been updated against a sufficient number of MI calculations, adopt the best PA parameters and stop the searching process.

The searched PA parameters are listed in Appendix A.4. Note that the effects of the geometrical alignment error will be discussed in Fig. 5.11.

We provide the specific examples of the designed PA parameters, where we have $\left(\Phi_{\frac{1}{2}}, \Psi_{\frac{1}{2}}\right) = (15°, 45°)$. Fig. 5.5 compared the constellations of the equal-power OSM scheme [78], the conventional PI-OSM scheme having $\beta = 1, 3, 4$ [dB] and the proposed PI-OSM scheme, where the number of transmit source lights was $M = 4$ and the size of PAM symbols was $\mathcal{L} = 2$. Observe in Fig. 5.5 that the constellations of the conventional PI-OSM scheme having $\beta = 3$ and 4 [dB] were biased, where the maximum symbol value was around 3.0. This is because the conventional formula of Eq. (2.57) exponentially increases the PA parameters upon increasing the single parameter β. Our proposed scheme has a higher degree of freedom to design the PA parameters. As shown in Fig. 5.5, the constellations of the proposed PI-OSM scheme were uniformly distributed from 0.0 to 2.0. In Fig. 5.5, we
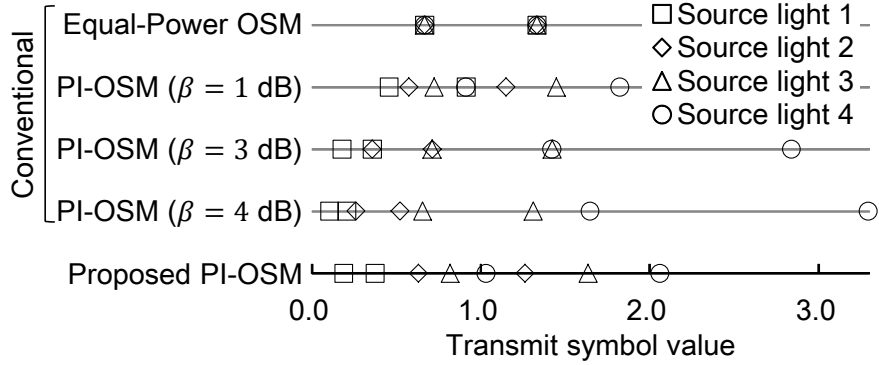
Figure 5.5 Constellation examples of the equal-power OSM, the conventional PI-OSM and the proposed PI-OSM. The number of transmit source lights was $M = 4$. The size of PAM constellation was $\mathcal{L} = 2$. Each mark corresponds to the emitted index of source light.

used the following PA parameters.

$$
\mathbf{A} = \begin{cases}
\text{diag}(1.0000,\ 1.0000,\ 1.0000,\ 1.0000) & (\text{Equal} - \text{power OSM}) \\
\text{diag}(0.6850,\ 0.8624,\ 1.0857,\ 1.3668) & (\text{Conventional PI} - \text{OSM having } \beta = 1\ [\text{dB}]) \\
\text{diag}(0.2681,\ 0.5349,\ 1.0673,\ 2.1296) & (\text{Conventional PI} - \text{OSM having } \beta = 3\ [\text{dB}]) \\
\text{diag}(0.1558,\ 0.3914,\ 0.9832,\ 2.4696) & (\text{Conventional PI} - \text{OSM having } \beta = 4\ [\text{dB}]) \\
\text{diag}(0.2814,\ 0.9459,\ 1.2276,\ 1.5451) & (\text{Proposed PI} - \text{OSM})
\end{cases}
$$

Here, the PA matrix for the proposed scheme was designed at the received SNR of $\rho = 25$ [dB].

5.3.2 EXIT-Chart Aided Design

The invention of EXIT charts enables us to analyze the convergence behavior of the iterative iterations at the receiver [20]. Fig. 5.6 shows the EXIT curves of the half-rate RSC code having the constraint length of 5, the $\mathcal{L} = 64$–PAM aided RC, and the $\mathcal{L} = 8$–PAM aided PI-OSM, where the received SNR was fixed to 32 [dB] and the numbers of transmit and receive elements were $(M,N) = (8,4)$. The transmission rate of each inner sub-code was fixed to 6.0 [bits/symbol]. Fig. 5.6 has 14 EXIT curves for the $\mathcal{L} = 8$–PAM aided PI-OSM scheme, where each PA matrix was designed at the 14 target SNRs of -20, -15, -10, -5, 0, 5, 10, 15, 20, 25, 30, 35, 40, and 45 [dB]. Observe in Fig. 5.6 that the EXIT curves of PI-OSM were diverse, although the system parameters $(M,\mathcal{L})$ were fixed. These diversities in EXIT curves were accomplished by the flexible PA architecture of the proposed PI-OSM scheme.
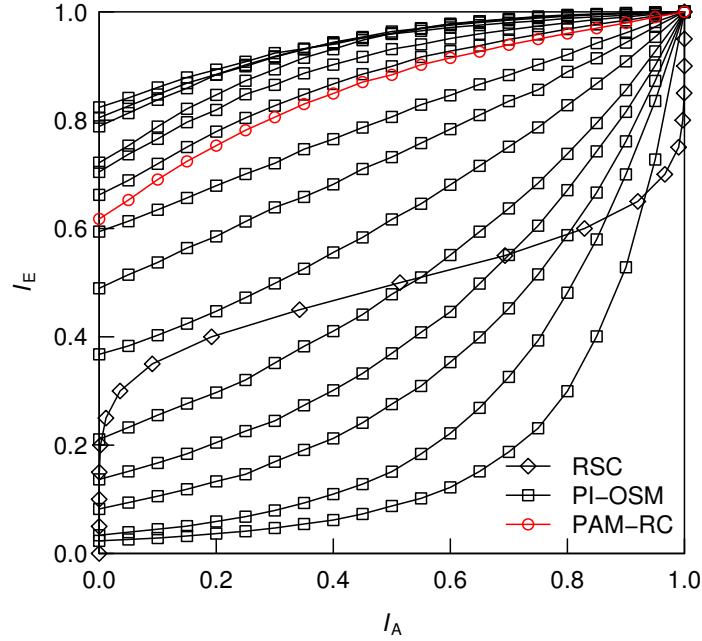
Figure 5.6 EXIT curves of the RSC– encoded and URC–encoded PAM-RC and PI-OSM, where we have SNR of $\rho = 32$ [dB] and $R = 6.0$ [bits/symbol]. The PA parameters of PI-OSM were designed to maximize the constrained MI at the target SNRs: $-20, -15, \cdots, 45$ [dB].

The EXIT function of the irregular-precoded inner code, that consists of multiple inner sub-codes, is given by [20]

$$I_E(I_A, \rho) = \sum_{p=1}^{P} \lambda_p I_E^{(p)}(I_A, \rho), \tag{5.13}$$

where $I_E^{(p)}(I_A, \rho)$ denotes the EXIT function of the pth inner code. Here, the received SNR ρ and *a priori* information I_A are given in advance. The irregular-partition ratio $\lambda \in \mathbb{R}^P$ is designed so as to minimize the area between Eq. (5.13) and the EXIT curve of the outer code $I_E^{\mathrm{RSC}}(I_A)$. Minimizing the area between $I_E(I_A, \rho)$ and $I_E^{\mathrm{RSC}}(I_A)$ is equivalent to maximizing the aggregate transmission rate of Eq. (5.10), which is further simplified to minimizing $\sum_{p=1}^{P} \lambda_p / R_p$ because R_{RSC} is a constant value.

The design guidelines for the Irr-PI-OSM scheme are summarized as follows.

1. Determine a target turbo-cliff SNR ρ_{target}.[1]

---

[1] At the turbo-cliff SNR, the BER curve exhibits a "cliff", where the BER drops to zero.

2. Prepare as many inner PI-OSM sub-codes as possible. The number of the prepared sub-codes is represented by P'. Also, the transmission rate of the pth inner sub-code is represented by R_p $(1 \leq p \leq P')$.

3. Calculate P' number of EXIT curves for the prepared sub-codes at SNR $= \rho_{\text{target}}$ [dB]. The pth EXIT curve is represented by $I_E^{(p)}(I_A, \rho_{\text{target}})$ $(1 \leq p \leq P')$.

4. Solve the following linear programming problem with respect to $\boldsymbol{\lambda} = [\lambda_1, \cdots, \lambda_{P'}]$.

$$
\begin{aligned}
\text{minimize} \quad & \sum_{p=1}^{P'} \lambda_p / R_p \\
\text{subject to} \quad & \sum_{p=1}^{P'} \lambda_p I_E^{(p)}(I_A, \rho_{\text{target}}) \geq I_E^{\text{RSC}}(I_A) \\
& \sum_{p=1}^{P'} \lambda_p = 1
\end{aligned}
$$

During the above optimization process, we employ the solving constraint integer programs (SCIP) [159], which is a non-commercial solver for the mixed integer linear/nonlinear programming. Note that the above guidelines are directly applicable to other encoding schemes, such as the PAM-RC and the conventional OSM. After the solution $\boldsymbol{\lambda}$ is determined, we obtain the aggregate transmission rate R. Hence, R is a function of the target SNR ρ_{target}. The above optimization converges immediately because the objective function $\sum_{p=1}^{P'} \lambda_p / R_p$ is a linear combination of $\boldsymbol{\lambda} = [\lambda_1, \cdots, \lambda_P]$.

5.3.3   Adaptive Operation

In Section 5.3, we presented the design guidelines for the proposed PI-OSM scheme. In Section 5.3.1, the flexible PA parameters are designed so as to maximize the constrained MI, while in Section 5.3.2 the irregular-partition ratio $\boldsymbol{\lambda}$ is designed so as to minimize the turbo-cliff SNR. Both guidelines depend on the target SNR ρ_{target}. Hence, the PI-OSM scheme designed for SNR $= \rho_{\text{target}}$ may not achieve a good performance in other SNR region. In order to combat this limitation, we further propose an adaptive operation method for the PI-OSM scheme. Here, we assume that a feedback link from the receiver to the transmitter, which exchanges the received SNR information at the receiver.

For the constrained MI case, we prepare N_s number of PA matrices $\mathbf{A}^{(1)}, \cdots, \mathbf{A}^{(N_s)}$ that are designed for the target SNRs $\rho^{(1)}, \cdots, \rho^{(N_s)}$. Both the transmitter and the receiver adaptively

Table 5.2 Simulation parameters of the conventional and proposed PI-OSM schemes.

Number of transmit source lights	$M = 2, 4, 8, 16, 32, 64, 128, 256$
Number of receive PDs	$N = 1, 2, 4, 8, 16$
Response of PD	$R_{\text{PD}} = 1$ [A/W]
Physical area of PD	$A_{\text{PD}} = 10^{-4}$
Field-of-view semi-angle of source light	$\Phi_{\frac{1}{2}} = 15°$
Field-of-view semi-angle of PD	$\Psi_{\frac{1}{2}} = 45°$
Height of the transmitter	2.5 [m]
Height of the receiver	0.75 [m]
Channel	Indoor MIMO-VLC path-loss model
Detector	Maximum-likelihood detection
Modulation	PAM ($\mathcal{L} = 2, 4, 16$)

select the PA matrix out of $\mathbf{A}^{(1)}, \cdots, \mathbf{A}^{(N_s)}$ based on the SNR at the receiver. Hence, the constrained MI is maximized at any SNR.

For the irregular-precoded case, we prepare N_s number of irregular-partition ratios $\lambda^{(1)}, \cdots, \lambda^{(N_s)}$ that are designed for the target SNRs $\rho^{(1)}, \cdots, \rho^{(N_s)}$. Similar to the constrained MI case, both the transmitter/receiver select the appropriate irregular-partition ratio based on the received SNR. Hence, the receiver achieves the error-free detection at any SNR, while the transmission rate also adaptively changes.

5.4 Performance Results

In this section, we investigate the achievable performance of our proposed scheme, in terms of the constrained MI and the BER in uncoded/coded scenarios. The unconstrained/constrained MI are formulated in Sections 2.2.1.1 and 2.2.1.2, which are directly applicable to the MIMO-VLCs. The unconstrained MI curve was depicted as a reference, in accordance with the constrained MI curves. The LoS MIMO-VLC channel environment is fixed to the geometrical model given in Section 5.2.2, where we have $\left(\Phi_{\frac{1}{2}}, \Psi_{\frac{1}{2}}\right) = (15°, 45°)$ and $d_{\text{Tx}} = d_{\text{Rx}} = 10$ [cm]. The PA matrix of PI-OSM was designed with the criteria provided in Section 5.3.1, while the irregular-partition ratio λ was designed with the criteria provided in Section 5.3.2. The simulation parameters considered in this section are summarized in Table 5.2.
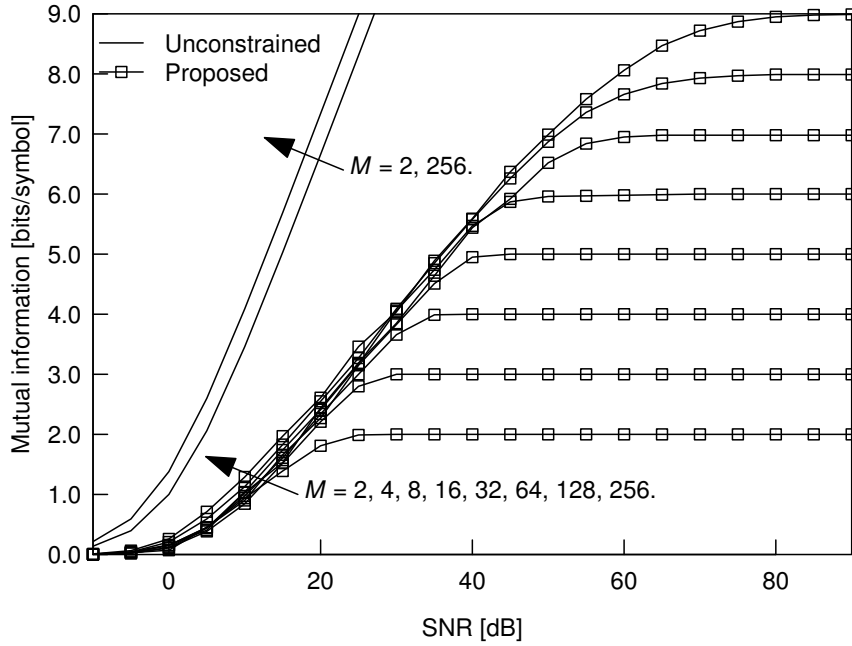
Figure 5.7 Constrained MI of the $\mathcal{L} = 2$–PAM aided PI-OSM having $M = 2, 4, 8, 16, 32, 64, 128$, and 256. The unconstrained MI for the $M = 2$ and 256 cases were also depicted as a reference. The number of PDs at the receiver was $N = 1$.

5.4.1 Average Mutual Information

In Fig. 5.7, we investigated the constrained MI of our proposed scheme, where the number of source lights was varied from $M = 2$ to 256. The number of PAM constellations and the number of PDs were fixed to $(\mathcal{L}, N) = (2, 1)$. The unconstrained MI was plotted in order to reveal the upper bound of the constrained MI. Observe in Fig. 5.7 that the achievable rate of the PI-OSM scheme monotonically increased upon increasing the number of source lights M. Note that in this simulation scenario, the rank of the channel matrix was constrained to $E[\text{rank}(\mathbf{H})] = 1$. Hence, the unconstrained MI for the $M = 2$ and 256 cases were close to each other, where there was the gap of 2.0 [dB].

In Fig. 5.8, we compared the constrained MI of our proposed scheme, the PAM-RC, and the equal-power OSM, where the number of source lights was $M = 2$ and the number of PDs was $N = 1$. We designed the PA matrix of the PI-OSM scheme both at the low SNR of 10 [dB] and the high SNR of 20 [dB] in order to investigate the effects of the target SNR. It was shown in Fig. 5.8 that the PI-OSM scheme designed for $\rho_{\text{target}} = 10$ [dB] achieved the best constrained MI at the half rate of 1.0 [bits/symbol]. Note the the PAM-RC scheme achieved the best performance in the SNR region between 13 and 27 [dB], where the PI-OSM scheme designed for $\rho_{\text{target}} = 20$ [dB] was worse than the PAM-RC scheme. Due to the high
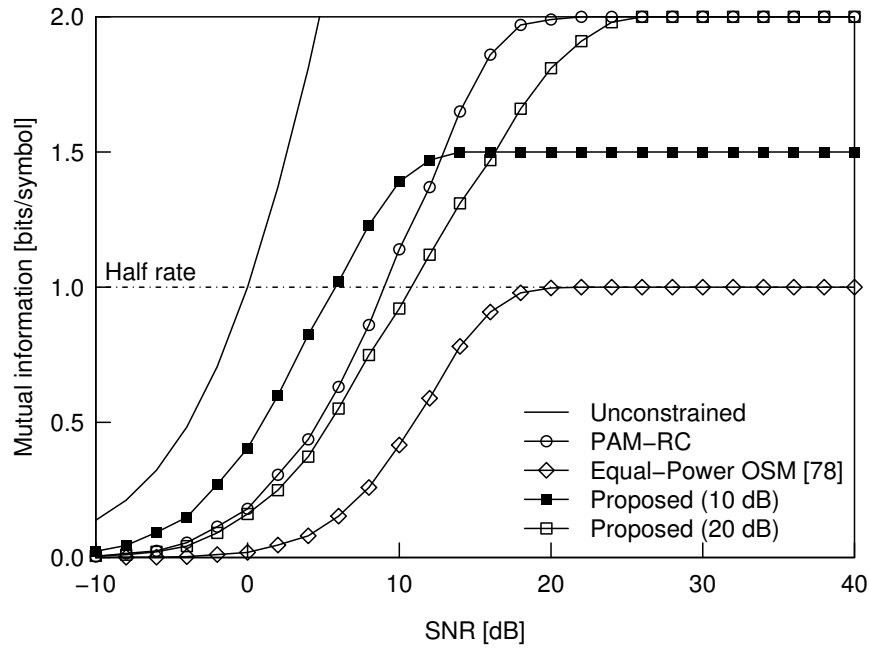
Figure 5.8 Constrained MI of the $\mathcal{L} = 2$–PAM aided PI-OSM, the $\mathcal{L} = 4$–PAM aided RC, and the $\mathcal{L} = 2$–PAM aided equal-power OSM, where we have $(M,N) = (2,1)$. The PA matrix of the proposed PI-OSM scheme was designed at $\rho_{\text{target}} = 10$ and 20 [dB]. All the schemes have the same rate of $R = 2.0$ [bits/symbol].

correlations between the channel coefficients, the conventional equal-power OSM achieved 1.0 [bits/symbol], which came from the $\mathcal{L} = 2$–PAM symbols.

In Fig. 5.9, we compared the constrained MI of our proposed adaptive scheme, the PAM-RC, the equal-power OSM, and the conventional PI-OSM, where the number of source lights was $M = 8$ and the number of PDs (a) $N = 1$ and (b) $N = 2$. The PA matrix of the adaptive PI-OSM was designed at the target SNRs $\rho_{\text{target}} = -10, -5, \cdots, 30$ [dB], while the PA matrix of the conventional PI-OSM scheme was generated with Eq. (2.57) having $\beta = 1.0, 3.0, 4.0$ [dB]. It was shown in Fig. 5.9(a) that the adaptive PI-OSM scheme achieved the highest constrained MI in the entire SNR region, both for the $N = 1$ and 2 cases. The constrained MI of the equal-power OSM increased upon increasing N, however, it did not reach the full rate of 4.0 [bits/symbol]. The conventional PI-OSM [101] improved this limitation and achieved a higher performance than the equal-power OSM. Note that the PAM-RC scheme achieved the best performance in the SNR region between 28 and 36 [dB].

In Fig. 5.10, we investigated the constrained MI of our proposed scheme, the equal-power OSM, and the conventional PI-OSM, where the number of PD was $N = 1$ and the size of PAM constellations was $\mathcal{L} = 2$. The number of source lights was set to $M = 4, 16, 64$, and 256. The PA matrix of both the proposed and conventional PI-OSM was designed with the

(a) $N = 1$.

(b) $N = 2$.

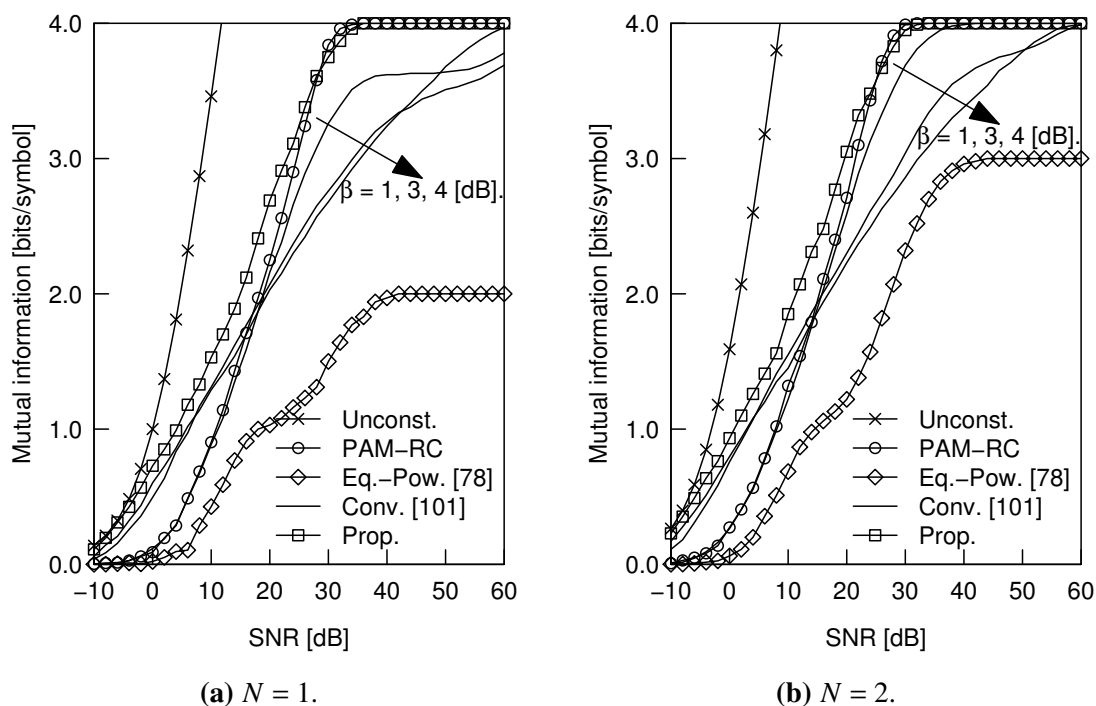**Figure 5.9** Constrained MI of the $\mathcal{L} = 2$–PAM aided adaptive PI-OSM, the $\mathcal{L} = 16$–PAM aided RC, the $\mathcal{L} = 2$–PAM aided equal-power OSM, and the $\mathcal{L} = 2$–PAM aided conventional PI-OSM, where the number of source lights was $M = 8$. All the schemes have the same rate of 4.0 [bits/symbol]. Our scheme is adaptively optimized corresponding with each SNR point.
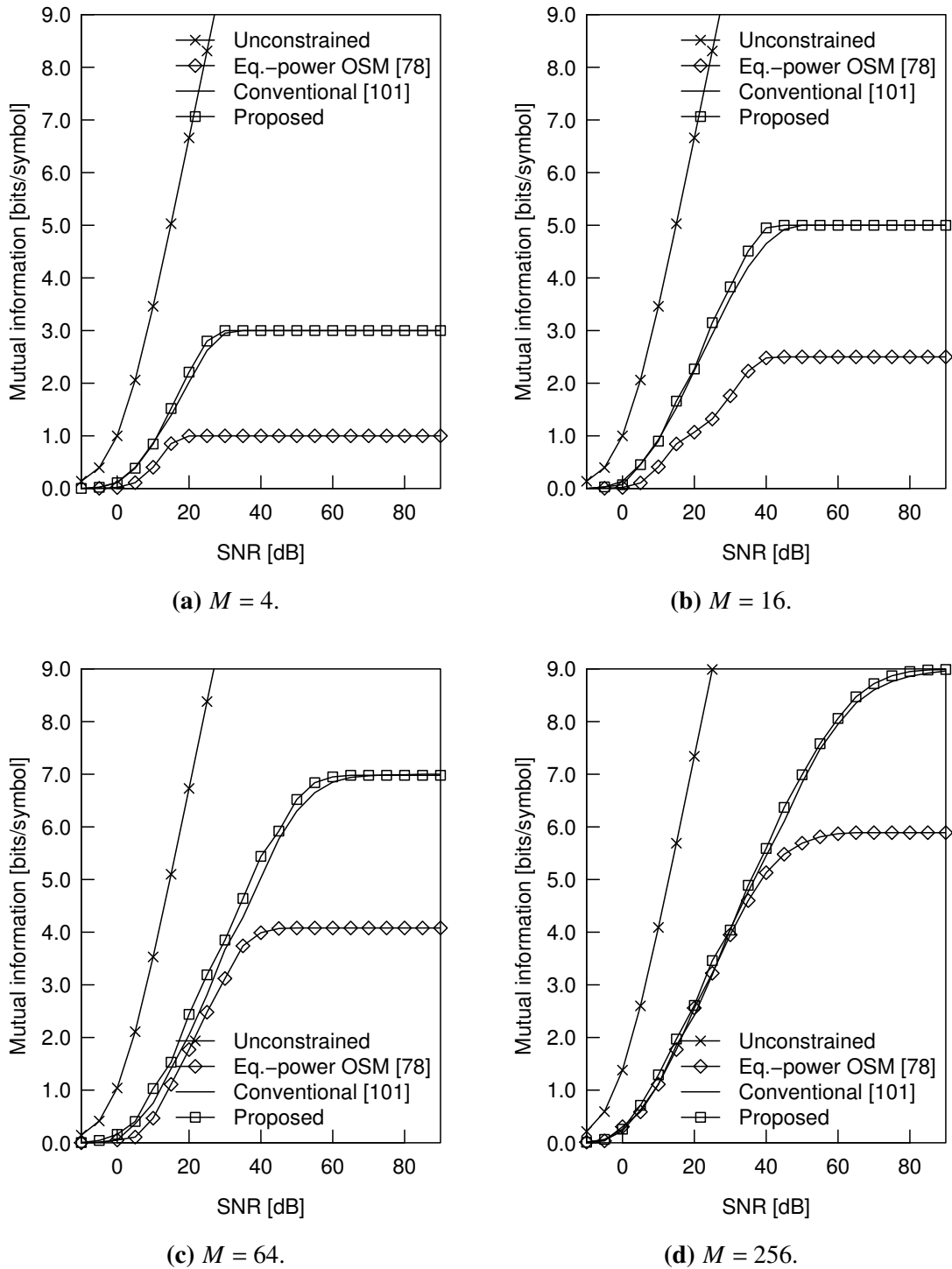
Figure 5.10 Constrained MI of the $\mathcal{L} = 2$–PAM aided PI-OSM, the equal-power OSM, and the conventional PI-OSM, where we have $M = 4,16,64,256$ and $N = 1$. The single PA parameter of β for the conventional PI-OSM was designed by our proposed guidelines.
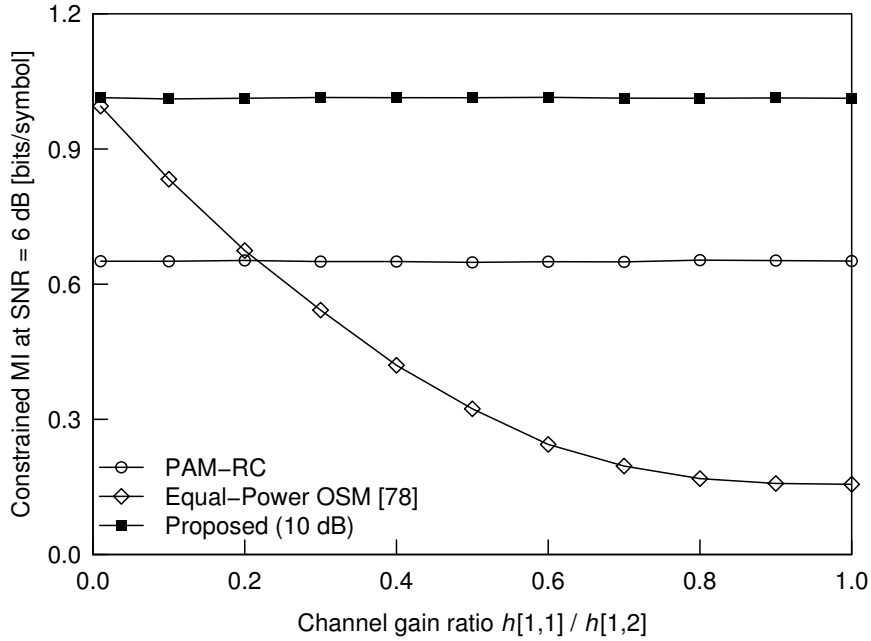
Figure 5.11 Effects of the channel correlation on the constrained MI of the proposed PI-OSM scheme, the PAM-RC scheme, and the conventional equal-power OSM scheme. All the simulation parameters were the same with those used in Fig. 5.8 except for the channel environment. The ratio of two channel coefficients was varied in the range of $0 < (h[1,1]/h[1,2]) \leq 1$, while maintaining the received SNR to be $\gamma = 6$ [dB].

same guidelines provided in Section 5.3.1, hence the constrained MI was maximized at the same target SNR. Under this assumption, the optimum single parameters for the conventional PI-OSM were $\beta = 2.02, 0.57, 0.10, 0.02$ [dB], corresponding to the $M = 4, 16, 64, 256$ cases. Note that these parameters β were not introduced in [101]. It was shown in Fig. 5.10 that the constrained MI of both the proposed and conventional PI-OSM were close to each other. However, the performance gains of the proposed PI-OSM scheme lasted for all the $M = 4, 16, 64, 256$ scenarios. Similar to Figs. 5.8 and 5.9, the equal-power OSM was difficult to attain its performance advantage in highly-correlated channel environments.

In Fig. 5.11, we investigated the effects of the channel correlation. Based on the scenario considered in Fig. 5.8, where we had the simplified $(M = 2)$-by-$(N = 1)$ MIMO-VLC arrangement, we changed the ratio between the two channel coefficients $h[1,1] \in \mathbb{R}$ and $h[1,2] \in \mathbb{R}$. Specifically, the ratio $h[1,1]/h[1,2]$ was varied in the range of $0 < (h[1,1]/h[1,2]) \leq 1$. It was shown in Fig. 5.11 that the proposed PI-OSM scheme exhibited a higher MI than the benchmark schemes. This is because our proposed PA matrix is capable of combating the effects of the highly-correlated channels. The performance gain of the proposed PI-OSM
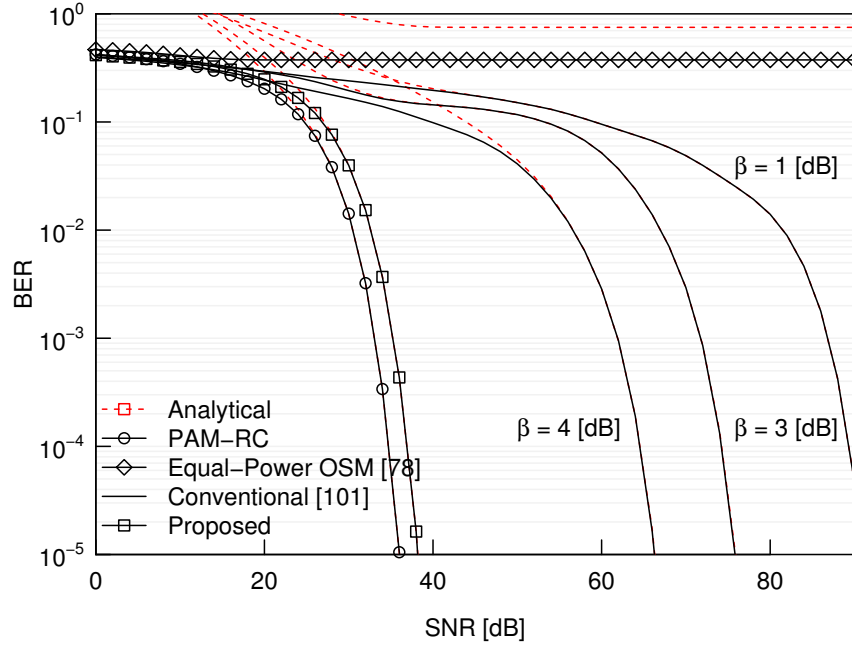
Figure 5.12 BER comparison of the schemes demonstrated in Fig. 5.9(a) in an uncoded scenario. All the simulation parameters were the same with those used in Fig. 5.9(a). The dotted lines represent theoretical BER values. 10^7 bits were randomly generated for each BER calculation.

scheme over the conventional equal-power OSM scheme was explicit in the high-correlation region.

5.4.2   BER in Uncoded and Coded Scenarios

In Fig. 5.12, we investigated the BER performances of the schemes considered in Fig. 5.9(a) in an uncoded scenario. The theoretical BER values were calculated by Eq. (2.58). It was shown in Fig. 5.12 that the conventional PAM-RC scheme outperformed the proposed PI-OSM scheme, where there was the gap of 2.0 [dB]. This is because our original target is the maximization of the constrained MI, which is effective in coded scenarios.

Later, we investigate the performance advantage of the proposed PI-OSM scheme in coded scenarios, assuming that we have $(M, N) = (8, 4)$ and $R = 2.0$ [bits/symbol]. The simulation parameters considered in the coded scenario are given in Table 5.3. We used the design criteria given in Section 5.3.2 for designing the irregular-precoded PAM-RC and PI-OSM. For the $(M, N, R) = (8, 4, 2)$ scenario, the designed irregular-precoded PAM-RC was composed of $(\mathcal{L} = 8)$ and $(\mathcal{L} = 1024)$–PAM aided RC with the ratio of $\lambda = [0.638, 0.362]$. Hence, the aggregate transmission rate was calculated by $R = R_{\text{RSC}}/(0.638/3 + 0.362/10) = 2.009$ [bits/symbol]. Also, the designed Irr-PI-OSM was composed of $(\mathcal{L} = 1)$ and $(\mathcal{L} = 128)$–PAM

Table 5.3 Simulation parameters of the irregular turbo-coded PI-OSM scheme.

Detector	Max-log MAP detector
Interleaver length	10^7
Outer channel code	Half-rate RSC ($R_{\mathrm{RSC}} = 1/2$)
RSC constraint length	5
RSC octal generator polynomials	[35 23]
Number of inner iterations	$I_{\mathrm{in}} = 30$
Number of outer iterations	$I_{\mathrm{out}} = 2$

aided PI-OSM, both designed at SNR = 10 [dB], with the ratio of $\lambda = [0.6428, 0.3572]$. The aggregate transmission rate was calculated by $R = R_{\mathrm{RSC}}/(0.6428/3 + 0.3572/10) = 2.000$ [bits/symbol].

Fig. 5.13 shows the constrained MI of the Irr-PI-OSM, the non-irregular coded PI-OSM, and the non-irregular coded PAM-RC, where we have $(M, N, R) = (8, 4, 2)$. Observe in Fig. 5.13 that the Irr-PI-OSM attained a higher constrained MI as compared to the benchmark schemes in the SNR between -20 and 15 [dB]. The Irr-PI-OSM reached the half-rate point at SNR = 9.01 [dB], which was smaller than the other benchmarks.

Fig. 5.14 shows the uncoded and coded BER comparisons of the PAM-RC and PI-OSM schemes. For the uncoded and three-stage coded scenarios, the $(\mathcal{L} = 16)$–PAM aided RC and $(\mathcal{L} = 2)$–PAM aided PI-OSM were considered, where the PA matrix was designed at $\rho_{\mathrm{target}} = 20$ [dB]. Observe in Fig. 5.14 that the non-irregular coded and irregular-coded PI-OSM outperformed the PAM-RC scheme. In the three-stage coded scenarios, the turbo-cliff SNR of the PI-OSM was lower than that of the PAM-RC by 0.64 [dB]. In the irregular coded scenarios, the turbo-cliff SNR of the PI-OSM was lower than that of the PAM-RC by 1.28 [dB]. Note that in the uncoded scenario, the proposed PI-OSM performed worse than the conventional PAM-RC, where there was the gap of 15.79 [dB] at the BER = 10^{-5}.

Fig. 5.15 shows the EXIT charts of the Irr-PI-OSM and its decoding trajectory, where the received SNR was 13 [dB]. The EXIT curve of Irr-PI-OSM was a weighted average of the EXIT curves of the inner sub-codes. Observe in Fig. 5.15 that the iterative decoding at the receiver succeeded in passing through the open EXIT tunnel between the inner and the outer codes. This EXIT-chart analysis successfully predicted the turbo-cliff SNR at 12.83 [dB] of Irr-PI-OSM, which is shown in Fig. 5.14.

In Fig. 5.16, we investigated the turbo-cliff SNRs of the irregular-precoded PAM-RC and PI-OSM in a comprehensive manner, where we have $(M, N) = (8, 4), (8, 8), (8, 16)$. The turbo-cliff SNR is the SNR required for achieving an infinitesimal BER. The $(M, N, R) = (8, 4, 2)$ point in Fig. 5.16 corresponds to the simulations shown in Figs. 5.13, 5.14, and 5.15. Observe
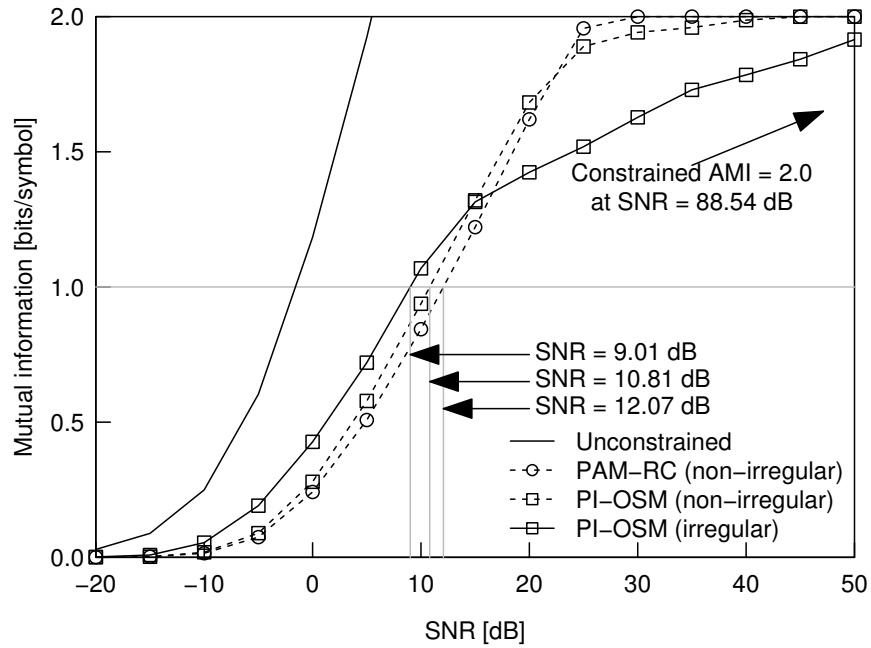
Figure 5.13 Constrained MI of the Irr-PI-OSM, the $\mathcal{L} = 2$–PAM aided PI-OSM, and the $\mathcal{L} = 16$–PAM aided RC, where we have $(M,N) = (8,4)$. The aggregate rate of each scheme was fixed to 2.0 [bits/symbol].
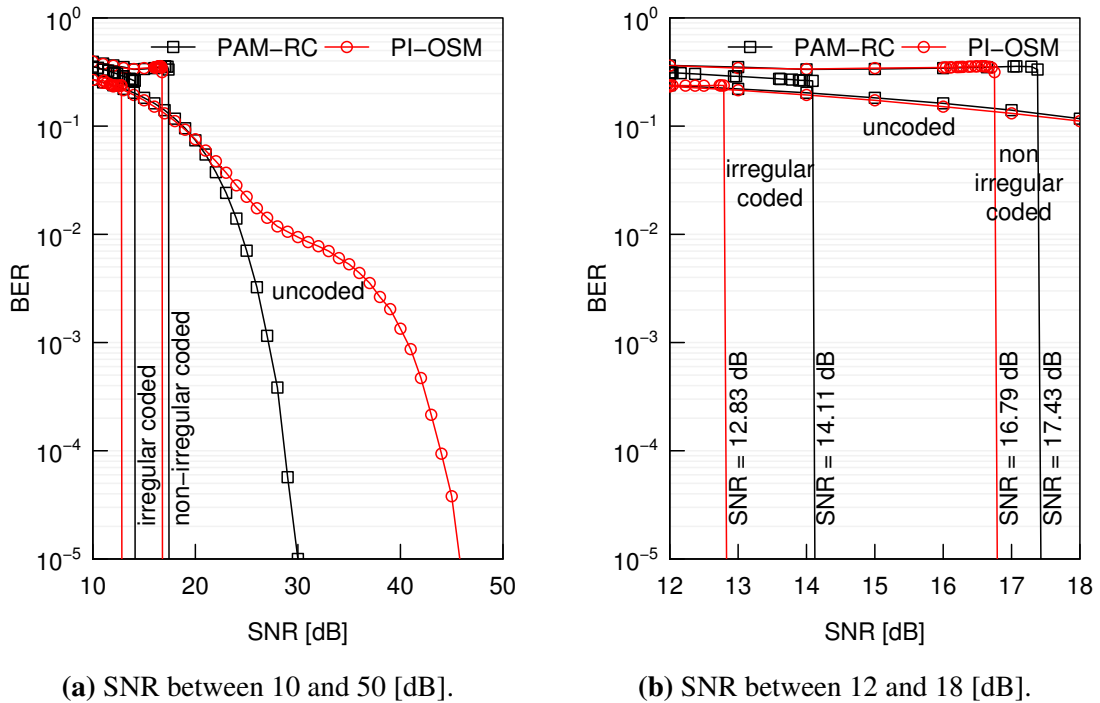
(a) SNR between 10 and 50 [dB].

(b) SNR between 12 and 18 [dB].

Figure 5.14 BER of the PAM-RC and the PI-OSM schemes where we have $(M,N) = (8,4)$ and $(N_{\text{out}}, N_{\text{in}}) = (2,30)$. Each scheme was simulated in the following three scenarios: uncoded, 3-stage coded, and irregular-precoded scenarios.

Figure 5.15 EXIT charts of the Irr-PI-OSM and its decoding trajectory at SNR = 13 [dB], which was observed in the BER simulations of Fig. 5.14.
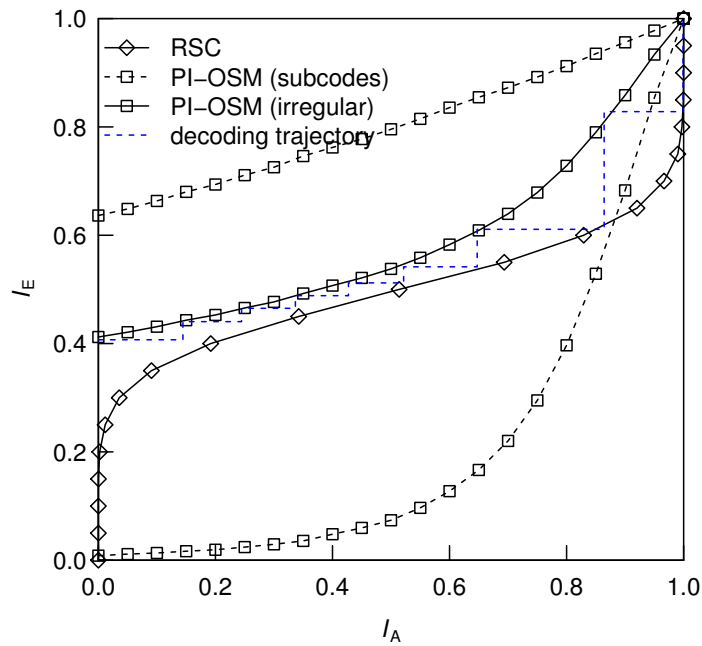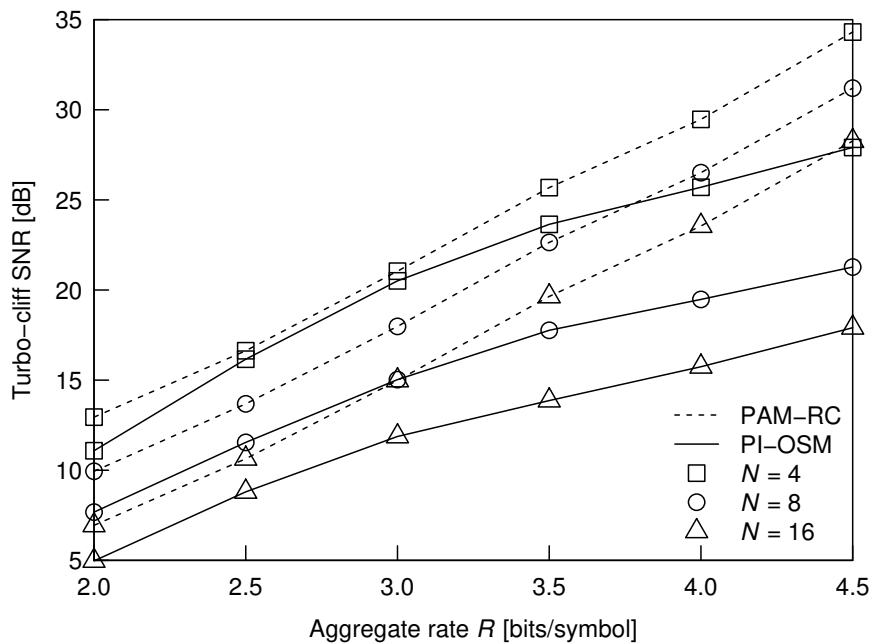

Figure 5.16 Comprehensive turbo-cliff SNR comparisons of the irregular-precoded PAM-RC and PI-OSM, where we considered $M = 8$ and $N = 4, 8, 16$.

in Fig. 5.16 that the Irr-PI-OSM exhibited a lower turbo-cliff SNR as compared to the PAM-RC. The performance advantage of the Irr-PI-OSM over PAM-RC monotonically increased upon increasing the transmission rate R. This implies that the proposed Irr-PI-OSM scheme is efficient in high-rate scenarios.

5.5   Chapter Conclusions

In this chapter, we evaluated the PM concept applied to VLC. We demonstrated that the constrained MI of the proposed PI-OSM scheme was significantly higher than that of the conventional PI-OSM and PAM-RC schemes, with the aid of the novel guidelines for the PA matrix and irregular-partition ratio. Our guidelines enable the MIMO-VLC system to carry out the adaptive operation based on the received SNR. In uncoded scenarios, the BER of the proposed scheme performed worse than that of the conventional schemes because our original aim is improving the constrained MI, which is effective in coded scenarios. In coded scenarios, we found that the performance advantage of our proposed scheme over the conventional scheme monotonically increased upon increasing the transmission rate. Hence, we conclude that the proposed PI-OSM and Irr-PI-OSM schemes are effective in high-rate scenarios.

Chapter 6

Permutation Modulation Based Multicarrier Communications

6.1 Introduction

In this chapter, we review the PM concept applied to multicarrier communications and analyze it in terms of the information-theoretic perspective. As mentioned in Chapter 1, OFDM is an established multicarrier communication technique that has played a key role in the numerous communication standards. The OFDM scheme is capable of exploiting the limited bandwidths effectively, while the available bandwidths per user are decreasing year by year against the rapidly increasing number of mobile devices. In Chapter 2, we reviewed the PM concept applied to OFDM, which is referred to as "subcarrier-index modulation (SIM)" [76], where its research background was detailed in Section 2.6. The OFDM scheme conveys the data symbols over all of the allocated subcarriers, while the SIM scheme activates a part of subcarriers. Here, the SIM scheme allocates additional bits by selecting the subcarrier-activation indices; similar to the SM concept. Hence, the key feature of SIM is the sparsity of the symbols distributed over the frequency domain. It has been shown in [160, 76, 96] that the sparsity of the SIM symbols affects bandwidth efficiency, reliability, power consumption, complexity, and PAPR.

In most of the previous studies, as introduced in Section 2.6, the SIM scheme has been evaluated in uncoded scenarios. In practice, the current wireless systems have to rely on the channel codes to attain a near-capacity performance against the severe fading channels. The only exceptions were found in [95] and [97]. In [95], the SIM scheme was evaluated

in the channel-coded system, where the BER of the SIM scheme outperformed that of the OFDM scheme in a specific scenario. However, no theory was provided in [95]. In [97], the maximum achievable rate (MAR) was derived by assuming the AWGN and fading channels. The derived MAR is a practical metric to estimate the performance upper-bound in coded scenarios. In terms of the PAPR analysis, the previous studies [76, 140] relied on the numerical calculations. Also, the maximum PAPR of the SIM scheme was derived in [141]. As mentioned in [161], it is important to derive the exact distribution of PAPR in order to characterize the time-variant signals, instead of deriving the maximum PAPR.

Against this background, in this chapter, we provide the information-theoretic analysis of the SIM scheme. First, we formulate the MED of the SIM symbols and derive its upper-bound. Based on the derived upper-bound of MED, we propose our design guidelines for the SIM scheme, which identify the optimal subcarrier-activation ratio for a given rate, in terms of maximizing the coding gain. Second, we derive the constrained and unconstrained AMI of the SIM scheme in AWGN and Rayleigh fading channels. Third, we characterize the PAPR of the SIM scheme by considering the level-crossing rate analysis of [161]. Finally, we justify the above analysis by numerical simulations, in terms of the BER in uncoded/coded scenarios, the unconstrained/constrained AMI, and the PAPR.

The remainder of this chapter is organized as follows. Section 6.2 reviews the system model of the SIM scheme proposed in [76, 96] and introduces the three-stage turbo-coded counterpart. Section 6.3 provides the information-theoretic analysis, in terms of the MED, the constrained/unconstrained AMI, and the PAPR. Section 6.4 compares the performance of the SIM and OFDM schemes with numerical and theoretical calculations. Finally, Section 6.5 concludes this chapter.

6.2   System Model

In this section, we review the system model of the SIM transmitter and its encoding principle. Then, we revisit the SIM receiver, including the channel model assumed in this chapter.

6.2.1   SIM Transmitter

Throughout this chapter, N denotes the length of whole system subcarriers and M denotes the length of grouped subcarriers. Here, N subcarriers are divided into subcarrier groups, each of which has the length of M, hence N is divisible by M.

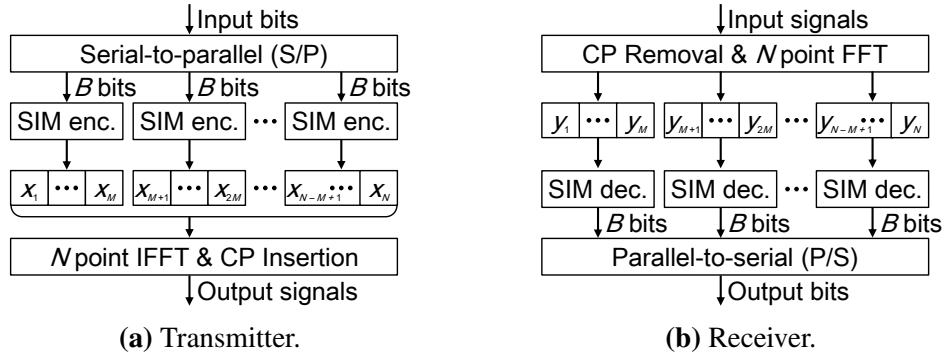**(a)** Transmitter.   **(b)** Receiver.

Figure 6.1 System schematic of the SIM transmitter and receiver.

Fig. 6.1(a) shows the schematic of the SIM transmitter. In Fig. 6.1(a), the input bits are divided into N/M number of groups. Each group is composed of the B bits and is modulated by the SIM encoder. The SIM encoder outputs a symbol vector having the length of M in the frequency domain. Then, the N/M number of generated vectors are merged into $\mathbf{x} \in \mathbb{C}^N$. In this chapter, the nth element of the vector $\mathbf{x}$ is denoted by x_n ($1 \le n \le N$). Finally, the vector $\mathbf{x}$ in the frequency domain is converted into the time-domain signals $x(t)$ ($0 \le t \le T_s$) with the N-point inverse Fourier transform (IFT):

$$x(t) = \frac{1}{\sqrt{N}} \sum_{n=1}^{N} x_n \exp\left(j\omega_n t\right), \tag{6.1}$$

where we have

$$\omega_n = \frac{2\pi}{T_s}\left(n - \frac{N+1}{2}\right). \tag{6.2}$$

Here, we ignore the CP insertion for simplicity, except for the PAPR simulations. The PAPR of the signals generated by Eq. (6.1) is given by

$$\text{PAPR} = \frac{\max_{0 \le t \le T_s} |x(t)|^2}{\sigma_x^2}, \tag{6.3}$$

where the mean of the data symbols x_n is zero and its variance is given by

$$\sigma_x^2 = \frac{1}{N} \cdot \text{E}\left[\sum_{n=1}^{N} |x_n|^2\right]. \tag{6.4}$$
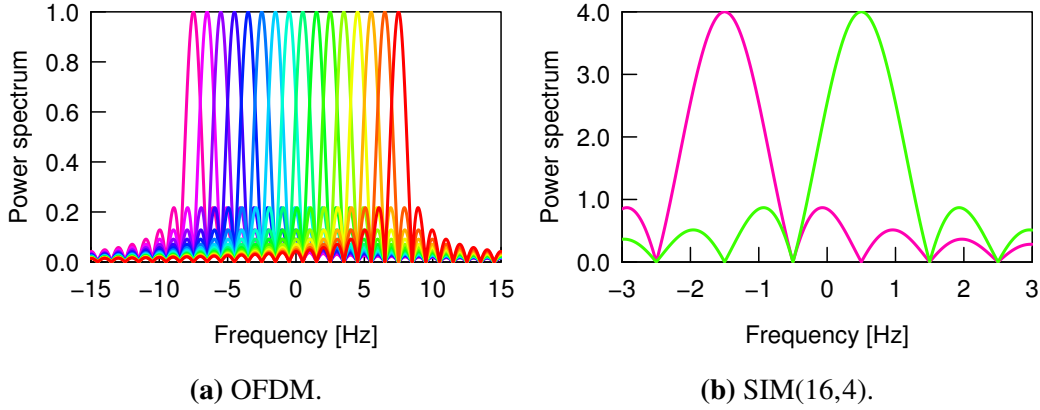
(a) OFDM.   (b) SIM(16,4).

Figure 6.2 Examples of power spectrum, where we have $T_s = 1$ [sec] and $N = 16$ subcarriers.

For fair comparisons, the transmit powers of OFDM and SIM are constrained to the same value. For example, Fig. 6.2 illustrates the power spectrum of OFDM and SIM, where we have $T_s = 1$ [sec] and $N = 16$ subcarriers. As shown in Fig. 6.2, OFDM uses the whole part of the allocated subcarriers in the frequency domain, while SIM activates a part of them. The transmit power of SIM and OFDM were the same in Fig. 6.2, since the peaks of the power spectrum were different.

The SIM encoder modulates $B = B_1 + B_2$ input bits into a complex-valued vector having the length of M, based on the GSM(M,P) encoding of Section 2.3.2. The modulated vector contains P number of non-zero elements and $M - P$ number of zeros. Later, the SIM system having the parameters M and P is represented by "SIM(M,P)", which is the same with the GSM(M,P) mapping. Based on the first $B_1 = P \log_2 \mathcal{L}$ [bits], P number of the traditional APSK symbols are modulated. Here, $\mathcal{L}$ denotes the size of APSK constellations. The modulated symbols are amplified by the power-scaling factor $\sqrt{M/P}$ to maintain the same transmit power. Based on the second $B_2 = \left\lfloor \log_2 \binom{M}{P} \right\rfloor$ bits, P number of subcarriers are selected out of M subcarriers. Here, we have $N_a = 2^{B_2}$ number of subcarrier activation patterns. For the ith activation pattern, the positions of non-zero elements are represented by the vector $\mathbf{a}_i \in \mathbb{Z}^P$. The above modulation process is the same with the GSM(M,P) encoding. Refer to Section 2.3.2 for further details and examples.

The transmission rate of the SIM transmitter is given by

$$R = \frac{B}{M} = \frac{B_1 + B_2}{M} = \frac{1}{M} \left(P \log_2 \mathcal{L} + \left\lfloor \log_2 \binom{M}{P} \right\rfloor \right) \quad \text{[bits/s/Hz]}. \quad (6.5)$$

Fig. 6.3 shows the maximum achievable rates of the SIM transmitter. In Fig. 6.3, for the given parameters $(M, \mathcal{L})$, the maximum value of R was searched by changing the number of
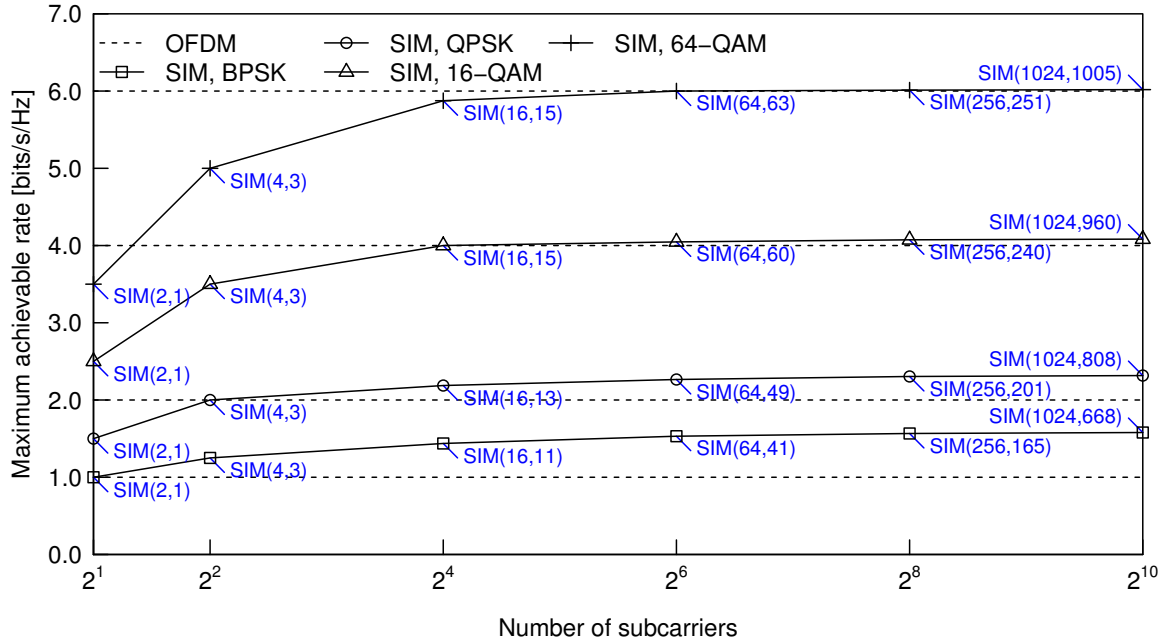
Figure 6.3 Maximum rates of the SIM transmitter, where the number of subcarriers was changed from $N = 2^1$ to 2^{10}. We considered $\mathcal{L} = 2, 4, 16, 64$–APSK modulations.

activated subcarriers P. The transmission rate of OFDM was also plotted for reference. For example, if we have $(M, \mathcal{L}) = (4, 4)$, the transmission rate is maximized at $P = 3$, where its transmission rate is calculated by 2.0 [bits/s/Hz]. As shown in Fig. 6.3, the maximum rate of the SIM system is upper-bounded by a certain value, which will be analyzed in Section 6.3.1.

6.2.2   SIM Receiver

Fig. 6.1(b) shows the schematic of the SIM receiver. After removing the CP and applying the fast Fourier transform, each received symbol y_n in the frequency domain is represented by

$$y_n = h_n x_n + v_n \ \in \mathbb{C} \ (1 \le n \le N), \tag{6.6}$$

where h_n and v_n follow complex-valued Gaussian distributions of $\mathcal{CN}(0, 1)$ and $\mathcal{CN}(0, \sigma_v^2)$, respectively. Here, we assume i.i.d. frequency-flat Rayleigh fading channels for simplicity. This assumption benefits the SIM system with the aid of the frequency diversity proved in [96]. It was shown in [97] that the interleaved grouping method designed for the SIM scheme achieved a nearly-uncorrelated Rayleigh fading performance in the correlated channel environment. Hence, even in the i.i.d. Rayleigh fading scenario, the theoretical/numerical comparisons will not overestimate the performance advantages of the SIM system. By
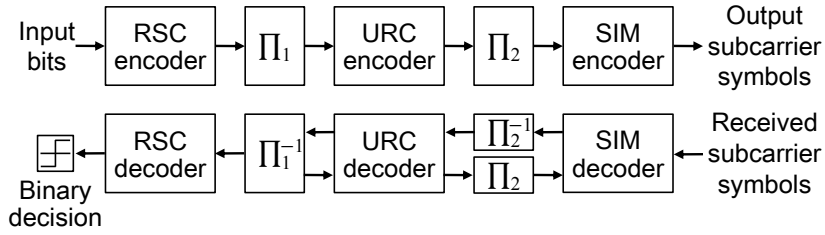
Figure 6.4 Schematic of the three-stage turbo-coded SIM transmitter and receiver

stacking the received symbols of Eq. (6.6), we alternatively have the channel model of $\mathbf{y} = \mathrm{diag}(\mathbf{h})\mathbf{x} + \mathbf{v} \in \mathbb{C}^{N \times 1}$. Here, the received SNR ρ is defined by $\rho = \sigma_s^2 / \sigma_v^2$. The variance of the symbol vector $\mathbf{x} \in \mathbb{C}^{M \times 1}$ in a subgroup, which is given in Eq. (6.4), is further simplified into

$$\sigma_x^2 = \frac{1}{N_a P} \sum_{i=1}^{N_a} \sum_{p=1}^{P} \left| x_{\mathbf{a}_i(p)} \right|^2 = \frac{M}{P} \sigma_s^2, \tag{6.7}$$

where σ_s^2 is the variance of APSK symbols.

The ML detector for the uncoded SIM receiver is given by

$$\hat{\mathbf{x}} = \arg\min_{\mathbf{x}} \|\mathbf{y} - \mathrm{diag}(\mathbf{h})\mathbf{x}\|^2 \tag{6.8}$$

where $\hat{\mathbf{x}}$ represents the estimated symbol vector. The low-complexity detectors for the SIM scheme have been proposed [96, 145–147], which exploits the sparse nature of the SIM symbols.

6.2.3   Three-Stage Turbo-Coded SIM System

The powerful channel coding schemes, such as turbo codes and low-density parity check codes, enable the wireless system to achieve the near-capacity performance [20]. In this chapter, we apply the three-stage concatenated encoder and decoder proposed in [162] for the SIM system and evaluate it in channel-coded scenarios. Fig. 6.4 shows the schematic of the three-stage turbo-coded SIM system. Generally, the three-stage system consists of the outer and inner codes, as well as the interleavers. Similar to [162], the RSC and URC codes are used as the outer and inner codes for the coded SIM system, respectively. The constraint length of the RSC code is set to 2 and the associated generator polynomials are [3 2]. The

max-log MAP detector is the same as that used in [162]. In the iterative decoding process, the number of iterations in the outer and inner code are denoted by N_{out} and N_{in}, respectively.

6.3   Theoretical Analysis

In this section, we analyze the SIM system in terms of the MED and AMI of the SIM symbols in the frequency domain, and the PAPR in the time domain.

6.3.1   Minimum Euclidean Distance

We formulate the MED of the SIM symbols. Then, we derive the upper-bound of the formulated MED. Based on the MED upper-bound, we propose our design guidelines for the SIM scheme. It was shown in [96] that the MED of SIM symbols $\mathbf{x}$ determines the BER in uncoded scenarios.

6.3.1.1   MED Formulation

The MED of SIM symbols is given by

$$
\min_{i \neq j} \prod_{m=1}^{\text{rank}(\mathbf{Q})} \alpha_m^{(i,j)}, \tag{6.9}
$$

where $\alpha_m^{(i,j)}$ is the mth singular value of $\mathbf{Q} = \left(\mathbf{x}^{(i)} - \mathbf{x}^{(j)}\right)\left(\mathbf{x}^{(i)} - \mathbf{x}^{(j)}\right)^{\text{H}}$. For the SIM and OFDM schemes having $\mathcal{L} \geq 4$, Eq. (6.9) is simplified to

$$
\text{MED}(M,P,\mathcal{L}) = \begin{cases} \dfrac{M}{P} \cdot 2\left(1 - \cos\left(\dfrac{2\pi}{\mathcal{L}}\right)\right) \cdot \sigma_s^2 & \text{(PSK)} \\[2ex] \dfrac{M}{P} \cdot 6/(\mathcal{L}-1) \cdot \sigma_s^2 & \text{(QAM)} \end{cases}. \tag{6.10}
$$

Further, for the $\mathcal{L} = 1$ and 2 cases, Eq. (6.9) is simplified to

$$
\text{MED}(M,P,\mathcal{L}) = \begin{cases} \dfrac{M}{P} \cdot 2 \cdot \sigma_s^2 & \text{(SIM)} \\[2ex] 4 \cdot \sigma_s^2 & \text{(OFDM)} \end{cases}. \tag{6.11}
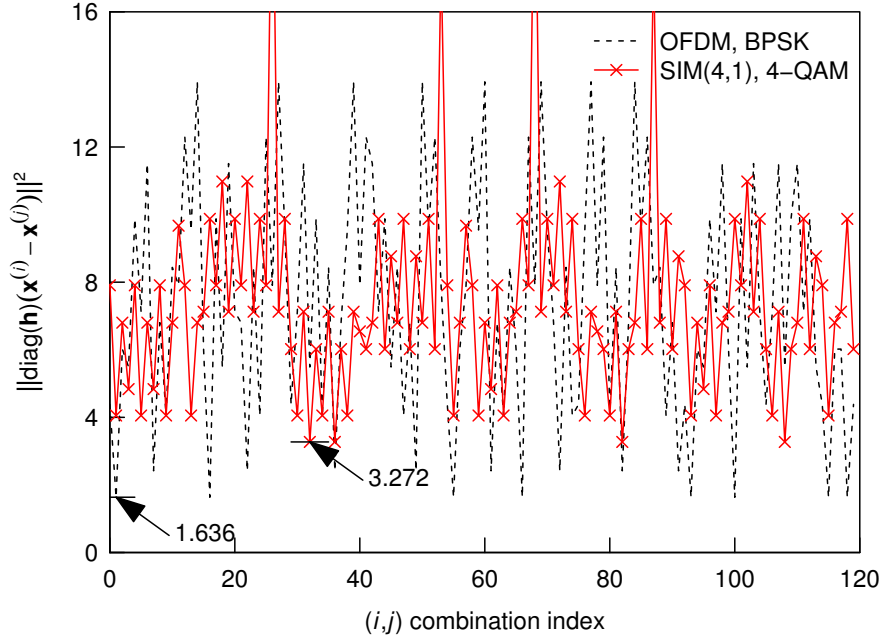$$

Figure 6.5 MED examples of the BPSK-aided OFDM and the 4-QAM-aided SIM(4,1) schemes, where we have the variance of the APSK symbol $\sigma_s^2 = 1$. The channel coefficients were diag$(-0.75389 + 0.19009j, 0.42396 - 1.09213j, 0.61548 + 0.17391j, -1.03636 + 0.14785j)$.

Eqs. (6.10) and (6.11) imply that the sparsity M/P of SIM symbols linearly increases the associated MED.

Fig. 6.5 shows the MED of OFDM and SIM symbols, where the metric $\left\| \text{diag}\,(\mathbf{h}) \left(\mathbf{x}^{(i)} - \mathbf{x}^{(j)} \right) \right\|^2$ was considered. The channel coefficients were fixed to the instantaneous values. As shown in Fig. 6.5, the SIM scheme achieved a higher MED than the OFDM scheme. More specifically, the MED of the OFDM symbols was 1.636, while that of the SIM symbols was 3.272. Here, the MED gain of $3.272/1.636 = 2.0$ was equal to the theoretical MED gain of $\text{MED}(4,1,4)/\text{MED}(4,4,2) = 2.0$, which were calculated by Eqs. (6.10) and (6.11).

Fig. 6.6 shows the correlation between the formulated MED and the simulated BER at SNR = 30 [dB]. The MEDs were calculated by Eqs. (6.10) and (6.11). It was shown in Fig. 6.6(a) and (b) that there was a correlation between the MED and the BER in uncoded scenarios.

6.3.1.2   Design Guidelines

For a given transmission rate $R \geq 2$, we propose our design guidelines for the SIM scheme, which maximize the MED of SIM symbols. The SIM parameters consist of $(M, P, \mathcal{L})$. Since the SIM transmission rate is given by the combinatorial number, as given in Eq. (6.5), there

(a) The inverse of the formulated MED.   **(b)** The simulated BER at 30 [dB].
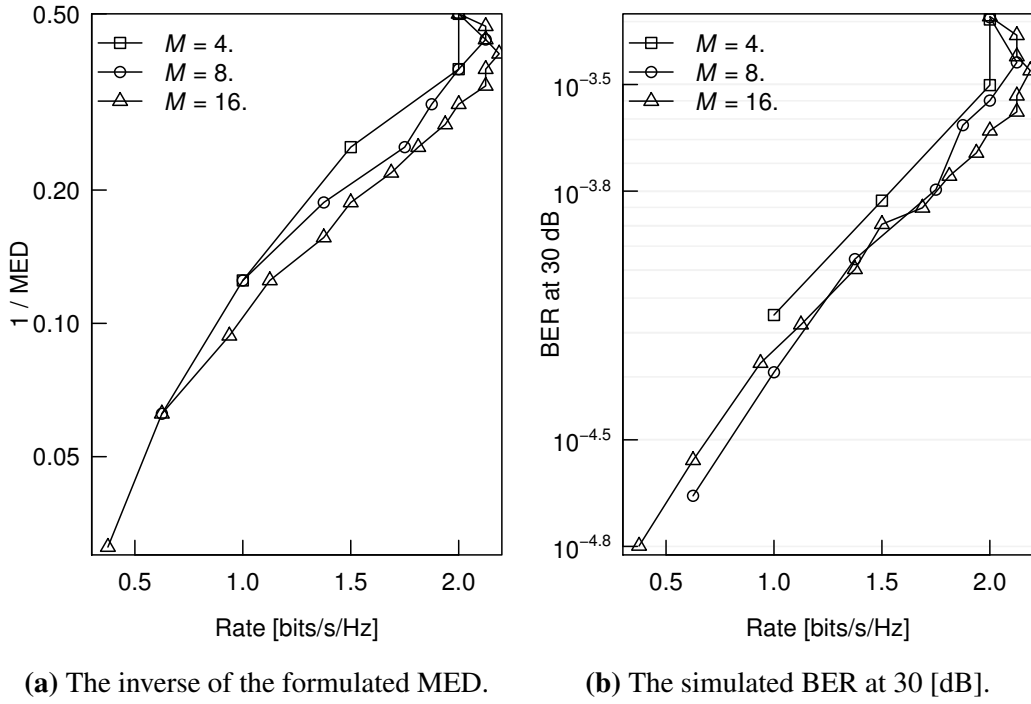
Figure 6.6 Correlation between the MED and BER, where the constellation size was $\mathcal{L} = 4$. The number of subcarriers was set to $M = 4, 8, 16$ and the number of selected subcarriers was changed from $P = 1$ to M.

are a combinatorial number of possible combinations that satisfy the given rate R. The proposed design guidelines, which maximize the MED of Eq. (6.10), are summarized as follows.

$$\text{Criterion 1} : \mathcal{L} = 2^R. \tag{6.12}$$

$$\text{Criterion 2} : \frac{P}{M} \approx \frac{2^{R+1} - e}{2^{R+1} + e}. \tag{6.13}$$

Criterion 1: This criterion determines the optimum constellation size $\mathcal{L}$ in terms of the MED. The transmission rate of the SIM system having $\mathcal{L} = 2^{R-1}$ is lower than R since we have the following inequality, which is transformed from Eq. (6.5):

$$R \leq \frac{1}{M} \left(P \log_2 \mathcal{L} + \log_2 \binom{M}{P} \right) \leq \frac{1}{M} \left(P \log_2 \mathcal{L} + M - 1 \right) < \log_2 \mathcal{L} + 1.$$
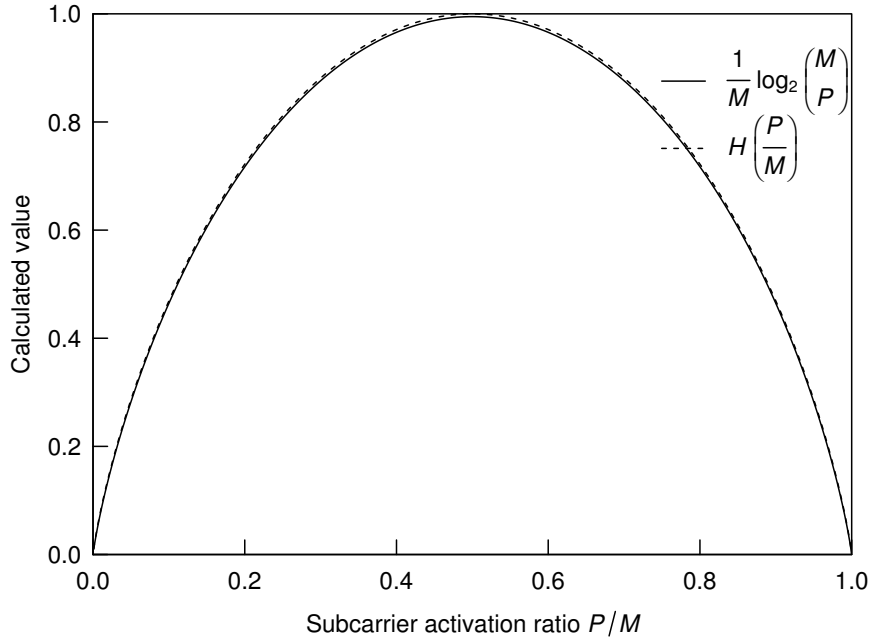
Figure 6.7 Example of Stirling's approximation, where we have $M = 1024$ and $1 \leq P < M$.

In addition, the following inequality is satisfied:

$$\max_{P_1}\left(\mathrm{MED}\left(M,P_1,2^R\right)\right) > \max_{P_2}\left(\mathrm{MED}\left(M,P_2,2^{R+1}\right)\right),$$

where P_1 and P_2 are integers that satisfy the same rate constraint of

$$P_1 R + \left\lfloor \log_2\binom{M}{P_1} \right\rfloor = P_2(R+1) + \left\lfloor \log_2\binom{M}{P_2} \right\rfloor.$$

Criterion 2: This criterion determines the optimum subcarrier-activation ratio $\xi = P/M$ in terms of the MED. We use the following Stirling's approximation [163] for deriving the upper-bound of R.

$$\frac{1}{M}\log_2\binom{M}{P} \leq \mathrm{H}\left(\frac{P}{M}\right). \tag{6.14}$$

Here, $\mathrm{H}(\cdot)$ represents the binary entropy function of $\mathrm{H}(\xi) = -\xi\log_2(\xi) - (1-\xi)\log_2(1-\xi)$. Fig. 6.7 shows the example of Stirling's approximation. As shown in Fig. 6.7, for a large M, the left and right terms of Eq. (6.14) are nearly equal. Then, the transmission rate of the SIM

scheme in Eq. (6.5) is upper-bounded by

$$R \le \frac{1}{M}\left(P\log_2 \mathcal{L} + \log_2 \binom{M}{P}\right) \le \frac{P}{M}\log_2 \mathcal{L} + H\left(\frac{P}{M}\right),\tag{6.15}$$

which implies that the maximum achievable rate B_2 of the subcarrier activation is upper bounded by $H(P/M) \le 1$. As given in Criterion 1, the MED of SIM symbols is maximized with the $\mathcal{L} = 2^R$ constellations. By substituting $\mathcal{L} = 2^R$ for Eq. (6.15), we have

$$R \le \frac{H(\xi)}{(1-\xi)} = \frac{H(1-\xi)}{(1-\xi)},\tag{6.16}$$

where ξ denotes the subcarrier-activation ratio $\xi = P/M$. Let us solve Eq. (6.16) with respect to ξ $(0 < \xi < 1)$ by assuming $R = H(1-\xi)/(1-\xi)$. We temporally represent $1-\xi$ as $v = 1-\xi$ $(0 < v < 1)$. Eq. (6.16) is transformed into

$$vR \le -v\log_2(v) - (1-v)\log_2(1-v)$$
$$\Leftrightarrow vR\ln(2) \le -v\ln(v) - (1-v)\ln(1-v).\tag{6.17}$$

Next, we assume that v approaches 0. Here, we have the approximations of $\ln(1-v) \approx -v - v^2/2$ and $v^2 \approx 0$. Then, Eq. (6.17) is expressed as

$$vR\ln(2) \le -v\ln(v) + v(1-v)\left(1+\frac{v}{2}\right)$$
$$\Leftrightarrow vR\ln(2) \le -v\ln(v) + v\left(1-\frac{v}{2}\right)$$
$$\Leftrightarrow R\ln(2) \le -\ln(v) + \left(1-\frac{v}{2}\right)\tag{6.18}$$
$$\Leftrightarrow v \le \underbrace{e^{1-R\ln(2)}}_{\equiv R'}\underbrace{e^{-v/2}}_{\equiv 1-v'}.\tag{6.19}$$

In Eq. (6.19), we temporarily represent $e^{1-R\ln(2)}$ and $e^{-v/2}$ as R' and $(1-v')$, respectively. By applying the Lambert W function [164], Eq. (6.19) is transformed into

$$\frac{v}{2}e^{\frac{v}{2}} \le \frac{R'}{2} \Leftrightarrow \frac{v}{2} \le W\left(\frac{R'}{2}\right).\tag{6.20}$$

Then, we arrive at

$$1 \geq \xi \geq 1 - 2W\left(e \cdot 2^{-(R+1)}\right) \geq 0. \tag{6.21}$$

Let us try to further simplify Eq. (6.21). By substituting $v = R'(1 - v')$ into Eq. (6.18), we obtain

$$v' = \frac{R'}{2 + R'} \Leftrightarrow v = R'\left(1 - \frac{R'}{2 + R'}\right). \tag{6.22}$$

Finally, we arrive at

$$\xi = 1 - v = \frac{2^{R+1} - e}{2^{R+1} + e}. \tag{6.23}$$

Note that the approximations of Eqs. (6.21) and (6.23) are valid only when ξ approaches 1. Eq. (6.23) implies that the optimum subcarrier-activation ratio $\xi = P/M$ that maximizes the MED is a function of the transmission rate R.

We derive the upper-bound of the MED of SIM symbols. Based on the proposed criteria, the MED of Eq. (6.10) is maximized if Criterion 1 & 2 consist. Then, the MED of Eq. (6.10) is roughly upper-bounded by

$$\mathrm{MED}(R) \leq \begin{cases} 2 \cdot \dfrac{2^{R+1} + e}{2^{R+1} - e} \cdot \left(1 - \cos\left(\dfrac{2\pi}{2^R}\right)\right) \cdot \sigma_s^2 & \text{(PSK)} \\[3ex] 6 \cdot \dfrac{2^{R+1} + e}{2^{R+1} - e} \cdot \dfrac{1}{(2^R - 1)} \cdot \sigma_s^2 & \text{(QAM)} \end{cases}, \tag{6.24}$$

where $\mathcal{L}$ and P/M in Eq. (6.10) are substituted by 2^R and $\left(2^{R+1} - e\right) / \left(2^{R+1} + e\right)$, respectively.

6.3.1.3   Numerical Evaluation

Let us numerically evaluate the proposed design criteria. Fig. 6.8 shows the searched MEDs of the SIM(M,P) symbols based on Eqs. (6.5) and Eq. (6.10). Here, the number of subcarriers M was set to 2^i ($1 \leq i \leq 10$) and the number of selected subcarriers was varied from 1 to M. The constellation size was also set to 2^1 and 2^{2i} ($1 \leq i \leq 5$). In Fig. 6.8, for $R \geq 2$, the SIM schemes designed by our criteria were shown, as well as the MED upper-bound of Eq. (6.24). It was shown in Fig. 6.8 that the performance advantage over
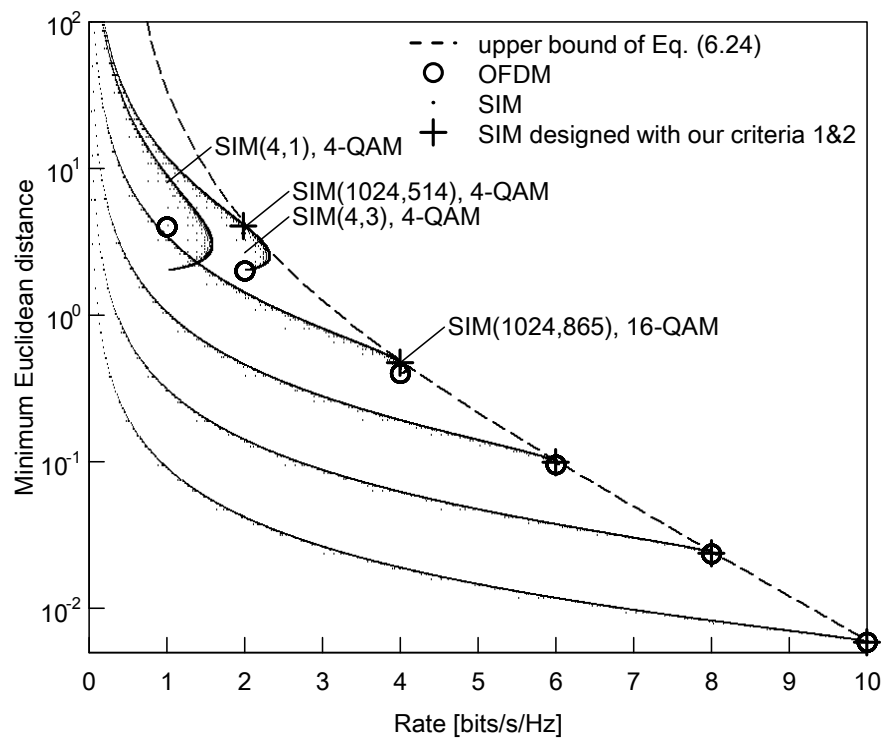
Figure 6.8 MEDs of the SIM(M,P) symbols, where the number of subcarriers M was set to $2^1, 2^2, \cdots, 2^{10}$ and the number of activated subcarriers P was varied from 1 to M. The constellations of BPSK and $2^2, 2^4, \cdots, 2^{10}$–QAM symbols were considered.
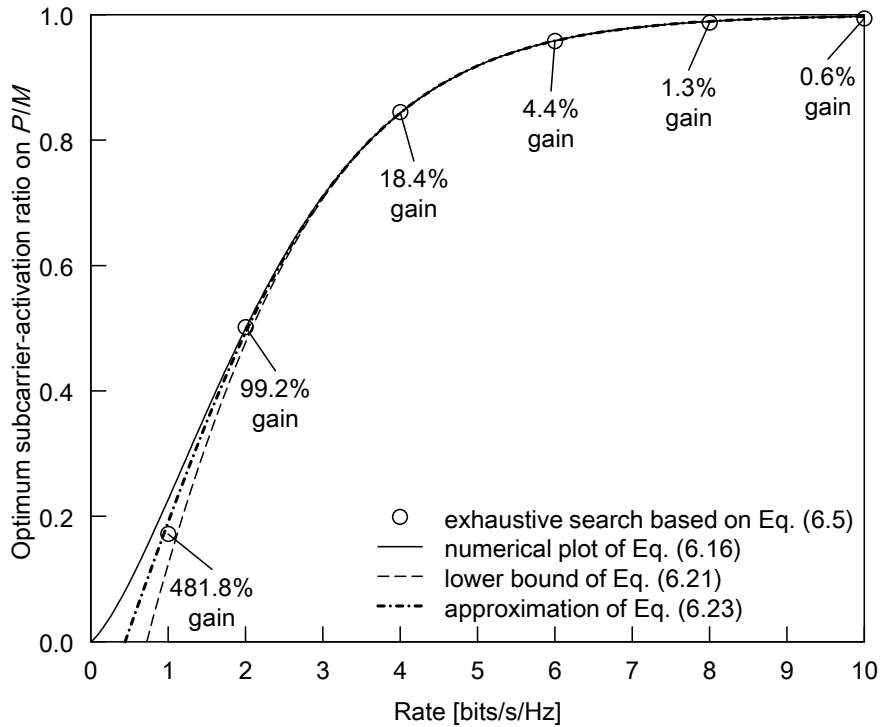
Figure 6.9 The optimum subcarrier-activation ratio ξ calculated by our design criterion 2.

OFDM was significant within the rate of $1 \leq R \leq 4$ [bits/s/Hz]. However, in the $R > 4$ region, the insignificant advantages were observed. In addition, the bound of Eq. (6.24) exactly represented the maximum MEDs over the $R \leq 2$ region, whereas it was not accurate in the $R < 2$ region due to the approximation of $\xi \to 1$. For example, if we consider the SIM scheme having $R = 2$ [bits/s/Hz], the maximum MED of SIM symbols is 3.984 with the 4–QAM aided SIM(1024,514) scheme, while the MED of the 4–QAM aided OFDM scheme is 2.000. Here, the optimum subcarrier-activation ratio is calculated by $(2^{2+1} - e)/(2^{2+1} + e) = 0.493$, which is close to the activation ratio of the SIM(1024,514), namely, $514/1024 = 0.501$.

Fig. 6.9 shows the optimum subcarrier-activation ratios ξ calculated by our design criterion 2 of Eq. (6.13), as well as the exhaustive search based ratios obtained in Fig. 6.8. In addition, Eqs. (6.16) and (6.21) were plotted for reference. Observe in Fig. 6.9 that the optimum subcarrier-activation ratio ξ was close to the searched ratios for the $R \geq 2$ region. Also, the optimum activation ratio ξ monotonically increased with the increase in R [bits/s/Hz], and converged into $\xi = 1$ at high rates. Note that the SIM scheme having $\xi = 1$ is equivalent to the OFDM scheme.

6.3.2   Average Mutual Information

We introduce the constrained and unconstrained AMI of SIM, which are effective metrics in channel-coded scenarios. We only consider the subgrouped SIM symbols of $\mathbf{x} \in \mathbb{C}^M$, without loss of generality. We assume the AWGN and i.i.d. Rayleigh fading channels, as described in Section 6.2, and ignore the CP insertion for simplicity.

The AMI assuming a finite APSK symbol set, which is referred to as the constrained AMI, is the same with the general expression provided in Section 2.2.1.2. Note that the maximum achievable rate derived in [97] is upper bounded by the constrained AMI of Section 2.2.1.2.

Let us derive the unconstrained AMI of SIM systems, under the assumption that the input signals follow Gaussian distribution. Our analysis is based on the unconstrained AMI derived for the SM system [120, 155]. The mutual information of two continuous random variables X and Y, which follow the distribution of the SIM symbol vectors $\mathbf{x} \in \mathbb{C}^M$ and the associated received symbol vectors $\mathbf{y} \in \mathbb{C}^M$, may be expressed as follows [120, 155]:

$$I(X;Y) = I(X_{\mathrm{sy}}, X_{\mathrm{ch}}; Y) = I(X_{\mathrm{sy}}; Y | X_{\mathrm{ch}}) + I(X_{\mathrm{ch}}; Y), \tag{6.25}$$

where X_{sy} and X_{ch} are random variables of the APSK symbols and the activated subcarriers, respectively. The unconstrained AMI is defined by

$$I_C = \frac{1}{M} \max_{\mathrm{p}(\mathbf{x})} I(X;Y) \text{ [bits/s/Hz]}, \tag{6.26}$$

where we have

$$\max_{\mathrm{p}(\mathbf{x})} I(X;Y) = \underbrace{\max_{\mathrm{p}(\mathbf{x})} I(X_{\mathrm{sy}}; Y | X_{\mathrm{ch}})}_{I_{C_1}} + \underbrace{\max_{\mathrm{p}(\mathbf{x})} I(X_{\mathrm{ch}}; Y)}_{I_{C_2}}. \tag{6.27}$$

Here, I_{C_1} represents the AMI associated with the APSK symbols, while I_{C_2} represents the AMI associated with the activated subcarrier indices. Later, the pdf of a complex-valued Gaussian symbol $z \in \mathbb{C}$ that obeys $\mathcal{CN}\left(0, \sigma_z^2\right)$ is denoted by

$$p(z) = \frac{1}{\sqrt{2\pi \frac{\sigma_z^2}{2}}} \exp\left(-\frac{\mathrm{Re}[z]^2}{2\frac{\sigma_z^2}{2}}\right) \cdot \frac{1}{\sqrt{2\pi \frac{\sigma_z^2}{2}}} \exp\left(-\frac{\mathrm{Im}[z]^2}{2\frac{\sigma_z^2}{2}}\right) = \frac{1}{\pi \sigma_z^2} \exp\left(-\frac{|z|^2}{\sigma_z^2}\right) \equiv \mathrm{q}(z, \sigma_z^2).$$

$$\tag{6.28}$$

We assume that the input symbols, which are associated with the activated subcarriers, follow the complex-valued Gaussian distribution of $\mathcal{CN}(0,1)$. The pdf of the single non-zero element inside the SIM vector $\mathbf{x}$ is given by

$$\mathrm{p}(x_p) = \mathrm{q}(x_p, 1) = \frac{1}{\pi} \exp\left(-|x_p|^2\right), \tag{6.29}$$

where p is an arbitrarily selected subcarrier index. For the subcarrier-activation pattern of $\mathbf{a}_i$, the joint pdf $\mathrm{p}(\mathbf{x}_{\mathbf{a}_i})$ of the multiple non-zero elements, which are associated with the activated subcarriers, is derived by a finite product of the Gaussian pdf given in Eq. (6.29).

$$\mathrm{p}\left(\mathbf{x}_{\mathbf{a}_i}\right) = \prod_{p=1}^{P} \mathrm{q}\left(\mathbf{x}_{\mathbf{a}_i(p)}, 1\right). \tag{6.30}$$

Similarly, the joint pdf of the AWGN $\mathbf{v} \in \mathbb{C}^M$ is given by

$$\mathrm{p}(\mathbf{v}) = \prod_{m=1}^{M} \mathrm{q}(v_m, \sigma_v^2), \tag{6.31}$$

where v_m is the mth element of $\mathbf{v}$. Next, let us derive the joint pdf $\mathrm{p}(\mathbf{y})$ of the received symbols $\mathbf{y} \in \mathbb{C}^M$. Let $\mathbf{h}_{\mathbf{a}_i} \in \mathbb{C}^M$ denote the channel coefficient vector associated with the activated indices $\mathbf{a}_i$. The mth element of $\mathbf{h}_{\mathbf{a}_i} \in \mathbb{C}^M$ is defined by

$$\mathbf{h}_{\mathbf{a}_i}(m) = \begin{cases} h_m & (m \in \mathbf{a}_i) \\ 0 & (m \notin \mathbf{a}_i) \end{cases} \quad (1 \le m \le M),$$

where h_m is the mth element of $\mathbf{h} \in \mathbb{C}^M$. For example, if we have $\mathbf{h} = [h_1,\ h_2,\ h_3,\ h_4]^{\mathrm{T}}$ and $\mathbf{a}_1 = [1,\ 2]$, $\mathbf{h}_{\mathbf{a}_1}$ represents the vector of $[\mathbf{h}_1\ \mathbf{h}_2\ 0\ 0]^{\mathrm{T}}$. The variance of the received symbol $y_m \in \mathbb{C}$ which is associated with the transmitted vector of $\mathbf{x}_{\mathbf{a}_i}$ is given by

$$\sigma_y^2(i,m) = |\mathbf{h}_{\mathbf{a}_i}(m)|^2 \sigma_x^2 + \sigma_v^2 = |\mathbf{h}_{\mathbf{a}_i}(m)|^2 \frac{M}{P} \sigma_s^2 + \sigma_v^2 \quad (1 \le m \le M). \tag{6.32}$$

The conditional pdf of the received symbol $y_m \in \mathbb{C}$, based on the channel model of Eq. (6.6), is defined by

$$p\left(y_m | \mathbf{h}_{\mathbf{a}_i}(m)\right) = q\left(y_m, \sigma_y^2(i, m)\right). \tag{6.33}$$

The conditional pdf of $p\left(\mathbf{y} | \mathbf{h}_{\mathbf{a}_i}\right)$, which is different from Eq. (6.33), is derived by a joint pdf of M number of the received symbols y_m as follows:

$$p\left(\mathbf{y} | \mathbf{h}_{\mathbf{a}_i}\right) = \prod_{m=1}^{M} p\left(y_m | \mathbf{h}_{\mathbf{a}_i}(m)\right). \tag{6.34}$$

Finally, the joint pdf $p(\mathbf{y})$ of the received symbol vector $\mathbf{y}$ is defined by the average of N_a number of subcarriers patterns.

$$p(\mathbf{y}) = \frac{1}{N_a} \sum_{i=1}^{N_a} p\left(\mathbf{y} | \mathbf{h}_{\mathbf{a}_i}\right) = \frac{1}{N_a} \sum_{i=1}^{N_a} \prod_{m=1}^{M} q\left(y_m, \sigma_y^2(i, m)\right). \tag{6.35}$$

Note that $p(\mathbf{y})$ does not follow Gaussian distribution because it is an average of multiple Gaussian distributions, each of which has a different variance.

Up to here, we formulated the unconstrained AMI C and the pdfs $p(\mathbf{x}_{\mathbf{a}_i})$, $p(\mathbf{v})$, and $p(\mathbf{y})$. Now, we derive the AMI I_{C_1} associated with the APSK symbols. First, we only focus on the ith subcarrier-activation pattern of $\mathbf{a}_i$. The unconstrained AMI of the SIM scheme having $N = M = P = 1$ is equivalent to that of the SISO system, which is given by

$$I_C^{\mathrm{SISO}}(\rho) = E_{\mathbf{h}}\left[\log_2\left(1 + \rho |h_1|^2\right)\right] \ [\mathrm{bits/s/Hz}], \tag{6.36}$$

where ρ represents the received SNR and $h_1 \in \mathbb{C}$ follows Gaussian distribution of $\mathcal{CN}(0,1)$. Note that the unconstrained AMI of the OFDM scheme is equivalent to that of the SISO system $I_C^{\mathrm{SISO}}(\rho)$ since it is normalized by the bandwidth. In analogy with the AMI of the SISO system $I_C^{\mathrm{SISO}}(\rho)$, for the given subcarrier-activation pattern $\mathbf{h}_{\mathbf{a}_i}$, the AMI of the P number of complex-valued Gaussian symbols is given by

$$I'_{C_1}(i) = \sum_{p=1}^{P} \log_2\left(1 + \frac{M}{P}\frac{\sigma_s^2}{\sigma_v^2} |\mathbf{h}_{\mathbf{a}_i(p)}|^2\right). \tag{6.37}$$

Then, the AMI I_{C_1} is expressed by the average of the N_a number of $I'_{C_1}(i)$ ($1 \leq i \leq N_a$) as follows:

$$I_{C_1} = \frac{1}{N_a} \sum_{i=1}^{N_a} I'_{C_1}(i). \tag{6.38}$$

Furthermore, if we assume the i.i.d. frequency-flat Rayleigh fading channels, the AMI I_{C_1} of Eq. (6.38) is simplified to

$$I_{C_1} = P I_C^{\text{SISO}} \left(\frac{M}{P} \frac{\sigma_s^2}{\sigma_v^2} \right), \tag{6.39}$$

which implies that the unconstrained AMI of the SIM scheme consists of the P number of the AMI of the SISO scheme I_C^{SISO}. Note that Eq. (6.39) allows us to avoid the combinatorial explosion problem, where the number of the subcarrier-activation patterns N_a may be large.

Next, let us derive the AMI I_{C_2}, which is associated with the subcarrier-activation patterns. The AMI between the channel vectors and the received symbol vectors is given by

$$
\begin{aligned}
I(X_{\text{ch}}; Y) &= H(X_{\text{ch}}) - H(X_{\text{ch}}|Y) \\
&= \lfloor \log_2(N_a) \rfloor - H(X_{\text{ch}}|Y) \\
&= B_2 - H(X_{\text{ch}}|Y),
\end{aligned} \tag{6.40}
$$

which implies that the AMI I_{C_2} is upper-bounded by B_2. The second term of Eq. (6.40) is defined by

$$
\begin{aligned}
H(X_{\text{ch}}|Y) &= \sum_{i=1}^{N_a} \int_{\mathbf{y}} p(\mathbf{h}_{\mathbf{a}_i}, \mathbf{y}) \log_2 \left(\frac{1}{p(\mathbf{h}_{\mathbf{a}_i}|\mathbf{y})} \right) d\mathbf{y} = \int_{\mathbf{y}} p(\mathbf{y}|\mathbf{h}_{\mathbf{a}_i}) p(\mathbf{h}_{\mathbf{a}_i}) \log_2 \left(\frac{\sum_{j=1}^{N_a} p(\mathbf{y}|\mathbf{h}_{\mathbf{a}_j})}{p(\mathbf{y}|\mathbf{h}_{\mathbf{a}_i})} \right) d\mathbf{y} \\
&= \frac{1}{N_a} \sum_{i=1}^{N_a} \underbrace{\int_{\mathbf{y}} p(\mathbf{y}|\mathbf{h}_{\mathbf{a}_i}) \log_2 \left(\frac{1}{p(\mathbf{y}|\mathbf{h}_{\mathbf{a}_i})} \right) d\mathbf{y}}_{I_{C_{21}}(i)} + \frac{1}{N_a} \sum_{i=1}^{N_a} \underbrace{\int_{\mathbf{y}} p(\mathbf{y}|\mathbf{h}_{\mathbf{a}_i}) \log_2 \left(\sum_{j=1}^{N_a} p(\mathbf{y}|\mathbf{h}_{\mathbf{a}_j}) \right) d\mathbf{y}}_{I_{C_{22}}(i)},
\end{aligned} \tag{6.41}
$$

where we have $p(\mathbf{h}_{\mathbf{a}_i}) = 1/N_a$. Here, we represent the first term of Eq. (6.41) as $I_{C_{21}}(i)$ and its second term as $I_{C_{22}}(i)$. The AMI $I_{C_{21}}(i)$ in Eq. (6.41) is calculated as follows:

$$
I_{C_{21}}(i) = -\underbrace{\int_{\mathbf{y}_1} \cdots \int_{y_m}}_{M-\text{fold}} \prod_{m=1}^{M} q\left(y_m, \sigma_y^2(i,m)\right) \cdot \sum_{m=1}^{M} \log_2 q\left(y_m, \sigma_y^2(i,m)\right) \underbrace{dy_m \cdots d\mathbf{y}_1}_{M-\text{fold}}
$$

$$
= -\sum_{m=1}^{M} \int_{y_m} q\left(y_m, \sigma_y^2(i,m)\right) \log_2 q\left(y_m, \sigma_y^2(i,m)\right) dy_m = \sum_{m=1}^{M} \log_2 \left(\pi e \sigma_y^2(i,m)\right).
$$

$$(6.42)$$

As shown in Eq. (6.42), the AMI $I_{C_{21}}(i)$ can be expressed in closed form, while the AMI $I_{C_{22}}(i)$ cannot be expressed in closed form. Hence, the calculation of $I_{C_{22}}(i)$ imposes a high complexity because $I_{C_{22}}(i)$ includes the $2M$-dimensional integration of a logarithm including $N_a \cdot M$ number of the function $q(\cdot)$. For example, if we consider the SIM($M = 128, P = 64$) case, N_a is calculated by $2^{\lfloor \log_2 \binom{128}{64} \rfloor} = 2^{124} \approx 2.1 \cdot 10^{37}$. Then, $I_{C_{22}}(i)$ is derived from the 256-dimensional integrations of the logarithm of a linear combination of $2^{124} \cdot 128$ number of the function $q(\cdot)$. Obviously, it is a challenging task to calculate $I_{C_{22}}(i)$ if N_a is large. Hence, let us further simplify $I_{C_{22}}(i)$ by applying the Monte Carlo integration. Since we have the relationship of $\int_{\mathbf{y}} p(\mathbf{y}|\mathbf{h}_{\mathbf{a}_i}) d\mathbf{y} = 1$, the AMI $I_{C_{22}}(i)$ of Eq. (6.41) is simplified to

$$
I_{C_{22}}(i) \approx E_{(\mathbf{y}|\mathbf{h}_{\mathbf{a}_i})}\left[\log_2\left(\sum_{j=1}^{N_a} p(\mathbf{y}|\mathbf{h}_{\mathbf{a}_j})\right)\right] = \frac{E_{(\mathbf{y}|\mathbf{h}_{\mathbf{a}_i})}\left[\text{lse}(\mu_1, \cdots, \mu_{N_a})\right]}{\ln 2} - M\log_2 \pi, \quad (6.43)
$$

where

$$
\mu_j = -\sum_{m=1}^{M}\left(\frac{|y_m|^2}{\sigma_y^2(j,m)} + \ln \sigma_y^2(j,m)\right). \quad (6.44)
$$

Here, $\text{lse}(\mu_1, \cdots, \mu_{N_a})$ denotes the log-sum-exp function, which mitigates the computation errors caused by the floating point numbers. The log-sum-exp function is defined by

$$
\text{lse}(\mu_1, \cdots, \mu_{N_a}) = \ln\left(\sum_{j=1}^{N_a} e^{\mu_j}\right) = \mu_{\max} + \ln\left(\sum_{j=1}^{N_a} e^{\mu_j - \mu_{\max}}\right), \quad (6.45)
$$

where $\mu_{\max}$ denotes the maximum of μ_j ($1 \le j \le N_a$). Note that the random variables $\mathbf{y} = [y_1, \cdots, y_m]^T$ have to follow the distribution of Eq. (6.34), thus y_m is a random variable that follows $\mathcal{CN}\left(0, \sigma_y^2(i,m)\right)$. Specifically, if we consider the SIM($M = 4$, $P = 2$) case, the random variables y_m ($1 \le m \le M$) assuming $\mathbf{a}_1 = [1,2]$ are generated as follows:

$$\mathbf{y} = [y_1, y_2, y_3, y_4]^T \sim \left[\mathcal{CN}\left(0, 2\sigma_s^2 + \sigma_v^2\right), \mathcal{CN}\left(0, 2\sigma_s^2 + \sigma_v^2\right), \mathcal{CN}\left(0, \sigma_v^2\right), \mathcal{CN}\left(0, \sigma_v^2\right)\right]^T.$$

Finally, for the i.i.d. frequency-flat Rayleigh fading channels, the unconstrained AMI of the subcarrier-activation is given by

$$I_{C_2}^{\text{Rayleigh}} = B_2 - \sum_{i=1}^{N_a} \left(I_{C_{21}}(i) + I_{C_{22}}(i)\right). \tag{6.46}$$

For the AWGN channels, the AMI I_{C_2} of Eq. (6.46) is simplified as follows:

$$I_{C_2}^{\text{AWGN}} = B_2 + \frac{\sum_{i=1}^{N_a}\left(M + E_{(\mathbf{y}|\mathbf{x}_{\mathbf{a}_i})}\left[\text{lse}\left(\mu_1', \cdots, \mu_{N_a}'\right)\right]\right)}{\ln 2}, \tag{6.47}$$

where

$$\mu_j' = -\sum_{m=1}^{M} \frac{|y_m|^2}{\sigma_y^2(j,m)}. \tag{6.48}$$

6.3.3   Peak-to-Average Power Ratio

We analyze the PAPR of both the OFDM and SIM schemes in order to characterize the beneficial region of the SIM scheme. As described in Section 6.2, the PAPR of the SIM scheme is represented by Eq. (6.3). First, we review the previous contributions [76, 140, 141]. Then, we investigate the time-domain signals generated by the SIM transmitter, based on the analysis proposed in [161].

6.3.3.1   Maximum PAPR Analysis

The maximum PAPR of both the OFDM and SIM schemes are given by [141]

$$\max\left(\text{PAPR}_{\text{OFDM}}\right) = \frac{3N\left(\sqrt{\mathcal{L}}-1\right)}{\sqrt{\mathcal{L}}+1}, \tag{6.49}$$

$$\max\left(\text{PAPR}_{\text{SIM}}\right) = \frac{3N\left(\sqrt{\mathcal{L}}-1\right)}{\sqrt{\mathcal{L}}+1} \cdot \frac{P}{M}. \tag{6.50}$$

Here, the probability that the SIM transmitter has the maximum PAPR of Eq. (6.50) is calculated by $4\mathcal{L}^{-NP/M}$. As mentioned in [161], the analysis of the maximum PAPR is not a practical metric since the transmitter seldom encounters it. For example, if we consider the SIM($M = 8, P = 4$) scheme having $(N, \mathcal{L}) = (64, 4)$, the maximum PAPR of 15 [dB] occurs with the probability of $2.2 \cdot 10^{-19}$. Hence, the transmitter having the symbol duration of $T_s = 100.0$ [μs] encounters it only once every 14.6 million years.

6.3.3.2   Level-Crossing Rate Analysis

We characterize the statistical distribution of the SIM time-domain signals, based on the analysis proposed in [161]. Eq. (6.1) defines the complex-valued baseband signals $x(t)$. Here, we focus on the real component of the baseband signals $x'(t) = \text{Re}[x(t)]$, and its derivative $\dot{x}'(t) = \mathrm{d}x'(t)/\mathrm{d}t$, which are given by

$$x'(t) = \frac{1}{\sqrt{N}} \sum_{n=1}^{N} |x_n| \cos\left(\omega_n t + \arg(x_n)\right) \tag{6.51}$$

$$\dot{x}'(t) = -\frac{1}{\sqrt{N}} \sum_{n=1}^{N} \omega_n |x_n| \sin\left(\omega_n t + \arg(x_n)\right). \tag{6.52}$$

Note that $x'(t)$ and $\dot{x}'(t)$ are assumed to follow Gaussian distribution. We represent the square root of the PAPR as r. The complementary cumulative distribution function (CCDF) of r is given by [161]

$$F_C(r) \approx \begin{cases} \left(1 - \dfrac{\bar{N}_p(r)}{\bar{N}_p(\bar{r})}\right)^{\bar{N}_p(\bar{r})} & (r > \bar{r}) \\ 0 & (r \leq \bar{r}) \end{cases}, \tag{6.53}$$

where $\bar{r}$ is the minimum threshold, which was set to $\sqrt{\pi}$ in [161]. In Eq. (6.53), $\bar{N}_p(a)$ is the mean number of peaks that exceed a level a in the time-domain signals. Here, $\bar{N}_p(a)$ is approximated by [161]

$$\bar{N}_p(a) \approx v_c^+(a)T_s, \tag{6.54}$$

where $v_c^+(a)$ is the mean number of upward crossings across the level a. Moreover, $v_c^+(a)$ is given by [161]

$$v_c^+(a) = \sqrt{\frac{\sigma_{\dot{x}'}^2}{\sigma_{x'}^2} \frac{1}{\pi}} a e^{-a^2}. \tag{6.55}$$

Here, $\sigma_{x'}^2$ and $\sigma_{\dot{x}'}^2$ are the variances of $x'(t)$ and $\dot{x}'(t)$, respectively. The variances $\sigma_{x'}^2$ of the OFDM and SIM schemes are the same value owing to their power constraint for fair comparisons. Thus, the integral of the power spectral density (PSD) in the frequency domain, which is calculated by $|\text{FFT}[x'(t)]|^2$, is constant both for the OFDM and SIM because of Parseval's theorem. The derivative is represented as $\dot{x}'(t) = \text{Re}[\text{IFFT}[j\omega_n x_n]]$. The variances $\sigma_{\dot{x}'}^2$ of the OFDM and SIM schemes are also the same value. This is because the integral of PSD for both the OFDM and SIM schemes are the same, namely, $\sum_{n=1}^N \omega_n^2 |x_n|^2$ is equal to the same value.[1]

6.4   Performance Results

In this section, we investigate the achievable performance of the SIM scheme. Throughout the simulations, the effects of the CP insertion were not taken into account, except for the PAPR comparisons. In the BER comparisons, 10^7 bits were randomly generated at each SNR. The transmission rate and the transmit power for the OFDM and SIM schemes were set to the same values in order to provide fair performance comparisons. The simulation parameters considered in this section are summarized in Table 6.1.

6.4.1   BER in Uncoded Scenarios

First, we compared the BER of the SIM and OFDM schemes in uncoded scenarios. Fig. 6.10

---

[1]Note that $\sum_{n=1}^N \omega_n^2 |x_n|^2$ of OFDM and SIM may be different if the positions of non-zero elements in the SIM symbol x_n are not uniformly distributed in the frequency domain.

Table 6.1 Simulation parameters of the SIM and OFDM schemes.

Number of transmit antenna	1
Number of receive antenna	1
Number of subcarriers	$N = 2048$
Number of subcarriers in a subgroup	$M = 2, 4, 8, 16$
Number of activated subcarriers	$P = 1, 2, \cdots, 16$
CP length	64
Channel	Frequency-flat Rayleigh fading and AWGN channels
Detector	Maximum-likelihood detection
Modulation	BPSK, QPSK, 8–PSK, 32–PSK, 64–QAM
Variance of the APSK signals	$\sigma_s^2 = 1$

Table 6.2 The schemes considered in the BER and PAPR comparisons of Figs. 6.10 and 6.11.

	Rate	Scheme	(M, P)	Constellation	MED	Sparsity P/M
	1.0	OFDM	(1,1)	BPSK	4.00	1.00
Fig. 6.10(a)	1.0	SIM	(2,1)	BPSK	4.00	0.50
Fig. 6.11(a)	1.0	SIM	(8,3)	BPSK	5.33	0.38
	1.0	SIM	(16,2)	32–PSK	0.31	0.13
	2.0	OFDM	(1,1)	4–QAM	2.00	1.00
Fig. 6.10(b)	2.0	SIM	(4,3)	4–QAM	2.67	0.75
Fig. 6.11(b)	2.0	SIM	(16,10)	4–QAM	3.20	0.63
	2.0	SIM	(4,1)	64–QAM	0.38	0.25
	3.0	OFDM	(1,1)	8–PSK	0.59	1.00
Fig. 6.10(c)	3.0	SIM	(8,7)	8–PSK	0.67	0.88
Fig. 6.11(c)	3.0	SIM	(16,13)	8–PSK	0.72	0.81
	3.0	SIM	(16,7)	32–PSK	0.09	0.44

(a) $R = 1.0$ [bits/s/Hz].   **(b)** $R = 2.0$ [bits/s/Hz].   **(c)** $R = 3.0$ [bits/s/Hz].
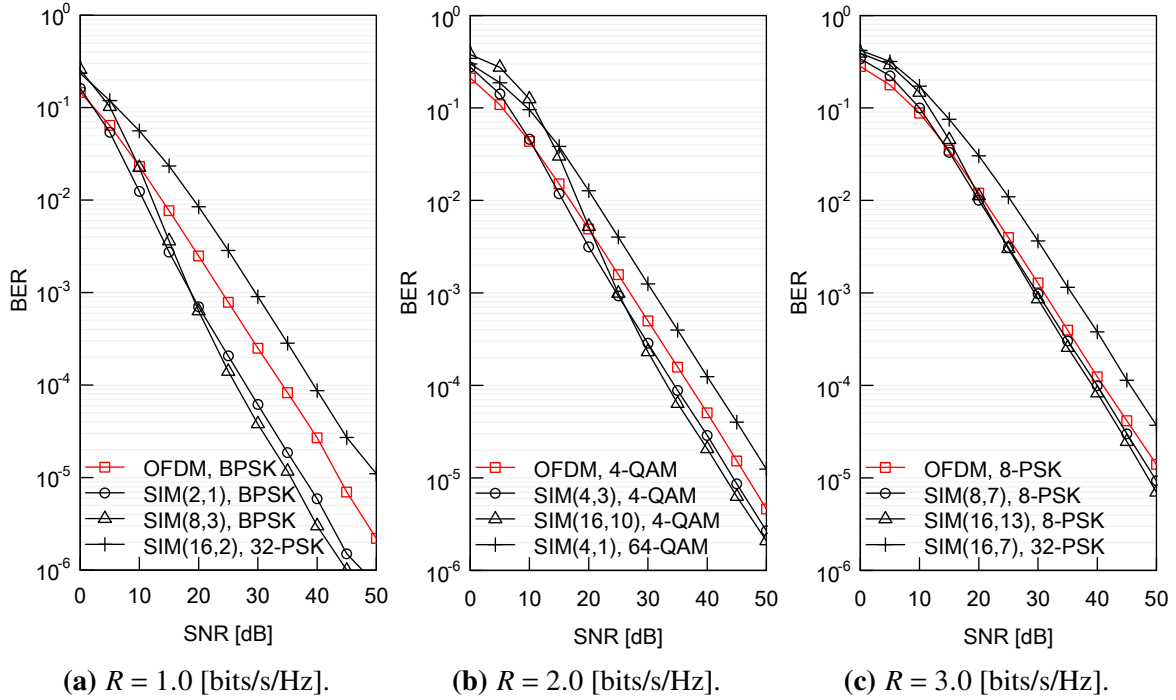
Figure 6.10 BER comparisons of OFDM and SIM, where the transmission rate R was changed from 1.0 to 3.0 [bits/s/Hz].

shows the BER comparisons of the SIM and OFDM schemes, where we considered the transmission rate of $R = 1.0$, 2.0, and 3.0 [bits/s/Hz]. The system parameters of the schemes considered in the BER comparisons were listed in Table 6.2. It was shown in Fig. 6.10 that the BER at high SNRs and the associated MED correlated to each other, except for the $R = 1.0$ [bits/s/Hz] case. As mentioned in the proposed design guidelines of Section 6.3.1.2, the MED criterion does not work for the $R < 2.0$ [bits/s/Hz] scenario, due to the irregular definition of the MED given in Eq. (6.11). Also, for the $R = 2.0$ and 3.0 [bits/s/Hz] cases, the optimum subcarrier-activation ratios are $\xi = 0.49$ and 0.71, which are calculated by Criterion 2 of Eq. (6.13). The SIM scheme having the near-optimal MED achieved a better BER than the other schemes at high SNRs, which justifies the proposed design guidelines.

6.4.2   PAPR

Next, the PAPRs of the SIM and OFDM schemes were also compared to verify the analysis given in Section 6.3.3. Based on Fig. 6.10, Fig. 6.11 shows the PAPR comparisons of the SIM and OFDM schemes, where we considered the transmission rate of $R = 1.0$, 2.0, and 3.0 [bits/s/Hz]. All PAPRs were calculated by Eq. (6.3). The system parameters of the schemes considered in the PAPR comparisons were listed in Table 6.2. As shown in Fig. 6.11, the
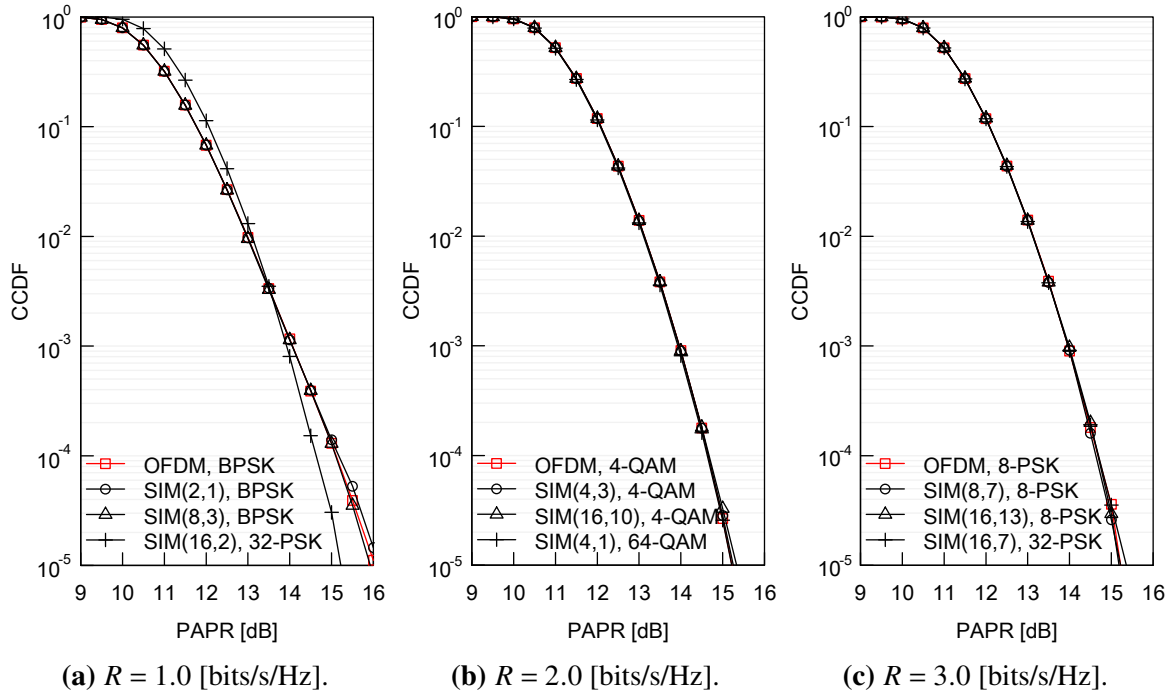
Figure 6.11 PAPR comparisons of OFDM and SIM, where the normalized rate R was 1.0 bits/s/Hz, the number of subcarriers was $N = 2048$, and the CP length was 64.

PAPRs of all the considered schemes were the same, as proved in Section 6.3.3. The only exception was found in Fig. 6.11(a) for the 32–PSK aided SIM(16,2) case. In Fig. 6.11(a), the 32–PSK aided SIM(16,2) scheme reached the PAPR of 15.22 [dB] at the CCDF of 10^{-5}. Observe in Fig. 6.11(c) that the 32–PSK aided SIM(16,7) scheme also reached the PAPR of 15.32 [dB] at the CCDF of 10^{-5}. Hence, we conclude that the PAPR improvement observed in Fig. 6.11(a) was caused by the larger constellation size of $\mathcal{L} = 32$–PSK, and was not caused by the sparsity of the SIM frequency-domain symbols.

6.4.3 Constrained and Unconstrained AMI

Third, we investigated the unconstrained and constrained AMI of the SIM and OFDM schemes. Fig. 6.12 shows the unconstrained AMI of the SIM scheme having $M = 16$ subcarriers and $P = 1, 2, \cdots, 16$ activated subcarriers. The channel coefficients were assumed to follow the frequency-flat i.i.d. Rayleigh fading. It was shown in Fig. 6.12 that the unconstrained AMI monotonically increased upon increasing the number of activated subcarriers P. Note that the SIM scheme having $M = P$ is equivalent to the OFDM scheme. At any SNR, the unconstrained AMI of the SIM scheme is upper-bounded by that of the OFDM scheme, which is equal to the Shannon capacity.
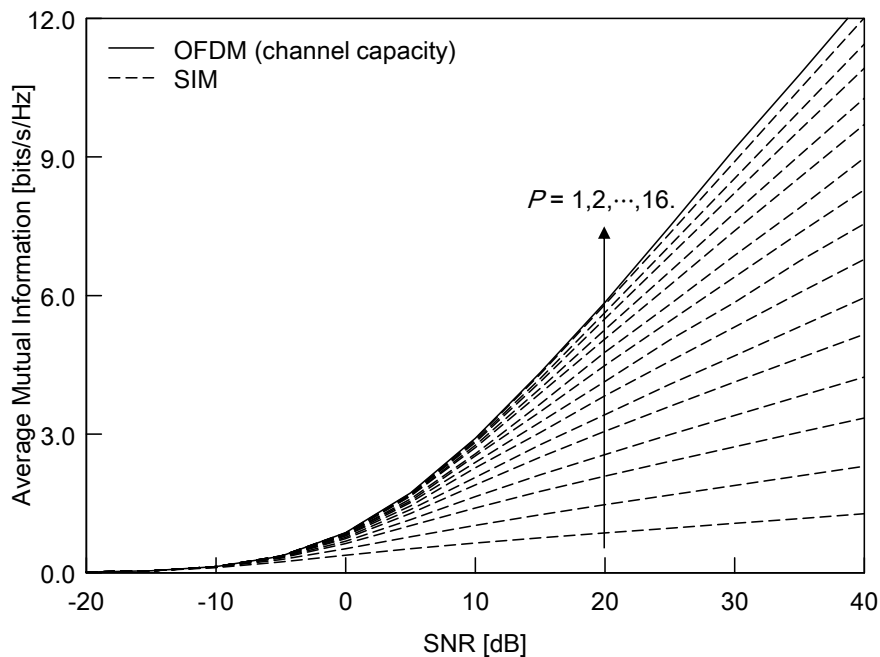
Figure 6.12 Unconstrained AMI comparisons of the SIM scheme in Rayleigh fading channels, where we had $M = 16$ and $P = 1, \cdots, 16$.
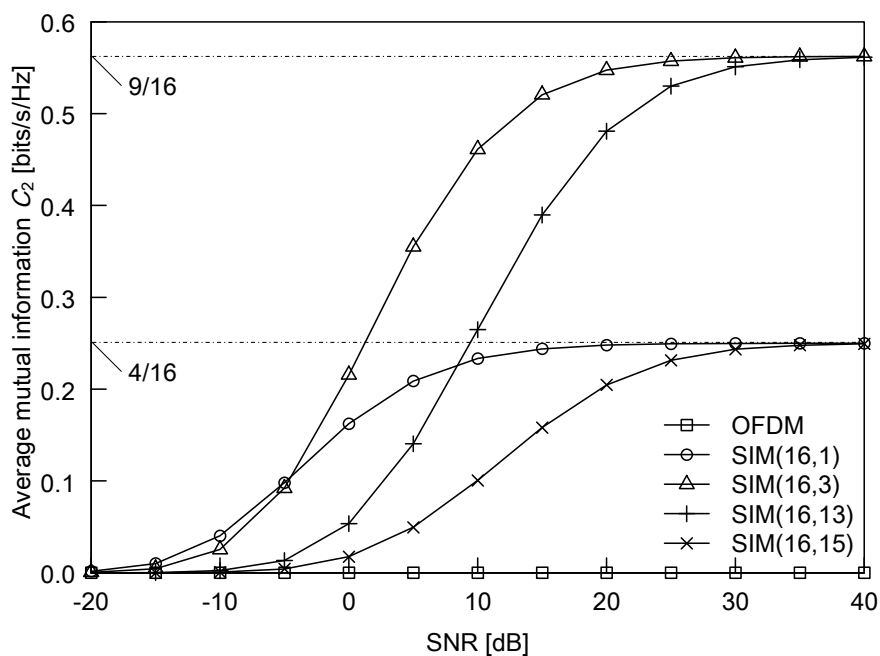
Figure 6.13 Unconstrained AMI I_{C_2} comparisons of the SIM and OFDM schemes, where we had $M = 16$ and $P = 1, 3, 13, 15, 16$.
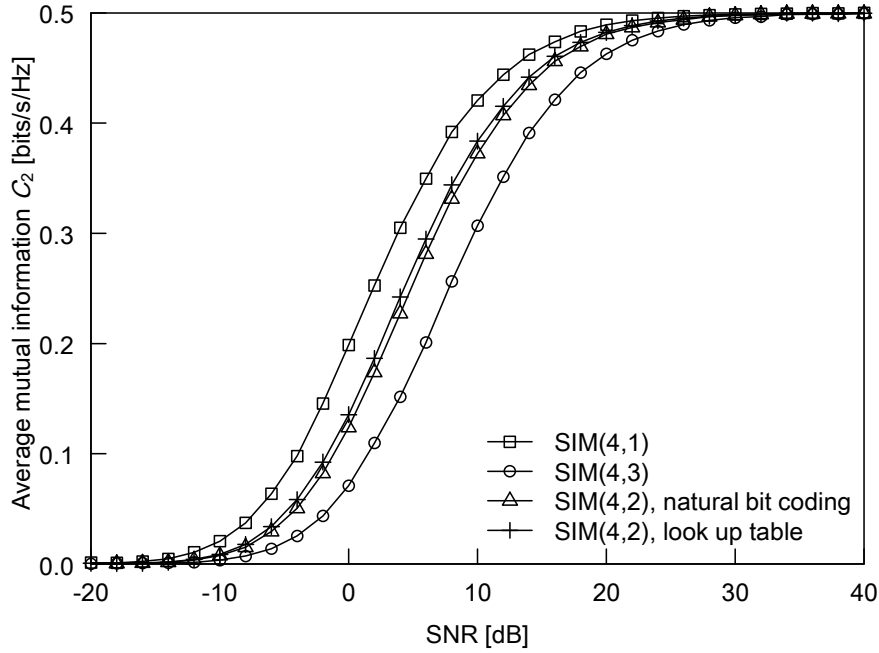
Figure 6.14 Unconstrained AMI I_{C_2} comparisons of the SIM system, where we had $M = 4$ and $P = 1, 2, 3, 4$.

Fig. 6.13 shows the unconstrained AMI I_{C_2} of the SIM and OFDM schemes, where the number of subcarriers was $M = 16$ and the number of activated subcarriers was set to $P = 1, 3, 13, 15, 16$. As given in Eqs. (6.39) and (6.46), the AMI I_{C_1} increases with the logarithm of the SNR, while the AMI I_{C_2} converges to B_2/M [bits/s/Hz]. Hence, the AMI I_{C_2} of the SIM(16,1) and SIM(16,15) converged to $B_2/M = \left\lfloor \log_2 \binom{16}{1} \right\rfloor / 16 = \left\lfloor \log_2 \binom{16}{15} \right\rfloor / 16 = 4/16$. Also, the AMI I_{C_2} of the SIM(16,3) and SIM(16,13) converged to $\left\lfloor \log_2 \binom{16}{3} \right\rfloor / 16 = \left\lfloor \log_2 \binom{16}{13} \right\rfloor / 16 = 9/16$. Note that the OFDM scheme carries no information via the subcarrier-activation. It was shown in Fig. 6.13 that the AMI I_{C_2} at low SNRs of all the schemes correlated with the MEDs having $\mathcal{L} = 1$. Specifically, the MEDs were 32.00, 10.67, 2.46, 2.13 for the $P = 1, 3, 15, 16$ cases, which were calculated by Eq. (6.11). Hence, the sparsity of the SIM symbols in the frequency-domain contributes to the increased MED as well as the AMI assuming $\mathcal{L} = 1$, even though each scheme has the same transmission rate.

Fig. 6.14 shows the unconstrained AMI I_{C_2} of the SIM scheme, where the number of subcarriers was $M = 4$ and the number of activated subcarriers was set to $P = 1, 2, 3$. The MEDs of the SIM schemes were 8.00, 4.00, 2.67 for the $P = 1, 2, 3$ cases, which were calculated by Eq. (6.11). In addition, in order to investigate the effects of subcarrier activation patterns, the natural bit coding (NBC) and LUT methods of [96] were compared for the $P = 2$ case. For the SIM(4,2) case, there are $\binom{6}{4} = 15$ combinations for subcarrier-activation, since
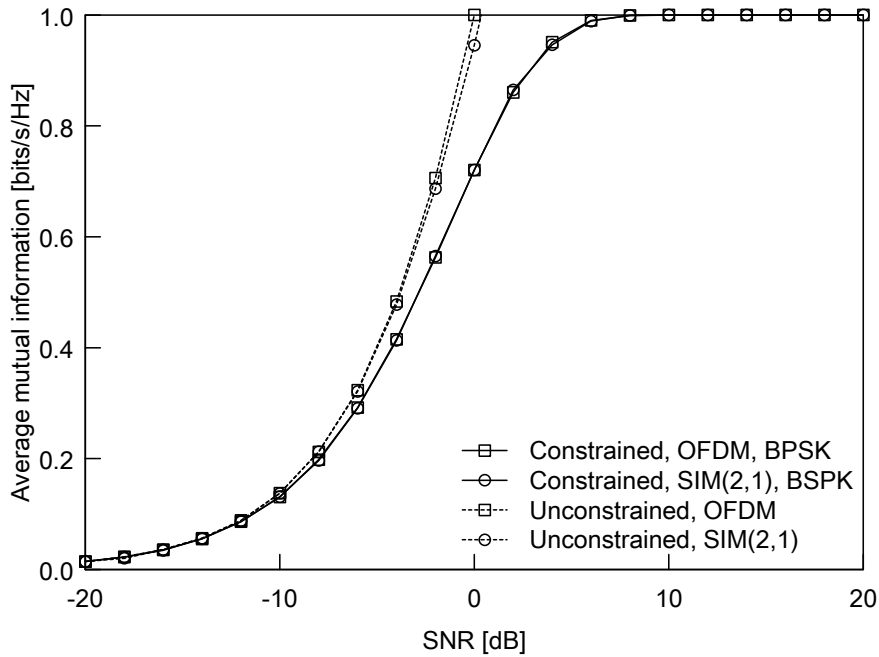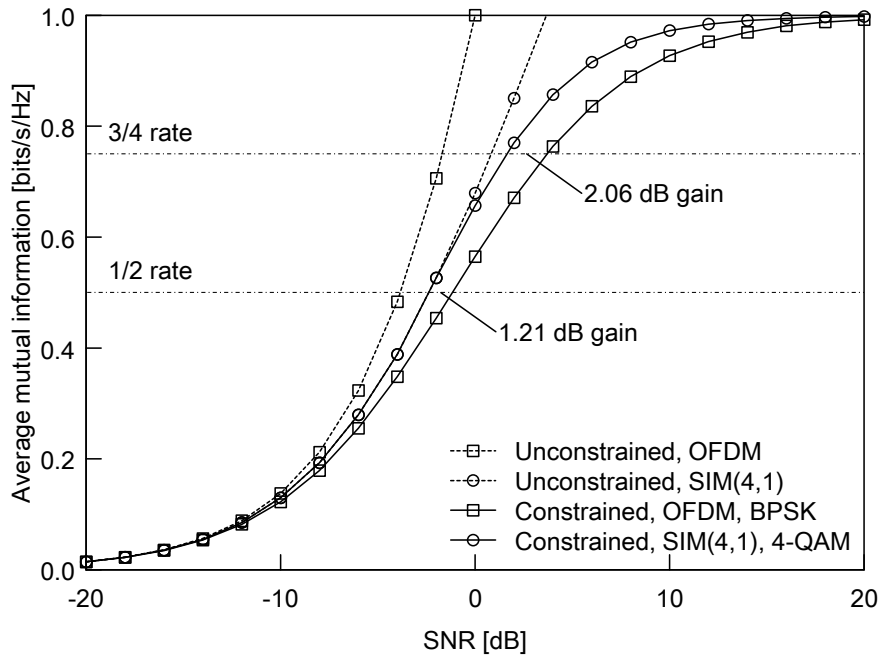
Figure 6.15 Constrained and unconstrained AMI comparisons of the OFDM and BPSK-aided SIM(2,1) schemes in AWGN channels, where the transmission rate was $R = 1.0$ [bits/s/Hz].

we have $\binom{4}{2} = 6$ and $N_a = 2^{\lfloor \log_2 \binom{4}{2} \rfloor} = 4$. Hence, for the NBC and LUT methods, the positions of non-zero elements in the SIM symbol vector are different. It was shown in Fig. 6.14 that the AMI I_{C_2} at low SNRs of all the schemes correlated with the MEDs, similar to those shown in Fig. 6.13. Also, the LUT method improved the AMI with the gap of 0.5 [dB] as compared to the NBC method. Note that for both the methods, the MEDs were the same because the parameters (M,P) were the same.

Fig. 6.15 shows the constrained AMI of the BPSK-aided OFDM and SIM(2,1) schemes in AWGN channels. In addition, the unconstrained AMI curves were plotted as a reference. Observe in Fig. 6.15 that there was no difference between the constrained AMI of the SIM and OFDM schemes, because the frequency-diversity [96] was not available in AWGN channels. Also, at low SNRs, the constrained AMI curves were asymptotic to the derived unconstrained AMI curves.

Fig. 6.16 shows the constrained AMI of the BPSK-aided OFDM and 4–QAM aided SIM(4,1) schemes in Rayleigh fading channels. It was shown in Fig. 6.16 that the constrained AMI of the SIM scheme performed better than that of the OFDM scheme. Specifically, the performance gains of 0.36 and 1.06 [dB] were achieved at the RSC rates of 1/2 and 3/4, respectively.

Fig. 6.17 shows the constrained AMI of the 4–QAM aided OFDM and SIM(4,3) schemes in Rayleigh fading channels. Observe in Fig. 6.17 that the 4–QAM aided SIM(4,3) scheme

Figure 6.16 Constrained and unconstrained AMI comparisons of the OFDM and 4–QAM aided SIM(4,1) schemes in Rayleigh fading channels, where the transmission rate was $R = 1.0$ [bits/s/Hz].
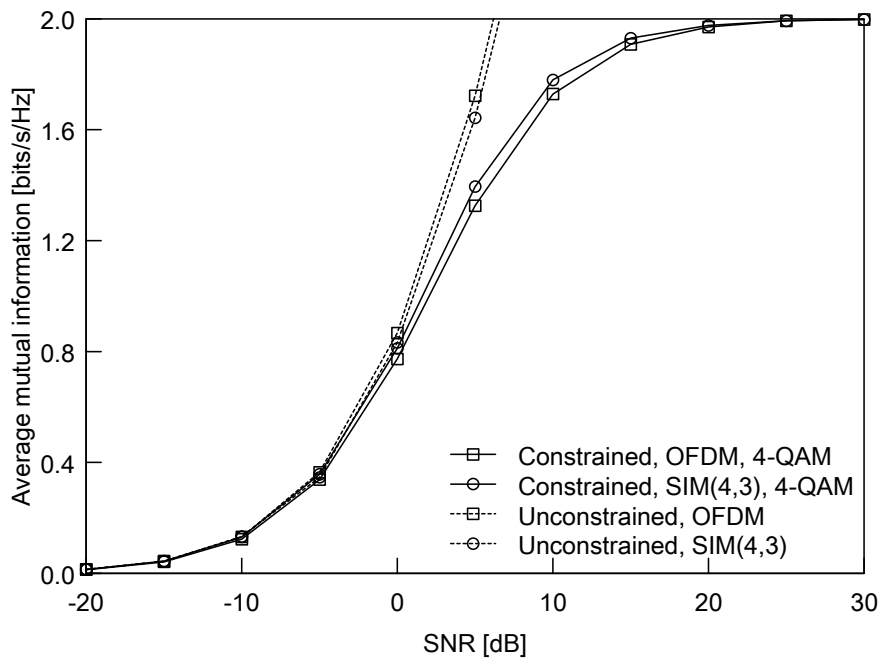

Figure 6.17 Constrained and unconstrained AMI comparisons of the 4–QAM aided OFDM and SIM(4,3) schemes in Rayleigh fading channels, where the transmission rate was $R = 2.0$ [bits/s/Hz].

Table 6.3 Simulation parameters of the three-stage turbo-coded SIM and OFDM scheme.

Detector	Max-log MAP detector
Interleaver length	10^7
Outer channel code	Half-rate RSC ($R_{\text{RSC}} = 1/2$)
RSC constraint length	2
RSC octal generator polynomials	[3 2]
Number of inner iterations	$N_{\text{in}} = 15$
Number of outer iterations	$N_{\text{out}} = 2$

achieved a higher constrained AMI than the OFDM scheme, in accordance with the MED analysis of Section 6.3.1.

6.4.4 BER in Coded Scenarios

Finally, we investigated the three-stage turbo-coded BER performance of the SIM and OFDM schemes. The simulation parameters considered in the coded scenario are given in Table 6.3.

Fig. 6.18 shows the three-stage turbo-coded BERs of the SIM and OFDM schemes, where the outer code was the half-rate RSC code. The schemes considered in Fig. 6.18(a) were the same with those used in Fig. 6.16, while The schemes of Fig. 6.18(b) were the same with Fig. 6.17. It was shown in Fig. 6.18 that the SIM schemes achieved a lower turbo-cliff SNRs than the OFDM schemes, where there were the gaps of 1.02 and 0.16 [dB] for the $R = 0.5$ and 1.0 [bits/s/Hz] cases, in accordance with the results shown in Figs. 6.16 and 6.17.

Fig. 6.19 shows the extrinsic information transfer (EXIT) charts of the 4–QAM aided SIM(4,1) scheme, where the received SNR was −0.8 [dB]. The considered schemes were the same with those used in Fig. 6.18(a). In Fig. 6.19, I_a and I_e represent *a priori* and *a posteriori* information of the SIM scheme's inner code, respectively. It was shown in Fig. 6.19 that the decoding trajectory successively passed through the open EXIT tunnel and reached the convergence point of $(I_a, I_e) = (1.0, 1.0)$. Thus, in Fig. 6.18(a), the 4–QAM aided SIM(4,1) achieved an infinitesimally low ber at SNR = −0.8 [dB].

6.5 Chapter Conclusions

In this chapter, we analyzed the SIM scheme in terms of MED, constrained/unconstrained AMI, and PAPR. First, based on our MED analysis, we proposed the novel design guidelines for the SIM scheme, which also reveled the beneficial region over the conventional OFDM
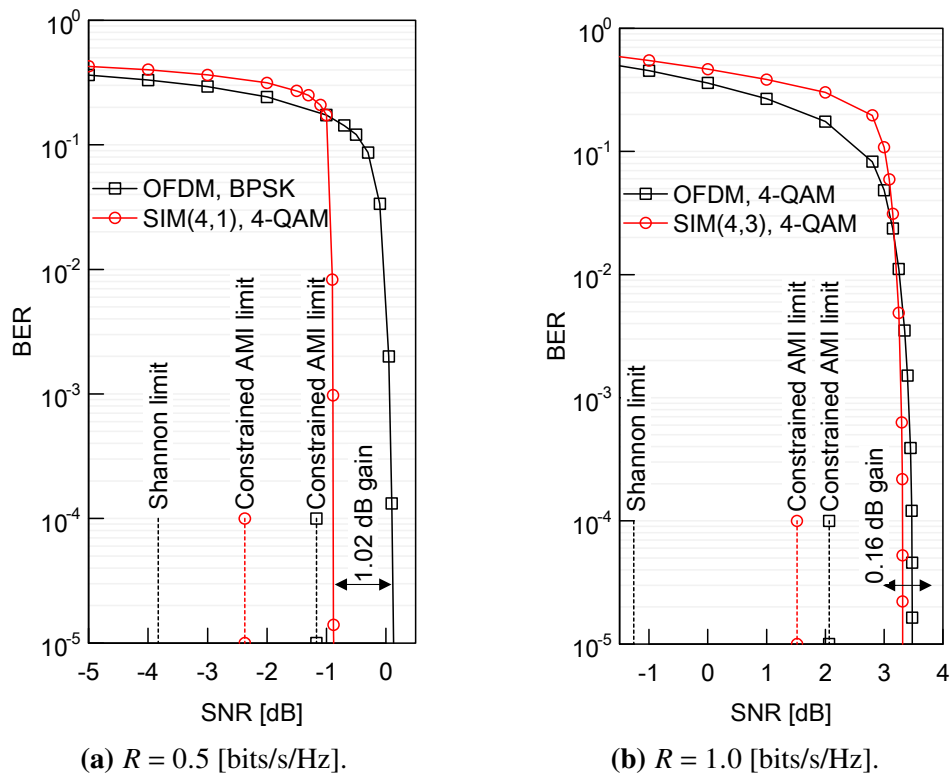
(a) $R = 0.5$ [bits/s/Hz].

(b) $R = 1.0$ [bits/s/Hz].

Figure 6.18 Three-stage turbo-coded BER comparisons of the SIM and OFDM schemes, where the transmission rate was $R = 0.5$ and 1.0 [bits/s/Hz]. All system parameters were listed in Table 6.3.
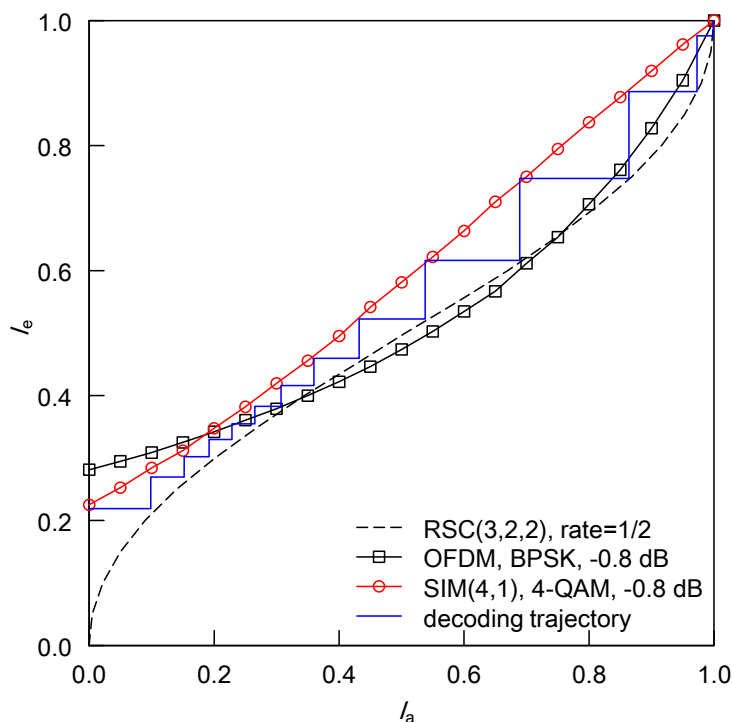
Figure 6.19 EXIT charts of the RSC-coded and 4–QAM aided SIM(4,1) scheme, as well as the BPSK-aided OFDM scheme. The decoding trajectory was plotted at the SNR of −0.8 [dB].

scheme. Specifically, according to our guidelines, the SIM scheme is beneficial in the transmission rate over 0.0 up to 2.0 [bits/s/Hz]. Next, we derived the unconstrained AMI of the SIM scheme, which is the upper-bound of the constrained AMI. The unconstrained and constrained AMI are effective metrics in channel-coded scenarios because both the AMI are capable of estimating the turbo-cliff SNR of the SIM system. Third, we characterized the PAPR of the SIM and OFDM schemes and proved that the PAPRs of both the schemes are identical if the transmit power is the same. The above-mentioned theoretical results were supported by our numerical simulations. All the numerical results were consistent with our established guidelines.

Chapter 7

Conclusions and Future Research

I n this chapter, we summarize Chapters 1–6, including the origin of the PM concept, the comprehensive survey on PM, and the proposals of the PM-based schemes. Then, we provide the research topics that are left for future work.

7.1   Summary and Conclusions

In this thesis, we have reviewed and analyzed the PM concept in the diverse environments, such as the single and multicarrier MIMO communications over the Rayleigh, the Rician, and the Jakes channels as well as MWC and VLC channels.

Chapter 1:   In Chapter 1, we reviewed the basic system model of the coherent MIMO communication. Then, we introduced the MIMO-MWC and MIMO-VLC milestones, which exploit the higher bandwidth than the current 2–5 [GHz] network. In parallel, we provided the historical background of the PM concept. Finally, we reconstituted the PM concept based on the original Slepian's PM paper [73]. The extended PM concept subsumes the conventional SM, SSK, GSTSK, DSM, PC, and SIM concepts.

- In Section 1.1, we detailed the general MIMO system model as well as the statistical channel models, such as the spatially uncorrelated and correlated Rayleigh, the Rician, and the Jakes channel models. Then, we reviewed the background and constitution of the MIMO technology, which was summarized in Tables 1.2 and 1.3.

- In Section 1.2, we introduced the MWC and VLC having been researched against the spectrum shortage issue. In MIMO-MWC systems, the number of RF chains is an

important metric because the mmWave RF chain is complicated and power-consuming. The reduced-RF MIMO-MWC schemes are basically based on the smart antenna scheme, which divides the transmit antenna elements into multiple subarrays. The literature related to the MWC and the smart antenna systems was summarized in Table 1.4. Also, in LED-aided MIMO-VLC systems, the deficient rank of the channel matrix is especially severe when the PDs are employed at the receiver. In contrast, the CMOS imaging sensors have solved the low-rank issue, while it sacrifices the additional complexity. In the highly-correlated channels, the simple PAM-RC scheme, which transmits the same PAM symbol from all the source lights, has been typically used. The VLC milestones were summarized in Table 1.5.

- In Section 1.3, we reviewed the original Slepian's PM concept. We showed that the PM concept is capable of subsuming the conventional SSK and DSM schemes. In the literature, the PM paper of [73] has not been referenced from the SM, the PC, and the SIM research papers. We reconstituted the PM concept in a broad sense, hence it subsumes the conventional SM, PC, and SIM schemes.

- In Section 1.4, we highlighted the novel contributions of this thesis.

Chapter 2: In Chapter 2, we reviewed the PM schemes having been proposed for the coherent and non-coherent MIMO, MIMO-VLC, and the multicarrier communications. Since the PM concept was reconstituted in Chapter 1, the conventional SM and PC schemes were considered as a PM family. We provided a range of simulation results that compares the performance of the PM and non-PM schemes.

- In Section 2.2, we introduced the three performance metrics: the unconstrained and constrained AMI, the RDC, and the computational complexity. The metrics are useful tools for evaluating the PM-aided schemes. The AMI of Section 2.2.1 estimates the upper-limit of the cliff-SNR in channel-coded scenarios, while the RDC analysis of Section 2.2.2 estimates the coding and diversity gains in uncoded scenarios. The computational complexity analysis of Section 2.2.3 is effective for evaluating the PM schemes because the PM family typically exhibits a lower complexity than the conventional non-PM schemes.

- The following Sections 2.3, 2.4, 2.5, and 2.6 introduced the PM family having been proposed for the coherent MIMO, the differential MIMO, the MIMO-VLC, and the multicarrier communications, which were summarized in Tables 2.1, 2.7, 2.10, and 2.12, respectively.

- In Section 2.3, we reviewed the diverse coherent MIMO schemes, such as the SM, the SSK, the GSM, and the GSTSK schemes, all of which are based on the PM concept introduced in Chapter 1. Then, we detailed the optimum hard ML and soft LLR-based detectors in Section 2.3.4. The PM-based schemes were compared in Section 2.3.5 in terms of AMI and BER.

- In Section 2.4, we reviewed the two kinds of the PM-based DSTBC schemes: the sparse-matrix-based schemes and the Cayley transform-based schemes. In Section 2.4.1, we introduced the DSM scheme, which relies on permutation matrices, while in Section 2.4.2, we introduced the NCGSM scheme, which relies on the permutation of the Hermitian matrices. In Section 2.4.3, we reviewed the ML-based detector for the general DSTBC scheme, which supports both the PM and non-PM schemes. In Section 2.4.4, we investigated the effects of the DM design of the NCGSM scheme. Then, we compared the achievable BER performance of the differential PSK, the NCGSM, and the DSM schemes.

- In Section 2.5, we reviewed the OSM scheme having been designed for the MIMO-VLC environment, which was directly imported from the microwave SM scheme. Before we reviewed the OSM scheme, in Section 2.5.2, we introduced the PAM-RC scheme, which simultaneously transmits the same PAM symbol from all of the source lights. Then, we reviewed the original OSM scheme in Section 2.5.3 and the improved OSM scheme in Section 2.5.4. The PAM-RC and the conventional and improved OSM schemes were compared in Section 2.5.5 in terms of BER, along with its theoretical upper-bound. It was shown in Section 2.5.5 that the PM-based MIMO-VLC scheme achieved a higher performance than the spatial multiplexing scheme in rank-deficient scenarios, owing to its reduced number of data streams.

- In Section 2.6, we reviewed the SIM concept, which was originally proposed in 1999 based on the conventional PC concept. Note that both the SIM and PC schemes are regarded as a PM family because both the schemes rely on the on-off combination architecture. The contributions to SIM were summarized in Table 2.12. In Sections 2.6.1, we introduced the system model of the SIM scheme assuming the i.i.d. Rayleigh fading. In Section 2.6.2, we reviewed the optimum hard decision ML-based detector as well as the near-optimum LLR-based detector. The SIM and the conventional OFDM schemes were compared in Section 2.6.3 in terms of BER.

Chapter 3 [4, 6]:   In Chapter 3, we proposed the differentially-encoded counterpart of the SM scheme. Since the proposed scheme depends on the permutation matrices, it is equivalent

to the PM concept applied to DSTBC. The SM scheme has difficulty in estimating the channel coefficients efficiently due to the single-RF architecture. The proposed scheme enables both the single-RF operation at the transmitter and the channel-estimation-free detection at the receiver.

- In Section 3.2, we proposed the PM-aided DSTBC scheme. More specifically, in Section 3.2.1, we proposed the flexible architecture that strikes the rate-diversity trade-off. In Section 3.2.2, we detailed that the proposed scheme subsumes the previously proposed scheme, which is referred to as binary DSM, with the aid of the complex-valued DMs. In Section 3.2.2, we provided the design guideline for the proposed scheme.

- In Section 3.3, we introduced the hard decision ML-based detector for the general uncoded DSTBC scheme. Then, in section 3.3.1, we reviewed the theoretical upper-bound of BER in uncoded scenario. In Section 3.3.2, we derived the computational complexity of the conventional DSTBC and the proposed DSM schemes. It was shown in Section 3.3.2 that the proposed scheme reduces complexity from $O(2^{RM}NM^2)$ to $O(2^{RM}NM)$.

- In Section 3.4, we evaluated the computational complexity and the BER of the proposed scheme. It was shown in Section 3.4.1 that the proposed scheme achieved lower complexity than the conventional DSTBC scheme. This is because the codewords of the proposed scheme are sparse, while those of the conventional scheme are dense. Also, in Section 3.4.2, the proposed scheme was shown to be capable of outperforming the conventional binary DSM scheme. In particular, the performance advantages were significant in the spatially correlated channels and the Rician channels. Upon increasing the number of transmit antennas, the proposed scheme achieved the expected diversity order. Note that in our simulations of Section 3.4, the channel coding schemes such as the turbo and LDPC codes were not taken into account.

Chapter 4 [1]: In Chapter 4, we proposed the PM-aided mmWave scheme. The encoding principle of the proposed scheme is basically the same with the conventional GSM scheme. We revealed that the proposed GSM-based mmWave transmitter was capable of reducing the number of RF chains, while maintaining the near-capacity performance of the spatial multiplexing scheme.

- In Section 4.2, we introduced the system model of the proposed transmitter, which reduces the number of RF chains at the transmitter. More specifically, the proposed

scheme relies on the hybrid analog- and digital-BF scheme, which is based on the smart antenna concept. For example, the GSM(8,2) aided transmitter reduces the number of RF chains to two, while the conventional spatial multiplexing scheme uses eight RF chains. Section 4.2.1 detailed the indoor and LoS-dominant channel model assumed in our simulations.

- In Section 4.3, we reviewed the optimum designs for the antenna element spacing and the ABF weights having been proposed for the mmWave schemes. Section 4.3.1 provided the spacing criterion for the antenna elements. The criterion maximizes the rank of the channel matrix. Hence, the performance advantages of the MIMO-MWC system are fully explored. Section 4.3.2 provided the ABF design criterion, which is designed for the LoS-dominant channels. The ABF design only relies on the AoA and AoD. Hence, there is no need to obtain the complex full-digital channel matrix at the transmitter.

- In Section 4.4, we compared the constrained AMI of the proposed, the single-stream BF, and the spatial multiplexing schemes. Section 4.4.1 illustrated the directive gain of the proposed scheme, which exhibited the increased number of side lobes. Section 4.4.2 demonstrated that the proposed scheme having two or four RF chains achieved nearly the same performance with the conventional scheme having four or eight RF chains, in terms of the constrained AMI. In Sections 4.4.3 and 4.4.4, we considered the misalignment and misdirection cases. In such cases, the proposed scheme still achieved the expected performance gains, which were observed in the idealistic environments of Section 4.4.2.

Chapter 5 [3, 5]:   In Chapter 5, we proposed the unified architecture that subsumes the conventional PI-OSM schemes, where the flexible PA parameters were conceived for combating the MIMO-VLC-specific low-rank channels. We designed our proposed scheme so as to maximize the mutual information or minimize the cliff-SNR observed in channel-coded scenarios. Our simulation results showed that the performance advantages of the proposed scheme ware significant upon increasing the transmission rate.

- In Section 5.2, we introduced our PM-based MIMO-VLC scheme, which was referred to as PI-OSM. The proposed PI-OSM scheme has the flexible PA parameters, which are designed by the designated metric. The flexible PA architecture was shown to be capable of subsuming the conventional power imbalance scheme. Our proposed scheme also supports the channel-coded scenario, as described in Section 5.2.1, where the

three-stage irregular encoding and decoding were considered. Section 5.2.2 provided the LoS-dominant channel assumed in our simulations.

- In Section 5.3, we proposed the two design criteria: the constrained AMI maximization of Section 5.3.1 and the turbo-cliff SNR minimization of Section 5.3.2. More specifically, in Section 5.3.1, we designed the multiple PA parameters so as to maximize the constrained AMI at the target SNR, where the PA parameters were randomly generated. In Section 5.3.2, we designed the irregular-partition ratios so as to fit the aggregated EXIT curve to the outer EXIT curve, which was formulated as a linear programming problem. Since both the criteria rely on the target SNR, we proposed the adaptive operation method in Section 5.3.3, which adaptively changes the PA parameters or the irregular-partition ratios based on the received SNR.

- In Section 5.4, we simulated the proposed and conventional PI-OSM schemes in uncoded and coded scenarios. In Section 5.4.1, we compared the schemes in terms of the unconstrained and constrained AMI, where the number of source lights was 256 at maximum. Our AMI comparisons showed that the proposed scheme was especially beneficial in low SNRs. In Section 5.4.2, we investigated the BER performance in channel-coded scenarios, where the proposed and conventional schemes were compared. Similar to the results shown in Section 5.4.1, the proposed irregular-coded scheme achieved a good constrained AMI at low SNRs. The performance advantages of the proposed scheme over the conventional PI-OSM and PAM-RC schemes were significant, where the gap increased upon increasing the transmission rate.

Chapter 6 [2]: In Chapter 6, we analyzed the PM-aided scheme applied to the multicarrier communications, which is referred to as SIM. More specifically, the SIM scheme is analyzed in terms of MED, constrained and unconstrained AMI, and PAPR. Based on our MED analysis, we proposed the novel design guidelines for the SIM scheme, which also revealed the beneficial region over the conventional OFDM scheme. According to our guidelines, the SIM scheme is beneficial in the transmission rate over 0.0 up to 2.0 [bits/s/Hz].

- In Section 6.2, we introduced the basic system model of the SIM scheme in uncoded and coded scenarios. The transmitter structure was detailed in Section 6.2.1, while the receiver was detailed in Section 6.2.2, where we assumed the i.i.d. Rayleigh fading channels. We also presented the three-stage turbo-coded SIM transmitter and receiver in Section 6.2.3.

- In Section 6.3, we provided the information-theoretic analysis on the SIM scheme in terms of MED, unconstrained and constrained AMI, and PAPR. First, we derived the

upper-bound for the MED of the SIM systems in Section 6.3.1. Based on the derived bound, we established the design guidelines for the SIM scheme, which determine the constellation size and the subcarrier-activation for the SIM scheme. Next, in Section 6.3.2, we derived the unconstrained and constrained AMI for the SIM systems. The derived unconstrained AMI was simplified with the Monte-Carlo integrations and the idealistic i.i.d. assumptions for the generation of channel coefficients. Third, in Section 6.3.3, the PAPR of the SIM systems was investigated based on the level-crossing rate analysis. If we assume that the input signals follow Gaussian and both the SIM and OFDM schemes have a unity transmission power, the mean number of upward crossing was the same for both schemes, which implied that the PAPR of both schemes was also expected to be the same.

- In Section 6.4, we compared the SIM scheme with the conventional OFDM scheme in a comprehensive manner, where we considered the BER in uncoded and coded scenarios, the PAPR, the constrained and unconstrained AMI. The achievable BER in uncoded scenarios was evaluated in Section 6.4.1, which showed that the BER at high SNRs was correlated with the MED if the transmission rate was over 1.0 [bits/s/Hz]. The simulations in Section 6.4.2 showed that the PAPR of both the SIM and OFDM schemes was basically the same. The sparsity of the frequency-domain symbols did not contribute to improving PAPR. In Section 6.4.3, we investigated the unconstrained and constrained AMI of the SIM scheme. The unconstrained AMI of the SIM scheme never exceeded that of the OFDM scheme, however, in low-rate scenarios the constrained AMI of SIM outperformed that of OFDM. This observation was supported by the BER simulations in Section 6.4.4, where we considered the three-stage turbo-encoding and decoding. We observed the performance advantages of the SIM scheme below the transmission rate of 2.0 [bits/s/Hz].

7.2   Future Work

In this section, we summarize the future works of the proposed schemes.

7.2.1   Exact constrained AMI Calculation for the DSTBC Schemes

The constrained AMI has been derived for the coherent schemes, such as the BPSK-aided SISO scheme [109] and the general MIMO schemes [110]. In [165], the constrained AMI for the differential BPSK and QPSK schemes were obtained from the EXIT chart. It was shown

in [165] that the obtained AMI curve was almost the same with the 3-dB-shifted counterpart of the coherent scheme, where a small gap was observed at low and high SNRs. To the best of our knowledge, the constrained AMI for the general DSTBC schemes has not been derived yet. As shown in [165], the 3-dB-shifting may not be accurate in some SNR region. Thus, we need to derive the constrained AMI, in order not to overestimate the performance of the DSTBC schemes.

7.2.2   The UDSM Scheme Having APSK Symbols

In Chapter 3, we proposed the UDSM scheme that relies on PSK symbols. Owing to the sparse and unitary DMs as well as the PSK signaling, the UDSM space-time codewords are constantly unitary matrices. However, the MED of the PSK symbol decreases upon increasing the constellation size $\mathcal{L}$. The MEDs of the PSK and QAM symbols are defined in Eq. (6.10). For example, the MEDs of $\mathcal{L} = 16$–aided PSK and QAM are 1.52×10^{-1} and 4.00. Also, the MEDs of $\mathcal{L} = 64$–aided PSK and QAM are 9.63×10^{-3} and 9.52×10^{-2}. The MED gain of the QAM signaling is approximated as follows:

$$\frac{\mathrm{MED_{QAM}}}{\mathrm{MED_{PSK}}} = \frac{3}{(\mathcal{L}-1) \cdot (1 - \cos{(2 \cdot \pi/\mathcal{L})})} \approx \frac{3}{2\pi^2}\mathcal{L}, \qquad (7.1)$$

where $\mathcal{L}$ approaches to infinity. Eq. (7.1) implies that the gain of the QAM signaling monotonically increases upon increasing the constellation size $\mathcal{L}$. Against this observation, the DSM scheme having APSK symbols has been proposed [166, 167] for improving the MED of codewords. More specifically, in [166], the DSM scheme having two-level $\mathcal{L} = 16$–APSK was investigated in time-varying fading channels. Also, the DSM scheme having four-level $\mathcal{L} = 64$–APSK was investigated in [166], where its average BER was theoretically derived. The simulations conducted in both [166] and [167] assumed the number of transmit antennas was $M = 2$. Here, we need to consider the general UDSM scheme that supports the arbitrary number of transmit antennas and power levels.

7.2.3   Systematic Construction of the UDSM DMs

In Chapter 3, we proposed the design guideline for the UDSM scheme, where the corresponding DMs are obtained through the exhaustive search. The search space of the UDSM scheme is smaller than the conventional DM-based schemes, such as the GSTSK scheme. However, its evaluation cost exponentially increases upon increasing the transmission rate R. More specifically, if we adopt the MED as an objective function, the complexity order

of its evaluation is $O\left(2^{2RM}M^3\right)$, which is caused by the increased number of space-time codewords. For the high-rate and large-scale MIMO scenarios, it is a challenging task to obtain the optimum DMs, because the transmission rate R and the number of antennas M are large. Against this limitation, the systematic construction method of DMs was proposed in [7], which was based on the field-extension theory of [168]. The construction scheme of [7] supports the DMs having $Q = M$, in order to reduce the computational complexity at the receiver. Here, if we pursue the high-complexity and high-reliability scenario, we need to consider a new construction scheme that supports the arbitrary number of DMs.

7.2.4   Non-Square Differential MIMO

As shown in Chapters 2 and 3, the transmission rate of the DSTBC schemes decreases upon increasing the number of transmit antennas because the space-time codewords have to be square unitary matrices. Typically, the performance gain of the DSTBC scheme vanishes in high-rate scenarios. This observation is caused by the limited symbol space imposed by the unitary constraint. Against this limitation, we need to consider a new scheme that supports the non-square space-time codewords, namely, $M > T$.

7.2.5   Exact PAPR Analysis Based on Non-Gaussian Assumption

In Chapter 6, we analyzed the PAPR of the SIM systems, assuming the input signals follow Gaussian distribution. However, we observed that the input signals do not follow Gaussian distribution when the number of activated subcarriers is low, i.e. the subcarrier-activation ratio $r = P/M$ is small. The PAPR analysis of the non-Gaussian behavior of SIM systems remains an open issue.

7.2.6   The GSM-Based mmWave Transmitter in Non-LoS Channels

In Chapter 4, the proposed mmWave transmitter was evaluated in LoS channels. In some previous studies [59, 60, 169], the channel model was assumed to be the non-LoS channels, where there was no LoS path. The performance of the proposed GSM scheme in non-LoS channels is still unknown. It would be worth considering the GSM-specific hybrid-BF designed for non-LoS channels.

Bibliography

[1] N. Ishikawa, R. Rajashekar, S. Sugiura, and L. Hanzo, "Generalized-spatial-modulation-based reduced-RF-chain millimeter-wave communications," *IEEE Transactions on Vehicular Technology*, vol. 66, no. 1, pp. 879–883, 2017.

[2] N. Ishikawa, S. Sugiura, and L. Hanzo, "Subcarrier-index modulation aided OFDM – will it work ?" *IEEE Access*, vol. 4, pp. 2580–2593, 2016.

[3] N. Ishikawa and S. Sugiura, "Maximizing constrained capacity of power-imbalanced optical wireless MIMO communications using spatial modulation," *Journal of Lightwave Technology*, vol. 33, no. 2, pp. 519–527, 2015.

[4] ——, "Unified differential spatial modulation," *IEEE Wireless Communications Letters*, vol. 3, no. 4, pp. 337–340, 2014.

[5] ——, "EXIT-chart-based design of irregular-precoded power-imbalanced optical spatial modulation," in *IEEE 82nd Vehicular Technology Conference*, Boston, USA., 2015.

[6] ——, "Single- and multiple-RF aided non-coherent generalized spatial modulation," in *IEEE 79th Vehicular Technology Conference Spring*, Seoul, Korea., 2014, pp. 1–5.

[7] R. Rajashekar, N. Ishikawa, S. Sugiura, K. V. S. Hari, and L. Hanzo, "Full-diversity dispersion matrices from algebraic field extensions for differential spatial modulation," *IEEE Transactions on Vehicular Technology*, vol. 66, no. 1, pp. 385–394, 2017.

[8] Ericsson, *Ericsson Mobility Report*, 2016.

[9] M. West and C. H. Ei, *Reading in the mobile era: a study of mobile reading in developing countries*. UNESCO, 2014.

[10] M. Kobayashi, "Experience of infrastructure damage caused by the Great East Japan Earthquake and countermeasures against future disasters," *IEEE Communications Magazine*, vol. 52, no. 3, pp. 23–29, 2014.

[11] A. Goldsmith, *Wireless Communications*. Cambridge University Press, 2005.

[12] J. H. Winters, "On the capacity of radio communication systems with diversity in a Rayleigh fading environment," *IEEE Journal on Selected Areas in Communications*, vol. SAC-5, no. 5, pp. 871–878, 1987.

[13] G. Foschini, "Layered space-time architecture for wireless communication in a fading environment when using multi-element antennas," *Bell labs technical journal*, vol. 1, no. 2, pp. 41–59, 1996.

[14] J. J. G. Andrews, S. Buzzi, W. Choi, S. V. S. Hanly, A. Lozano, A. A. C. K. Soong, and J. J. C. Zhang, "What will 5G be?" *IEEE Journal on Selected Areas in Communications*, vol. 32, no. 6, pp. 1065–1082, 2014.

[15] L. Verma, M. Fakharzadeh, and S. Choi, "Wi-Fi on steroids: 802.11ac and 802.11ad," *IEEE Wireless Communications*, vol. 20, no. 6, pp. 30–35, 2013.

[16] C. E. Shannon, "A mathematical theory of communication," *Bell System Technical Journal*, vol. 27, pp. 379–423, 623–656, 1948.

[17] C. Berrou, A. Glavieux, and P. Thitimajshima, "Near Shannon limit error-correcting coding and decoding: turbo-codes," *IEEE International Conference on Communications*, vol. 2, pp. 1064–1070, 1993.

[18] N. Wiberg, H. Loeliger, and R. Kotter, "Codes and iterative decoding on general graphs," *European Transactions on telecommunications*, vol. 6, no. 5, pp. 513–525, 1995.

[19] D. MacKay and R. Neal, "Near Shannon limit performance of low density parity check codes," *Electronics letters*, vol. 33, no. 6, pp. 457–458, 1997.

[20] L. Hanzo, O. Alamri, M. El-Hajjar, and N. Wu, *Near-capacity multi-functional MIMO systems*. John Wiley & Sons, Ltd, 2009.

[21] J. Wallace and M. Jensen, "Modeling the indoor MIMO wireless channel," *IEEE Transactions on Antennas and Propagation*, vol. 50, no. 5, pp. 591–599, 2002.

[22] S. Rice, "Mathematical analysis of random noise," *Bell System Technical Journal*, pp. 282–332, 1944.

[23] F. Farrokhi, G. Foschini, A. Lozano, and R. Valenzuela, "Link-optimal space-time processing with multiple transmit and receive antennas," *IEEE Communications Letters*, vol. 5, no. 3, pp. 85–87, 2001.

[24] W. Jakes, *Microwave mobile communications*. Wiley, 1974.

[25] E. Telatar, "Capacity of multi-antenna Gaussian channels," *European transactions on telecommunications*, vol. 10, no. 6, pp. 585–595, 1999.

[26] N. Amitay and J. Salz, "Linear equalization theory in digital data transmission over dually polarized fading radio channels," *AT&T Bell Laboratories Technical Journal*, vol. 63, no. 10, pp. 2215–2259, 1984.

[27] S. Sugiura, S. Chen, and L. Hanzo, "A universal space-time architecture for multiple-antenna aided systems," *IEEE Communications Surveys & Tutorials*, vol. 14, no. 2, pp. 401–420, 2012.

[28] S. Alamouti, "A simple transmit diversity technique for wireless communications," *IEEE Journal on Selected Areas in Communications*, vol. 16, no. 8, pp. 1451–1458, 1998.

[29] T. L. Marzetta, "Noncooperative cellular wireless with unlimited numbers of base station antennas," *IEEE Transactions on Wireless Communications*, vol. 9, no. 11, pp. 3590–3600, 2010.

[30] W. Schmidt and N. Shimasaki, *Satellite on-board switching utilizing space-division and spot beam antennas.* US3711855 A, 1973.

[31] Q. H. Spencer, C. B. Peel, A. L. Swindlehurst, and M. Haardt, "An introduction to the multi-user MIMO downlink," *IEEE Communications Magazine*, vol. 42, no. 10, pp. 60–67, 2004.

[32] L. Zheng and D. Tse, "Diversity and multiplexing: a fundamental tradeoff in multiple-antenna channels," *IEEE Transactions on Information Theory*, vol. 49, no. 5, pp. 1073–1096, 2003.

[33] G. Foschini and M. Gans, "On limits of wireless communications in a fading environment when using multiple antennas," *Wireless personal communications*, vol. 6, no. 3, pp. 311–335, 1998.

[34] P. Wolniansky, G. Foschini, G. Golden, and R. Valenzuela, "V-BLAST: an architecture for realizing very high data rates over the rich-scattering wireless channel," in *Proceedings of the International Symposium on Signals, Systems, and Electronics*, 1998.

[35] L. Zeng, D. C. O'Brien, H. Le Minh, G. E. Faulkner, K. Lee, D. Jung, Y. Oh, and E. T. Won, "High data rate multiple input multiple output (MIMO) optical wireless communications using white LED lighting," *IEEE Journal on Selected Areas in Communications*, vol. 27, no. 9, pp. 1654–1662, 2009.

[36] B. Hassibi and B. Hochwald, "High-rate codes that are linear in space and time," *IEEE Transactions on Information Theory*, vol. 48, no. 7, pp. 1804–1824, 2002.

[37] H. O. Peterson, *Diversity receiving system.* US2290992 A, 1942.

[38] R. G. Clark, "Communications system for simultaneous communications on a single channel," 1968.

[39] S. Sugiura, S. Chen, and L. Hanzo, "Coherent and differential space-time shift keying: a dispersion matrix approach," *IEEE Transactions on Communications*, vol. 58, no. 11, pp. 3219–3230, 2010.

[40] B. M. Hochwald and T. L. Marzetta, "Unitary space-time modulation for multiple-antenna communications in Rayleigh flat fading," *IEEE Transactions on Information Theory*, vol. 46, no. 2, pp. 543–564, 2000.

[41] V. Tarokh and H. Jafarkhani, "A differential detection scheme for transmit diversity," *IEEE Journal on Selected Areas in Communications*, vol. 18, no. 7, pp. 1169–1174, 2000.

[42] B. L. Hughes, "Differential space-time modulation," *IEEE Transactions on Information Theory*, vol. 46, no. 7, pp. 2567–2578, 2000.

[43] B. M. Hochwald, T. L. Marzetta, T. J. Richardson, W. Sweldens, and R. Urbanke, "Systematic design of unitary space-time constellations," *IEEE Transactions on Information Theory*, vol. 46, no. 6, pp. 1962–1973, 2000.

[44] B. M. Hochwald and W. Sweldens, "Differential unitary space-time modulation," *IEEE Transactions on Communications*, vol. 48, no. 12, pp. 2041–2052, 2000.

[45] B. Hassibi and B. Hochwald, "Cayley differential unitary space-time codes," *IEEE Transactions on Information Theory*, vol. 48, no. 6, pp. 1485–1503, 2002.

[46] X. G. Xia, "Differentially en/decoded orthogonal space-time block codes with APSK signals," *IEEE Communications Letters*, vol. 6, no. 4, pp. 150–152, 2002.

[47] Y. Zhu and H. Jafarkhani, "Differential modulation based on quasi-orthogonal codes," *IEEE Transactions on Wireless Communications*, vol. 4, no. 6, pp. 3018–3030, 2005.

[48] M. Bhatnagar, A. Hjorungnes, and L. S. L. Song, "Differential coding for non-orthogonal space-time block codes with non-unitary constellations over arbitrarily correlated rayleigh channels," *IEEE Transactions on Wireless Communications*, vol. 8, no. 8, pp. 3985–3995, 2009.

[49] V. Tarokh, S. M. Alamouti, and P. Poon, "New detection schemes for transmit diversity with no channel estimation," in *IEEE International Conference on Universal Personal Communications*, 1998.

[50] T. S. Rappaport, R. Mayzus, Y. Azar, K. Wang, G. N. Wong, J. K. Schulz, M. Samimi, and F. Gutierrez, "Millimeter Wave Mobile Communications for 5G Cellular: It Will Work!" *IEEE Access*, vol. 1, pp. 335–349, 2013.

[51] T. Komine and M. Nakagawa, "Fundamental analysis for visible-light communication system using LED lights," *IEEE Transactions on Consumer Electronics*, vol. 50, no. 1, pp. 100–107, 2004.

[52] Y. Shoji, H. Sawada, C. S. Choi, and H. Ogawa, "A modified SV-model suitable for line-of-sight desktop usage of millimeter-wave WPAN systems," *IEEE Transactions on Antennas and Propagation*, vol. 57, no. 10, pp. 2940–2948, 2009.

[53] S. Rangan, T. S. Rappaport, and E. Erkip, "Millimeter-wave cellular wireless networks: Potentials and challenges," *Proceedings of the IEEE*, vol. 102, no. 3, pp. 366–385, 2014.

[54] A. Van, *Electromagnetic reflector*. US2908002 A, 1959.

[55] N. Celik, M. F. Iskander, R. Emrick, S. J. Franson, and J. Holmes, "Implementation and experimental verification of a smart antenna system operating at 60 GHz band," *IEEE Transactions on Antennas and Propagation*, vol. 56, no. 9, pp. 2790–2800, 2008.

[56] Z. Zhang, M. F. Iskander, Z. Yun, and A. Høst-Madsen, "Hybrid smart antenna system using directional elements — performance analysis in flat Rayleigh fading," *IEEE Transactions on Antennas and Propagation*, vol. 51, no. 10, pp. 2926–2935, 2003.

[57] S. Sugiura, N. Kikuma, and H. Iizuka, "Eigenspace-based blind pattern optimisations of steerable antenna array for interference cancellation," *IET Microwaves, Antennas & Propagation*, vol. 2, no. 4, pp. 358–366, 2008.

[58] Y. J. Guo, X. Huang, and V. Dyadyuk, "A hybrid adaptive antenna array for long-range mm-wave communications," *IEEE Antennas and Propagation Magazine*, vol. 54, no. 2, pp. 271–282, 2012.

[59] A. Alkhateeb, O. El Ayach, G. Leus, and R. W. Heath, "Hybrid precoding for millimeter wave cellular systems with partial channel knowledge," in *Information Theory and Applications Workshop*, 2013.

[60] O. E. Ayach, S. Rajagopal, S. Abu-Surra, Z. Pi, and R. W. Heath, "Spatially sparse precoding in millimeter wave MIMO systems," *IEEE Transactions on Wireless Communications*, vol. 13, no. 3, pp. 1499–1513, 2014.

[61] S. Han, I. Chih-Lin, Z. Xu, and C. Rowell, "Large-scale antenna systems with hybrid analog and digital beamforming for millimeter wave 5G," *IEEE Communications Magazine*, vol. 53, no. 1, pp. 186–194, 2015.

[62] F. Bøhagen, P. Orten, and G. E. Øien, "Design of optimal high-rank line-of-sight MIMO channels," *IEEE Transactions on Wireless Communications*, vol. 6, no. 4, pp. 1420–1424, 2007.

[63] E. Torkildson, U. Madhow, and M. Rodwell, "Indoor millimeter wave MIMO: Feasibility and performance," *IEEE Transactions on Wireless Communications*, vol. 10, no. 12, pp. 4150–4160, 2011.

[64] Y. Tanaka, T. Komine, S. Haruyama, and M. Nakagawa, "Indoor visible light data transmission system utilizing white LED lights," *IEICE Transactions on Communications*, vol. E86-B, no. 8, pp. 2440–2454, 2003.

[65] K. Kamiya, *Optical data transmission system*. JP2000387660A, 2002.

[66] H. L. Minh, D. O. Brien, G. Faulkner, L. Zeng, K. Lee, D. Jung, and Y. Oh, "High-speed visible light communications using multiple-resonant equalization," *IEEE Photonics Technology Letters*, vol. 20, no. 14, pp. 1243–1245, 2008.

[67] A. G. Bell, "The photophone," *Science*, vol. 1, no. 11, pp. 130–134, 1880.

[68] M. Simon and V. Vilnrotter, "Alamouti-type space-time coding for free-space optical communication with direct detection," *IEEE Transactions on Wireless Communications*, vol. 4, no. 1, pp. 35–39, 2005.

[69] T. Komine, S. Haruyama, and M. Nakagawa, "A Study of Shadowing on Indoor Visible-Light Wireless Communication Utilizing Plural White LED Lightings," *Wireless Personal Communications*, vol. 34, no. 1, pp. 211–225, 2005.

[70] M. Safari and M. Uysal, "Do we really need OSTBCs for free-space optical communication with direct detection?" *IEEE Transactions on Wireless Communications*, vol. 7, no. 11, pp. 4445–4448, 2008.

[71] A. M. Khalid, G. Cossu, R. Corsini, P. Choudhury, and E. Ciaramella, "1-Gb/s transmission over a phosphorescent white LED by using rate-adaptive discrete multitone modulation," *IEEE Photonics Journal*, vol. 4, no. 5, pp. 1465–1473, 2012.

[72] R. Tian-Peng, C. Yuen, Y. L. Guan, and G. S. Tang, "High-order intensity modulations for ostbc in free-space optical mimo communications," *IEEE Wireless Communications Letters*, vol. 2, no. 6, pp. 607–610, 2013.

[73] D. Slepian, "Permutation modulation," *Proceedings of the IEEE*, vol. 53, no. 3, pp. 228–236, 1965.

[74] Y. Bian, M. Wen, X. Cheng, H. Poor, and B. Jiao, "A differential scheme for spatial modulation," in *IEEE Global Communications Conference*, Atlanta, GA, USA, 2013.

[75] S. Sasaki, J. Zhu, and G. Marubayashi, "Performance of parallel combinatory spread spectrum multiple access communication systems," in *IEEE International Symposium on Personal, Indoor and Mobile Radio Communications*, 1991.

[76] P. K. Frenger and N. A. B. Svensson, "Parallel combinatory OFDM signaling," *IEEE Transactions on Communications*, vol. 47, no. 4, pp. 558–567, 1999.

[77] Y. A. Chau and S.-H. Yu, "Space modulation on wireless fading channels," in *IEEE Vehicular Technology Conference*, 2001.

[78] R. Mesleh, H. Elgala, and H. Haas, "Optical spatial modulation," *Journal of Optical Communications and Networking*, vol. 3, no. 3, p. 234, 2011.

[79] D. H. Lehmer, "Teaching combinatorial tricks to a computer," *Proceedings of Symposia in Applied Mathematics*, vol. 10, pp. 179–193, 1960.

[80] D. Slepian, *Permutation code signaling*. US3196351A, 1965.

[81] H. L. Schneider, "Data transmission with FSK permutation modulation," *Bell Labs Technical Journal*, vol. 47, pp. 1131–1138, 1968.

[82] T. Berger, F. Jelinek, and J. K. Wolf, "Permutation codes for sources," *IEEE Transactions on Information Theory*, vol. 18, no. 1, pp. 160–169, 1972.

[83] G. E. Atkin and H. P. Corrales, "An Efficient Modulation/Coding Scheme for MFSK Systems on Bandwidth Constrained Channels," *IEEE Journal on Selected Areas in Communications*, vol. 7, no. 9, pp. 1396–1401, 1989.

[84] W. Li, *Study of hybrid permutation frequency phase modulation*. Master Thesis, University of Ottawa, 1996.

[85] A. Yongacoglu and W. Li, "Hybrid permutation frequency phase modulation," in *IEEE Canadian Conference on Electrical and Computer Engineering*, 1997.

[86] C. Savage, "A survey of combinatorial Gray codes," *SIAM Review*, vol. 39, no. 4, pp. 605–629, 1997.

[87] T. Mittelholzer, "An information-theoretic approach to steganography and watermarking," in *International Workshop on Information Hiding*. Springer Berlin Heidelberg, 1999.

[88] B. M. King and M. A. Neifeld, "Low-complexity maximum-likelihood decoding of shortened enumerative permutation codes for holographic storage," *IEEE Journal on Selected Areas in Communications*, vol. 19, no. 4, pp. 783–790, 2001.

[89] D. Silva and W. A. Finamore, "Vector permutation modulation," *IEEE Communications Letters*, vol. 9, no. 8, pp. 673–675, 2005.

[90] A. Jiang, R. Mateescu, M. Schwarts, and J. Bruck, "Rank modulation for flash memories," *IEEE Transactions on Information Theory*, vol. 55, no. 6, pp. 2659–2673, 2009.

[91] M. Shi, C. D'Amours, and A. Yongacoglu, "Design of spreading permutations for MIMO-CDMA based on space-time block codes," *IEEE Communications Letters*, vol. 14, no. 1, pp. 36–38, 2010.

[92] T. Mittelholzer, N. Papandreou, and C. Pozidis, *Data encoding in solid-state storage devices*. US8578246 B2, 2013.

[93] S. Ishimura and K. Kikuchi, "Multi-dimensional permutation-modulation format for coherent optical communications," *Optics Express*, vol. 23, no. 12, pp. 15 587–15 597, 2015.

[94] J. Jeganathan, A. Ghrayeb, and L. Szczecinski, "Generalized space shift keying modulation for MIMO channels," in *IEEE International Symposium on Personal, Indoor and Mobile Radio Communications*, 2008.

[95] R. Abu-Alhiga and H. Haas, "Subcarrier-index modulation OFDM," in *IEEE 20th International Symposium on Personal, Indoor and Mobile Radio Communications*, Tokyo, Japan, 2009, pp. 177–181.

[96] E. Basar, U. Aygolu, E. Panayirci, and H. V. Poor, "Orthogonal frequency division multiplexing with index modulation," *IEEE Transactions of Signal Processing*, vol. 61, no. 22, pp. 5536–5549, 2013.

[97] M. Wen, X. Cheng, M. Ma, B. Jiao, and H. V. Poor, "On the achievable rate of OFDM with index modulation," *IEEE Transactions on Signal Processing*, vol. 64, no. 8, pp. 1919 – 1932, 2015.

[98] K. Ishibashi and S. Sugiura, "Effects of antenna switching on band-limited spatial modulation," *IEEE Wireless Communications Letters*, vol. 3, no. 4, pp. 345–348, 2014.

[99] R. Mesleh, R. Mehmood, H. Elgala, and H. Haas, "Indoor MIMO optical wireless communication using spatial modulation," in *IEEE International Conference on Communications*, 2010.

[100] P. Liu and A. Springer, "Space shift keying for LOS communication at mmWave frequencies," *IEEE Wireless Communications Letters*, vol. 4, no. 2, pp. 121–124, 2015.

[101] T. Fath and H. Haas, "Performance comparison of MIMO techniques for optical wireless communications in indoor environments," *IEEE Transactions on Communications*, vol. 61, no. 2, pp. 733–742, 2013.

[102] M. D. Renzo, H. Haas, and P. Grant, "Spatial modulation for multiple-antenna wireless systems: A survey," *IEEE Communications Magazine*, vol. 49, no. 12, pp. 182–191, 2011.

[103] P. Yang, M. Di Renzo, Y. Xiao, S. Li, and L. Hanzo, "Design Guidelines for Spatial Modulation," *IEEE Communications Surveys & Tutorials*, vol. 17, no. 1, pp. 6–26, 2015.

[104] M. Di Renzo, H. Haas, A. Ghrayeb, S. Sugiura, and L. Hanzo, "Spatial modulation for generalized MIMO: Challenges, opportunities, and implementation," *Proceedings of the IEEE*, vol. 102, no. 1, pp. 56–103, 2014.

[105] P. Yang, Y. Xiao, Y. L. Guan, K. Hari, A. Chockalingam, S. Sugiura, H. Haas, M. Di Renzo, C. Masouros, Z. Liu, L. Xiao, S. Li, and L. Hanzo, "Single-carrier spatial modulation: A promising design for large-scale broadband antenna systems," *IEEE Communications Surveys & Tutorials*, 2016.

[106] M. I. Kadir, S. Sugiura, S. Chen, and L. Hanzo, "Unified MIMO-multicarrier designs: A space–time shift keying approach," *IEEE Communications Surveys & Tutorials*, vol. 17, no. 2, pp. 550–579, 2015.

[107] S. Sugiura, S. Chen, and L. Hanzo, "MIMO-aided near-capacity turbo transceivers: taxonomy and performance versus complexity," *IEEE Communications Surveys & Tutorials*, vol. 14, no. 2, pp. 421–442, 2012.

[108] D. A. Basnayaka, M. Di Renzo, and H. Haas, "Massive but few active MIMO," *IEEE Transactions on Vehicular Technology*, vol. 65, no. 9, pp. 6861–6877, 2016.

[109] J. G. Proakis and M. Salehi, *Digital Communications*, 5th ed. McGraw-Hill, 2008.

[110] S. X. Ng and L. Hanzo, "On the MIMO channel capacity of multi-dimensional signal sets," *IEEE Transactions on Vehicular Technology*, vol. 55, no. 2, pp. 528–536, 2006.

[111] S. Sugiura and L. Hanzo, "On the joint optimization of dispersion matrices and constellations for near-capacity irregular precoded space-time shift keying," *IEEE Transactions on Wireless Communications*, vol. 12, no. 1, pp. 380–387, 2013.

[112] V. Tarokh, N. Seshadri, and A. Calderbank, "Space-time codes for high data rate wireless communication: performance criterion and code construction," *IEEE Transactions on Information Theory*, vol. 44, no. 2, pp. 744–765, 1998.

[113] R. Heath and A. Paulraj, "Linear dispersion codes for MIMO systems based on frame theory," *IEEE Transactions on Signal Processing*, vol. 50, no. 10, pp. 2429–2441, 2002.

[114] E. Cavus and B. Daneshrad, "A very low-complexity space-time block decoder (STBD) ASIC for wireless systems," *IEEE Transactions on Circuits and Systems I: Regular Papers*, vol. 53, no. 1, pp. 60–69, 2006.

[115] R. Y. Mesleh, H. Haas, S. Sinanovic, C. Ahn, and S. Yun, "Spatial modulation," *IEEE Transactions on Vehicular Technology*, vol. 57, no. 4, pp. 2228–2241, 2008.

[116] J. Jeganathan, A. Ghrayeb, and L. Szczecinski, "Spatial modulation: Optimal detection and performance analysis," *IEEE Communications Letters*, vol. 12, no. 8, pp. 545–547, 2008.

[117] Y. Yang and B. Jiao, "Information-guided channel-hopping for high data rate wireless communication," *IEEE Communications Letters*, vol. 12, no. 4, pp. 225–227, 2008.

[118] H. Ngo, C. Xu, S. Sugiura, and L. Hanzo, "Space-time-frequency shift keying for dispersive channels," *IEEE Signal Processing Letters*, vol. 18, no. 3, pp. 177–180, 2011.

[119] S. Sugiura, S. Chen, and L. Hanzo, "Generalized space-time shift keying designed for flexible diversity-, multiplexing-and complexity-tradeoffs," *IEEE Transactions on Wireless Communications*, vol. 10, no. 4, pp. 1144–1153, 2011.

[120] Y. Yang and S. Aíssa, "Information guided channel hopping with an arbitrary number of transmit antennas," *IEEE Communications Letters*, vol. 16, no. 10, pp. 1552–1555, 2012.

[121] A. Younis, N. Serafimovski, R. Mesleh, and H. Haas, "Generalised spatial modulation," in *Conference Record of the Forty Fourth Asilomar Conference on Signals, Systems and Computers*, 2010.

[122] T. Bayes and R. Price, "An essay towards solving a problem in the doctrine of chances. By the late rev. Mr. Bayes, communicated by Mr. Price, in a letter to John Canton, M. A. and F. R. S." *Philosophical Transactions of the Royal Society of London*, vol. 53, no. 0, pp. 370–418, 1763.

[123] F. Oggier, "Cyclic algebras for noncoherent differential space-time coding," *IEEE Transactions on Information Theory*, vol. 53, no. 9, pp. 3053–3065, 2007.

[124] S. Sugiura, C. Xu, S. Ng, and L. Hanzo, "Reduced-complexity coherent versus non-coherent QAM-aided space-time shift keying," *IEEE Transactions on Communications*, vol. 59, no. 11, pp. 3090–3101, 2011.

[125] M. Wen, Z. Ding, X. Cheng, Y. Bian, H. Poor, and B. Jiao, "Performance analysis of differential spatial modulation with two transmit antennas," *IEEE Communications Letters*, vol. 18, no. 3, pp. 475–478, 2014.

[126] Y. Bian, X. Cheng, M. Wen, L. Yang, H. V. Poor, and B. Jiao, "Differential spatial modulation," *IEEE Transactions on Vehicular Technology*, vol. 64, no. 7, pp. 3262–3268, 2015.

[127] T. Fath, M. D. Renzo, and H. Haas, "On the performance of space shift keying for optical wireless communications," in *IEEE GLOBECOM Workshops*, 2010.

[128] J. Jeganathan, A. Ghrayeb, L. Szczecinski, and A. Ceron, "Space shift keying modulation for MIMO channels," *IEEE Transactions on Wireless Communications*, vol. 8, no. 7, pp. 3692–3703, 2009.

[129] T. Fath, H. Haas, M. Di Renzo, and R. Mesleh, "Spatial modulation applied to optical wireless communications in indoor LOS environments," in *IEEE Global Telecommunications Conference*, Houston, 2011.

[130] W. Popoola, E. Poves, and H. Haas, "Spatial pulse position modulation for optical communications," *Journal of Lightwave Technology*, vol. 30, no. 18, pp. 2948–2954, 2012.

[131] E. Poves, W. Popoola, H. Haas, J. Thompson, and D. Cárdenas, "Experimental results on the performance of optical spatial modulation systems," in *IEEE Vehicular Technology Conference Fall*, Quebec, 2012.

[132] W. Popoola, E. Poves, and H. Haas, "Error performance of generalised space shift keying for indoor visible light communications," *IEEE Transactions on Communications*, vol. 61, no. 5, pp. 1968–1976, 2013.

[133] T. Fath and H. Haas, "Optical spatial modulation using colour LEDs," in *IEEE International Conference on Communications*, Budapest, 2013, pp. 3938–3942.

[134] W. Popoola and H. Haas, "Demonstration of the merit and limitation of generalised space shift keying for indoor visible light communications," *Journal of Lightwave Technology*, vol. 32, no. 10, pp. 1960–1965, 2014.

[135] J. Kahn and J. Barry, "Wireless infrared communications," *Proceedings of the IEEE*, vol. 85, no. 2, pp. 265–298, 1997.

[136] S. Sasaki, H. Kikuchi, Z. Jinkang, and G. Marubayashi, "Performance of parallel combinatory SS communication systems in Rayleigh fading channel," *IEICE Transactions on Fundamentals of Electronics, Communications and Computer Sciences*, vol. 77, no. 6, pp. 1028–1032, 1994.

[137] S. Sasaki, H. Kikuchi, J. Zhu, and G. Marubayashi, "Multiple access performance of parallel combinatory spread spectrum communication systems in nonfading and Rayleigh fading channels," *IEICE Transactions on Communications*, vol. E78-B, no. 8, pp. 1152–1161, 1995.

[138] N. Kitamoto and T. Ohtsuki, "Parallel combinatory multiple-subcarrier optical wireless communication systems," *International Journal of Communication Systems*, vol. 18, no. 3, pp. 195–203, 2005.

[139] Y. Hou and M. Hamamura, "A novel modulation with parallel combinatory and high compaction multi-carrier modulation," *IEICE Transactions on Fundamentals*, vol. E90-A, no. 11, pp. 2556–2567, 2007.

[140] Y. Hou and T. Hase, "New OFDM structure with parallel combinatory code," *IEEE Transactions on Consumer Electronics*, vol. 55, no. 4, pp. 1854–1859, 2009.

[141] D. Tsonev, S. Sinanovic, and H. Haas, "Enhanced subcarrier index modulation (SIM) OFDM," in *IEEE GLOBECOM Workshops*, Texas, USA, 2011.

[142] Y. Xiao, S. Wang, L. Dan, X. Lei, P. Yang, and W. Xiang, "OFDM With Interleaved Subcarrier-Index Modulation," *IEEE Communications Letters*, vol. 18, no. 8, pp. 1447–1450, 2014.

[143] R. Fan, Y. J. Yu, and Y. L. Guan, "Generalization of orthogonal frequency division multiplexing with index modulation," *IEEE Transactions on Wireless Communications*, vol. 14, no. 10, pp. 5350–5359, 2015.

[144] E. Basar, "OFDM with index modulation using coordinate interleaving," *IEEE Wireless Communications Letters*, vol. 4, no. 4, pp. 381–384, 2015.

[145] B. Zheng, F. Chen, M. Wen, F. Ji, H. Yu, and Y. Liu, "Low-complexity ML detector and performance analysis for OFDM with in-phase/quadrature index modulation," *IEEE Communications Letters*, vol. 19, no. 11, pp. 1893–1896, 2015.

[146] E. Basar, "Multiple-input multiple-output OFDM with index modulation," *IEEE Signal Processing Letters*, vol. 22, no. 12, pp. 2259–2263, 2015.

[147] T. Datta, H. Eshwaraiah, and A. Chockalingam, "Generalized space-and-frequency index modulation," *IEEE Transactions on Vehicular Technology*, vol. 65, no. 7, pp. 4911–4924, 2015.

[148] E. Basar, "On multiple-input multiple-output OFDM with index modulation for next generation wireless networks," *IEEE Transactions on Signal Processing*, vol. 64, no. 1, pp. 3868–3878, 2016.

[149] V. Tarokh, H. Jafarkhani, and A. Calderbank, "Space-time block codes from orthogonal designs," *IEEE Transactions on Information Theory*, vol. 45, no. 5, pp. 1456–1467, 1999.

[150] S. Sugiura, "Coherent versus non-coherent space-time shift keying for co-located and distributed MIMO systems," Ph.D. dissertation, University of Southampton, 2010.

[151] R. Schober, S. Member, W. H. Gerstacker, and J. B. Huber, "Decision-Feedback Differential Detection of MDPSK for Flat Rayleigh Fading Channels," *IEEE Transactions on Communications*, vol. 47, no. 7, pp. 1025–1035, 1999.

[152] C. S. Hwang, S. H. Nam, J. Chung, and V. Tarokh, "Differential space time block codes using nonconstant modulus constellations," *IEEE Transactions on Signal Processing*, vol. 51, no. 11, pp. 2955–2964, 2003.

[153] L. Zhou and Y. Ohashi, "Fast codebook-based beamforming training for mmWave MIMO systems with subarray structures," in *IEEE Vehicular Technology Conference Fall*, 2015.

[154] C. Xu, S. Sugiura, S. X. Ng, and L. Hanzo, "Spatial modulation and space-time shift keying: Optimal performance at a reduced detection complexity," *IEEE Transactions on Communications*, vol. 61, no. 1, pp. 206–216, 2013.

[155] R. Rajashekar, K. V. S. Hari, and L. Hanzo, "Reduced-complexity ML detection and capacity-optimized training for spatial modulation systems," *IEEE Transactions on Communications*, vol. 62, no. 1, pp. 112–125, 2014.

[156] I. Sarris and A. R. Nix, "Ricean K-factor measurements in a home and an office environment in the 60 GHz band," in *16th IST Mobile and Wireless Communications Summit*, 2007.

[157] P. Yang, Y. Xiao, B. Zhang, M. El-hajjar, S. Li, and L. Hanzo, "Phase rotation-based precoding for spatial modulation systems," *IET Communications*, vol. 9, no. 10, pp. 1315–1323, 2015.

[158] W. Popoola, "Merits and limitations of spatial modulation for optical wireless communications," in *International Workshop on Optical Wireless Communications*, 2013.

[159] T. Achterberg, "SCIP: Solving constraint integer programs," *Mathematical Programming Computation*, vol. 1, no. 1, pp. 1–41, 2009.

[160] J. Zhu, S. Sasaki, and G. Marubayashi, "Proposal of parallel combinatory spread spectrum communication system," *Transactions of IEICE (B-2)*, vol. J74-B-2, no. 5, pp. 207–214, 1991.

[161] H. Ochiai and H. Imai, "On the distribution of the peak-to-average power ratio in OFDM signals," *IEEE Transactions on Communications*, vol. 49, no. 2, pp. 282–289, 2001.

[162] S. Sugiura and L. Hanzo, "Single-RF spatial modulation requires single-carrier transmission: frequency-domain turbo equalization for dispersive channels," *IEEE Transactions on Vehicular Technology*, vol. 64, no. 10, pp. 4870–4875, 2015.

[163] D. J. MacKay, *Information theory, inference and learning algorithms*. Cambridge University Press, 2003.

[164] F. Chapeau-Blondeau and A. Monir, "Numerical evaluation of the Lambert W function and application to generation of generalized Gaussian noise with exponent 1/2," *IEEE Transactions on Signal Processing*, vol. 50, no. 9, pp. 2160–2165, 2002.

[165] H. V. Nguyen, C. Xu, S. X. Ng, and L. Hanzo, "Near-capacity wireless system design principles," *IEEE Communications Surveys & Tutorials*, vol. 17, no. 4, pp. 1806–1833, 2015.

[166] P. A. Martin, "Differential spatial modulation for APSK in time-varying fading channels," *IEEE Communications Letters*, vol. 19, no. 7, pp. 1261–1264, 2015.

[167] J. Liu, L. Dan, P. Yang, L. Xiao, F. Yu, and Y. Xiao, "High-rate APSK-aided differential spatial modulation: design method and performance analysis," *IEEE Communications Letters*, 2016.

[168] B. A. Sethuraman, B. Sundar Rajan, and V. Shashidhar, "Full-diversity, high-rate space-time block codes from division algebras," *IEEE Transactions on Information Theory*, vol. 49, no. 10, pp. 2596–2616, 2003.

[169] J. Singh and S. Ramakrishna, "On the feasibility of codebook-based beamforming in millimeter wave systems with multiple antenna arrays," *IEEE Transactions on Wireless Communications*, vol. 14, no. 5, pp. 2670–2683, 2015.

Dispersion Matrices and

Power-Allocation Factors

In this Appendix, we provide the DMs and the PA factors of the GSTSK, the NCGSM, the UDSM, and the PI-OSM schemes, which were used in our simulations. All of the DMs and PA factors were obtained by the author's numerical search program. If the reader uses the following materials in research publication, please cite this thesis.

A.1   Generalized Space-Time Shift Keying

GSTSK$(2,N,2,2,1)$, BPSK

$$\mathbf{A}_1 = \begin{bmatrix} 0.59\exp(-j0.74\pi) & 0.82\exp(+j0.44\pi) \\ 0.79\exp(+j0.16\pi) & 0.59\exp(+j0.16\pi) \end{bmatrix}, \mathbf{A}_2 = \begin{bmatrix} 0.80\exp(-j0.81\pi) & 0.57\exp(-j0.53\pi) \\ 0.62\exp(-j0.77\pi) & 0.80\exp(+j0.19\pi) \end{bmatrix}.$$

GSTSK$(2,N,2,4,1)$, BPSK

$$\mathbf{A}_1 = \begin{bmatrix} 0.69\exp(-j0.62\pi) & 0.72\exp(-j0.71\pi) \\ 0.72\exp(+j0.64\pi) & 0.69\exp(-j0.50\pi) \end{bmatrix}, \mathbf{A}_2 = \begin{bmatrix} 0.67\exp(+j0.35\pi) & 0.73\exp(-j0.91\pi) \\ 0.76\exp(+j0.79\pi) & 0.66\exp(+j0.54\pi) \end{bmatrix},$$

$$\mathbf{A}_3 = \begin{bmatrix} 0.94\exp(+j0.91\pi) & 0.34\exp(+j0.77\pi) \\ 0.30\exp(-j0.80\pi) & 0.95\exp(+j0.01\pi) \end{bmatrix}, \mathbf{A}_4 = \begin{bmatrix} 0.42\exp(-j0.32\pi) & 0.92\exp(+j0.69\pi) \\ 0.90\exp(-j0.76\pi) & 0.43\exp(-j0.73\pi) \end{bmatrix}.$$

GSTSK$(2,N,2,4,2)$, BPSK

$$\mathbf{A}_1 = \begin{bmatrix} 0.53\exp(+j0.77\pi) & 0.43\exp(-j0.45\pi) \\ 0.43\exp(-j0.31\pi) & 0.60\exp(-j0.48\pi) \end{bmatrix}, \mathbf{A}_2 = \begin{bmatrix} 0.44\exp(-j0.03\pi) & 0.55\exp(-j0.22\pi) \\ 0.55\exp(-j0.35\pi) & 0.46\exp(+j0.36\pi) \end{bmatrix},$$

$$\mathbf{A}_3 = \begin{bmatrix} 0.62\exp(+j0.42\pi) & 0.34\exp(+j0.40\pi) \\ 0.36\exp(-j0.99\pi) & 0.61\exp(-j0.03\pi) \end{bmatrix}, \mathbf{A}_4 = \begin{bmatrix} 0.40\exp(+j0.08\pi) & 0.59\exp(-j0.83\pi) \\ 0.59\exp(+j0.38\pi) & 0.39\exp(+j0.27\pi) \end{bmatrix}.$$

GSTSK(2,N,2,4,3), BPSK

$$\mathbf{A}_1 = \begin{bmatrix} 0.47\exp(+j0.51\pi) & 0.33\exp(+j0.84\pi) \\ 0.33\exp(+j0.27\pi) & 0.47\exp(-j0.42\pi) \end{bmatrix}, \mathbf{A}_2 = \begin{bmatrix} 0.24\exp(+j0.51\pi) & 0.53\exp(+j0.10\pi) \\ 0.52\exp(+j0.98\pi) & 0.24\exp(-j0.43\pi) \end{bmatrix},$$

$$\mathbf{A}_3 = \begin{bmatrix} 0.43\exp(+j0.17\pi) & 0.38\exp(-j0.43\pi) \\ 0.39\exp(-j0.43\pi) & 0.43\exp(-j0.02\pi) \end{bmatrix}, \mathbf{A}_4 = \begin{bmatrix} 0.43\exp(+j0.87\pi) & 0.37\exp(-j0.44\pi) \\ 0.38\exp(-j0.43\pi) & 0.44\exp(-j0.79\pi) \end{bmatrix}.$$

GSTSK(2,N,2,4,4), BPSK

$$\mathbf{A}_1 = \begin{bmatrix} 0.15\exp(+j0.68\pi) & 0.48\exp(+j0.12\pi) \\ 0.48\exp(-j0.48\pi) & 0.15\exp(-j0.30\pi) \end{bmatrix}, \mathbf{A}_2 = \begin{bmatrix} 0.48\exp(+j0.35\pi) & 0.15\exp(-j0.40\pi) \\ 0.15\exp(-j0.05\pi) & 0.48\exp(+j0.20\pi) \end{bmatrix},$$

$$\mathbf{A}_3 = \begin{bmatrix} 0.24\exp(+j0.52\pi) & 0.44\exp(+j0.65\pi) \\ 0.40\exp(+j0.92\pi) & 0.31\exp(+j0.05\pi) \end{bmatrix}, \mathbf{A}_4 = \begin{bmatrix} 0.39\exp(+j0.75\pi) & 0.31\exp(-j0.76\pi) \\ 0.31\exp(+j0.20\pi) & 0.39\exp(-j0.31\pi) \end{bmatrix}.$$

GSTSK(2,N,2,16,1), QPSK

$$\mathbf{A}_1 = \begin{bmatrix} 0.65\exp(-j0.41\pi) & 0.92\exp(-j0.48\pi) \\ 0.75\exp(-j0.79\pi) & 0.41\exp(-j0.05\pi) \end{bmatrix}, \mathbf{A}_2 = \begin{bmatrix} 0.72\exp(-j0.23\pi) & 0.24\exp(-j0.15\pi) \\ 0.49\exp(-j0.43\pi) & 1.09\exp(-j0.74\pi) \end{bmatrix},$$

$$\mathbf{A}_3 = \begin{bmatrix} 0.48\exp(-j0.36\pi) & 0.35\exp(-j0.18\pi) \\ 0.99\exp(+j0.90\pi) & 0.82\exp(+j0.01\pi) \end{bmatrix}, \mathbf{A}_4 = \begin{bmatrix} 0.70\exp(-j0.53\pi) & 0.99\exp(-j0.91\pi) \\ 0.68\exp(-j0.57\pi) & 0.26\exp(-j0.19\pi) \end{bmatrix},$$

$$\mathbf{A}_5 = \begin{bmatrix} 0.13\exp(-j0.81\pi) & 0.71\exp(+j0.46\pi) \\ 0.42\exp(-j0.09\pi) & 1.14\exp(+j0.62\pi) \end{bmatrix}, \mathbf{A}_6 = \begin{bmatrix} 0.79\exp(-j0.99\pi) & 0.49\exp(-j0.90\pi) \\ 0.72\exp(-j0.47\pi) & 0.79\exp(-j0.69\pi) \end{bmatrix},$$

$$\mathbf{A}_7 = \begin{bmatrix} 0.95\exp(-j0.83\pi) & 0.50\exp(+j0.24\pi) \\ 0.82\exp(-j0.33\pi) & 0.41\exp(+j0.21\pi) \end{bmatrix}, \mathbf{A}_8 = \begin{bmatrix} 1.03\exp(+j0.47\pi) & 0.36\exp(-j0.50\pi) \\ 0.12\exp(+j0.06\pi) & 0.89\exp(-j0.04\pi) \end{bmatrix},$$

$$\mathbf{A}_9 = \begin{bmatrix} 0.83\exp(+j0.22\pi) & 0.86\exp(+j0.57\pi) \\ 0.37\exp(-j0.38\pi) & 0.65\exp(+j0.45\pi) \end{bmatrix}, \mathbf{A}_{10} = \begin{bmatrix} 0.91\exp(-j0.26\pi) & 0.90\exp(-j0.76\pi) \\ 0.29\exp(+j0.35\pi) & 0.52\exp(+j0.79\pi) \end{bmatrix},$$

$$\mathbf{A}_{11} = \begin{bmatrix} 0.70\exp(-j0.22\pi) & 0.64\exp(-j0.32\pi) \\ 0.66\exp(+j0.59\pi) & 0.81\exp(-j0.95\pi) \end{bmatrix}, \mathbf{A}_{12} = \begin{bmatrix} 0.39\exp(-j0.23\pi) & 0.29\exp(+j0.43\pi) \\ 1.32\exp(+j0.61\pi) & 0.16\exp(-j0.25\pi) \end{bmatrix},$$

$$\mathbf{A}_{13} = \begin{bmatrix} 0.43\exp(+j0.47\pi) & 0.66\exp(-j0.20\pi) \\ 0.93\exp(+j0.77\pi) & 0.72\exp(+j0.76\pi) \end{bmatrix}, \mathbf{A}_{14} = \begin{bmatrix} 1.04\exp(-j0.09\pi) & 0.71\exp(+j0.12\pi) \\ 0.39\exp(+j0.94\pi) & 0.51\exp(+j0.98\pi) \end{bmatrix},$$

$$\mathbf{A}_{15} = \begin{bmatrix} 0.98\exp(+j0.13\pi) & 0.24\exp(+j0.38\pi) \\ 0.64\exp(+j0.34\pi) & 0.76\exp(-j0.68\pi) \end{bmatrix}, \mathbf{A}_{16} = \begin{bmatrix} 0.70\exp(+j0.10\pi) & 0.81\exp(+j0.78\pi) \\ 0.55\exp(-j0.91\pi) & 0.74\exp(+j0.15\pi) \end{bmatrix}.$$

GSTSK(3,*N*,3,3,3), 4–QAM

$$
\mathbf{A}_1 = \begin{bmatrix} 0.38\exp(+j0.17\pi) & 0.24\exp(+j0.48\pi) & 0.23\exp(+j0.35\pi) \\ 0.56\exp(+j0.94\pi) & 0.08\exp(+j0.44\pi) & 0.33\exp(+j0.35\pi) \\ 0.37\exp(-j0.83\pi) & 0.28\exp(-j0.91\pi) & 0.31\exp(+j0.17\pi) \end{bmatrix},
$$

$$
\mathbf{A}_2 = \begin{bmatrix} 0.38\exp(-j0.58\pi) & 0.47\exp(-j0.82\pi) & 0.09\exp(+j0.02\pi) \\ 0.36\exp(+j0.72\pi) & 0.31\exp(-j0.66\pi) & 0.40\exp(-j0.73\pi) \\ 0.05\exp(-j0.62\pi) & 0.32\exp(+j0.40\pi) & 0.37\exp(+j0.96\pi) \end{bmatrix},
$$

$$
\mathbf{A}_3 = \begin{bmatrix} 0.44\exp(-j0.33\pi) & 0.11\exp(+j0.91\pi) & 0.37\exp(-j0.64\pi) \\ 0.24\exp(+j0.24\pi) & 0.41\exp(+j0.10\pi) & 0.26\exp(-j0.77\pi) \\ 0.33\exp(-j0.12\pi) & 0.47\exp(+j0.84\pi) & 0.18\exp(-j0.02\pi) \end{bmatrix}.
$$

GSTSK(4,*N*,4,16,1), 16–PSK

$$
\mathbf{A}_1 = \begin{bmatrix} 0.44\exp(+j0.75\pi) & 0.59\exp(-j0.85\pi) & 0.26\exp(-j0.03\pi) & 0.61\exp(+j0.93\pi) \\ 0.09\exp(-j0.70\pi) & 0.58\exp(+j0.49\pi) & 0.84\exp(+j0.69\pi) & 0.26\exp(-j0.85\pi) \\ 0.82\exp(-j0.26\pi) & 0.46\exp(-j0.85\pi) & 0.29\exp(+j0.28\pi) & 0.25\exp(+j0.91\pi) \\ 0.10\exp(-j0.31\pi) & 0.55\exp(+j0.17\pi) & 0.55\exp(-j0.54\pi) & 0.52\exp(+j0.94\pi) \end{bmatrix},
$$

$$
\mathbf{A}_2 = \begin{bmatrix} 0.62\exp(-j0.37\pi) & 0.17\exp(-j0.72\pi) & 0.66\exp(-j0.55\pi) & 0.26\exp(+j0.26\pi) \\ 0.59\exp(-j0.97\pi) & 0.45\exp(+j0.78\pi) & 0.44\exp(+j0.04\pi) & 0.51\exp(+j0.64\pi) \\ 0.60\exp(-j0.66\pi) & 0.72\exp(+j0.04\pi) & 0.46\exp(+j0.16\pi) & 0.24\exp(+j0.10\pi) \\ 0.16\exp(-j0.36\pi) & 0.46\exp(-j0.32\pi) & 0.42\exp(+j0.83\pi) & 0.71\exp(+j0.44\pi) \end{bmatrix},
$$

$$
\mathbf{A}_3 = \begin{bmatrix} 0.42\exp(-j0.57\pi) & 0.38\exp(-j0.58\pi) & 0.71\exp(-j0.15\pi) & 0.23\exp(-j0.97\pi) \\ 0.36\exp(+j0.47\pi) & 0.44\exp(-j0.27\pi) & 0.19\exp(-j0.11\pi) & 0.83\exp(+j0.03\pi) \\ 0.68\exp(-j0.43\pi) & 0.48\exp(-j0.30\pi) & 0.38\exp(-j0.88\pi) & 0.27\exp(+j0.44\pi) \\ 0.52\exp(-j0.23\pi) & 0.69\exp(+j0.83\pi) & 0.24\exp(+j0.11\pi) & 0.61\exp(+j0.07\pi) \end{bmatrix},
$$

$$
\mathbf{A}_4 = \begin{bmatrix} 0.56\exp(-j0.24\pi) & 0.33\exp(-j0.28\pi) & 0.55\exp(+j0.82\pi) & 0.15\exp(-j0.25\pi) \\ 0.52\exp(-j0.60\pi) & 0.76\exp(+j0.18\pi) & 0.33\exp(-j0.31\pi) & 0.37\exp(+j0.25\pi) \\ 0.30\exp(-j0.99\pi) & 0.40\exp(+j0.55\pi) & 0.61\exp(-j0.89\pi) & 0.71\exp(-j0.97\pi) \\ 0.33\exp(-j0.88\pi) & 0.70\exp(+j0.85\pi) & 0.38\exp(+j0.95\pi) & 0.54\exp(+j0.08\pi) \end{bmatrix},
$$

$$
\mathbf{A}_5 = \begin{bmatrix} 0.56\exp(-j0.08\pi) & 0.14\exp(-j0.33\pi) & 0.61\exp(+j0.63\pi) & 0.53\exp(-j0.90\pi) \\ 0.35\exp(-j0.48\pi) & 0.79\exp(+j0.67\pi) & 0.25\exp(-j0.84\pi) & 0.12\exp(-j0.28\pi) \\ 0.42\exp(-j0.71\pi) & 0.35\exp(-j0.45\pi) & 0.45\exp(+j0.85\pi) & 0.61\exp(-j0.01\pi) \\ 0.58\exp(+j0.79\pi) & 0.26\exp(+j0.74\pi) & 0.65\exp(+j0.82\pi) & 0.70\exp(+j0.62\pi) \end{bmatrix},
$$

$$\mathbf{A}_6 = \begin{bmatrix} 0.31\exp(-j0.73\pi) & 0.55\exp(-j0.61\pi) & 0.65\exp(-j0.35\pi) & 0.53\exp(-j0.32\pi) \\ 0.51\exp(+j0.63\pi) & 0.56\exp(+j0.40\pi) & 0.34\exp(-j0.29\pi) & 0.46\exp(-j0.20\pi) \\ 0.25\exp(+j0.58\pi) & 0.15\exp(-j0.15\pi) & 0.59\exp(-j0.56\pi) & 0.71\exp(+j0.64\pi) \\ 0.75\exp(+j0.26\pi) & 0.50\exp(-j0.83\pi) & 0.43\exp(+j0.16\pi) & 0.28\exp(+j0.63\pi) \end{bmatrix},$$

$$\mathbf{A}_7 = \begin{bmatrix} 0.24\exp(+j0.48\pi) & 0.98\exp(-j0.61\pi) & 0.27\exp(+j0.38\pi) & 0.27\exp(-j0.97\pi) \\ 0.35\exp(+j0.92\pi) & 0.25\exp(-j0.59\pi) & 0.37\exp(-j0.99\pi) & 0.76\exp(+j0.15\pi) \\ 0.72\exp(-j0.09\pi) & 0.38\exp(-j0.64\pi) & 0.46\exp(-j0.67\pi) & 0.39\exp(-j0.24\pi) \\ 0.49\exp(-j0.42\pi) & 0.32\exp(-j0.53\pi) & 0.64\exp(+j0.14\pi) & 0.40\exp(-j0.04\pi) \end{bmatrix},$$

$$\mathbf{A}_8 = \begin{bmatrix} 0.54\exp(-j0.60\pi) & 0.16\exp(+j0.63\pi) & 0.73\exp(+j0.76\pi) & 0.48\exp(+j0.15\pi) \\ 0.78\exp(+j0.28\pi) & 0.33\exp(+j0.30\pi) & 0.11\exp(+j0.98\pi) & 0.48\exp(-j0.15\pi) \\ 0.26\exp(-j0.77\pi) & 0.52\exp(-j0.01\pi) & 0.64\exp(-j0.47\pi) & 0.29\exp(-j0.20\pi) \\ 0.17\exp(-j0.81\pi) & 0.78\exp(+j0.61\pi) & 0.21\exp(+j0.94\pi) & 0.66\exp(-j0.67\pi) \end{bmatrix},$$

$$\mathbf{A}_9 = \begin{bmatrix} 0.63\exp(-j0.72\pi) & 0.22\exp(-j0.81\pi) & 0.50\exp(-j0.96\pi) & 0.39\exp(+j0.82\pi) \\ 0.40\exp(+j0.77\pi) & 0.11\exp(+j0.75\pi) & 0.07\exp(+j0.15\pi) & 0.92\exp(-j0.83\pi) \\ 0.63\exp(-j0.71\pi) & 0.49\exp(+j0.69\pi) & 0.76\exp(+j0.03\pi) & 0.26\exp(+j0.78\pi) \\ 0.28\exp(-j0.03\pi) & 0.73\exp(+j0.52\pi) & 0.46\exp(-j0.99\pi) & 0.16\exp(-j0.50\pi) \end{bmatrix},$$

$$\mathbf{A}_{10} = \begin{bmatrix} 0.27\exp(-j0.67\pi) & 0.45\exp(-j0.09\pi) & 0.77\exp(+j0.92\pi) & 0.25\exp(+j0.96\pi) \\ 0.65\exp(-j0.96\pi) & 0.45\exp(-j0.84\pi) & 0.12\exp(-j0.75\pi) & 0.60\exp(-j0.57\pi) \\ 0.73\exp(+j0.89\pi) & 0.38\exp(+j0.13\pi) & 0.42\exp(-j0.19\pi) & 0.23\exp(+j0.22\pi) \\ 0.25\exp(-j0.13\pi) & 0.64\exp(-j0.02\pi) & 0.44\exp(+j0.04\pi) & 0.70\exp(-j0.62\pi) \end{bmatrix},$$

$$\mathbf{A}_{11} = \begin{bmatrix} 0.31\exp(+j0.89\pi) & 0.70\exp(+j0.86\pi) & 0.64\exp(+j0.46\pi) & 0.38\exp(+j0.27\pi) \\ 0.38\exp(-j0.96\pi) & 0.43\exp(+j0.35\pi) & 0.62\exp(-j0.55\pi) & 0.41\exp(+j0.55\pi) \\ 0.33\exp(+j0.93\pi) & 0.51\exp(-j0.38\pi) & 0.53\exp(+j0.05\pi) & 0.48\exp(+j0.27\pi) \\ 0.88\exp(-j0.83\pi) & 0.01\exp(-j0.73\pi) & 0.16\exp(+j0.87\pi) & 0.53\exp(-j0.31\pi) \end{bmatrix},$$

$$\mathbf{A}_{12} = \begin{bmatrix} 0.69\exp(+j0.33\pi) & 0.42\exp(-j0.04\pi) & 0.36\exp(-j0.24\pi) & 0.53\exp(+j0.91\pi) \\ 0.59\exp(+j0.10\pi) & 0.74\exp(+j0.66\pi) & 0.35\exp(+j0.60\pi) & 0.36\exp(-j0.10\pi) \\ 0.26\exp(+j0.14\pi) & 0.46\exp(-j0.68\pi) & 0.30\exp(-j0.07\pi) & 0.75\exp(-j0.36\pi) \\ 0.10\exp(+j0.25\pi) & 0.41\exp(-j0.44\pi) & 0.75\exp(+j0.67\pi) & 0.36\exp(+j0.93\pi) \end{bmatrix},$$

$$
\mathbf{A}_{13} = \begin{bmatrix}
0.80\exp(+j0.45\pi) & 0.32\exp(-j0.95\pi) & 0.61\exp(+j0.59\pi) & 0.46\exp(+j0.10\pi) \\
0.48\exp(-j0.36\pi) & 0.57\exp(-j0.45\pi) & 0.30\exp(+j0.60\pi) & 0.44\exp(+j0.23\pi) \\
0.26\exp(+j0.08\pi) & 0.49\exp(-j0.58\pi) & 0.48\exp(+j0.83\pi) & 0.69\exp(-j0.68\pi) \\
0.26\exp(+j0.37\pi) & 0.48\exp(-j0.54\pi) & 0.67\exp(-j0.23\pi) & 0.26\exp(+j0.87\pi)
\end{bmatrix},
$$

$$
\mathbf{A}_{14} = \begin{bmatrix}
0.31\exp(+j0.21\pi) & 0.57\exp(+j0.97\pi) & 0.56\exp(-j0.26\pi) & 0.65\exp(+j0.12\pi) \\
0.56\exp(+j0.20\pi) & 0.68\exp(-j0.09\pi) & 0.17\exp(+j0.22\pi) & 0.48\exp(-j0.38\pi) \\
0.54\exp(+j0.81\pi) & 0.42\exp(-j0.75\pi) & 0.40\exp(+j0.75\pi) & 0.51\exp(-j0.47\pi) \\
0.50\exp(+j0.65\pi) & 0.26\exp(-j0.19\pi) & 0.62\exp(-j0.58\pi) & 0.45\exp(+j0.97\pi)
\end{bmatrix},
$$

$$
\mathbf{A}_{15} = \begin{bmatrix}
0.75\exp(+j0.19\pi) & 0.34\exp(+j0.71\pi) & 0.10\exp(-j0.77\pi) & 0.52\exp(-j0.54\pi) \\
0.48\exp(+j0.43\pi) & 0.51\exp(+j0.38\pi) & 0.63\exp(+j0.30\pi) & 0.45\exp(+j0.51\pi) \\
0.49\exp(-j0.23\pi) & 0.28\exp(+j0.57\pi) & 0.56\exp(+j0.75\pi) & 0.61\exp(-j0.02\pi) \\
0.42\exp(-j0.28\pi) & 0.67\exp(+j0.96\pi) & 0.57\exp(-j0.06\pi) & 0.12\exp(+j0.37\pi)
\end{bmatrix},
$$

$$
\mathbf{A}_{16} = \begin{bmatrix}
0.40\exp(+j0.98\pi) & 0.60\exp(+j0.99\pi) & 0.38\exp(+j0.87\pi) & 0.64\exp(+j0.24\pi) \\
0.31\exp(-j0.06\pi) & 0.52\exp(-j0.54\pi) & 0.44\exp(-j0.59\pi) & 0.66\exp(-j0.09\pi) \\
0.15\exp(-j0.07\pi) & 0.64\exp(-j0.02\pi) & 0.77\exp(+j0.95\pi) & 0.12\exp(+j0.09\pi) \\
0.73\exp(+j0.89\pi) & 0.30\exp(-j0.32\pi) & 0.24\exp(-j0.71\pi) & 0.45\exp(-j0.46\pi)
\end{bmatrix}.
$$

A.2   Non-Coherent Generalized Spatial Modulation

Non-Coherent GSM(2,N,2,4,2), 2–PAM

$$\mathbf{A}_1 = \begin{bmatrix} 0.09\exp(+j0.00\pi) & 0.65\exp(-j0.22\pi) \\ 0.65\exp(+j0.22\pi) & 0.01\exp(+j1.00\pi) \end{bmatrix}, \mathbf{A}_2 = \begin{bmatrix} 0.60\exp(+j1.00\pi) & 0.38\exp(+j0.09\pi) \\ 0.38\exp(-j0.09\pi) & 0.58\exp(+j0.00\pi) \end{bmatrix},$$

$$\mathbf{A}_3 = \begin{bmatrix} 0.35\exp(+j0.00\pi) & 0.82\exp(+j0.31\pi) \\ 0.82\exp(-j0.31\pi) & 0.19\exp(+j1.00\pi) \end{bmatrix}, \mathbf{A}_4 = \begin{bmatrix} 0.25\exp(+j0.00\pi) & 0.46\exp(-j0.11\pi) \\ 0.46\exp(+j0.11\pi) & 0.05\exp(+j1.00\pi) \end{bmatrix}.$$

Non-Coherent GSM(2,N,2,4,2), 4–PAM

$$\mathbf{A}_1 = \begin{bmatrix} 0.00 & 0.61\exp(-j0.47\pi) \\ 0.61\exp(+j0.47\pi) & 0.52\exp(+j0.00\pi) \end{bmatrix}, \mathbf{A}_2 = \begin{bmatrix} 0.00 & 0.63\exp(-j0.06\pi) \\ 0.63\exp(+j0.06\pi) & 0.51\exp(+j0.00\pi) \end{bmatrix},$$

$$\mathbf{A}_3 = \begin{bmatrix} 0.87\exp(+j0.00\pi) & 0.45\exp(-j0.25\pi) \\ 0.45\exp(+j0.25\pi) & 0.00 \end{bmatrix}, \mathbf{A}_4 = \begin{bmatrix} 0.17\exp(+j0.00\pi) & 0.69\exp(-j0.64\pi) \\ 0.69\exp(+j0.64\pi) & 0.21\exp(+j0.00\pi) \end{bmatrix}.$$

Non-Coherent GSM(2,N,2,16,1), 4–PAM

$$\mathbf{A}_1 = \begin{bmatrix} 0.48\exp(+j0.00\pi) & 0.74\exp(-j0.63\pi) \\ 0.74\exp(+j0.63\pi) & 0.71\exp(+j1.00\pi) \end{bmatrix}, \mathbf{A}_2 = \begin{bmatrix} 0.99\exp(+j0.00\pi) & 1.20\exp(-j0.00\pi) \\ 1.20\exp(+j0.00\pi) & 0.88\exp(+j1.00\pi) \end{bmatrix},$$

$$\mathbf{A}_3 = \begin{bmatrix} 1.28\exp(+j0.00\pi) & 0.88\exp(+j0.66\pi) \\ 0.88\exp(-j0.66\pi) & 1.07\exp(+j1.00\pi) \end{bmatrix}, \mathbf{A}_4 = \begin{bmatrix} 0.93\exp(+j0.00\pi) & 1.14\exp(-j0.66\pi) \\ 1.14\exp(+j0.66\pi) & 1.81\exp(+j1.00\pi) \end{bmatrix},$$

$$\mathbf{A}_5 = \begin{bmatrix} 0.21\exp(+j1.00\pi) & 1.14\exp(-j0.51\pi) \\ 1.14\exp(+j0.51\pi) & 0.44\exp(+j1.00\pi) \end{bmatrix}, \mathbf{A}_6 = \begin{bmatrix} 3.21\exp(+j0.00\pi) & 0.49\exp(+j0.07\pi) \\ 0.49\exp(-j0.07\pi) & 2.59\exp(+j1.00\pi) \end{bmatrix},$$

$$\mathbf{A}_7 = \begin{bmatrix} 1.28\exp(+j0.00\pi) & 0.89\exp(-j0.27\pi) \\ 0.89\exp(+j0.27\pi) & 0.98\exp(+j1.00\pi) \end{bmatrix}, \mathbf{A}_8 = \begin{bmatrix} 1.58\exp(+j1.00\pi) & 2.32\exp(+j0.75\pi) \\ 2.32\exp(-j0.75\pi) & 0.76\exp(+j0.00\pi) \end{bmatrix},$$

$$\mathbf{A}_9 = \begin{bmatrix} 0.77\exp(+j1.00\pi) & 1.05\exp(-j0.28\pi) \\ 1.05\exp(+j0.28\pi) & 0.00 \end{bmatrix}, \mathbf{A}_{10} = \begin{bmatrix} 0.74\exp(+j1.00\pi) & 1.91\exp(-j0.57\pi) \\ 1.91\exp(+j0.57\pi) & 0.01\exp(+j1.00\pi) \end{bmatrix},$$

$$\mathbf{A}_{11} = \begin{bmatrix} 0.65\exp(+j0.00\pi) & 0.84\exp(+j0.27\pi) \\ 0.84\exp(-j0.27\pi) & 0.80\exp(+j1.00\pi) \end{bmatrix}, \mathbf{A}_{12} = \begin{bmatrix} 0.00 & 0.71\exp(+j0.05\pi) \\ 0.71\exp(-j0.05\pi) & 0.12\exp(+j1.00\pi) \end{bmatrix},$$

$$\mathbf{A}_{13} = \begin{bmatrix} 0.65\exp(+j0.00\pi) & 0.55\exp(-j0.09\pi) \\ 0.55\exp(+j0.09\pi) & 0.60\exp(+j1.00\pi) \end{bmatrix}, \mathbf{A}_{14} = \begin{bmatrix} 0.85\exp(+j1.00\pi) & 3.50\exp(+j0.06\pi) \\ 3.50\exp(-j0.06\pi) & 0.00 \end{bmatrix},$$

$$\mathbf{A}_{15} = \begin{bmatrix} 0.27\exp(+j0.00\pi) & 0.03\exp(-j0.60\pi) \\ 0.03\exp(+j0.60\pi) & 0.46\exp(+j1.00\pi) \end{bmatrix}, \mathbf{A}_{16} = \begin{bmatrix} 0.00 & 1.61\exp(-j0.10\pi) \\ 1.61\exp(+j0.10\pi) & 0.00 \end{bmatrix}.$$

Non-Coherent GSM$(3,N,3,3,3)$, 4–PAM

$$\mathbf{A}_1 = \begin{bmatrix} 0.00 & 0.32\exp(-j0.61\pi) & 0.95\exp(+j0.96\pi) \\ 0.32\exp(+j0.61\pi) & 0.72\exp(+j0.00\pi) & 0.29\exp(+j0.21\pi) \\ 0.95\exp(-j0.96\pi) & 0.29\exp(-j0.21\pi) & 0.46\exp(+j0.00\pi) \end{bmatrix},$$

$$\mathbf{A}_2 = \begin{bmatrix} 0.60\exp(+j0.00\pi) & 0.05\exp(+j0.56\pi) & 0.23\exp(-j0.72\pi) \\ 0.05\exp(-j0.56\pi) & 0.27\exp(+j0.00\pi) & 0.91\exp(-j0.39\pi) \\ 0.23\exp(+j0.72\pi) & 0.91\exp(+j0.39\pi) & 0.00 \end{bmatrix},$$

$$\mathbf{A}_3 = \begin{bmatrix} 0.98\exp(+j0.00\pi) & 0.00 & 0.00 \\ 0.00 & 0.45\exp(+j1.00\pi) & 0.49\exp(+j0.10\pi) \\ 0.00 & 0.49\exp(-j0.10\pi) & 0.68\exp(+j0.00\pi) \end{bmatrix}.$$

Single-RF Non-Coherent GSM$(2,N,2,2,1)$, 2–PAM

$$\mathbf{A}_1 = \text{diag}(+0.41, +2.41), \ \mathbf{A}_2 = \text{diag}(+2.41, +0.41).$$

Single-RF Non-Coherent GSM$(3,N,3,5,1)$, 2–PAM

$$\mathbf{A}_1 = \text{diag}(+0.56, +0.11, +1.74), \ \mathbf{A}_2 = \text{diag}(+1.88, +3.56, +5.11),$$

$$\mathbf{A}_3 = \text{diag}(+0.24, +1.78, +0.22), \ \mathbf{A}_4 = \text{diag}(+11.04, +0.72, +0.74),$$

$$\mathbf{A}_5 = \text{diag}(+5.59, +7.35, +11.04).$$

Single-RF Non-Coherent GSM$(4,N,4,14,1)$, 2–PAM

$$\mathbf{A}_1 = \text{diag}(+0.72, +0.35, +2.60, +0.04), \ \mathbf{A}_2 = \text{diag}(+1.73, +0.66, +0.03, +0.46),$$

$$\mathbf{A}_3 = \text{diag}(+3.36, +0.04, +1.30, +1.05), \ \mathbf{A}_4 = \text{diag}(+0.19, +2.17, +9.94, +0.69),$$

$$\mathbf{A}_5 = \text{diag}(+0.64, +22.96, +0.24, +1.26), \ \mathbf{A}_6 = \text{diag}(+0.10, +0.22, +0.48, +3.43),$$

$$\mathbf{A}_7 = \text{diag}(+1.09, +1.43, +0.95, +39.19), \ \mathbf{A}_8 = \text{diag}(+8.30, +3.11, +0.62, +0.14),$$

$$\mathbf{A}_9 = \text{diag}(+0.58, +4.36, +3.45, +1.46), \ \mathbf{A}_{10} = \text{diag}(+9.66, +4.58, +3.59, +2.23),$$

$$\mathbf{A}_{11} = \text{diag}(+2.52, +0.00, +6.18, +1.43), \ \mathbf{A}_{12} = \text{diag}(+3.07, +3.76, +5.85, +6.72),$$

$$\mathbf{A}_{13} = \text{diag}(+0.05, +7.08, +12.44, +7.62), \ \mathbf{A}_{14} = \text{diag}(+1.08, +5.39, +9.03, +11.47).$$

Single-RF Non-Coherent GSM$(7,N,7,6,3)$, 2–PAM

$$\mathbf{A}_1 = \text{diag}(-0.87, -0.09, +0.24, -0.83, +0.95, -1.30, +0.94),$$

$$\mathbf{A}_2 = \text{diag}(+0.44, -0.03, -1.95, -0.17, -0.65, -0.46, +0.21),$$

$$\mathbf{A}_3 = \text{diag}(+0.66, +0.90, +0.71, +1.25, -0.89, -1.23, +1.30),$$

$$\mathbf{A}_4 = \text{diag}(-0.50, +0.50, -0.35, -1.30, -1.33, +0.32, +1.22),$$

$$\mathbf{A}_5 = \mathrm{diag}(-0.51, -1.12, +0.89, +1.00, -0.90, +0.88, +0.27),$$

$$\mathbf{A}_6 = \mathrm{diag}(-0.72, +0.82, +0.28, +0.25, -0.38, +0.09, -1.35).$$

Single-RF Non-Coherent GSM$(10, N, 10, 8, 4)$, 2–PAM

$$\mathbf{A}_1 = \mathrm{diag}(+0.67, -0.32, -1.21, +1.22, -0.02, +0.75, -0.01, -0.46, -0.35, +0.60),$$

$$\mathbf{A}_2 = \mathrm{diag}(-1.61, -0.06, -1.10, -0.02, +0.17, -0.07, +2.01, -0.70, -0.86, -1.47),$$

$$\mathbf{A}_3 = \mathrm{diag}(+0.75, -0.21, -0.46, -0.77, -1.01, +0.58, +0.47, -0.74, +1.09, -0.90),$$

$$\mathbf{A}_4 = \mathrm{diag}(-0.13, +1.17, +0.41, +0.69, -0.08, -0.12, +1.21, -0.08, +0.14, -1.95),$$

$$\mathbf{A}_5 = \mathrm{diag}(-1.19, +0.26, +1.53, +1.32, -0.04, +2.03, +2.11, +0.31, +1.76, +0.37),$$

$$\mathbf{A}_6 = \mathrm{diag}(+1.31, -2.53, +0.78, +0.82, +0.34, +1.47, -0.94, +0.34, -0.64, -1.74),$$

$$\mathbf{A}_7 = \mathrm{diag}(+0.96, +1.94, -0.95, -0.46, +2.24, +0.24, -0.27, +0.30, +0.55, -0.42),$$

$$\mathbf{A}_8 = \mathrm{diag}(-0.92, -0.26, -0.14, -0.54, +0.30, +1.07, +0.09, +2.90, -0.63, +1.04).$$

A.3   Unified Differential Spatial Modulation

Binary DSM ($M = 2$, $Q = 2$)

$$\mathbf{A}_1 = \begin{bmatrix} 1 & 0 \\ 0 & 1 \end{bmatrix}, \mathbf{A}_2 = \begin{bmatrix} 0 & 1 \\ 1 & 0 \end{bmatrix}.$$

Binary DSM ($M = 3$, $Q = 4$)

$$\mathbf{A}_1 = \begin{bmatrix} 1 & 0 & 0 \\ 0 & 1 & 0 \\ 0 & 0 & 1 \end{bmatrix}, \mathbf{A}_2 = \begin{bmatrix} 1 & 0 & 0 \\ 0 & 0 & 1 \\ 0 & 1 & 0 \end{bmatrix}, \mathbf{A}_3 = \begin{bmatrix} 0 & 1 & 0 \\ 1 & 0 & 0 \\ 0 & 0 & 1 \end{bmatrix}, \mathbf{A}_4 = \begin{bmatrix} 0 & 0 & 1 \\ 1 & 0 & 0 \\ 0 & 1 & 0 \end{bmatrix}.$$

Binary DSM ($M = 4$, $Q = 16$)

$$\mathbf{A}_1 = \begin{bmatrix} 1 & 0 & 0 & 0 \\ 0 & 1 & 0 & 0 \\ 0 & 0 & 1 & 0 \\ 0 & 0 & 0 & 1 \end{bmatrix}, \mathbf{A}_2 = \begin{bmatrix} 1 & 0 & 0 & 0 \\ 0 & 1 & 0 & 0 \\ 0 & 0 & 0 & 1 \\ 0 & 0 & 1 & 0 \end{bmatrix}, \mathbf{A}_3 = \begin{bmatrix} 1 & 0 & 0 & 0 \\ 0 & 0 & 1 & 0 \\ 0 & 1 & 0 & 0 \\ 0 & 0 & 0 & 1 \end{bmatrix}, \mathbf{A}_4 = \begin{bmatrix} 1 & 0 & 0 & 0 \\ 0 & 0 & 0 & 1 \\ 0 & 1 & 0 & 0 \\ 0 & 0 & 1 & 0 \end{bmatrix},$$

$$\mathbf{A}_5 = \begin{bmatrix} 1 & 0 & 0 & 0 \\ 0 & 0 & 1 & 0 \\ 0 & 0 & 0 & 1 \\ 0 & 1 & 0 & 0 \end{bmatrix}, \mathbf{A}_6 = \begin{bmatrix} 1 & 0 & 0 & 0 \\ 0 & 0 & 0 & 1 \\ 0 & 0 & 1 & 0 \\ 0 & 1 & 0 & 0 \end{bmatrix}, \mathbf{A}_7 = \begin{bmatrix} 0 & 1 & 0 & 0 \\ 1 & 0 & 0 & 0 \\ 0 & 0 & 1 & 0 \\ 0 & 0 & 0 & 1 \end{bmatrix}, \mathbf{A}_8 = \begin{bmatrix} 0 & 1 & 0 & 0 \\ 1 & 0 & 0 & 0 \\ 0 & 0 & 0 & 1 \\ 0 & 0 & 1 & 0 \end{bmatrix},$$

$$\mathbf{A}_9 = \begin{bmatrix} 0 & 0 & 1 & 0 \\ 1 & 0 & 0 & 0 \\ 0 & 1 & 0 & 0 \\ 0 & 0 & 0 & 1 \end{bmatrix}, \mathbf{A}_{10} = \begin{bmatrix} 0 & 0 & 0 & 1 \\ 1 & 0 & 0 & 0 \\ 0 & 1 & 0 & 0 \\ 0 & 0 & 1 & 0 \end{bmatrix}, \mathbf{A}_{11} = \begin{bmatrix} 0 & 0 & 1 & 0 \\ 1 & 0 & 0 & 0 \\ 0 & 0 & 0 & 1 \\ 0 & 1 & 0 & 0 \end{bmatrix}, \mathbf{A}_{12} = \begin{bmatrix} 0 & 0 & 0 & 1 \\ 1 & 0 & 0 & 0 \\ 0 & 0 & 1 & 0 \\ 0 & 1 & 0 & 0 \end{bmatrix},$$

$$\mathbf{A}_{13} = \begin{bmatrix} 0 & 1 & 0 & 0 \\ 0 & 0 & 1 & 0 \\ 1 & 0 & 0 & 0 \\ 0 & 0 & 0 & 1 \end{bmatrix}, \mathbf{A}_{14} = \begin{bmatrix} 0 & 1 & 0 & 0 \\ 0 & 0 & 0 & 1 \\ 1 & 0 & 0 & 0 \\ 0 & 0 & 1 & 0 \end{bmatrix}, \mathbf{A}_{15} = \begin{bmatrix} 0 & 0 & 1 & 0 \\ 0 & 1 & 0 & 0 \\ 1 & 0 & 0 & 0 \\ 0 & 0 & 0 & 1 \end{bmatrix}, \mathbf{A}_{16} = \begin{bmatrix} 0 & 0 & 0 & 1 \\ 0 & 1 & 0 & 0 \\ 1 & 0 & 0 & 0 \\ 0 & 0 & 1 & 0 \end{bmatrix}.$$

UDSM ($M = 2$, $Q = 2$, $\mathbf{L} = [2,2]$)

$$\mathbf{A}_1 = \begin{bmatrix} \exp(-j0.82\pi) & 0.00 \\ 0.00 & \exp(+j0.42\pi) \end{bmatrix}, \mathbf{A}_2 = \begin{bmatrix} 0.00 & \exp(-j0.01\pi) \\ \exp(+j0.10\pi) & 0.00 \end{bmatrix}.$$

UDSM ($M = 2$, $Q = 2$, $\mathbf{L} = [2,4]$)

$$\mathbf{A}_1 = \begin{bmatrix} \exp(-j0.59\pi) & 0.00 \\ 0.00 & \exp(-j0.77\pi) \end{bmatrix}, \mathbf{A}_2 = \begin{bmatrix} 0.00 & \exp(-j0.69\pi) \\ \exp(+j0.08\pi) & 0.00 \end{bmatrix}.$$

UDSM ($M = 2$, $Q = 2$, $\mathbf{L} = [(4,4)]$)

$$\mathbf{A}_1 = \begin{bmatrix} \exp(-j0.71\pi) & 0.00 \\ 0.00 & \exp(+j0.22\pi) \end{bmatrix}, \mathbf{A}_2 = \begin{bmatrix} 0.00 & \exp(+j0.39\pi) \\ \exp(-j0.39\pi) & 0.00 \end{bmatrix}.$$

UDSM ($M = 2$, $Q = 2$, $\mathbf{L} = [4,8]$)

$$\mathbf{A}_1 = \begin{bmatrix} \exp(-j0.98\pi) & 0.00 \\ 0.00 & \exp(-j0.21\pi) \end{bmatrix}, \mathbf{A}_2 = \begin{bmatrix} 0.00 & \exp(+j0.17\pi) \\ \exp(+j0.02\pi) & 0.00 \end{bmatrix}.$$

UDSM ($M = 2$, $Q = 2$, $\mathbf{L} = [8,16]$)

$$\mathbf{A}_1 = \begin{bmatrix} \exp(-j0.73\pi) & 0.00 \\ 0.00 & \exp(+j0.00\pi) \end{bmatrix}, \mathbf{A}_2 = \begin{bmatrix} 0.00 & \exp(+j0.09\pi) \\ \exp(-j0.25\pi) & 0.00 \end{bmatrix}.$$

UDSM ($M = 2$, $Q = 2$, $\mathbf{L} = [(16,16)]$)

$$\mathbf{A}_1 = \begin{bmatrix} \exp(-j0.21\pi) & 0.00 \\ 0.00 & \exp(-j0.93\pi) \end{bmatrix}, \mathbf{A}_2 = \begin{bmatrix} 0.00 & \exp(+j0.00\pi) \\ \exp(-j0.20\pi) & 0.00 \end{bmatrix}.$$

UDSM ($M = 4$, $Q = 4$, $\mathbf{L} = [4,4,4,4]$)

$$\mathbf{A}_1 = \begin{bmatrix} \exp(+j0.11\pi) & 0.00 & 0.00 & 0.00 \\ 0.00 & \exp(-j0.68\pi) & 0.00 & 0.00 \\ 0.00 & 0.00 & \exp(+j0.66\pi) & 0.00 \\ 0.00 & 0.00 & 0.00 & \exp(+j0.58\pi) \end{bmatrix},$$

$$\mathbf{A}_2 = \begin{bmatrix} 0.00 & 0.00 & 0.00 & \exp(-j0.76\pi) \\ \exp(-j0.55\pi) & 0.00 & 0.00 & 0.00 \\ 0.00 & \exp(-j0.89\pi) & 0.00 & 0.00 \\ 0.00 & 0.00 & \exp(-j0.15\pi) & 0.00 \end{bmatrix},$$

$$\mathbf{A}_3 = \begin{bmatrix} 0.00 & 0.00 & \exp(+j0.81\pi) & 0.00 \\ 0.00 & 0.00 & 0.00 & \exp(+j0.22\pi) \\ \exp(-j0.55\pi) & 0.00 & 0.00 & 0.00 \\ 0.00 & \exp(+j0.17\pi) & 0.00 & 0.00 \end{bmatrix},$$

$$\mathbf{A}_4 = \begin{bmatrix} 0.00 & \exp(-j0.49\pi) & 0.00 & 0.00 \\ 0.00 & 0.00 & \exp(-j0.36\pi) & 0.00 \\ 0.00 & 0.00 & 0.00 & \exp(-j0.65\pi) \\ \exp(-j0.83\pi) & 0.00 & 0.00 & 0.00 \end{bmatrix}.$$

UDSM ($M = 4$, $Q = 4$, $\mathbf{L} = [(16,16,16,16)]$)

$$\mathbf{A}_1 = \begin{bmatrix} \exp(+j0.54\pi) & 0.00 & 0.00 & 0.00 \\ 0.00 & \exp(+j0.42\pi) & 0.00 & 0.00 \\ 0.00 & 0.00 & \exp(-j0.45\pi) & 0.00 \\ 0.00 & 0.00 & 0.00 & \exp(-j0.59\pi) \end{bmatrix},$$

$$\mathbf{A}_2 = \begin{bmatrix} 0.00 & 0.00 & 0.00 & \exp(+j0.84\pi) \\ \exp(+j0.95\pi) & 0.00 & 0.00 & 0.00 \\ 0.00 & \exp(+j0.04\pi) & 0.00 & 0.00 \\ 0.00 & 0.00 & \exp(-j0.80\pi) & 0.00 \end{bmatrix},$$

$$\mathbf{A}_3 = \begin{bmatrix} 0.00 & 0.00 & \exp(-j0.69\pi) & 0.00 \\ 0.00 & 0.00 & 0.00 & \exp(-j0.10\pi) \\ \exp(-j0.53\pi) & 0.00 & 0.00 & 0.00 \\ 0.00 & \exp(-j0.74\pi) & 0.00 & 0.00 \end{bmatrix},$$

$$\mathbf{A}_4 = \begin{bmatrix} 0.00 & \exp(+j0.71\pi) & 0.00 & 0.00 \\ 0.00 & 0.00 & \exp(+j0.00\pi) & 0.00 \\ 0.00 & 0.00 & 0.00 & \exp(+j0.76\pi) \\ \exp(-j0.43\pi) & 0.00 & 0.00 & 0.00 \end{bmatrix}.$$

UDSM ($M = 4$, $Q = 8$, $\mathbf{L} = [(2,2),(2,2)]$)

$$\mathbf{A}_1 = \begin{bmatrix} \exp(+j0.06\pi) & 0.00 & 0.00 & 0.00 \\ 0.00 & \exp(-j0.04\pi) & 0.00 & 0.00 \\ 0.00 & 0.00 & 0.00 & \exp(-j0.88\pi) \\ 0.00 & 0.00 & \exp(+j0.99\pi) & 0.00 \end{bmatrix},$$

$$\mathbf{A}_2 = \begin{bmatrix} \exp(+j0.51\pi) & 0.00 & 0.00 & 0.00 \\ 0.00 & 0.00 & 0.00 & \exp(-j0.60\pi) \\ 0.00 & 0.00 & \exp(+j0.18\pi) & 0.00 \\ 0.00 & \exp(-j0.91\pi) & 0.00 & 0.00 \end{bmatrix},$$

$$\mathbf{A}_3 = \begin{bmatrix} 0.00 & \exp(+j0.81\pi) & 0.00 & 0.00 \\ \exp(+j0.39\pi) & 0.00 & 0.00 & 0.00 \\ 0.00 & 0.00 & \exp(+j0.48\pi) & 0.00 \\ 0.00 & 0.00 & 0.00 & \exp(+j0.49\pi) \end{bmatrix},$$

$$\mathbf{A}_4 = \begin{bmatrix} 0.00 & 0.00 & 0.00 & \exp(+j0.79\pi) \\ \exp(+j0.68\pi) & 0.00 & 0.00 & 0.00 \\ 0.00 & \exp(+j0.34\pi) & 0.00 & 0.00 \\ 0.00 & 0.00 & \exp(-j0.60\pi) & 0.00 \end{bmatrix},$$

$$\mathbf{A}_5 = \begin{bmatrix} 0.00 & 0.00 & \exp(-j0.50\pi) & 0.00 \\ 0.00 & \exp(+j0.64\pi) & 0.00 & 0.00 \\ \exp(+j0.78\pi) & 0.00 & 0.00 & 0.00 \\ 0.00 & 0.00 & 0.00 & \exp(+j0.21\pi) \end{bmatrix},$$

$$\mathbf{A}_6 = \begin{bmatrix} 0.00 & 0.00 & 0.00 & \exp(+j0.26\pi) \\ 0.00 & 0.00 & \exp(+j0.81\pi) & 0.00 \\ \exp(+j0.53\pi) & 0.00 & 0.00 & 0.00 \\ 0.00 & \exp(+j0.64\pi) & 0.00 & 0.00 \end{bmatrix},$$

$$\mathbf{A}_7 = \begin{bmatrix} 0.00 & \exp(+j0.14\pi) & 0.00 & 0.00 \\ 0.00 & 0.00 & \exp(+j0.42\pi) & 0.00 \\ 0.00 & 0.00 & 0.00 & \exp(-j0.39\pi) \\ \exp(-j0.95\pi) & 0.00 & 0.00 & 0.00 \end{bmatrix},$$

$$\mathbf{A}_8 = \begin{bmatrix} 0.00 & 0.00 & \exp(-j0.88\pi) & 0.00 \\ 0.00 & 0.00 & 0.00 & \exp(+j0.92\pi) \\ 0.00 & \exp(+j0.88\pi) & 0.00 & 0.00 \\ \exp(-j0.54\pi) & 0.00 & 0.00 & 0.00 \end{bmatrix}.$$

UDSM ($M = 4$, $Q = 8$, $\mathbf{L} = [(4,4),(4,4)]$)

$$\mathbf{A}_1 = \begin{bmatrix} \exp(-j0.12\pi) & 0.00 & 0.00 & 0.00 \\ 0.00 & \exp(-j0.96\pi) & 0.00 & 0.00 \\ 0.00 & 0.00 & 0.00 & \exp(+j0.30\pi) \\ 0.00 & 0.00 & \exp(+j0.13\pi) & 0.00 \end{bmatrix},$$

$$\mathbf{A}_2 = \begin{bmatrix} \exp(-j0.85\pi) & 0.00 & 0.00 & 0.00 \\ 0.00 & 0.00 & 0.00 & \exp(-j0.67\pi) \\ 0.00 & 0.00 & \exp(+j0.07\pi) & 0.00 \\ 0.00 & \exp(-j0.70\pi) & 0.00 & 0.00 \end{bmatrix},$$

$$\mathbf{A}_3 = \begin{bmatrix} 0.00 & \exp(+j0.92\pi) & 0.00 & 0.00 \\ \exp(+j0.28\pi) & 0.00 & 0.00 & 0.00 \\ 0.00 & 0.00 & \exp(+j0.81\pi) & 0.00 \\ 0.00 & 0.00 & 0.00 & \exp(-j0.61\pi) \end{bmatrix},$$

$$\mathbf{A}_4 = \begin{bmatrix} 0.00 & 0.00 & 0.00 & \exp(-j0.26\pi) \\ \exp(+j0.43\pi) & 0.00 & 0.00 & 0.00 \\ 0.00 & \exp(+j0.28\pi) & 0.00 & 0.00 \\ 0.00 & 0.00 & \exp(-j0.55\pi) & 0.00 \end{bmatrix},$$

$$\mathbf{A}_5 = \begin{bmatrix} 0.00 & 0.00 & \exp(-j0.29\pi) & 0.00 \\ 0.00 & \exp(-j0.65\pi) & 0.00 & 0.00 \\ \exp(+j0.14\pi) & 0.00 & 0.00 & 0.00 \\ 0.00 & 0.00 & 0.00 & \exp(+j0.71\pi) \end{bmatrix},$$

$$\mathbf{A}_6 = \begin{bmatrix} 0.00 & 0.00 & 0.00 & \exp(+j0.51\pi) \\ 0.00 & 0.00 & \exp(+j0.86\pi) & 0.00 \\ \exp(-j0.53\pi) & 0.00 & 0.00 & 0.00 \\ 0.00 & \exp(+j0.58\pi) & 0.00 & 0.00 \end{bmatrix},$$

$$\mathbf{A}_7 = \begin{bmatrix} 0.00 & \exp(+j0.66\pi) & 0.00 & 0.00 \\ 0.00 & 0.00 & \exp(-j0.95\pi) & 0.00 \\ 0.00 & 0.00 & 0.00 & \exp(-j0.37\pi) \\ \exp(+j0.55\pi) & 0.00 & 0.00 & 0.00 \end{bmatrix},$$

$$\mathbf{A}_8 = \begin{bmatrix} 0.00 & 0.00 & \exp(-j0.03\pi) & 0.00 \\ 0.00 & 0.00 & 0.00 & \exp(-j0.32\pi) \\ 0.00 & \exp(+j0.43\pi) & 0.00 & 0.00 \\ \exp(-j0.71\pi) & 0.00 & 0.00 & 0.00 \end{bmatrix}.$$

UDSM ($M = 4$, $Q = 8$, $\mathbf{L} = [(16,16),(16,16)]$)

$$\mathbf{A}_1 = \begin{bmatrix} \exp(-j0.40\pi) & 0.00 & 0.00 & 0.00 \\ 0.00 & \exp(+j0.49\pi) & 0.00 & 0.00 \\ 0.00 & 0.00 & 0.00 & \exp(+j0.81\pi) \\ 0.00 & 0.00 & \exp(+j0.87\pi) & 0.00 \end{bmatrix},$$

$$\mathbf{A}_2 = \begin{bmatrix} \exp(-j0.57\pi) & 0.00 & 0.00 & 0.00 \\ 0.00 & 0.00 & 0.00 & \exp(+j0.72\pi) \\ 0.00 & 0.00 & \exp(-j0.29\pi) & 0.00 \\ 0.00 & \exp(-j0.58\pi) & 0.00 & 0.00 \end{bmatrix},$$

$$\mathbf{A}_3 = \begin{bmatrix} 0.00 & \exp(+j0.91\pi) & 0.00 & 0.00 \\ \exp(+j0.24\pi) & 0.00 & 0.00 & 0.00 \\ 0.00 & 0.00 & \exp(-j0.03\pi) & 0.00 \\ 0.00 & 0.00 & 0.00 & \exp(-j0.68\pi) \end{bmatrix},$$

$$\mathbf{A}_4 = \begin{bmatrix} 0.00 & 0.00 & 0.00 & \exp(+j0.87\pi) \\ \exp(+j0.68\pi) & 0.00 & 0.00 & 0.00 \\ 0.00 & \exp(-j0.45\pi) & 0.00 & 0.00 \\ 0.00 & 0.00 & \exp(+j0.95\pi) & 0.00 \end{bmatrix},$$

$$\mathbf{A}_5 = \begin{bmatrix} 0.00 & 0.00 & \exp(-j0.05\pi) & 0.00 \\ 0.00 & \exp(-j0.16\pi) & 0.00 & 0.00 \\ \exp(-j0.25\pi) & 0.00 & 0.00 & 0.00 \\ 0.00 & 0.00 & 0.00 & \exp(+j0.89\pi) \end{bmatrix},$$

$$\mathbf{A}_6 = \begin{bmatrix} 0.00 & 0.00 & 0.00 & \exp(-j0.65\pi) \\ 0.00 & 0.00 & \exp(+j0.62\pi) & 0.00 \\ \exp(+j0.05\pi) & 0.00 & 0.00 & 0.00 \\ 0.00 & \exp(+j0.61\pi) & 0.00 & 0.00 \end{bmatrix},$$

$$\mathbf{A}_7 = \begin{bmatrix} 0.00 & \exp(+j0.09\pi) & 0.00 & 0.00 \\ 0.00 & 0.00 & \exp(+j0.59\pi) & 0.00 \\ 0.00 & 0.00 & 0.00 & \exp(-j0.98\pi) \\ \exp(-j0.41\pi) & 0.00 & 0.00 & 0.00 \end{bmatrix},$$

$$\mathbf{A}_8 = \begin{bmatrix} 0.00 & 0.00 & \exp(-j0.99\pi) & 0.00 \\ 0.00 & 0.00 & 0.00 & \exp(+j0.17\pi) \\ 0.00 & \exp(+j0.97\pi) & 0.00 & 0.00 \\ \exp(+j0.29\pi) & 0.00 & 0.00 & 0.00 \end{bmatrix}.$$

UDSM ($M = 4$, $Q = 16$, $\mathbf{L} = [(4,4),(4,4)]$)

$$\mathbf{A}_1 = \begin{bmatrix} \exp(+j0.45\pi) & 0.00 & 0.00 & 0.00 \\ 0.00 & \exp(-j0.44\pi) & 0.00 & 0.00 \\ 0.00 & 0.00 & \exp(+j0.91\pi) & 0.00 \\ 0.00 & 0.00 & 0.00 & \exp(+j0.24\pi) \end{bmatrix},$$

$$\mathbf{A}_2 = \begin{bmatrix} \exp(+j0.85\pi) & 0.00 & 0.00 & 0.00 \\ 0.00 & \exp(+j0.63\pi) & 0.00 & 0.00 \\ 0.00 & 0.00 & 0.00 & \exp(-j0.54\pi) \\ 0.00 & 0.00 & \exp(-j0.81\pi) & 0.00 \end{bmatrix},$$

$$\mathbf{A}_3 = \begin{bmatrix} \exp(+j0.10\pi) & 0.00 & 0.00 & 0.00 \\ 0.00 & 0.00 & \exp(+j0.56\pi) & 0.00 \\ 0.00 & 0.00 & 0.00 & \exp(-j0.12\pi) \\ 0.00 & \exp(+j0.68\pi) & 0.00 & 0.00 \end{bmatrix},$$

$$\mathbf{A}_4 = \begin{bmatrix} \exp(-j0.43\pi) & 0.00 & 0.00 & 0.00 \\ 0.00 & 0.00 & 0.00 & \exp(-j0.16\pi) \\ 0.00 & 0.00 & \exp(-j0.24\pi) & 0.00 \\ 0.00 & \exp(-j0.72\pi) & 0.00 & 0.00 \end{bmatrix},$$

$$\mathbf{A}_5 = \begin{bmatrix} 0.00 & \exp(+j0.99\pi) & 0.00 & 0.00 \\ \exp(+j0.58\pi) & 0.00 & 0.00 & 0.00 \\ 0.00 & 0.00 & \exp(+j0.32\pi) & 0.00 \\ 0.00 & 0.00 & 0.00 & \exp(+j0.33\pi) \end{bmatrix},$$

$$\mathbf{A}_6 = \begin{bmatrix} 0.00 & \exp(-j0.37\pi) & 0.00 & 0.00 \\ \exp(-j0.95\pi) & 0.00 & 0.00 & 0.00 \\ 0.00 & 0.00 & 0.00 & \exp(+j0.20\pi) \\ 0.00 & 0.00 & \exp(+j0.88\pi) & 0.00 \end{bmatrix},$$

$$\mathbf{A}_7 = \begin{bmatrix} 0.00 & 0.00 & \exp(+j0.82\pi) & 0.00 \\ \exp(+j0.76\pi) & 0.00 & 0.00 & 0.00 \\ 0.00 & \exp(+j0.55\pi) & 0.00 & 0.00 \\ 0.00 & 0.00 & 0.00 & \exp(+j0.12\pi) \end{bmatrix},$$

$$\mathbf{A}_8 = \begin{bmatrix} 0.00 & 0.00 & 0.00 & \exp(+j0.08\pi) \\ \exp(+j0.79\pi) & 0.00 & 0.00 & 0.00 \\ 0.00 & 0.00 & \exp(+j0.04\pi) & 0.00 \\ 0.00 & \exp(-j0.79\pi) & 0.00 & 0.00 \end{bmatrix},$$

$$\mathbf{A}_9 = \begin{bmatrix} 0.00 & \exp(+j0.80\pi) & 0.00 & 0.00 \\ 0.00 & 0.00 & \exp(-j0.02\pi) & 0.00 \\ \exp(+j0.70\pi) & 0.00 & 0.00 & 0.00 \\ 0.00 & 0.00 & 0.00 & \exp(-j0.66\pi) \end{bmatrix},$$

$$\mathbf{A}_{10} = \begin{bmatrix} 0.00 & \exp(+j0.66\pi) & 0.00 & 0.00 \\ 0.00 & 0.00 & 0.00 & \exp(+j0.97\pi) \\ \exp(+j0.30\pi) & 0.00 & 0.00 & 0.00 \\ 0.00 & 0.00 & \exp(+j0.41\pi) & 0.00 \end{bmatrix},$$

$$\mathbf{A}_{11} = \begin{bmatrix} 0.00 & 0.00 & \exp(+j0.72\pi) & 0.00 \\ 0.00 & \exp(+j0.97\pi) & 0.00 & 0.00 \\ \exp(+j0.87\pi) & 0.00 & 0.00 & 0.00 \\ 0.00 & 0.00 & 0.00 & \exp(+j0.43\pi) \end{bmatrix},$$

$$\mathbf{A}_{12} = \begin{bmatrix} 0.00 & 0.00 & 0.00 & \exp(+j0.67\pi) \\ 0.00 & \exp(-j0.41\pi) & 0.00 & 0.00 \\ \exp(+j0.44\pi) & 0.00 & 0.00 & 0.00 \\ 0.00 & 0.00 & \exp(-j0.06\pi) & 0.00 \end{bmatrix},$$

$$\mathbf{A}_{13} = \begin{bmatrix} 0.00 & 0.00 & 0.00 & \exp(-j0.61\pi) \\ 0.00 & 0.00 & \exp(+j0.71\pi) & 0.00 \\ \exp(+j0.54\pi) & 0.00 & 0.00 & 0.00 \\ 0.00 & \exp(+j0.95\pi) & 0.00 & 0.00 \end{bmatrix},$$

$$\mathbf{A}_{14} = \begin{bmatrix} 0.00 & 0.00 & 0.00 & \exp(-j0.20\pi) \\ 0.00 & \exp(+j0.82\pi) & 0.00 & 0.00 \\ 0.00 & 0.00 & \exp(-j0.90\pi) & 0.00 \\ \exp(+j0.85\pi) & 0.00 & 0.00 & 0.00 \end{bmatrix},$$

$$\mathbf{A}_{15} = \begin{bmatrix} 0.00 & 0.00 & \exp(+j0.78\pi) & 0.00 \\ 0.00 & 0.00 & 0.00 & \exp(+j0.64\pi) \\ 0.00 & \exp(+j0.42\pi) & 0.00 & 0.00 \\ \exp(+j0.95\pi) & 0.00 & 0.00 & 0.00 \end{bmatrix},$$

$$\mathbf{A}_{16} = \begin{bmatrix} 0.00 & 0.00 & 0.00 & \exp(+j0.01\pi) \\ 0.00 & 0.00 & \exp(+j0.06\pi) & 0.00 \\ 0.00 & \exp(+j0.88\pi) & 0.00 & 0.00 \\ \exp(+j0.01\pi) & 0.00 & 0.00 & 0.00 \end{bmatrix}.$$

UDSM ($M = 4$, $Q = 16$, $\mathbf{L} = [4,4,4,4]$)

$$\mathbf{A}_1 = \begin{bmatrix} \exp(-j0.07\pi) & 0.00 & 0.00 & 0.00 \\ 0.00 & \exp(-j0.70\pi) & 0.00 & 0.00 \\ 0.00 & 0.00 & \exp(+j0.50\pi) & 0.00 \\ 0.00 & 0.00 & 0.00 & \exp(+j0.97\pi) \end{bmatrix},$$

$$\mathbf{A}_2 = \begin{bmatrix} \exp(-j0.83\pi) & 0.00 & 0.00 & 0.00 \\ 0.00 & \exp(+j0.94\pi) & 0.00 & 0.00 \\ 0.00 & 0.00 & 0.00 & \exp(+j0.72\pi) \\ 0.00 & 0.00 & \exp(-j0.55\pi) & 0.00 \end{bmatrix},$$

$$\mathbf{A}_3 = \begin{bmatrix} \exp(+j0.99\pi) & 0.00 & 0.00 & 0.00 \\ 0.00 & 0.00 & 0.00 & \exp(+j0.58\pi) \\ 0.00 & \exp(-j0.19\pi) & 0.00 & 0.00 \\ 0.00 & 0.00 & \exp(-j0.16\pi) & 0.00 \end{bmatrix},$$

$$\mathbf{A}_4 = \begin{bmatrix} \exp(-j0.63\pi) & 0.00 & 0.00 & 0.00 \\ 0.00 & 0.00 & \exp(+j0.84\pi) & 0.00 \\ 0.00 & 0.00 & 0.00 & \exp(-j0.07\pi) \\ 0.00 & \exp(+j0.92\pi) & 0.00 & 0.00 \end{bmatrix},$$

$$\mathbf{A}_5 = \begin{bmatrix} 0.00 & \exp(+j0.17\pi) & 0.00 & 0.00 \\ \exp(-j0.18\pi) & 0.00 & 0.00 & 0.00 \\ 0.00 & 0.00 & \exp(+j0.24\pi) & 0.00 \\ 0.00 & 0.00 & 0.00 & \exp(-j0.96\pi) \end{bmatrix},$$

$$\mathbf{A}_6 = \begin{bmatrix} 0.00 & \exp(+j0.89\pi) & 0.00 & 0.00 \\ \exp(-j0.00\pi) & 0.00 & 0.00 & 0.00 \\ 0.00 & 0.00 & 0.00 & \exp(+j0.15\pi) \\ 0.00 & 0.00 & \exp(+j0.70\pi) & 0.00 \end{bmatrix},$$

$$\mathbf{A}_7 = \begin{bmatrix} 0.00 & 0.00 & \exp(-j0.51\pi) & 0.00 \\ \exp(+j0.90\pi) & 0.00 & 0.00 & 0.00 \\ 0.00 & \exp(-j0.42\pi) & 0.00 & 0.00 \\ 0.00 & 0.00 & 0.00 & \exp(-j0.61\pi) \end{bmatrix},$$

$$\mathbf{A}_8 = \begin{bmatrix} 0.00 & 0.00 & 0.00 & \exp(+j0.83\pi) \\ \exp(-j0.83\pi) & 0.00 & 0.00 & 0.00 \\ 0.00 & 0.00 & \exp(+j0.91\pi) & 0.00 \\ 0.00 & \exp(-j0.29\pi) & 0.00 & 0.00 \end{bmatrix},$$

$$\mathbf{A}_9 = \begin{bmatrix} 0.00 & \exp(+j0.37\pi) & 0.00 & 0.00 \\ 0.00 & 0.00 & \exp(-j0.43\pi) & 0.00 \\ \exp(+j0.24\pi) & 0.00 & 0.00 & 0.00 \\ 0.00 & 0.00 & 0.00 & \exp(+j0.86\pi) \end{bmatrix},$$

$$\mathbf{A}_{10} = \begin{bmatrix} 0.00 & 0.00 & 0.00 & \exp(+j0.89\pi) \\ 0.00 & \exp(+j0.60\pi) & 0.00 & 0.00 \\ \exp(+j0.78\pi) & 0.00 & 0.00 & 0.00 \\ 0.00 & 0.00 & \exp(+j0.47\pi) & 0.00 \end{bmatrix},$$

$$\mathbf{A}_{11} = \begin{bmatrix} 0.00 & 0.00 & \exp(+j0.82\pi) & 0.00 \\ 0.00 & 0.00 & 0.00 & \exp(+j0.23\pi) \\ \exp(+j0.99\pi) & 0.00 & 0.00 & 0.00 \\ 0.00 & \exp(-j0.05\pi) & 0.00 & 0.00 \end{bmatrix},$$

$$\mathbf{A}_{12} = \begin{bmatrix} 0.00 & 0.00 & 0.00 & \exp(+j0.07\pi) \\ 0.00 & 0.00 & \exp(-j0.83\pi) & 0.00 \\ \exp(+j0.38\pi) & 0.00 & 0.00 & 0.00 \\ 0.00 & \exp(-j0.25\pi) & 0.00 & 0.00 \end{bmatrix},$$

$$\mathbf{A}_{13} = \begin{bmatrix} 0.00 & \exp(-j0.53\pi) & 0.00 & 0.00 \\ 0.00 & 0.00 & 0.00 & \exp(-j0.59\pi) \\ 0.00 & 0.00 & \exp(+j0.10\pi) & 0.00 \\ \exp(+j0.18\pi) & 0.00 & 0.00 & 0.00 \end{bmatrix},$$

$$\mathbf{A}_{14} = \begin{bmatrix} 0.00 & 0.00 & \exp(+j0.66\pi) & 0.00 \\ 0.00 & \exp(+j0.05\pi) & 0.00 & 0.00 \\ 0.00 & 0.00 & 0.00 & \exp(+j0.54\pi) \\ \exp(+j0.86\pi) & 0.00 & 0.00 & 0.00 \end{bmatrix},$$

$$\mathbf{A}_{15} = \begin{bmatrix} 0.00 & 0.00 & \exp(-j0.07\pi) & 0.00 \\ 0.00 & 0.00 & 0.00 & \exp(+j0.10\pi) \\ 0.00 & \exp(-j0.01\pi) & 0.00 & 0.00 \\ \exp(-j0.95\pi) & 0.00 & 0.00 & 0.00 \end{bmatrix},$$

$$\mathbf{A}_{16} = \begin{bmatrix} 0.00 & 0.00 & 0.00 & \exp(+j0.35\pi) \\ 0.00 & 0.00 & \exp(+j0.77\pi) & 0.00 \\ 0.00 & \exp(+j0.84\pi) & 0.00 & 0.00 \\ \exp(+j0.48\pi) & 0.00 & 0.00 & 0.00 \end{bmatrix}.$$

UDSM ($M = 4$, $Q = 16$, $\mathbf{L} = [8,8,8,8]$)

$$\mathbf{A}_{1} = \begin{bmatrix} \exp(+j0.00\pi) & 0.00 & 0.00 & 0.00 \\ 0.00 & \exp(+j0.00\pi) & 0.00 & 0.00 \\ 0.00 & 0.00 & \exp(+j0.00\pi) & 0.00 \\ 0.00 & 0.00 & 0.00 & \exp(+j0.00\pi) \end{bmatrix},$$

$$\mathbf{A}_{2} = \begin{bmatrix} \exp(+j0.00\pi) & 0.00 & 0.00 & 0.00 \\ 0.00 & \exp(+j0.00\pi) & 0.00 & 0.00 \\ 0.00 & 0.00 & 0.00 & \exp(+j0.00\pi) \\ 0.00 & 0.00 & \exp(+j0.00\pi) & 0.00 \end{bmatrix},$$

$$\mathbf{A}_{3} = \begin{bmatrix} \exp(+j0.00\pi) & 0.00 & 0.00 & 0.00 \\ 0.00 & 0.00 & 0.00 & \exp(+j0.00\pi) \\ 0.00 & \exp(+j0.00\pi) & 0.00 & 0.00 \\ 0.00 & 0.00 & \exp(+j0.00\pi) & 0.00 \end{bmatrix},$$

$$\mathbf{A}_4 = \begin{bmatrix} \exp(+j0.00\pi) & 0.00 & 0.00 & 0.00 \\ 0.00 & 0.00 & \exp(+j0.00\pi) & 0.00 \\ 0.00 & 0.00 & 0.00 & \exp(+j0.00\pi) \\ 0.00 & \exp(+j0.00\pi) & 0.00 & 0.00 \end{bmatrix},$$

$$\mathbf{A}_5 = \begin{bmatrix} 0.00 & \exp(+j0.00\pi) & 0.00 & 0.00 \\ \exp(+j0.00\pi) & 0.00 & 0.00 & 0.00 \\ 0.00 & 0.00 & \exp(+j0.00\pi) & 0.00 \\ 0.00 & 0.00 & 0.00 & \exp(+j0.00\pi) \end{bmatrix},$$

$$\mathbf{A}_6 = \begin{bmatrix} 0.00 & \exp(+j0.00\pi) & 0.00 & 0.00 \\ \exp(+j0.00\pi) & 0.00 & 0.00 & 0.00 \\ 0.00 & 0.00 & 0.00 & \exp(+j0.00\pi) \\ 0.00 & 0.00 & \exp(+j0.00\pi) & 0.00 \end{bmatrix},$$

$$\mathbf{A}_7 = \begin{bmatrix} 0.00 & 0.00 & \exp(+j0.00\pi) & 0.00 \\ \exp(+j0.00\pi) & 0.00 & 0.00 & 0.00 \\ 0.00 & \exp(+j0.00\pi) & 0.00 & 0.00 \\ 0.00 & 0.00 & 0.00 & \exp(+j0.00\pi) \end{bmatrix},$$

$$\mathbf{A}_8 = \begin{bmatrix} 0.00 & 0.00 & 0.00 & \exp(+j0.00\pi) \\ \exp(+j0.00\pi) & 0.00 & 0.00 & 0.00 \\ 0.00 & 0.00 & \exp(+j0.00\pi) & 0.00 \\ 0.00 & \exp(+j0.00\pi) & 0.00 & 0.00 \end{bmatrix},$$

$$\mathbf{A}_9 = \begin{bmatrix} 0.00 & \exp(+j0.00\pi) & 0.00 & 0.00 \\ 0.00 & 0.00 & \exp(+j0.00\pi) & 0.00 \\ \exp(+j0.00\pi) & 0.00 & 0.00 & 0.00 \\ 0.00 & 0.00 & 0.00 & \exp(+j0.00\pi) \end{bmatrix},$$

$$\mathbf{A}_{10} = \begin{bmatrix} 0.00 & 0.00 & 0.00 & \exp(+j0.00\pi) \\ 0.00 & \exp(+j0.00\pi) & 0.00 & 0.00 \\ \exp(+j0.00\pi) & 0.00 & 0.00 & 0.00 \\ 0.00 & 0.00 & \exp(+j0.00\pi) & 0.00 \end{bmatrix},$$

$$
\mathbf{A}_{11} = \begin{bmatrix} 0.00 & 0.00 & \exp(+j0.00\pi) & 0.00 \\ 0.00 & 0.00 & 0.00 & \exp(+j0.00\pi) \\ \exp(+j0.00\pi) & 0.00 & 0.00 & 0.00 \\ 0.00 & \exp(+j0.00\pi) & 0.00 & 0.00 \end{bmatrix},
$$

$$
\mathbf{A}_{12} = \begin{bmatrix} 0.00 & 0.00 & 0.00 & \exp(+j0.00\pi) \\ 0.00 & 0.00 & \exp(+j0.00\pi) & 0.00 \\ \exp(+j0.00\pi) & 0.00 & 0.00 & 0.00 \\ 0.00 & \exp(+j0.00\pi) & 0.00 & 0.00 \end{bmatrix},
$$

$$
\mathbf{A}_{13} = \begin{bmatrix} 0.00 & \exp(+j0.00\pi) & 0.00 & 0.00 \\ 0.00 & 0.00 & 0.00 & \exp(+j0.00\pi) \\ 0.00 & 0.00 & \exp(+j0.00\pi) & 0.00 \\ \exp(+j0.00\pi) & 0.00 & 0.00 & 0.00 \end{bmatrix},
$$

$$
\mathbf{A}_{14} = \begin{bmatrix} 0.00 & 0.00 & \exp(+j0.00\pi) & 0.00 \\ 0.00 & \exp(+j0.00\pi) & 0.00 & 0.00 \\ 0.00 & 0.00 & 0.00 & \exp(+j0.00\pi) \\ \exp(+j0.00\pi) & 0.00 & 0.00 & 0.00 \end{bmatrix},
$$

$$
\mathbf{A}_{15} = \begin{bmatrix} 0.00 & 0.00 & \exp(+j0.00\pi) & 0.00 \\ 0.00 & 0.00 & 0.00 & \exp(+j0.00\pi) \\ 0.00 & \exp(+j0.00\pi) & 0.00 & 0.00 \\ \exp(+j0.00\pi) & 0.00 & 0.00 & 0.00 \end{bmatrix},
$$

$$
\mathbf{A}_{16} = \begin{bmatrix} 0.00 & 0.00 & 0.00 & \exp(+j0.00\pi) \\ 0.00 & 0.00 & \exp(+j0.00\pi) & 0.00 \\ 0.00 & \exp(+j0.00\pi) & 0.00 & 0.00 \\ \exp(+j0.00\pi) & 0.00 & 0.00 & 0.00 \end{bmatrix}.
$$

UDSM ($M = 4$, $Q = 16$, $\mathbf{L} = [(16,16,16,16)]$)

$$
\mathbf{A}_1 = \begin{bmatrix} \exp(-j0.55\pi) & 0.00 & 0.00 & 0.00 \\ 0.00 & \exp(-j0.76\pi) & 0.00 & 0.00 \\ 0.00 & 0.00 & \exp(+j0.77\pi) & 0.00 \\ 0.00 & 0.00 & 0.00 & \exp(+j0.84\pi) \end{bmatrix},
$$

$$
\mathbf{A}_2 = \begin{bmatrix} \exp(+j0.51\pi) & 0.00 & 0.00 & 0.00 \\ 0.00 & \exp(-j0.50\pi) & 0.00 & 0.00 \\ 0.00 & 0.00 & 0.00 & \exp(-j0.48\pi) \\ 0.00 & 0.00 & \exp(+j0.07\pi) & 0.00 \end{bmatrix},
$$

$$
\mathbf{A}_3 = \begin{bmatrix} \exp(+j0.42\pi) & 0.00 & 0.00 & 0.00 \\ 0.00 & 0.00 & 0.00 & \exp(+j0.41\pi) \\ 0.00 & \exp(+j0.04\pi) & 0.00 & 0.00 \\ 0.00 & 0.00 & \exp(-j0.43\pi) & 0.00 \end{bmatrix},
$$

$$
\mathbf{A}_4 = \begin{bmatrix} \exp(+j0.39\pi) & 0.00 & 0.00 & 0.00 \\ 0.00 & 0.00 & \exp(+j0.64\pi) & 0.00 \\ 0.00 & 0.00 & 0.00 & \exp(+j0.72\pi) \\ 0.00 & \exp(+j0.01\pi) & 0.00 & 0.00 \end{bmatrix},
$$

$$
\mathbf{A}_5 = \begin{bmatrix} \exp(-j0.81\pi) & 0.00 & 0.00 & 0.00 \\ 0.00 & 0.00 & 0.00 & \exp(-j0.22\pi) \\ 0.00 & 0.00 & \exp(-j0.73\pi) & 0.00 \\ 0.00 & \exp(+j0.45\pi) & 0.00 & 0.00 \end{bmatrix},
$$

$$
\mathbf{A}_6 = \begin{bmatrix} 0.00 & \exp(-j0.30\pi) & 0.00 & 0.00 \\ \exp(+j0.25\pi) & 0.00 & 0.00 & 0.00 \\ 0.00 & 0.00 & 0.00 & \exp(+j0.87\pi) \\ 0.00 & 0.00 & \exp(-j0.17\pi) & 0.00 \end{bmatrix},
$$

$$
\mathbf{A}_7 = \begin{bmatrix} 0.00 & 0.00 & \exp(-j0.48\pi) & 0.00 \\ \exp(-j0.58\pi) & 0.00 & 0.00 & 0.00 \\ 0.00 & \exp(-j0.98\pi) & 0.00 & 0.00 \\ 0.00 & 0.00 & 0.00 & \exp(-j0.53\pi) \end{bmatrix},
$$

$$
\mathbf{A}_8 = \begin{bmatrix} 0.00 & 0.00 & 0.00 & \exp(+j0.49\pi) \\ \exp(-j0.61\pi) & 0.00 & 0.00 & 0.00 \\ 0.00 & \exp(-j0.22\pi) & 0.00 & 0.00 \\ 0.00 & 0.00 & \exp(-j0.38\pi) & 0.00 \end{bmatrix},
$$

$$\mathbf{A}_9 = \begin{bmatrix} 0.00 & 0.00 & 0.00 & \exp(+j0.49\pi) \\ \exp(+j0.51\pi) & 0.00 & 0.00 & 0.00 \\ 0.00 & 0.00 & \exp(-j0.76\pi) & 0.00 \\ 0.00 & \exp(-j0.73\pi) & 0.00 & 0.00 \end{bmatrix},$$

$$\mathbf{A}_{10} = \begin{bmatrix} 0.00 & \exp(+j0.05\pi) & 0.00 & 0.00 \\ 0.00 & 0.00 & \exp(-j0.43\pi) & 0.00 \\ \exp(+j0.87\pi) & 0.00 & 0.00 & 0.00 \\ 0.00 & 0.00 & 0.00 & \exp(+j0.85\pi) \end{bmatrix},$$

$$\mathbf{A}_{11} = \begin{bmatrix} 0.00 & \exp(-j0.31\pi) & 0.00 & 0.00 \\ 0.00 & 0.00 & 0.00 & \exp(+j0.73\pi) \\ \exp(+j0.82\pi) & 0.00 & 0.00 & 0.00 \\ 0.00 & 0.00 & \exp(+j0.28\pi) & 0.00 \end{bmatrix},$$

$$\mathbf{A}_{12} = \begin{bmatrix} 0.00 & 0.00 & \exp(-j0.83\pi) & 0.00 \\ 0.00 & \exp(-j0.12\pi) & 0.00 & 0.00 \\ \exp(+j0.81\pi) & 0.00 & 0.00 & 0.00 \\ 0.00 & 0.00 & 0.00 & \exp(+j0.06\pi) \end{bmatrix},$$

$$\mathbf{A}_{13} = \begin{bmatrix} 0.00 & 0.00 & 0.00 & \exp(+j0.54\pi) \\ 0.00 & \exp(+j0.36\pi) & 0.00 & 0.00 \\ \exp(-j0.79\pi) & 0.00 & 0.00 & 0.00 \\ 0.00 & 0.00 & \exp(+j0.20\pi) & 0.00 \end{bmatrix},$$

$$\mathbf{A}_{14} = \begin{bmatrix} 0.00 & 0.00 & 0.00 & \exp(-j0.73\pi) \\ 0.00 & 0.00 & \exp(+j0.60\pi) & 0.00 \\ \exp(+j0.75\pi) & 0.00 & 0.00 & 0.00 \\ 0.00 & \exp(-j0.70\pi) & 0.00 & 0.00 \end{bmatrix},$$

$$\mathbf{A}_{15} = \begin{bmatrix} 0.00 & 0.00 & \exp(-j0.84\pi) & 0.00 \\ 0.00 & 0.00 & 0.00 & \exp(+j0.74\pi) \\ 0.00 & \exp(+j0.95\pi) & 0.00 & 0.00 \\ \exp(+j0.03\pi) & 0.00 & 0.00 & 0.00 \end{bmatrix},$$

$$\mathbf{A}_{16} = \begin{bmatrix} 0.00 & 0.00 & 0.00 & \exp(+j0.65\pi) \\ 0.00 & 0.00 & \exp(-j0.44\pi) & 0.00 \\ 0.00 & \exp(-j0.74\pi) & 0.00 & 0.00 \\ \exp(-j0.60\pi) & 0.00 & 0.00 & 0.00 \end{bmatrix}.$$

A.4 Power Imbalanced-Optical Spatial Modulation

The following PA factors were designed so as to maximize the constrained MI at the SNR of ρ_{target}, where we had $\left(\Phi_{\frac{1}{2}}, \Psi_{\frac{1}{2}}\right) = (15°, 45°)$ and $d_{\text{Tx}} = d_{\text{Rx}} = 10$ [cm]. The simulation parameters considered in this section were summarized in Table 5.2.

A.4.1 The PI-OSM scheme having $\mathcal{L} = 2$ and $N = 1$

$M = 2$ and $\rho_{\text{target}} = 10$ [dB]:

$$a_1 = 0.0000, \ a_2 = 2.0000.$$

$M = 2$ and $\rho_{\text{target}} = 20$ [dB]:

$$a_1 = 0.4471, \ a_2 = 1.5529.$$

$M = 4$ and $\rho_{\text{target}} = 25$ [dB]:

$$a_1 = 0.2821, \ a_2 = 0.9449, \ a_3 = 1.2249, \ a_4 = 1.5482.$$

$M = 8$ and $\rho_{\text{target}} = 0$ [dB]:

$$a_1 = 0.0000, \ a_2 = 0.0000, \ a_3 = 0.0000, \ a_4 = 0.0025, \ a_5 = 0.0026, \ a_6 = 0.0026, \ a_7 = 2.6195, \ a_8 = 5.3728.$$

$M = 8$ and $\rho_{\text{target}} = 5$ [dB]:

$$a_1 = 0.0000, \ a_2 = 0.0000, \ a_3 = 0.0000, \ a_4 = 0.0000, \ a_5 = 0.0003, \ a_6 = 1.3882, \ a_7 = 2.5537, \ a_8 = 4.0578.$$

$M = 8$ and $\rho_{\text{target}} = 10$ [dB]:

$$a_1 = 0.0000, \ a_2 = 0.0000, \ a_3 = 0.0000, \ a_4 = 0.0004, \ a_5 = 1.7027, \ a_6 = 1.7032, \ a_7 = 1.7039, \ a_8 = 2.8898.$$

$M = 8$ and $\rho_{\text{target}} = 15$ [dB]:

$$a_1 = 0.0004, \ a_2 = 0.0004, \ a_3 = 0.0004, \ a_4 = 0.7245, \ a_5 = 0.7262, \ a_6 = 1.6456, \ a_7 = 2.0886, \ a_8 = 2.8138.$$

$M = 8$ and $\rho_{\text{target}} = 20$ [dB]:

$$a_1 = 0.0001, \ a_2 = 0.0001, \ a_3 = 0.4514, \ a_4 = 0.4844, \ a_5 = 1.3874, \ a_6 = 1.5297, \ a_7 = 1.8190, \ a_8 = 2.3278.$$

$M = 8$ and $\rho_{\text{target}} = 25$ [dB]:

$$a_1 = 0.0001, \ a_2 = 0.3031, \ a_3 = 0.3035, \ a_4 = 0.9745, \ a_5 = 1.2637, \ a_6 = 1.3643, \ a_7 = 1.5783, \ a_8 = 2.2125.$$

$M = 8$ and $\rho_{\text{target}} = 30$ [dB]:

$$a_1 = 0.0001, \ a_2 = 0.1738, \ a_3 = 0.5166, \ a_4 = 0.6935, \ a_5 = 0.9073, \ a_6 = 1.4799, \ a_7 = 1.9049, \ a_8 = 2.3240.$$

$M = 8$ and $\rho_{\text{target}} = 35$ [dB]:

$a_1 = 0.1222$, $a_2 = 0.3553$, $a_3 = 0.5090$, $a_4 = 0.9202$, $a_5 = 1.2548$, $a_6 = 1.3193$, $a_7 = 1.4876$, $a_8 = 2.0316$.

$M = 16$ and $\rho_{\text{target}} = 40$ [dB]:

$a_1 = 0.0833$, $a_2 = 0.2370$, $a_3 = 0.3228$, $a_4 = 0.4230$, $a_5 = 0.5610$, $a_6 = 0.8010$, $a_7 = 0.9701$,

$a_8 = 0.9749$, $a_9 = 1.1984$, $a_{10} = 1.2815$, $a_{11} = 1.3304$, $a_{12} = 1.3306$, $a_{13} = 1.3669$, $a_{14} = 1.5413$,

$a_{15} = 1.6377$, $a_{16} = 1.9400$.

$M = 32$ and $\rho_{\text{target}} = 40$ [dB]:

$a_1 = 0.0029$, $a_2 = 0.0553$, $a_3 = 0.1439$, $a_4 = 0.1809$, $a_5 = 0.2478$, $a_6 = 0.4457$, $a_7 = 0.4458$,

$a_8 = 0.5270$, $a_9 = 0.5906$, $a_{10} = 0.6541$, $a_{11} = 0.8054$, $a_{12} = 0.8156$, $a_{13} = 0.8227$, $a_{14} = 0.8262$,

$a_{15} = 0.8900$, $a_{16} = 0.9504$, $a_{17} = 0.9818$, $a_{18} = 1.0563$, $a_{19} = 1.0602$, $a_{20} = 1.0628$, $a_{21} = 1.1912$,

$a_{22} = 1.2845$, $a_{23} = 1.3094$, $a_{24} = 1.3355$, $a_{25} = 1.4914$, $a_{26} = 1.5906$, $a_{27} = 1.5968$, $a_{28} = 1.7074$,

$a_{29} = 1.8190$, $a_{30} = 1.8836$, $a_{31} = 1.9231$, $a_{32} = 2.3020$.

$M = 64$ and $\rho_{\text{target}} = 55$ [dB]:

$a_1 = 0.0331$, $a_2 = 0.0766$, $a_3 = 0.0868$, $a_4 = 0.0914$, $a_5 = 0.1668$, $a_6 = 0.2258$, $a_7 = 0.2467$,

$a_8 = 0.2486$, $a_9 = 0.2797$, $a_{10} = 0.2952$, $a_{11} = 0.2958$, $a_{12} = 0.3049$, $a_{13} = 0.4251$, $a_{14} = 0.5236$,

$a_{15} = 0.5486$, $a_{16} = 0.5698$, $a_{17} = 0.5948$, $a_{18} = 0.6742$, $a_{19} = 0.6946$, $a_{20} = 0.7476$, $a_{21} = 0.7728$,

$a_{22} = 0.7818$, $a_{23} = 0.8441$, $a_{24} = 0.8528$, $a_{25} = 0.8687$, $a_{26} = 0.8702$, $a_{27} = 0.8829$, $a_{28} = 0.8865$,

$a_{29} = 0.9178$, $a_{30} = 0.9640$, $a_{31} = 0.9903$, $a_{32} = 1.0095$, $a_{33} = 1.0702$, $a_{34} = 1.0715$, $a_{35} = 1.1218$,

$a_{36} = 1.1276$, $a_{37} = 1.1323$, $a_{38} = 1.1560$, $a_{39} = 1.2184$, $a_{40} = 1.2648$, $a_{41} = 1.2763$, $a_{42} = 1.3332$,

$a_{43} = 1.3414$, $a_{44} = 1.3444$, $a_{45} = 1.3704$, $a_{46} = 1.3718$, $a_{47} = 1.3783$, $a_{48} = 1.4244$, $a_{49} = 1.4519$,

$a_{50} = 1.4926$, $a_{51} = 1.4929$, $a_{52} = 1.5297$, $a_{53} = 1.5368$, $a_{54} = 1.5743$, $a_{55} = 1.6122$, $a_{56} = 1.6257$,

$a_{57} = 1.6492$, $a_{58} = 1.6795$, $a_{59} = 1.6938$, $a_{60} = 1.6985$, $a_{61} = 1.7345$, $a_{62} = 1.7671$, $a_{63} = 1.7691$,

$a_{64} = 1.9184$.

$M = 128$ and $\rho_{\text{target}} = 60$ [dB]:

$a_1 = 0.0212$, $a_2 = 0.0220$, $a_3 = 0.0256$, $a_4 = 0.0293$, $a_5 = 0.0364$, $a_6 = 0.0736$, $a_7 = 0.1073$,

$a_8 = 0.1101$, $a_9 = 0.1219$, $a_{10} = 0.1308$, $a_{11} = 0.1318$, $a_{12} = 0.1326$, $a_{13} = 0.1331$, $a_{14} = 0.1403$,

$a_{15} = 0.1608$, $a_{16} = 0.1800$, $a_{17} = 0.2046$, $a_{18} = 0.2089$, $a_{19} = 0.2203$, $a_{20} = 0.2501$, $a_{21} = 0.2904$,

$a_{22} = 0.3337$, $a_{23} = 0.3359$, $a_{24} = 0.3709$, $a_{25} = 0.3711$, $a_{26} = 0.3896$, $a_{27} = 0.4165$, $a_{28} = 0.4201$,

$a_{29} = 0.4320$, $a_{30} = 0.4650$, $a_{31} = 0.4712$, $a_{32} = 0.4787$, $a_{33} = 0.4847$, $a_{34} = 0.5386$, $a_{35} = 0.5640$,

$a_{36} = 0.6050$, $a_{37} = 0.6107$, $a_{38} = 0.6261$, $a_{39} = 0.6334$, $a_{40} = 0.6559$, $a_{41} = 0.6632$, $a_{42} = 0.6770$,

$a_{43} = 0.6901$, $a_{44} = 0.6916$, $a_{45} = 0.7209$, $a_{46} = 0.7229$, $a_{47} = 0.7326$, $a_{48} = 0.7467$, $a_{49} = 0.7721$,

$a_{50} = 0.7875$, $a_{51} = 0.8002$, $a_{52} = 0.8104$, $a_{53} = 0.8160$, $a_{54} = 0.8331$, $a_{55} = 0.8477$, $a_{56} = 0.8610$,

$a_{57} = 0.8876$, $a_{58} = 0.9195$, $a_{59} = 0.9279$, $a_{60} = 0.9281$, $a_{61} = 0.9445$, $a_{62} = 0.9647$, $a_{63} = 0.9693$,

$a_{64} = 0.9943$, $a_{65} = 0.9977$, $a_{66} = 1.0014$, $a_{67} = 1.0213$, $a_{68} = 1.0363$, $a_{69} = 1.0634$, $a_{70} = 1.0712$,

$a_{71} = 1.1305$, $a_{72} = 1.1399$, $a_{73} = 1.1413$, $a_{74} = 1.1414$, $a_{75} = 1.1603$, $a_{76} = 1.1605$, $a_{77} = 1.1613$,

$a_{78} = 1.1630$, $a_{79} = 1.2215$, $a_{80} = 1.2298$, $a_{81} = 1.2553$, $a_{82} = 1.2811$, $a_{83} = 1.3022$, $a_{84} = 1.3145$,

$a_{85} = 1.3344$, $a_{86} = 1.3394$, $a_{87} = 1.3542$, $a_{88} = 1.3760$, $a_{89} = 1.4099$, $a_{90} = 1.4240$, $a_{91} = 1.4369$,

$a_{92} = 1.4506$, $a_{93} = 1.4666$, $a_{94} = 1.4843$, $a_{95} = 1.4869$, $a_{96} = 1.4883$, $a_{97} = 1.4914$, $a_{98} = 1.4953$,

$a_{99} = 1.5165$, $a_{100} = 1.5200$, $a_{101} = 1.5272$, $a_{102} = 1.5421$, $a_{103} = 1.5849$, $a_{104} = 1.5923$, $a_{105} = 1.6152$,

$a_{106} = 1.6354$, $a_{107} = 1.6402$, $a_{108} = 1.6422$, $a_{109} = 1.7334$, $a_{110} = 1.7354$, $a_{111} = 1.7357$, $a_{112} = 1.7369$,

$a_{113} = 1.7370$, $a_{114} = 1.7516$, $a_{115} = 1.7540$, $a_{116} = 1.7644$, $a_{117} = 1.7782$, $a_{118} = 1.7959$, $a_{119} = 1.8509$,

$a_{120} = 1.9199$, $a_{121} = 1.9678$, $a_{122} = 1.9923$, $a_{123} = 2.0007$, $a_{124} = 2.0192$, $a_{125} = 2.0431$, $a_{126} = 2.0564$,

$$a_{127} = 2.0587, \ a_{128} = 2.0774.$$

$M = 256$ and $\rho_{\text{target}} = 75$ [dB]:

$a_1 = 0.0023$, $a_2 = 0.0080$, $a_3 = 0.0122$, $a_4 = 0.0135$, $a_5 = 0.0220$, $a_6 = 0.0269$, $a_7 = 0.0403$,

$a_8 = 0.0500$, $a_9 = 0.0614$, $a_{10} = 0.0661$, $a_{11} = 0.0727$, $a_{12} = 0.0738$, $a_{13} = 0.0956$, $a_{14} = 0.1194$,

$a_{15} = 0.1268$, $a_{16} = 0.1309$, $a_{17} = 0.1406$, $a_{18} = 0.1640$, $a_{19} = 0.1734$, $a_{20} = 0.1811$, $a_{21} = 0.1875$,

$a_{22} = 0.2039$, $a_{23} = 0.2072$, $a_{24} = 0.2086$, $a_{25} = 0.2336$, $a_{26} = 0.2369$, $a_{27} = 0.2416$, $a_{28} = 0.2621$,

$a_{29} = 0.2668$, $a_{30} = 0.2672$, $a_{31} = 0.2694$, $a_{32} = 0.2723$, $a_{33} = 0.2731$, $a_{34} = 0.3084$, $a_{35} = 0.3105$,

$a_{36} = 0.3110$, $a_{37} = 0.3524$, $a_{38} = 0.3529$, $a_{39} = 0.3653$, $a_{40} = 0.3671$, $a_{41} = 0.3745$, $a_{42} = 0.3865$,

$a_{43} = 0.3891$, $a_{44} = 0.4124$, $a_{45} = 0.4274$, $a_{46} = 0.4347$, $a_{47} = 0.4362$, $a_{48} = 0.4434$, $a_{49} = 0.4444$,

$a_{50} = 0.4485$, $a_{51} = 0.4712$, $a_{52} = 0.5011$, $a_{53} = 0.5058$, $a_{54} = 0.5073$, $a_{55} = 0.5091$, $a_{56} = 0.5119$,

$a_{57} = 0.5159$, $a_{58} = 0.5253$, $a_{59} = 0.5273$, $a_{60} = 0.5278$, $a_{61} = 0.5346$, $a_{62} = 0.5450$, $a_{63} = 0.5478$,

$a_{64} = 0.5519$, $a_{65} = 0.5638$, $a_{66} = 0.5719$, $a_{67} = 0.5727$, $a_{68} = 0.5753$, $a_{69} = 0.5796$, $a_{70} = 0.5817$,

$a_{71} = 0.5820$, $a_{72} = 0.5904$, $a_{73} = 0.5995$, $a_{74} = 0.6036$, $a_{75} = 0.6042$, $a_{76} = 0.6049$, $a_{77} = 0.6071$,

$a_{78} = 0.6269$, $a_{79} = 0.6347$, $a_{80} = 0.6383$, $a_{81} = 0.6397$, $a_{82} = 0.6479$, $a_{83} = 0.6488$, $a_{84} = 0.6538$,

$a_{85} = 0.6782$, $a_{86} = 0.6863$, $a_{87} = 0.6886$, $a_{88} = 0.6924$, $a_{89} = 0.6941$, $a_{90} = 0.6990$, $a_{91} = 0.7023$,

$a_{92} = 0.7355$, $a_{93} = 0.7441$, $a_{94} = 0.7679$, $a_{95} = 0.7727$, $a_{96} = 0.7778$, $a_{97} = 0.7939$, $a_{98} = 0.7969$,

$a_{99} = 0.7980$, $a_{100} = 0.8161$, $a_{101} = 0.8207$, $a_{102} = 0.8249$, $a_{103} = 0.8364$, $a_{104} = 0.8523$, $a_{105} = 0.8548$,

$a_{106} = 0.8555$, $a_{107} = 0.8593$, $a_{108} = 0.8657$, $a_{109} = 0.8762$, $a_{110} = 0.8786$, $a_{111} = 0.8874$, $a_{112} = 0.9005$,

$a_{113} = 0.9052$, $a_{114} = 0.9100$, $a_{115} = 0.9421$, $a_{116} = 0.9477$, $a_{117} = 0.9512$, $a_{118} = 0.9617$, $a_{119} = 0.9629$,

$a_{120} = 0.9715$, $a_{121} = 0.9787$, $a_{122} = 0.9809$, $a_{123} = 0.9907$, $a_{124} = 1.0110$, $a_{125} = 1.0215$, $a_{126} = 1.0255$,

$a_{127} = 1.0275$, $a_{128} = 1.0283$, $a_{129} = 1.0555$, $a_{130} = 1.0572$, $a_{131} = 1.0696$, $a_{132} = 1.0779$, $a_{133} = 1.0966$,

$a_{134} = 1.1136$, $a_{135} = 1.1149$, $a_{136} = 1.1279$, $a_{137} = 1.1294$, $a_{138} = 1.1298$, $a_{139} = 1.1345$, $a_{140} = 1.1364$,

$a_{141} = 1.1391$, $a_{142} = 1.1442$, $a_{143} = 1.1486$, $a_{144} = 1.1543$, $a_{145} = 1.1632$, $a_{146} = 1.1636$, $a_{147} = 1.1658$,

$a_{148} = 1.1774$, $a_{149} = 1.1868$, $a_{150} = 1.1961$, $a_{151} = 1.1991$, $a_{152} = 1.2009$, $a_{153} = 1.2152$, $a_{154} = 1.2161$,

$a_{155} = 1.2249$, $a_{156} = 1.2344$, $a_{157} = 1.2436$, $a_{158} = 1.2513$, $a_{159} = 1.2562$, $a_{160} = 1.2578$, $a_{161} = 1.2652$,

$a_{162} = 1.2767$, $a_{163} = 1.2770$, $a_{164} = 1.2831$, $a_{165} = 1.2892$, $a_{166} = 1.2933$, $a_{167} = 1.3025$, $a_{168} = 1.3161$,

$a_{169} = 1.3189$, $a_{170} = 1.3266$, $a_{171} = 1.3348$, $a_{172} = 1.3449$, $a_{173} = 1.3464$, $a_{174} = 1.3488$, $a_{175} = 1.3515$,

$a_{176} = 1.3558$, $a_{177} = 1.3647$, $a_{178} = 1.3681$, $a_{179} = 1.3690$, $a_{180} = 1.3692$, $a_{181} = 1.3725$, $a_{182} = 1.3792$,

$a_{183} = 1.3808$, $a_{184} = 1.3919$, $a_{185} = 1.4006$, $a_{186} = 1.4180$, $a_{187} = 1.4255$, $a_{188} = 1.4317$, $a_{189} = 1.4360$,

$a_{190} = 1.4412$, $a_{191} = 1.4446$, $a_{192} = 1.4503$, $a_{193} = 1.4595$, $a_{194} = 1.4732$, $a_{195} = 1.4785$, $a_{196} = 1.4828$,

$a_{197} = 1.4889$, $a_{198} = 1.4964$, $a_{199} = 1.5232$, $a_{200} = 1.5287$, $a_{201} = 1.5322$, $a_{202} = 1.5407$, $a_{203} = 1.5419$,

$a_{204} = 1.5478$, $a_{205} = 1.5500$, $a_{206} = 1.5570$, $a_{207} = 1.5614$, $a_{208} = 1.5695$, $a_{209} = 1.5774$, $a_{210} = 1.5828$,

$a_{211} = 1.5848$, $a_{212} = 1.5867$, $a_{213} = 1.5919$, $a_{214} = 1.6048$, $a_{215} = 1.6113$, $a_{216} = 1.6220$, $a_{217} = 1.6225$,

$a_{218} = 1.6257$, $a_{219} = 1.6311$, $a_{220} = 1.6419$, $a_{221} = 1.6577$, $a_{222} = 1.6603$, $a_{223} = 1.6640$, $a_{224} = 1.6672$,

$a_{225} = 1.6695$, $a_{226} = 1.6757$, $a_{227} = 1.6814$, $a_{228} = 1.7085$, $a_{229} = 1.7107$, $a_{230} = 1.7113$, $a_{231} = 1.7131$,

$a_{232} = 1.7139$, $a_{233} = 1.7165$, $a_{234} = 1.7205$, $a_{235} = 1.7307$, $a_{236} = 1.7307$, $a_{237} = 1.7358$, $a_{238} = 1.7550$,

$a_{239} = 1.7755$, $a_{240} = 1.7828$, $a_{241} = 1.7879$, $a_{242} = 1.7907$, $a_{243} = 1.7965$, $a_{244} = 1.8036$, $a_{245} = 1.8055$,

$a_{246} = 1.8090$, $a_{247} = 1.8119$, $a_{248} = 1.8146$, $a_{249} = 1.8191$, $a_{250} = 1.8222$, $a_{251} = 1.8230$, $a_{252} = 1.8307$,

$a_{253} = 1.8335$, $a_{254} = 1.8386$, $a_{255} = 1.8390$, $a_{256} = 1.8653$.

A.4.2   The PI-OSM scheme having $\mathcal{L} = 2$ and $N = 2$

$M = 8$ and $\rho_{\text{target}} = 0$ [dB]:

$a_1 = 0.0000$, $a_2 = 0.0000$, $a_3 = 0.0000$, $a_4 = 0.0025$, $a_5 = 0.0026$, $a_6 = 0.0026$, $a_7 = 3.1826$, $a_8 = 4.8098$.

$M = 8$ and $\rho_{\text{target}} = 5$ [dB]:

$a_1 = 0.0000$, $a_2 = 0.0000$, $a_3 = 0.0000$, $a_4 = 0.0002$, $a_5 = 0.0002$, $a_6 = 2.2256$, $a_7 = 2.2261$, $a_8 = 3.5479$.

$M = 8$ and $\rho_{\text{target}} = 10$ [dB]:

$a_1 = 0.0003$, $a_2 = 0.0004$, $a_3 = 0.0004$, $a_4 = 0.5277$, $a_5 = 0.9098$, $a_6 = 1.6007$, $a_7 = 2.0669$, $a_8 = 2.8939$.

$M = 8$ and $\rho_{\text{target}} = 15$ [dB]:

$a_1 = 0.0003$, $a_2 = 0.0003$, $a_3 = 0.0003$, $a_4 = 0.6511$, $a_5 = 0.6514$, $a_6 = 1.6993$, $a_7 = 2.1234$, $a_8 = 2.8739$.

$M = 8$ and $\rho_{\text{target}} = 20$ [dB]:

$a_1 = 0.0000$, $a_2 = 0.3065$, $a_3 = 0.3067$, $a_4 = 0.9809$, $a_5 = 1.1110$, $a_6 = 1.3154$, $a_7 = 1.5546$, $a_8 = 2.4248$.

$M = 8$ and $\rho_{\text{target}} = 25$ [dB]:

$a_1 = 0.0001$, $a_2 = 0.2315$, $a_3 = 0.6903$, $a_4 = 0.9682$, $a_5 = 1.0827$, $a_6 = 1.1940$, $a_7 = 1.5896$, $a_8 = 2.2436$.

$M = 8$ and $\rho_{\text{target}} = 30$ [dB]:

$a_1 = 0.1332$, $a_2 = 0.3956$, $a_3 = 0.6015$, $a_4 = 1.0191$, $a_5 = 1.1330$, $a_6 = 1.3600$, $a_7 = 1.5272$, $a_8 = 1.8305$.

$M = 8$ and $\rho_{\text{target}} = 35$ [dB]:

$a_1 = 0.1553$, $a_2 = 0.4364$, $a_3 = 0.5983$, $a_4 = 1.0681$, $a_5 = 1.1624$, $a_6 = 1.3391$, $a_7 = 1.4870$, $a_8 = 1.7534$.

A.4.3   The Irr-PI-OSM scheme having $M = 8$ and $N = 4$

$\mathcal{L} = 1$ and $\rho_{\text{target}} = 10$ [dB]:

$a_1 = 0.0066$, $a_2 = 0.0115$, $a_3 = 0.4432$, $a_4 = 0.5131$, $a_5 = 0.9763$, $a_6 = 1.3804$, $a_7 = 1.9080$, $a_8 = 2.7609$.

$\mathcal{L} = 128$ and $\rho_{\text{target}} = 10$ [dB]:

$a_1 = 0.0032$, $a_2 = 0.0095$, $a_3 = 0.4484$, $a_4 = 0.7470$, $a_5 = 1.0967$, $a_6 = 1.3201$, $a_7 = 1.7125$, $a_8 = 2.6625$.

Index

Author Index